Characterising the broadband polarisation properties of extragalactic radio sources at 3 GHz

Dissertation
zur
Erlangung des Doktorgrades (Dr. rer. nat.)
der
Mathematisch-Naturwissenschaftlichen Fakultät
der
Rheinischen Friedrich-Wilhelms-Universität Bonn

vorgelegt von
Shilpa Ranchod
aus
Kapstadt, Südafrika

Bonn, 24.11.2025

Angefertigt mit Genehmigung der Mathematisch-Naturwissenschaftlichen Fakultät der Rheinischen Friedrich-Wilhelms-Universität Bonn

Gutachter/Betreuer:	Prof. Dr. Michael Kramer
Gutachter:	Prof. Dr. Cristiano Porciani
Tag der Promotion:	30.04.2026
Erscheinungsjahr:	2026

Abstract

Magnetic fields are ubiquitous in the Universe and are fundamentally linked to galaxy evolution, influencing star-formation, cosmic-ray propagation and feedback mechanisms. The radio frequency regime, at centimetre wavelengths, is a powerful probe of cosmic magnetic fields through the detection of galaxies emitting linearly polarised synchrotron emission. The Faraday rotation measure (RM) of this emission can be used to study the properties of both the emitting source and the intervening magneto-ionic media (e.g. the Galactic interstellar medium). Large, dense samples of polarised extragalactic sources form RM grids that can be used to map the foreground magnetic field of the Milky Way. Over the past few years, the increasing sensitivity of modern interferometers has given new accessibility to the μJy radio sky, increasing the RM sky density. It is therefore key to establish a clear understanding of the faint polarised source population and the foreground effects that shape RM measurements. Broadband spectro-polarimetry provides an enhanced perspective on this, revealing Faraday complexities in the Stokes Q and U spectral behaviour, which trace turbulence or differential Faraday rotation along the line-of-sight. Through the projects presented in this thesis, I aim to address two important factors in improving our interpretation of RM grid experiments, (i) understanding both the observational biases and physical nature of Faraday complexity at low Galactic latitudes, (ii) characterising the extragalactic polarised source population.

Firstly, in analysing the SPASS/ATCA RM catalogue (Schnitzeler et al., 2019), the most extensive broadband polarisation catalogue in the southern sky, we report a Galactic latitude dependence of Faraday complexity for polarised sources at $|b| < 10^{\circ}$, with the degree of complexity increasing towards the Galactic plane. Through higher angular resolution ($\theta = 15''$) follow-up observations of 95 sources, we find that this trend is primarily driven by contamination from large-scale Galactic polarised emission in the SPASS/ATCA spectra, which we effectively filter out. We find 42% of the observed sources in our sample are Faraday complex, with an increased fraction of Faraday complex sources surrounding the spiral arm tangents and towards the Galactic centre. We constrain the scale of this complexity to < 2.4 pc, consistent with turbulent injection scales in the spiral arms. These results emphasise the importance of broadband spectro-polarimetric observations to fully characterise small-scale and/or turbulent structures in the Galactic magnetic field, and that it is essential to correctly filter contaminating polarised emission when interpreting foreground turbulence.

Secondly, we reprocess the VLA-COSMOS 3 GHz Large Project (Smolčić et al., 2017a), one of the deepest S-band continuum surveys (2.3 μJy beam^{-1}), for polarisation calibration and imaging. Here, we present the deepest polarised source count at 3 GHz to date, and the second deepest overall, returning an RM density of 42 deg^{-2}. We find that these source counts are consistent with those

at the more typically-studied 1.4 GHz band, a combined effect of spectral index and depolarisation, which we attribute to differential Faraday rotation in the lobes of radio galaxies. Through the available multi-wavelength catalogues, we identify all polarised sources as radio galaxies (i.e. active galactic nuclei), and confirm that no star-forming galaxies are detected in polarisation. We place an upper limit on the density of polarised star-forming galaxies to be < 0.58 deg^{-2}, implying that surveys much deeper than 2.6 μJy beam^{-1} will be required to readily probe this population, even at higher frequencies where Faraday depolarisation effects are less pronounced.

Finally, I present a demonstrator project with the recently installed MeerKAT S-band receivers, with a focus on extragalactic wide-field imaging. We present MeerKAT S-band observations of the DEEP2 field, the emptiest radio field in the southern sky. The total intensity source counts are consistent with those from the literature, and also show that only a fraction of integration time is required with MeerKAT for comparable results with legacy S-band surveys. Here, I also present the science goals and survey design for the MeerKAT+ S-band Legacy survey, a 3000 hour, full-Stokes survey of the southern sky at Dec $\leq -40^{\circ}$. This survey will be extremely versatile across Galactic, galaxy evolution, magnetism and transient science, and with an expected 10^5 polarised source detections, will provide a higher frequency perspective on the RM grid of the southern sky.

To my Aji and Aja

Acknowledgements

This work would not have been possible without those who have guided me, and provided scientific or emotional support over the past four years.

First, I would like to thank my advisor, Sui Ann Mao for giving me the opportunity to work on these exciting projects. Your guidance and encouragement throughout this PhD has kept me motivated to push myself further and has greatly contributed to my development in becoming an independent researcher.

To my co-advisor, Roger Deane, thank you for your insight and guidance over the past 7 years, and for motivating me to pursue a PhD. I always appreciate your advice and input regarding science, writing and my career. Thank you for always welcoming me at Wits and UP (and your generosity in terms of computing resources!), and keeping me connected to the South African astronomy community.

Thank you to my official supervisor, Michael Kramer for your guidance and leadership, and for giving me this opportunity. It has been enriching being part of your wonderful, active research group.

To Hans-Rainer Klöckner, thank you for my being my "adopted" advisor for part of my PhD and for looking out for me. It was certainly an interesting time working together, and I enjoyed our conversations about radio astronomy and life.

A big thank you to the postdocs that were involved in my thesis and have been extremely helpful along the way and provided constructive feedback on paper drafts. Particularly to Sarrvesh, who guided me into the world of polarisation and magnetism at the very beginning. To Jackie, for sharing your expertise on observing with ATCA and Galactic magnetism. To Ancor, for many conversations regarding data processing. To Jack, for many in depth discussions surrounding Faraday complexity that were extremely helpful. To Jonah, for the help with source counts, completeness and statistics.

Thank you to other senior researchers in the fundi group and elsewhere that have played some part in bringing this thesis together. To Rainer Beck, for many helpful conversations about cosmic magnetism. Your expert input on my work and paper manuscripts is really appreciated. To Aritra Basu, for teaching me so much about the intricacies of polarisation data calibration and for your input on my observing proposals. To Vernesa Smolčić and Larry Rudnick for your input on the VLA-COSMOS project and Olaf Wucknitz for your contribution to the DEEP2 project. Thank you to David Champion for your constructive feedback on presentations and your help in my preparation for postdoc interviews and to Ramesh Karuppusamy for coming to the rescue during a big computing crisis.

I have been lucky to have great office mates throughout my PhD, who all contributed to making this experience a lot more fun. Thank you to the "cool office", Miquel, Jaswanth and Jonah for being my first friends in Bonn, and for the endless laughs and shenanigans in the first year. Although a short time, to Kathrin and Jedrzej for also being great company in that office in the corner. A very big thank you to my long term office mate and "mommy chicken" Isabella. You have been such a source of inspiration, support, and mentorship. I am very glad to have had you by my side.

Thank you to the friends I have made at MPIfR, particularly to my gals, Arunima and Denisha. Thank you for always being there to listen to my rants, your support over the difficult times, the constant supply of snacks. Your friendship means a lot to me, and I will miss you so much. To Miquel, you have taught me more about life than you may know. To Ferdi, Surya, Jaswanth, Kathrin, Jedrzej, Tim, Timea, Jompoj, Andrei, Joscha, Lynn, Kamalpreet, Lucy and the rest of the fundi group, past and present, thank you for making this such a wonderful, entertaining environment to work in over the past few years. A special thank you to Robert Wharton for inspiring the final sentences of my thesis.

I would also like to thank the group secretaries, Kira and Silvia, and the other administrative staff, Tuyet-Le Tran and Barbara Menten, for making the transition to living in Germany so much easier. I appreciate all your help in booking trips and all the other bureaucracy over my time at MPIfR. Thank you to IMPRS, and the coordinators for financial support over the years.

Thank you to my parents and my brothers for their constant support. Particularly to my parents, for being such a great source of emotional support and strength over the hard times, and for encouraging me to pursue this PhD despite it moving me to the other side of the world.

Finally, to my special collaborator, Jonah. Thank you for being my biggest supporter, both in my PhD and outside of work. I truly could not have done this without you.

Contents

CHAPTER 1

Introduction

Magnetic fields are ubiquitous in the Universe. Evidence of their presence has been found across a full range of astrophysical scales, from the km scales of pulsars (Lorimer and Kramer, 2012), to the Mpc scales of galaxy clusters (Carilli and Taylor, 2002). On the ~kpc scales of galaxies, they are embedded in the interstellar medium (ISM; Heiles and Haverkorn, 2012) and are fundamentally involved in the regulation of star-formation, the transport of charged particles and the feedback processes in galaxies. As such, they have a key role in galaxy formation and evolution. Despite this, our understanding of magnetic fields in galaxies is largely incomplete, as they cannot be directly observed. Rather, we rely on studying the effect they have on their surroundings and the electromagnetic radiation emitted by magnetised astrophysical objects, which can be most effectively probed at radio frequencies.

A powerful method of measuring cosmic magnetic fields is through the Faraday rotation of linearly polarised synchrotron radiation emitted from extragalactic sources, typically distant active galactic nuclei (AGN). This effectively probes the magnetic field structure of these galaxies, as well as magneto-ionic media along the line of sight. In this thesis, I will employ this method to provide new insight into the magnetic field properties of the extragalactic source population and the effect of the intervening magnetised ISM of the Milky Way. As I will detail in this chapter, I also aim to leverage the relatively unexplored 3 GHz frequency window and the capabilities of modern radio telescopes to provide a higher frequency perspective on the faint polarised radio sky.

1.1 The radio continuum sky

The radio frequency regime offers a vastly different perspective on the Universe in comparison to the optical part of the electromagnetic spectrum. While the extent of the densest part of the Milky Way remains the brightest part of the sky at radio frequencies (e.g. Figure 1.1; Haslam et al., 1982), it is not dominated by starlight, but rather the diffuse ionised gas in the interstellar medium. In fact, the majority of stars in our galaxy do not emit significant radiation in the radio (with some exceptions, e.g. pulsars). In addition, the entire sky is populated by bright *extragalactic* radio sources, consisting of the powerful active galactic nuclei of galaxies whose relativistic jets emit synchrotron radiation, as well as galaxies undergoing star-formation, emitting via a combination of thermal and non-thermal processes.

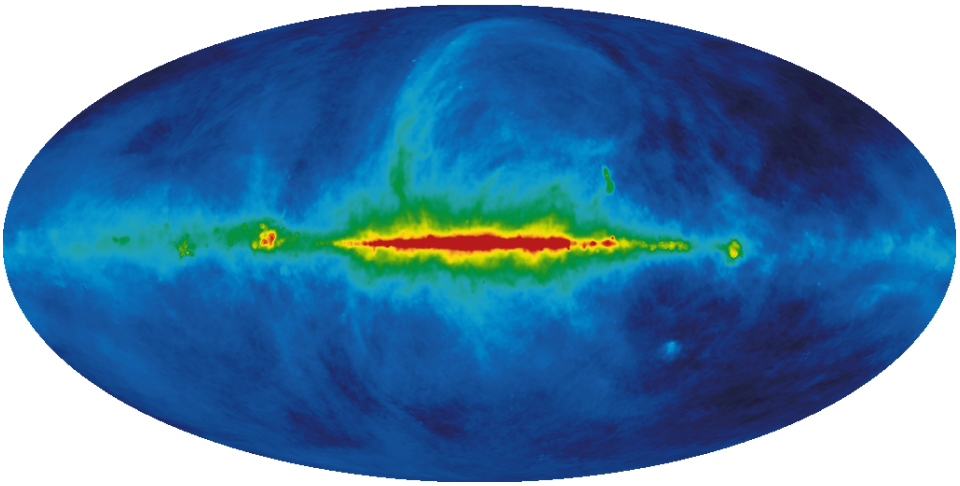

Figure 1.1: The Haslam et al. (1982) map of the full radio sky taken at 408 MHz using the Effelsberg 100 m Telescope, the Parkes 64 m Telescope and the Jodrell Bank MkI and MkIA telescopes. The map is shown in Galactic coordinates and is colourised in log scale from 10 to 250 K. The radio sky is dominated by Galactic synchrotron emission, brightest around the Galactic plane.

Synchrotron radiation is particularly important in this thesis, as it is a signature of cosmic magnetic fields. The physics of synchrotron radiation is detailed in textbooks, such as *Radiative Processes in Astrophysics* by Rybicki and Lightman (1979) and here I will summarise the key concepts relevant in this work. In brief, synchrotron radiation is produced by relativistic electrons spiralling, or accelerating, around magnetic field lines. It is therefore also referred to as non-thermal radiation. To break this down, we understand from Maxwell's equations that accelerated charged particles will produce radiation. When particles encounter a magnetic field, they are forced into a helical trajectory around the magnetic field lines due to the Lorentz force. In cases where the particle velocity v is much smaller than the speed of light c, the particle follows this trajectory at a constant velocity. However, as I will introduce in the following section, the particles we are interested in, typically electrons, originate from highly energetic environments, and therefore have relativistic speeds. This results in the emission of synchrotron radiation when they are subjected to the Lorentz force, beamed in the direction of motion of the electron. The total power P of the synchrotron radiation emitted by a relativistic electron is

$$P = \frac{2}{3} \frac{e^4 \gamma^2 B_\perp^2}{m_0 c^3}, \tag{1.1}$$

where e is the charge of the electron, γ is the Lorentz factor, $B_\perp$ is the component of the magnetic field perpendicular to the line of sight (e.g. on the plane of the sky) and m_0 is the rest electron mass. For emission at radio frequencies, $\gamma \sim 10^4$. This radiation will have the maximum power at a critical frequency ν_c, given by

$$\nu_c = \frac{3}{4\pi} \frac{e B_\perp \gamma^2}{m_0 c}. \tag{1.2}$$

In radio observations, we have to consider the combined radiation of an ensemble of electrons with a broad distribution of energies $N(E)$, given as a power law,

$$N(E)\mathrm{d}E \propto E^{\delta}\mathrm{d}E, \tag{1.3}$$

where δ is the energy distribution index. Observations show that the spectrum of a synchrotron-emitting object is continuous over a large range of radio frequencies ($\sim$100 MHz $\lesssim \nu \lesssim$ 100 GHz), similarly following a power law,

$$S(\nu) \propto \nu^{\alpha}, \tag{1.4}$$

where $S(\nu)$ is the measured flux density at a given frequency and α is the spectral index which is related to the energy distribution index with $\alpha = (1+\delta)/2$.

A key property of synchrotron radiation, central to this thesis, is that it is linearly polarised. The plane of polarisation is perpendicular to the magnetic field and the degree of polarisation, or fractional polarisation p is given as

$$p = \frac{3\delta - 3}{3\delta + 7} = \frac{3\alpha - 3}{3\alpha - 5}. \tag{1.5}$$

For typical synchrotron values of $\delta = -2.4$ (or $\alpha = -0.7$), the maximum fractional polarisation is $p \approx 72\%$. This requires an absolutely uniform magnetic field, and the observed degree of polarisation is usually significantly lower, with $p \sim 10\%$, as astrophysical magnetic fields are not typically ordered. The presence of disordered or random magnetic fields varying across the limited telescope beam, as well as Faraday effects (Section 1.2.1) result in depolarisation (detailed in Chapter 2). As such, the degree of polarisation is a key observable in understanding the magnetic field geometry and ordering in astrophysical radio sources.

1.1.1 Radio source populations

Historically, untargeted surveys of the radio sky have revealed that discrete radio sources emit over a large range of flux densities and are distributed over cosmological distances (e.g. Condon, 1984). Radio source counts can be used to study the distribution of underlying extragalactic source populations. Traditionally, these are represented as Euclidean-normalised differential counts, depicted in Figure 1.2. This shows the number of sources N per bin, centred at a given flux density S, expressed differentially as $\mathrm{d}N/\mathrm{d}S$. The Euclidean normalisation factor $S^{5/2}$ describes a uniform source distribution in a spherical volume ($V \propto r^3$) for radius r, assuming a static Euclidean Universe[1]. Following this assumption, a source at a distance r will have a flux density $S \propto r^{-2}$. As a result, the differential number counts in such a Universe should have

$$\frac{\mathrm{d}N}{\mathrm{d}S} \propto S^{-5/2}, \tag{1.6}$$

[1] Ryle and Scheuer (1955) used the radio source counts to show a deviation from the non-evolving static Euclidean Universe, important evidence supporting the expanding Universe. In the Euclidean-normalised counts shown in Figure 1.2, the monotonic decrease towards fainter flux densities similarly shows a deviation from the horizontal distribution expected for a static Universe.

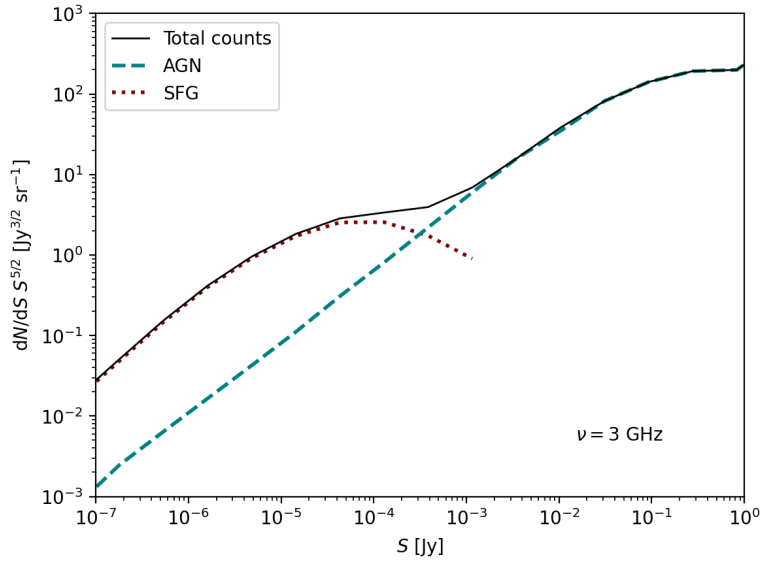

Figure 1.2: Euclidean-normalised differential source counts at a frequency of 3 GHz. The total source counts are shown by the black solid line. The counts for the AGN and SFG populations are indicated by the teal dashed line and the maroon dotted line, respectively. These source counts are produced from the Tiered Radio Extragalactic Continuum Simulation (T-RECS; Bonaldi et al., 2019).

and after Euclidean-normalisation, should be a horizontal line.

Large area legacy sky surveys e.g. the NRAO VLA Sky Survey (NVSS; Condon et al., 1998), constrained the flux density distribution of the extragalactic source population for $S \gtrsim 1$ mJy. While the faint, sub-mJy source population requires significantly longer observation times to be detected over large, cosmologically significant sky areas, it has been probed through deep observations of smaller sky regions (e.g. Smolčić et al., 2017a), and is becoming readily more accessible with the improved sensitivities of modern radio telescopes (e.g. Matthews et al., 2021b; Hale et al., 2023). Figure 1.2 shows that the source counts are divided into two distinct populations. The bright active galactic nuclei (AGN)-powered population that dominates at $S \gtrsim 1$ mJy, and the fainter population of star-forming galaxies (SFGs) at $S \lesssim 0.1$ mJy.

Active Galactic Nuclei

Active galactic nuclei are formed when material is accreted onto the central super-massive black hole of a galaxy, resulting in highly collimated relativistic jets being launched from the vicinity of the black hole perpendicular to the accretion disk (Begelman et al., 1984). The launching of these jets is dependent on a strong magnetic field (with magnetic field strength B) around a spinning black hole, and the power of the jets P is proportional to B^2 (Blandford and Znajek, 1977). These powerful sources emit brightly across the electromagnetic spectrum, and historically have been classified into various taxonomies according to their observed morphologies, spectral properties, and associated emission lines (Kauffmann et al., 2003; Best and Heckman, 2012). The physical origin of these differences is an active area of research and current theories describe a single unified model, where properties differ according to the viewing

angle (Urry and Padovani, 1995). Due to their bright synchrotron emission, we understand that AGN are magnetised objects, for which under the correct conditions, we observe to be linearly polarised (Saikia and Salter, 1988).

At GHz frequencies, we observe two main classifications of AGN, namely quasars and radio galaxies. Quasars are the extremely bright, synchrotron-emitting centres of galaxies appearing as point sources (e.g. Matthews and Sandage, 1963). They can be described as AGN viewed almost face-on, and their bright central regions outshine any other components of the galaxy. In contrast, radio galaxies are viewed edge-on, consisting of a bright core and synchrotron-emitting jets that feed relativistic plasma into lobes. Radio galaxies can be further classified by their Fanaroff-Riley (FR; Fanaroff and Riley, 1974) morphology, examples of which are shown in Figure 1.3. FRI-type galaxies are "core-dominated" or "edge-darkened", exhibiting bright cores. Their jets are relatively less collimated, while flaring out and becoming fainter towards the edge of the lobes. FRII-type galaxies typically have higher luminosities than FRI galaxies. They are "lobe-dominated" or "edge-brightened" and have more collimated jets and distinct hotspots in their lobes where the jets terminate. With limited angular resolution, these sources can be observed as triple (or double, when the core is no longer active) point sources. Even when unresolved, linearly polarised AGN are a powerful probe for intergalactic and Galactic magnetic fields, through Faraday rotation (Section 1.2.1). These sources have large observed fractional polarisations ($p_{3\ \mathrm{GHz}} \sim 0.15$; e.g. Clarke et al., 1992; O'Sullivan et al., 2017), a result of their ordered magnetic field geometry, as revealed via the polarisation angle of polarised synchrotron emission (e.g. Figure 1.4). The fractional polarisation typically increases towards the edge of the radio lobes in FRII sources (e.g. Elmouttie et al., 1995), a result of magnetic field compression as the lobe interacts with the surrounding media (more typically in dense cluster or group environments for FRI galaxies, e.g. Laing et al., 2011). Due to their large fractional polarisation and high intrinsic luminosity, these sources are readily detected in polarisation up to high redshifts ($z \sim 3$; e.g. O'Sullivan et al., 2017).

Star-forming galaxies

Star-forming galaxies (SFGs) are more prevalent at the faint end of the radio flux density distribution. These sources generally contain a large reservoir of cold atomic and molecular gas that fuels star-formation. In a prototypical spiral galaxy (e.g. M51, see Figure 1.5), a fair proportion (approximately 25%; Condon, 1992) of the radio continuum emission is attributed to the free-free (thermal) emission from the hot, ionised gas surrounding young stars (HII regions). However, synchrotron emission dominates, giving SFGs a characteristic spectral index of $\alpha = -0.7$ (e.g. Klein et al., 2018)[2]. This is produced by cosmic ray electrons being accelerated through the magnetised ISM by energetic supernova explosions. According to current theories, supernovae have a key role in the generation of galaxy-scale magnetic fields (Gressel et al., 2008). They inject small-scale turbulence into the ISM, amplifying the weak seed magnetic fields. These "turbulent" magnetic fields can be directly traced by unpolarised synchrotron emission and are intimately linked to star formation, as observed from the tight infrared–radio correlation (Bell, 2003, where the infrared luminosity is a direct tracer of star formation). Spiral galaxies also contain a large-scale ordered magnetic field, a combined effect of the turbulent motion and the differential rotation of the galaxy, called the $\alpha - \Omega$ dynamo (Ruzmaikin et al., 1988; Beck et al., 1996). For nearby galaxies ($z < 0.01$), the ordered field is typically strongest in the inter-arm regions and in extreme

[2] SFGs don't always host AGN, but even when they do, the star-formation-powered synchrotron radiation dominates at radio frequencies.

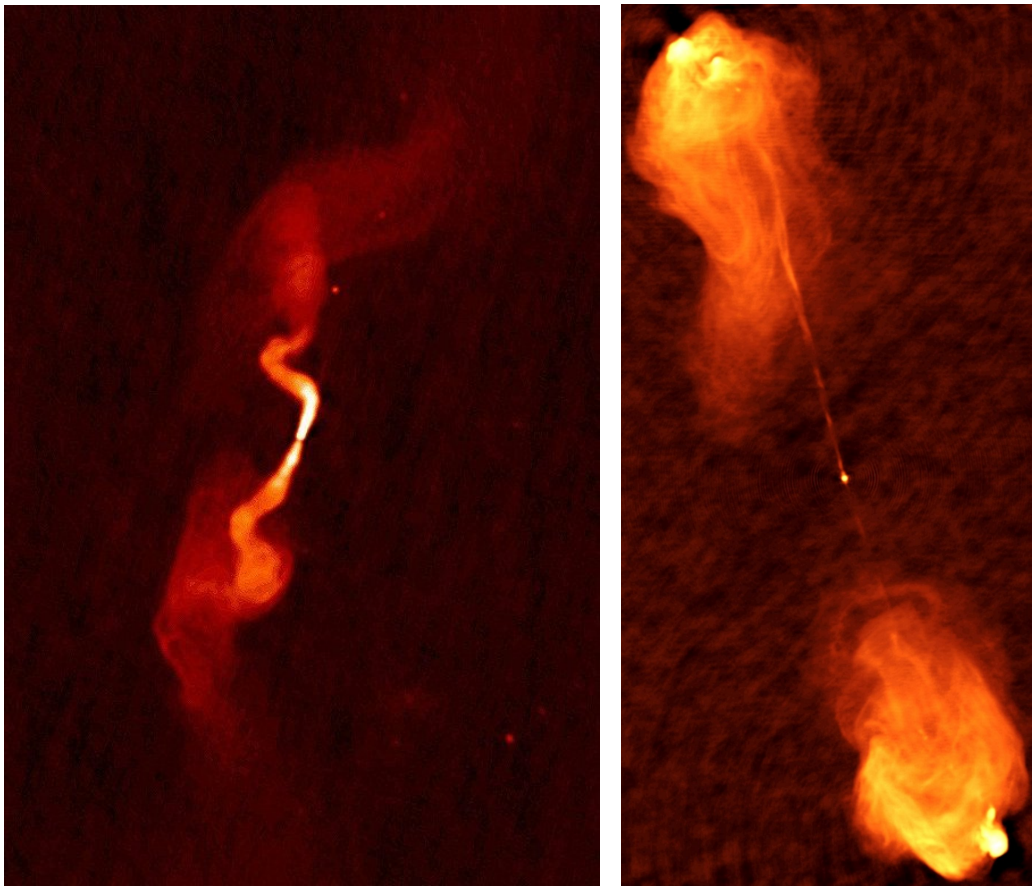

Figure 1.3: Examples of Fanaroff-Riley radio galaxies. *Left:* FRI galaxy 3C 31 (Laing et al., 2008). *Right:* FRII galaxy Cygnus A (Perley et al., 1984). Both images were produced using the Karl G. Jansky Very Large Array (VLA) at 1.4 GHz.

cases can result in fractional polarisations up to 50%. However, due to a combination of Faraday and systematic effects (Sokoloff et al., 1998, detailed in Chapter 2), the fractional polarisation of unresolved star-forming galaxies diminishes to $\lesssim 5\%$ (e.g. Stil et al., 2009; Sun and Reich, 2012), and as a result, this population, already faint in total intensity, is even more difficult to detect in linear polarisation. To date, deep polarisation surveys at 1.4 GHz have not directly detected the star-forming polarised population, classifying all of their detected sources as AGN (e.g. Taylor et al., 2024; Loi et al., 2025). Therefore, it is not well-constrained which sensitivity is required to readily detect the SFG population in polarisation (O'Sullivan et al., 2008), and whether higher frequencies and angular resolutions might more effectively probe this faint source population (e.g. Sun and Reich, 2012).

There remains much to be discovered about the role of magnetic fields in the evolution of both AGN and SFGs. The observation of linearly polarised synchrotron emission is key for understanding the magnetic field geometry and ordering within these sources (Baldwin et al., 1970; Bridle and Perley, 1984). Such observations can be used to address open questions about the physical nature of the faint polarised population, such as the prevalence of AGN with various radiative modes, and how magnetic

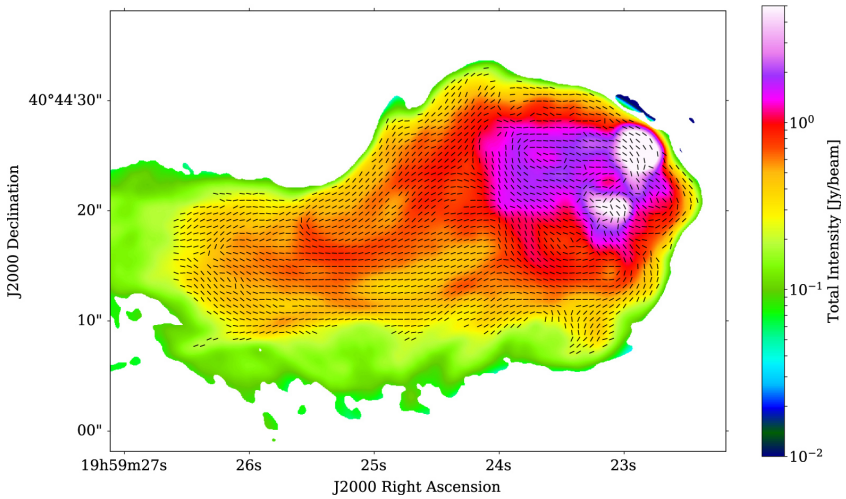

Figure 1.4: Total intensity emission of one of the radio lobes of Cygnus A, obtained with using the VLA at 4 GHz, directly reproduced from Sebokolodi et al. (2020). The black vectors trace out the magnetic field geometry of the radio lobe.

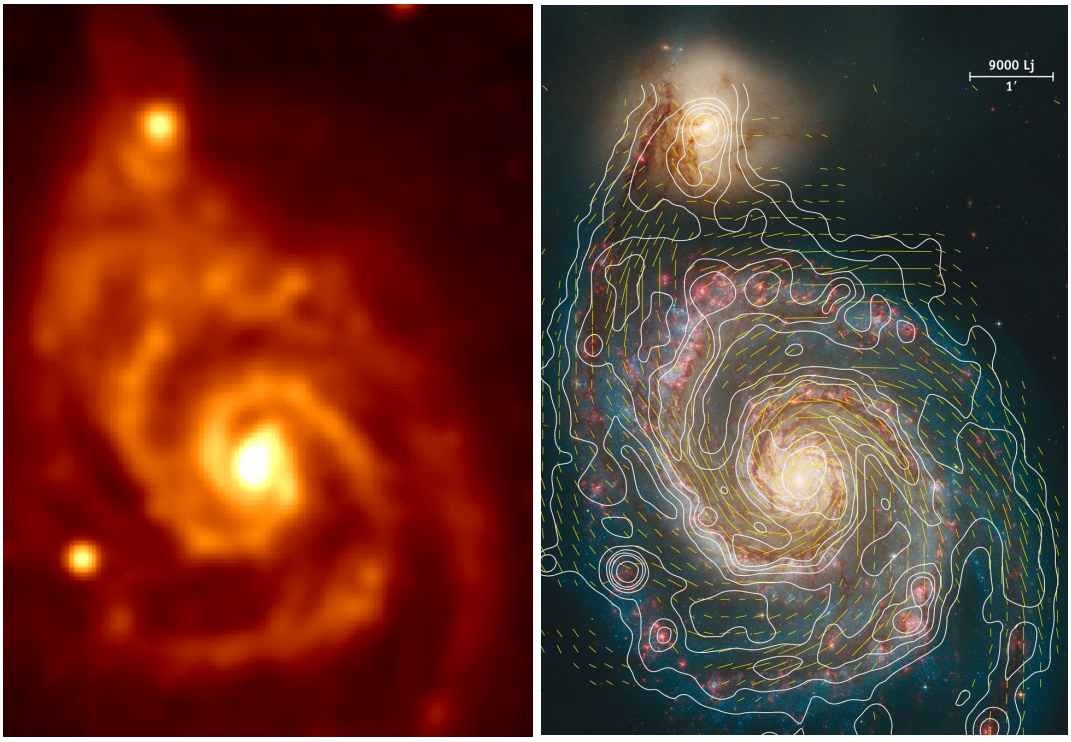

Figure 1.5: *Left:* Radio continuum image of prototypical face-on spiral galaxy M51, produced by the VLA at 1.4 GHz (Fletcher et al., 2011). *Right:* The same radio continuum image plotted as contours on the *Hubble Space telescope* colour composite image at optical wavelengths (NASA/ESA/Hubble Heritage Team). The yellow vectors trace out the magnetic fields, inferred through observed linearly polarised synchrotron emission (Fletcher et al., 2011).

field ordering is related to the morphology of AGN and the environment of their host galaxies. With deep surveys into the μJy regime only *recently* accessible with modern radio telescopes, a new parameter space has been opened to detect a statistically significant sample of linearly polarised extragalactic sources, which will enable us to trace their characteristics and evolution as a population. Similar to total intensity source counts, the Euclidean-normalised *polarised* source counts are an important diagnostic for understanding the contribution of various source populations to the polarised radio sky, and their representative degree of polarisation (e.g. Tucci and Toffolatti, 2012; Hales et al., 2014). While understanding the composition of the polarised source population is important in the physical context of galaxy evolution as well as the practical context of designing future surveys (e.g. O'Sullivan et al., 2008), the detection of large samples of polarised sources has much broader scientific relevance in terms of cosmic magnetism, as I will detail in the following sections.

1.2 Our Galactic vantage point

Our galaxy, the Milky Way, is an ideal target for studying astrophysical magnetic fields over a large range of scales (for a review, see Haverkorn, 2015). This ranges from the kpc-scale ordered field, to smaller scale fields associated with magneto-ionic turbulence, or discrete magnetised objects such as supernova remnants (e.g. Kothes et al., 2006; Reynolds et al., 2012; West et al., 2016) and HII regions (e.g. Harvey-Smith et al., 2011; Raycheva et al., 2022). The Milky Way is a typical barred spiral galaxy consisting of a Galactic disk and halo, illustrated in Figure 1.6. From its dense central region ($\lesssim$ 3 kpc), protrude the two major spiral arms, Perseus and Scutum-Centaurus, and two minor arms, Norma and Carina-Sagittarius (e.g. Vallée, 2014). From our viewpoint, indicated on Figure 1.6 as the Sun, we refer to the disk of the Milky Way as the *Galactic Plane*, and the Galactic longitude ranges at which our line-of-sight passes through the spiral arms are referred to as *spiral arm tangents*. Regarding magnetic fields, the current state of the literature shows evidence of a large-scale ordered magnetic field with a strength of $B \sim 2$ μG (Haverkorn, 2015) with a spiral-like orientation in the plane of the Galactic disk. This ordered disk field shows one well-characterised direction reversal (Thomson and Nelson, 1980; Simard-Normandin and Kronberg, 1980), while the existence and location of further reversals remains under debate. The total disk magnetic field (including the random isotropic component) amounts to $B \sim 8$ μG. Towards the Galactic centre, the disk magnetic field is much stronger, up to ~ 10 μG within 3 kpc (Beck, 2001) and even at high Galactic latitudes, our line-of-sight passes through the Galactic halo with azimuthal field strengths of $B_\phi \sim 2$ μG and $B_\phi \sim 7$ μG for the North and South Galactic Poles, respectively (Mao et al., 2012).

Our position within the Milky Way provides an up close view of discrete magnetised objects, such as supernova remnants, pulsar wind nebulae (e.g. Reynolds et al., 2012; Kothes et al., 2018) and HII regions (e.g. Harvey-Smith et al., 2011; Raycheva et al., 2022) as well as the diffuse ISM. Moreover, measuring the magnetic field strength and structure of the Milky Way is essential for understanding the dynamics of the magnetised ISM and the evolution of spiral galaxies in general. However, this vantage point comes with significant challenges. Most obviously, we cannot remove ourselves from the Galaxy to obtain a global view of its field structure. In measuring properties of the large-scale Galactic magnetic field, we have the possibility of being confused with local features, as mentioned above, which can have a large angular extent on the sky. In addition, our position complicates the study of extragalactic polarised populations and their magnetic fields. As I will detail below, the synchrotron emission from

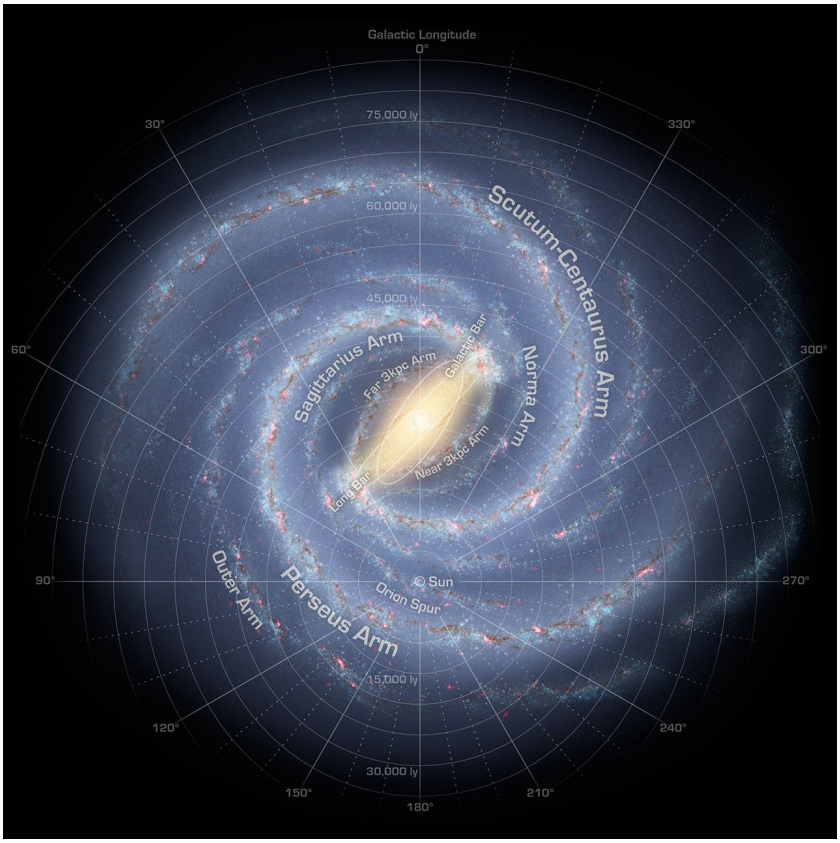

Figure 1.6: Artists rendition of the Milky Way, as observed from above. Our position in the Milky way is indicated by the Sun. The Galactic coordinate system (i.e. Galactic latitude b and Galactic longitude l) used throughout this work is shown, as well as the major and minor spiral arms. Image credit: NASA/JPL-Caltech/R. Hurt (SSC/Caltech)

extragalactic sources passes through the Galactic magneto-ionic ISM, a screen that distorts and modifies the signal through *Faraday rotation*. As such, we require a detailed, accurate understanding of the Milky Way magnetic field and of our immediate Galactic neighbourhood to correctly interpret observations of extragalactic polarised sources.

1.2.1 Faraday rotation

Faraday rotation (Faraday, 1846) is the change in the polarisation angle of an electromagnetic wave as it propagates through a magneto-ionic medium. A linearly polarised wave can be described as the superposition of two circularly polarised waves with right- and left-handed circular polarisation (RHC and LHC), respectively. The polarisation angle of the linear polarisation χ is determined by the phase difference of the two circular components. In a magneto-ionised medium (i.e. containing magnetic fields and free electrons), the RHC and LHC components propagate with different phase velocities (i.e. cosmic birefringence), resulting in a change in phase difference and therefore, a change in the angle of linear polarisation $\Delta\chi$, with respect to its intrinsic polarisation angle χ_0 (see Ferrière et al., 2021, for a detailed

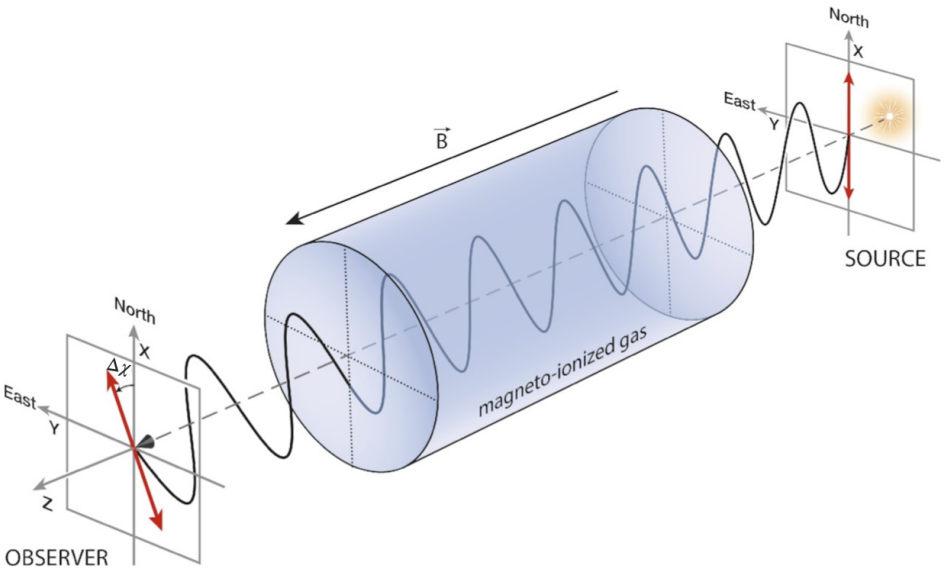

Figure 1.7: A diagram of Faraday rotation adapted from Ferrière et al. (2021). The polarised electro-magnetic wave is emitted from the source (right). As the radiation propagates through the magnetised-ionised gas, with a magnetic field strength B, towards the observer (left), it experiences a change in polarisation angle $\Delta\chi$.

explanation). In astrophysical contexts, the $\Delta\chi$ is given as

$$\Delta\chi = \mathrm{RM}\,\lambda^2, \tag{1.7}$$

where RM is the so-called *rotation measure* and λ is the wavelength of the electromagnetic wave. The strong linear λ^2-dependence of RM was confirmed observationally by early radio studies (e.g. Cooper and Price, 1962; Gardner and Whiteoak, 1966). As a result, RM was traditionally computed by observing a source in multiple frequency bands and fitting the linear slope over a function of λ^2. This quantity encodes properties of the transversed magneto-ionic medium, weighted by the electron density of the medium, and can be used to probe the magnetic field strength and direction along the line of sight.

$$\mathrm{RM} = \frac{e^3}{2\pi m_0^2 c^4} \int_l^0 n_e B_{||} \mathrm{d}s, \tag{1.8}$$

where n_e is the electron density of the magneto-ionised medium, $B_{||}$ is the magnetic field strength parallel to the direction of wave propagation and l is the path length between the synchrotron-emitting source and the observer. Following the convention defined by Manchester (1972), RM > 0 indicates a $B_{||}$ pointed towards the observer and RM < 0 indicates a $B_{||}$ pointed away from the observer. This concept is illustrated in Figure 1.7. In more convenient units, the RM can be expressed as

$$\mathrm{RM} = 0.81 \int_l^0 \left(\frac{n_e}{\mathrm{cm}^{-3}}\right)\left(\frac{B_{||}}{\mu\mathrm{G}}\right)\left(\frac{\mathrm{d}s}{\mathrm{pc}}\right)\ \mathrm{rad\,m}^{-2}. \tag{1.9}$$

1.2.2 The RM sky

In general, RM is a key observable concerning cosmic magnetic fields, particularly in the context of the Milky Way. By observing background polarised extragalactic sources (EGS), such as AGN and SFGs, and computing their RM, we can directly measure the direction and strength (weighted by n_e) of the foreground Galactic magnetic field at that position in the sky. By observing a large number of polarised EGS over a sky area, we can map out the Galactic magnetic field over that sky region. This is called an RM grid and is a major motivator for maximising the source counts of polarised EGSs. To fully model the Galactic magnetic field (e.g. Hutschenreuter et al., 2022), we would ideally require an RM grid covering the entire sky. While the Milky Way RM grid (detailed below) is the most relevant in this thesis, this method has also been used in the literature to study the foreground magnetic field structure of nearby SFGs (e.g. Gaensler et al., 2005; Mao et al., 2008; Livingston et al., 2022) and the magnetised intra-cluster medium of galaxy clusters (e.g. Anderson et al., 2021; Loi et al., 2025; Osinga et al., 2025).

In the 2000s, our knowledge of the RM sky was greatly improved with a number of targeted RM grid surveys on smaller regions of the Galactic plane. For example, the Southern Galactic Plane Survey (SGPS; Gaensler et al., 2001) with the Australian Telescope Compact Array (ATCA) was a survey of the Galactic Plane in the southern hemisphere covering $253^\circ < l < 358^\circ$ and $|b| < 1.5^\circ$. The detection of 148 EGSs in this survey resulted in an RM density of ~ 0.5 deg^{-2}. In the northern hemisphere, the Canadian Galactic Plane Survey (CGPS; Taylor et al., 2003; Brown et al., 2003) with the Dominion Radio Astrophysical Observatory (DRAO) Synthesis Telescope produced an RM density of ~ 0.9 deg^{-2} over the longitude ranges $82^\circ < l < 96^\circ$ and $115^\circ < l < 146^\circ$ within $-3.6^\circ < b < +5.6^\circ$. The combination of these surveys, as well as other legacy observations across the Galactic plane, were used to produce a detailed model of the Galactic disk magnetic field (Van Eck et al., 2011). At higher Galactic latitudes (i.e. away from the plane), Mao et al. (2012) probed the azimuthal Galactic halo field, by observing a latitude strip $|b| < 30^\circ$ at $100^\circ < l < 117^\circ$ with the VLA. Through these observations, they determined the transition between the disk and halo magnetic fields to be at a scale height of $|z| \sim 540$ pc. Finally, to study the vertical Galactic halo fields, Mao et al. (2010) observe the Galactic poles using the Westerbork Synthesis Radio Telescope (WSRT) and ATCA, resulting in the detection of 813 polarised EGSs and an RM density of ~ 0.77 deg^{-2}. They concluded that there is no evidence of a regular vertical fields towards the Galactic north pole, and weak vertical field ($B_z < 1$ μG) pointing from the Galactic south pole towards the plane.

The NVSS RM catalogue (Taylor et al., 2009), produced by re-analysing the NVSS survey (Condon et al., 1998), facilitated new advances in our knowledge of the RM sky. This was the first "all-sky" RM catalogue, containing 37 543 RMs (~ 1.1 deg^{-2}) for Dec $\geq -40^\circ$. Despite its limitations due to narrow-band spectro-polarimetry (i.e. producing an $n\pi$ ambiguity on the RM values, Ma et al., 2019a) and instrumental effects (i.e. no correction for off-axis leakage, Ma et al., 2019b), this catalogue was transformative in the field of Galactic magnetism (e.g. Schnitzeler, 2010; McClure-Griffiths et al., 2010; Harvey-Smith et al., 2011; Oppermann et al., 2012), as well as extragalactic cosmic magnetism in general (e.g. Johnston-Hollitt and Grimwood, 2011; Banfield et al., 2014; Farnes et al., 2014; Pshirkov et al., 2016). The Declination limit of the NVSS left a "southern hole" in the RM sky, which was recently patched by the S-band Polarization All-Sky Survey (S-PASS) ATCA survey (Schnitzeler et al., 2019). This survey involved targeted ATCA observations of 6 934 polarised point sources identified in the single-dish S-PASS survey (Carretti et al., 2019), producing an RM density of ~ 0.25 deg^{-2} at

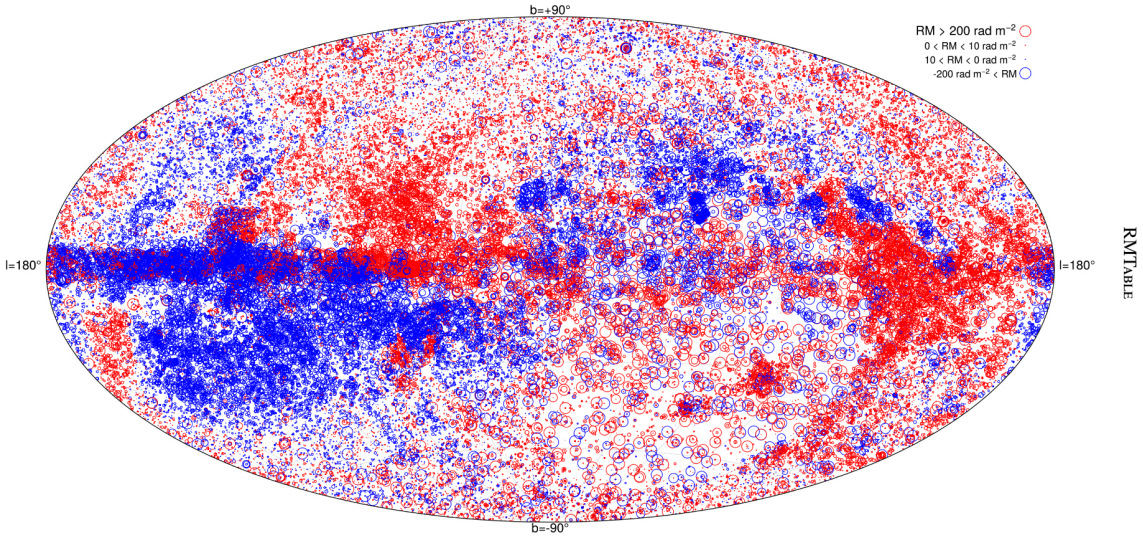

Figure 1.8: The all-sky RM distribution, adapted from Van Eck et al. (2023), plotted in Galactic coordinates. The sources with positive RMs are shown in red and those with negative RMs are shown in blue, while the marker size is proportional to the RM magnitude. The lower-right portion of the figure has a lower density of RMs, due to the declination limit of the NVSS (Taylor et al., 2009) catalogue.

Dec $\leq 0^{\circ}$. In contrast to the other RM grid observations mentioned thus far, the SPASS-ATCA survey was conducted with broadband receivers and at a higher frequency (1.1–3.1 GHz), in comparison to the narrowband observations centred at 1.4 GHz. The broadband approach, as well as the 'S-band' frequency range provide a different perspective of the polarised sky and are central to the work presented in this thesis, as I will detail in Section 1.3. Building on these large-area surveys, Van Eck et al. (2023) produced a compilation of RMs across the literature over a wide range of instruments and observations. Figure 1.8 shows the RM grid from the Van Eck et al. (2023) catalogue (Version 1.1.0), containing approximately 55 000 sources. Using this catalogue, Hutschenreuter et al. (2022) modelled the Galactic RM contribution using a Bayesian inference scheme. This is the most detailed model of the Galactic RM sky to date, with an angular resolution of ~ 46.8 arcmin^2, and over the past few years it has been readily applied in the literature for correcting the foreground Milky Way RM contribution when studying AGN populations (e.g. Piras et al., 2025), galaxy clusters (e.g. Riseley et al., 2025) and other extragalactic polarised sources (e.g. Taziaux et al., 2025).

An important note is that RM can be a limited descriptor, as it only quantifies the net change in polarisation angle along the full path from the source to the observer. Realistically, there might exist multiple sources of polarised intensity or multiple foreground magneto-ionic media (i.e. *Faraday screens*) along the line of sight, causing a non-linear change in polarisation angle as the polarised emission propagates towards the observer (Burn, 1966). A more practical quantity is Faraday depth ϕ,

$$\phi(l) = 0.81 \int_{l}^{0} n_e B_{||} \, \mathrm{d}s. \tag{1.10}$$

This is a more generalised form of Equation 1.9, accounting for the realistic case of sources being observed to have multiple discrete or a continuous range of Faraday depth values (i.e. *Faraday complexity*). While

ϕ and RM are sometimes used interchangeably in the literature, these terms are only equivalent under the assumption that there is a single polarised-emitting source, with one intervening Faraday screen between the source and the observer. Throughout this thesis, I will specify the assumptions taken when using either ϕ or RM. As I will detail in Chapter 2, the development of broadband receivers on modern radio telescopes, which simultaneously observe at multiple frequency values, have enabled advanced methods in measuring ϕ (e.g. RM synthesis and QU-fitting). These methods do not necessarily assume a linear $\Delta\chi(\lambda^2)$, allowing for a better characterisation of both the polarised sources and the intervening magneto-ionic media via the λ^2-dependent behaviour of their spectra.

1.3 This thesis

The Square Kilometre Array (SKA) is set to be the most sensitive radio interferometer in the world, and will be operational from the 2030's. One of the key science goals of the SKA is to produce a dense RM grid (Heald et al., 2020), detecting 2–3 million polarised sources across the sky. This unprecedented RM density will enable detailed statistical studies of foreground magneto-ionic structures, such as the Milky Way, individual galaxies and galaxy clusters. Ahead of the SKA, the so-called pre-SKA era has led to significant advancements in radio astronomy instrumentation. Modern interferometers such as MeerKAT, the Australian SKA Pathfinder (ASKAP) and the LOw Frequency ARray (LOFAR) have enhanced sensitivity and survey speed and are currently carrying out the new generation of polarisation surveys into the μJy regime. For example, at GHz frequencies, we have the POlarization Sky Survey of the Universe's Magnetism (POSSUM; Gaensler et al., 2025), the MPIfR MeerKAT Galactic Plane Survey (MMGPS; Padmanabh et al., 2023), the MeerKAT International GHz Tiered Extragalactic Exploration (MIGHTEE; Jarvis et al., 2016) and the VLA Sky Survey (VLASS; Lacy et al., 2020), while at low $\sim$ 100 MHz frequencies, we have the LOFAR Two-metre Sky Survey (LoTSS; Shimwell et al., 2017). Such surveys will lay the groundwork for studying the magnetised Universe with SKA over the next decades.

While these pre-SKA surveys will increase the RM sky density by an order of magnitude, it is important to have a good understanding of any observational effects and biases that may affect the RM measurement, particularly when dealing with such large catalogues. Previous studies have shown that the detection of Faraday complexity increases for sources measured with higher signal-to-noise ratios (e.g. Anderson et al., 2015), as expected for these sensitive surveys. Our understanding of Faraday complexity is limited, as we only recently have had the instrumentation available to detect large numbers of such sources (e.g. Schnitzeler et al., 2019). In order to correctly incorporate Faraday complex sources into models of the Milky Way RM contribution (and in extension, the Galactic magnetic field), we need to

a) understand the *physical origin* of Faraday complexity, e.g. extragalactic Faraday screens, such as galaxy clusters, discrete foreground Galactic objects (e.g. HII regions), turbulence in the Galactic ISM, or multiple sources of emission within the background EGS (e.g. Anderson et al., 2015; Livingston et al., 2021).

b) develop a method to remove any contributions to the measured RM that might not be purely due to Faraday rotation in the Galactic plane.

The latter involves an in-depth investigation into the classification of Faraday complexity and how this is affected by observational parameters, such as angular resolution, maximum angular scale, bandwidth and

channel resolution. In this thesis, I aim to develop our understanding of the imprint of Galactic magnetic fields on Faraday complexity – a necessary step in further defining Faraday complexity. This work focuses on brightly polarised sources in the wide area SPASS/ATCA survey (Schnitzeler et al., 2019), addressing the question as to *whether turbulence in the Milky Way ISM produces enhanced Faraday complexity in the observation of background EGSs*.

While I have already highlighted the importance of an accurate Galactic RM model to study the EGS population, the converse is also true: a good characterisation of the EGS population is essential for constraining our interpretation of the Galactic RM, e.g. to remove EGS outliers with intrinsic high RMs, understand biases in sky coverage caused by depolarisation (local or external to the EGS) and identify the optimal source populations for RM grid experiments. In this thesis, I aim to improve our understanding of *the nature of the background sources* themselves, using deep, high angular resolution observations of the COSMOS field (Smolčić et al., 2017a). Through the projects presented in this thesis, I will focus on both cases described above, i.e. the background EGSs and the foreground magneto-ionic media, using new broadband observations with the ATCA and VLA at S-band frequencies ($\sim$ 3 GHz).

The 3 GHz frequency regime has been relatively unexplored in polarisation compared to the more commonly used 1.4 GHz band[3], and offers a number of advantages regarding both total intensity and polarisation studies. Observationally, radio images at higher frequencies have higher angular resolution, from which we can better distinguish between different emitting components of radio galaxies as well as diffuse foreground structures. Furthermore, high angular resolution is essential for mitigating beam depolarisation effects (see Chapter 2). From a science perspective, the λ^2-dependence of Faraday rotation and depolarisation results in two major advantages at higher frequencies. Firstly, these polarised sources observed at 3 GHz are less susceptible to depolarisation in comparison to lower frequencies, where they may be totally depolarised, and therefore undetected in polarisation, reducing the source count. This work will be the first to explore the μJy polarised source population at 3 GHz, a beneficial contribution to our knowledge of the RM sky, and in selecting the optimal frequency range for large-scale RM grid experiments. I will reprocess the VLA-COSMOS 3 GHz survey (Smolčić et al., 2017a), one of the deepest S-band surveys to date, to include linear polarisation data products. Due to the relative lack of depolarisation at higher frequencies, this will provide a unique perspective on the faint polarised population, with which we can better anchor the intrinsic polarisation properties of EGSs, e.g. polarisation fraction and polarisation angle, to infer the magnetic field geometry within these sources. Investigating the polarised source counts in this deep field will help us identify and diagnose any polarised flux density-dependent changes in the overall polarised source population, and at 3 GHz, is a realistic attempt to probe the polarised SFG population. Here, I will address key questions, such as, *what is the polarised source count at S-band?*, and *do we detect the polarised star-forming galaxy population at μJy sensitivities?*. This high frequency approach goes hand-in-hand with the importance of broadband observations. Our ATCA (1.1–3.1 GHz), VLA (2–4 GHz) and MeerKAT (1.75–3.50 GHz) observations in this work all cover broadband frequency ranges, essential for disentangling and diagnosing any Faraday

[3] Studies of polarised radio sources, or the radio sky in general, have historically been more commonly done at L-band (1.4 GHz) frequencies predominantly due to practical reasons. 1.4 GHz corresponds to the emission line frequency of neutral hydrogen, a key tracer of gas dynamics in the Milky Way and external galaxies. As a result, L-band receivers have historically received priority in development, and instrumentation for cm-wavelength telescopes has generally been optimised for this frequency band. As I will detail in Chapter 2, there are also technical advantages of L-band surveys, particularly increased survey speed, in comparison to higher frequencies, a result of the larger field of view.

complexities along the line-of-sight.

1.3.1 Thesis outline

This thesis consists of three main parts, each using a data from a different radio telescope and with a different scientific context, as will be introduced in the relevant chapters:

1. **An investigation into the Galactic latitude dependence of Faraday complexity in the S-PASS/ATCA RM catalogue (Schnitzeler et al., 2019).** Through higher angular resolution follow-up observations of low Galactic latitude EGSs with the ATCA, I aim to understand the origin of Faraday complexity in these sources. This work also investigates the effect of observational parameters on our classification of Faraday complexity and how it effects our interpretation of the Milky Way foreground. This work is presented in Chapter 3 and is based on my published paper, *The Galactic latitude dependency of Faraday complexity in the SPASS/ATCA RM catalogue*, Ranchod et al. (2024).

2. **The characterisation of the μJy polarised source population at 3 GHz in the VLA-COSMOS field.** In this work, I produce the deepest catalogue of polarised sources at 3 GHz to date. This includes an investigation into the frequency-dependence of polarised source counts as well as the characterisation of the polarised sources based on their multi-wavelength properties. In finding that all detected polarised sources are AGN, this work provides a comprehensive analysis on the intrinsic fractional polarisation for various AGN sub-classes. In addition, I compute an upper limit for the density of polarised star-forming galaxies. This work is presented in Chapter 4, and a paper is currently in preparation.

3. **An analysis on the prospects of new instrumentation and future pre-SKA surveys.** In Chapter 5, I present the science verification of the newly installed S-band (1.75–3.50 GHz) receivers on the MeerKAT telescope. This work involves the observations and source count analysis on the DEEP2 extragalactic field, and a discussion surrounding the capabilities of this new instrumentation with respect to other S-band interferometers. This work is based on my published paper, *A first glimpse at the MeerKAT DEEP2 field at S-band*, Ranchod et al. (2025). Furthermore, in Chapter 6 I present a summary of the recently approved *MeerKAT+ S-band Legacy Survey*, a wide area polarisation survey with the upgraded MeerKAT array. The preparation of the proposal for this survey formed a significant part of this thesis work, and the relevant calculations and simulations are also presented in this chapter.

To complement these science chapters, in Chapter 2 I introduce the technical and scientific techniques used in the analysis of the data. Finally, Chapter 7 summarises the results of this thesis and provides an outlook into how these results can be applied to shape future research in this field.

CHAPTER 2

Methods

2.1 A brief introduction to radio interferometry

As established in Chapter 1, the detection of synchrotron emission from extragalactic sources is most effective at radio wavelengths. This technique was fathered by Karl G. Jansky, who first identified the source of noisy static interrupting radio communications as the Milky Way, marking the beginning of radio astronomy. Jansky's work was then continued by Grote Reber, who produced the first radio frequency sky map at 160 MHz in 1941. The radio frequency regime spans from 10 MHz to a few hundred GHz (Condon and Ransom, 2016), over which the Earth's atmosphere is almost fully transparent to radiation. This has allowed for the development of advanced ground-based radio observing facilities, both single dish and interferometric. In this chapter, I will provide a brief introduction to radio interferometry, defining key concepts and terminology discussed throughout this thesis (predominantly based on the textbook *"Essential Radio Astronomy"* by Condon and Ransom, 2016). I will also outline the methods used in converting signals from radio telescopes into calibrated images, and extracting measurable quantities for astrophysical application.

For the frequency range we are interested in ($\nu \sim 3$ GHz), a simple description of a radio telescope is a parabolic dish (or antenna), off which radio waves are reflected and focused onto a receiver. The power response of an antenna with a uniformly illuminated aperture can be described by a sinc function. The main lobe is called the *primary beam* and its full width at half maximum (FWHM) defines the angular resolution θ of the dish, determined by the dish diameter D and observing wavelength λ,

$$\theta = 1.22\frac{\lambda}{D}. \tag{2.1}$$

At cm wavelengths, however, we are typically limited in angular resolution, even for very large dishes (e.g. the 100 m Effelsberg telescope has an angular resolution of $\theta_{3\ \mathrm{GHz}} \approx 3'$), and require an interferometric approach to achieve high enough angular resolution for the detailed imaging of extragalactic sources. An interferometer correlates the signals received by pairs of antennas, pointed at the same source. The correlation accounts for the geometric delay $\tau = \frac{D\hat{s}}{c}$, determined by the distance between antennas or

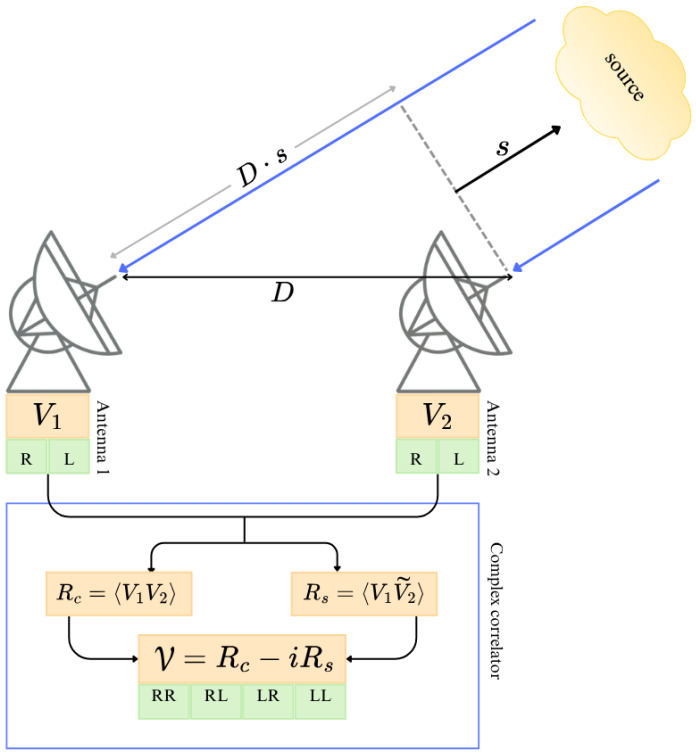

Figure 2.1: Schematic diagram of a two-element interferometer, with antennas 1 and 2 separated by the baseline D. Here, s indicates the direction towards the source. This illustrates an example with circular feeds, returning R and L voltages per receiver. The bottom portion of the diagram shows the complex correlator, consisting of the cosine R_c and sine R_s correlators. The 90° offset for the sine correlator is indicated by the tilde. The observed complex visibility $\mathcal{V}$ is shown for the four correlations RR, RL, LR and LL.

baseline D. The time-averaged correlated output voltage R has the form

$$R = \langle V_1 V_2 \rangle = \left(\frac{V^2}{2} \cos(\omega \tau_g) \right), \tag{2.2}$$

with $\omega = 2\pi\nu$, and is quasi-sinusoidal as the Earth rotates. These sinusoids are called fringes. The schematic of the 2-element interferometer is illustrated in Figure 2.1. As illustrated, when observing a source with an arbitrary brightness $I(s)$, the signal received by an antenna pair is equal to the sky distribution multiplied by the fringe pattern,

$$R_c = \int I(s) \cos(2\pi B \dot{s}/c) d\Omega. \tag{2.3}$$

The cosine fringe only detects the even component of extended emission, and should be complemented by a sine fringe, detected by a sine correlator R_s

$$R_s = \int I_\nu(S) \sin(2\pi\nu D s/c) d\Omega. \tag{2.4}$$

This is implemented by a 90° phase delay in the output of one antenna. These are the two components of the complex correlator, which can be combined using Euler's formula to define the complex visibility as $\mathcal{V} \equiv R_c - iR_s$. Following Equations 2.3 and 2.4, the relationship between the sky brightness (i.e. the image plane) and the observed complex visibility (i.e. the visibility plane) can be described by the following

$$\mathcal{V} = \int I(s) \exp(-2\pi Bs/\lambda) d\Omega, \tag{2.5}$$

a simplified version of the van Cittert-Zernike theorem (van Cittert, 1934; Zernike, 1938).

This concept can be expanded to an N-element interferometer and treated as $N(N-1)/2$ independent 2-element interferometers. The relationship between each antenna can be mapped out on the visibility plane (or uv-plane) using a coordinate system (u, v, w) which we define to be the interferometer as viewed from the observing target. Here, w is the normal to the uv-plane in the direction of the source s. The image plane (l, m, n) represents the sky distribution. Equation 2.5 can therefore be expanded to

$$\mathcal{V}(u, v, w) = \int \int \frac{I(l, m)}{n} \exp[-2i\pi(ul + vn + wn)] dl dm, \tag{2.6}$$

where the observed sky area is $d\Omega = dldn/n$. By assuming that $w = 0$, i.e. projected onto a 2D plane, this equation can be reduced to a 2D Fourier transform,

$$\mathcal{V}(u, v) = \int \int I(l, m) \exp[-2i\pi(ul + vm)] dl dm. \tag{2.7}$$

This is the foundation of aperture synthesis. The observed visibilities are measured at discrete time intervals, and as the Earth (and the interferometer) rotates with respect to the source position, we sample multiple points on the uv-plane. By maximising the area over which the uv-plane is sampled (increasing the uv-coverage), we can obtain the angular resolution corresponding to a much larger effective aperture. The sensitivity pattern of the interferometer, called the *point spread function* (PSF) is the inverse Fourier transform of the sampling function of the uv-plane. The uv-coverage for our Australia Telescope Compact Array (ATCA) observations of a polarised source (Chapter 3) and the corresponding PSF is shown in Figure 2.2. With sufficient uv-coverage, the PSF can be modelled as a 2D Gaussian function called the *restoring beam*, for which the FWHM characterises the angular resolution θ to first order as

$$\theta = \frac{\lambda}{D_{\max}}, \tag{2.8}$$

where $D_{\max}$ is the length of the longest baseline. Similarly, the maximum angular scale to which we are sensitive is characterised by the length of the shortest baseline. Depending on the science goals, we can assign weights to certain baselines to prioritise angular resolution, or sensitivity to diffuse emission. This will be discussed in Section 2.1.2.

The above explanation assumes a monochromatic interferometer, i.e. observing at a single frequency. Modern radio interferometers have broad bandwidth receivers, providing a continuous frequency coverage within a finite frequency range. In post-observation processing, all telescopes used in this thesis

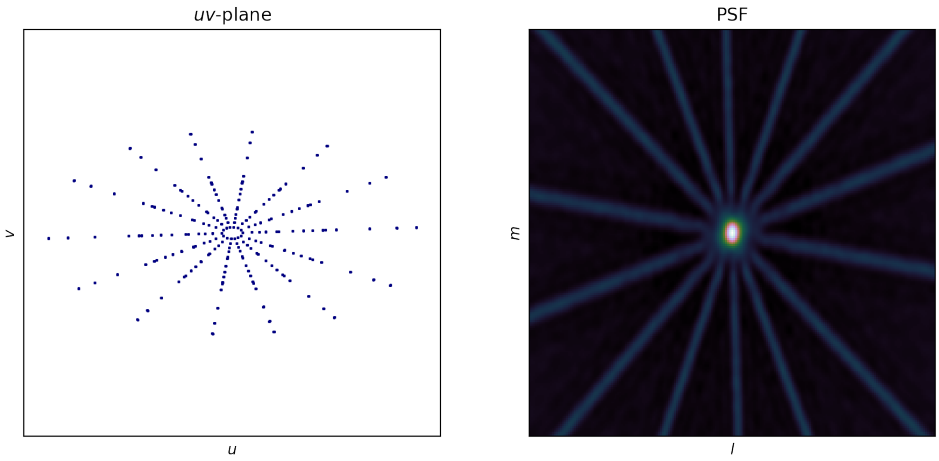

Figure 2.2: An example of the *uv*-plane (left) with the corresponding PSF (right) for our ATCA observations of polarised source NVSS J171309–341830. The observations are detailed in Chapter 3.

Table 2.1: Frequency bandwidth properties of interferometers used in this thesis

Telescope	Band name	Central freq [GHz]	Freq range [MHz]	Min chan width [kHz]	Relevant chapters
ATCA	16cm	2.1	1100–3100	1000	3
VLA	S-band	3.0	2000–4000	2000	4
MeerKAT	S1	2.4	1969–2843	214	5, 6
MeerKAT	S4	3.1	2625–3500	214	5

allow for the bandwidth to be split into smaller frequency chunks or *channels* with a finite minimum frequency resolution. Table 2.1 summarises the relevant telescopes and their frequency band properties. Broadband receivers have been a relatively recent technological advancement for radio interferometers; The ATCA's Compact Array Broad-band Backend (CABB) was first commissioned in 2010 (Wilson et al., 2011), the Karl G. Jansky Very Large Array (VLA) integrated their Wideband Interferometric Digital ARchitecture (WIDAR) correlator into the array in 2011 (Perley et al., 2011) and the MeerKAT telescope only recently had its first light in 2018 (Jonas and MeerKAT Team, 2016), already equipped with broadband receivers. By producing images for each individual channel, we can carry out broadband spectro-polarimetric analysis, e.g. study the Faraday rotation as a function of λ^2. Examples of such methods used in this work are detailed in Section 2.2.

2.1.1 Measuring radio polarisation

The measurement of linearly polarised synchrotron emission is a key diagnostic of extragalactic and Galactic magnetic fields, through observables such as fractional polarisation, polarisation angle and Faraday rotation. Classically, electromagnetic waves can be described by the electric field vector $\vec{E}$ and its Cartesian components E_x and E_y, in the monochromatic case. Considering a wave propagating in the

$\hat{z}$ direction (i.e. between the emitting source and the observer),

$$\vec{E} = \vec{E}_x + \vec{E}_y, \tag{2.9}$$

where

$$\vec{E}_x = E_x \cos(\vec{k} \cdot \hat{z} - \omega t) \tag{2.10}$$

$$\vec{E}_y = E_y \cos(\vec{k} \cdot \hat{z} - \omega t + \delta_{xy}). \tag{2.11}$$

Here, E is the amplitude of the respective orthogonal components, $\vec{k}$ is the wave vector, $\omega = 2\pi\nu$ is the angular frequency, t is time, and δ_{xy} is the phase difference between the two components. The wave traces an ellipse on the plane perpendicular to the direction of propagation. In a circular basis, this ellipse can also be considered combination of right-hand circular polarised $\vec{E}_R$ and left-hand circular polarised $\vec{E}_L$ components, with a phase offset of δ_{RL}. The ellipticity is described by δ_{xy}, which also defines the state of polarisation: if $\delta_{xy} = 0$, the wave is linearly polarised, if $\delta_{xy} = \pm\pi/2$, it is circularly polarised, and in other cases, it is elliptically polarised.

In radio astronomy, we characterise the polarisation via the *Stokes parameters* (Stokes, 1851; Chandrasekhar, 1946), which describe the total, linear and circular polarisation, expressed in terms of the orthogonal components of $\vec{E}$,

$$\begin{aligned} I &= \langle E_x^2 \rangle + \langle E_y^2 \rangle &&= \langle E_R^2 \rangle + \langle E_L^2 \rangle \\ Q &= \langle E_x^2 \rangle - \langle E_y^2 \rangle &&= 2\langle E_R E_L \rangle \cos\delta_{RL} \\ U &= 2\langle E_x E_y \rangle \cos\delta_{xy} &&= 2\langle E_R E_L \rangle \sin\delta_{RL} \\ V &= 2\langle E_x E_y \rangle \sin\delta_{xy} &&= \langle E_L^2 \rangle - \langle E_R^2 \rangle. \end{aligned} \tag{2.12}$$

As the monochromatic assumption is not realistic, in practice we typically take the time-averaged E-field vectors, indicated by the angled brackets above. The Stokes parameter I indicates the total intensity of the radiation, Stokes Q and U describe the linear polarisation, and Stokes V is the circular polarisation.

To efficiently detect all emission, radio receivers require two orthogonally polarised feeds. Some interferometers use linear feeds (xy-dipole) e.g. ATCA and MeerKAT, and some use circular feeds (right- and left-helical) e.g. VLA. Since this thesis uses examples of both, I will outline the notations used for both types of systems. Following Equation 2.2 and 2.7, two orthogonal voltages are recorded per receiver, V_x and V_y (or V_R and V_L), and four correlated complex visibilities are therefore produced per antenna pair $\mathcal{V}_{x1x2}$, $\mathcal{V}_{x1y2}$, $\mathcal{V}_{y1x2}$ and $\mathcal{V}_{y1y2}$ (or $\mathcal{V}_{R1R2}$, $\mathcal{V}_{R1L2}$, $\mathcal{V}_{L1R2}$ and $\mathcal{V}_{L1L2}$), where 1 and 2 refer to the respective antennas (see Figure 2.1). These are typically represented in a 2×2 *visibility matrix*. Accordingly, we can represent the observed Stokes parameters as a combination of these observed

correlated visibilities as,

$$\begin{aligned} I &= \mathcal{V}_{x1x2} + \mathcal{V}_{y1y2} = \mathcal{V}_{R1R2} + \mathcal{V}_{L1L2} \\ Q &= \mathcal{V}_{x1x2} - \mathcal{V}_{y1y2} = \mathcal{V}_{R1L2} + \mathcal{V}_{L1R2} \\ U &= \mathcal{V}_{x1y2} + \mathcal{V}_{y1x2} = i(\mathcal{V}_{R1L2} - \mathcal{V}_{L1R2}) \\ V &= i(\mathcal{V}_{x1y2} - \mathcal{V}_{y1x2}) = \mathcal{V}_{R1R2} - \mathcal{V}_{L1L2}. \end{aligned} \tag{2.13}$$

Using the Stokes parameters we can define a number of observables. The linear *polarised intensity* (i.e. $V = 0$) is given as

$$P = \sqrt{Q^2 + U^2}. \tag{2.14}$$

The polarised intensity (again, assuming $V = 0$, as typical for radio galaxies), can only be a fraction of the total intensity, and we therefore define *fractional polarisation*, or degree of polarisation as

$$p = \frac{\sqrt{Q^2 + U^2}}{I} = \frac{P}{I}. \tag{2.15}$$

This observable can help diagnose the degree of magnetic field ordering in a source, and is also related to the depolarisation that the polarised emission is subject to (see Section 2.2.2). The *polarisation angle* χ is expressed as

$$\chi = \frac{1}{2} \arctan\left(\frac{U}{Q}\right). \tag{2.16}$$

As described in Chapter 1, the Faraday rotation measure can be obtained by measuring the change in polarisation angle $\Delta\chi$ as a function of λ^2, which is directly related to the magnetic field strength and direction along the line-of-sight (Equation 1.8). These parameters can also be represented as the *complex polarisation*, which we define to be

$$\mathbf{P} = Q + iU = P \exp(2i\chi). \tag{2.17}$$

Throughout this thesis, we extract the measurement of the Stokes parameters directly from image cubes. The process for producing these images is detailed in the following sections.

2.1.2 Calibration and imaging

Data calibration is an essential step in radio interferometric science. The visibilities measured by radio telescopes can be contaminated by instrumental and environmental factors, which need to be accounted for when interpreting the data. This can be best described by the Radio Interferometer Measurement Equation (RIME), e.g. for antennas 1 and 2 (Hamaker et al., 1996):

$$\vec{\mathcal{V}}_{12}^{\text{obs}} = \vec{J}_{12} \vec{\mathcal{V}}_{12}^{\text{true}}, \tag{2.18}$$

where $\vec{\mathcal{V}}_{12}^{\text{obs}}$ and $\vec{\mathcal{V}}_{12}^{\text{true}}$ are the observed and true visibility matrices. $\vec{J}_{12}$ is the Jones matrix, which represents all time- and frequency-dependent contamination effects that modify the incoming signal. These effects are primarily due to the antenna response (e.g. electronic gain response, instrumental delay, instrumentation imperfections), or environmental and propagation effects (e.g. weather, Faraday rotation from the ionosphere, geometric delay). For polarisation calibration, accounting for instrumental polarisation (i.e. on-axis leakage between the orthogonal feeds), parallactic angle and polarisation angle is also required. Another significant environmental effect is radio frequency interference (RFI). RFI is the contamination at various frequencies or timestamps due to artificial radio sources, such as cell phones, aircraft transponders and satellites. This is mitigated by flagging affected visibilities.

The procedures for calibrating such data are well-developed and documented in the literature (e.g. Taylor et al., 1999), which typically involve observing a well-modelled calibrator source alongside the target observations. Novel procedures are currently being developed to further improve the data quality and maximise the scientific output (e.g. Smirnov, 2011; Tasse et al., 2018; Tasse, 2023). As we only use the conventional calibration methods in this thesis, a detailed explanation is beyond the scope of this work, and we refer the readers to the above references. We detail the instrumental effects that affect polarisation measurements specifically (e.g. polarisation leakage) in Section 2.1.3.

As introduced above, Equation 2.7 describes the relationship between the image-plane and the visibility-plane as a 2D Fourier transform. In interferometry, the process of transferring measurements from the visibility-plane to the image-plane is called *imaging*, and is used to obtain a visual representation of the observed sky area. By simply Fourier transforming the visibilities sampled over the uv-plane, we produce a *dirty image*, which is the true sky intensity convolved with the PSF, with some added statistical and systematic noise. As shown in Figure 2.2, the PSF contains associated sidelobes, which will be present as artefacts on all sources in the dirty image. We can obtain the true sky image via deconvolution, which we perform using the CLEAN algorithm.

In brief, the well-known Högbom CLEAN algorithm (Högbom, 1974) is as follows:

1. Create a copy of the dirty image, called the *residual image*.
2. For each iteration, locate the pixel of highest intensity in the residual image and subtract an amplitude-scaled PSF from this position.
3. The position and intensity of the subtracted pixel is recorded on the *model image*.
4. This process is repeated for a specified number of iterations or until a specified threshold in the residual image is reached. If suitably calibrated, at this stage, the remaining residual image should resemble Gaussian noise.
5. Finally, the model image is convolved with the restoring beam and added to the residual image. This output is called the *clean image*.

An example of the dirty image, clean image, model image and residual image for source NVSS J171309–341830 observed with ATCA (Chapter 3) is shown in Figure 2.3. From this figure, the dirty image clearly shows the artefacts from the PSF, as in Figure 2.2. For this example, the residual image shows further artefacts that are a result of imperfect calibration. Finally, the cleaned image is no longer affected

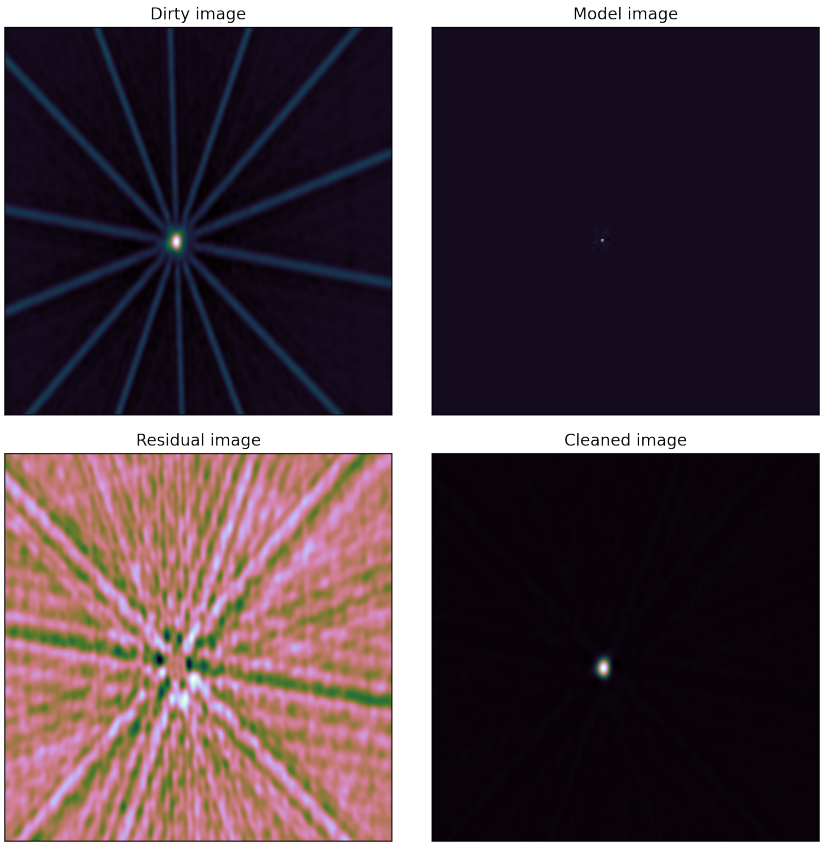

Figure 2.3: Example of a dirty image (top left), model image (top right), residual image (bottom left) and cleaned image (bottom right) for source NVSS J171309–341830 (Chapter 3). Note that that flux scaling is not consistent between the images.

by the shape of the PSF. We can produce images for each of the Stokes parameters separately. Modern software used to perform interferometric imaging, e.g. WSClean (Offringa et al., 2014) includes more advanced features than the basic Högbom CLEAN. For example, masks can be used to restrict the cleaned region, multi-scale imaging allows for the model image to be comprised of regions of various sizes, rather than only individual pixels. This results in a more accurate model image for extended, diffuse emission. Multi-frequency synthesis (MFS) images can be produced by combining all visibilities across the frequency band into a single image. From Equation 2.8, we expect the restoring beam size to change across the band. The MFS algorithm searches for peak intensity across the full band, but deconvolves each channel by their respective restoring beam. In this combined image, each channel is weighted inverse to their noise level to maximise the sensitivity of the MFS image. For the spectro-polarimetric analysis done in this thesis, we require Stokes I, Q and U *image cubes*, for which each frequency channel is imaged separately, then stitched together along a third (frequency) axis.

The Fourier transform to produce the dirty image is performed numerically using a fast Fourier transform (FFT), requiring the visibilites on the uv-plane to be discretised. This is done though a process called *gridding*. As the uv-plane is not uniformly sampled, we can select a weighting for the visibilities in

a designated grid cell to optimise the image for our specific science goal. This alters the angular resolution and sensitivity of the image. *Natural weighting* assigns an equal weighting to all visibilities, which optimises the brightness temperature sensitivity at the cost of angular resolution. *Uniform weighting* assigns equal weighting to all gridding cells, irrespective of cell sampling density. This typically favours longer baselines, resulting in higher angular resolution and lower sensitivity. *Briggs weighting* (Briggs, 1995) provides a continuum between these two extremes with a robust parameter that ranges between −2 and 2 (CASA notation) for uniform and natural weighting, respectively. We explore this in detail in Chapter 5, where we select the optimal Briggs robust weighting for observations of deep extragalactic fields with the MeerKAT S-bands (Table 2.1).

2.1.3 Instrumental effects

As shown above, the power response of a radio antenna describes the angular resolution for a single dish telescope. However, in the context of interferometry, the power response of the dish rather describes the field of view (FoV) of the interferometer. Images are typically cropped before the first null of the sinc function, for an approximately Gaussian response (i.e. the primary beam). In practice, the observed sky brightness is the true sky brightness convolved by the primary beam response. This can be corrected for during or after the imaging process, provided we have an accurate model of the primary beam. The primary beam is frequency dependent (Equation 2.1), and for most telescopes also varies with time, as the sky rotates with respect to the observer.

The primary beam response of individual antennas can be affected by slight deformations in the dishes due to temperature fluctuations or gravity. Detailed models of the primary beams are usually generated using ray-tracing or holography measurements (e.g. de Villiers, 2023). In Stokes I (total intensity) we can correct for the primary beam response by dividing by the primary beam model. However, this becomes more complicated when working with full Stokes images. The two feeds on a radio antenna are not always perfectly orthogonal due to manufacturing imperfections, which can cause *polarisation leakage* (also called instrumental polarisation) between Stokes parameters. We define the Mueller matrix

$$\vec{M}_{12} = \vec{J}_1 \otimes \vec{J}_2, \tag{2.19}$$

where $\vec{M}_{12}$ is the Kronecker product of the Jones matrix antenna responses from antennas 1 and 2. Rather than being in terms of xy or RL, the 4×4 Mueller matrix encodes the Stokes parameters, where rows and columns represent I, Q, U and V. For perfectly orthogonal feeds, the Mueller matrix should be a diagonal matrix, containing the primary beam response for each Stokes parameter. Here, the off-diagonal terms represent leakage between respective Stokes parameters. Given that Stokes I contains the brightest emission, the leakage of Stokes I into Q and U can be a complication in polarisation measurements, resulting in spurious polarised source detections. The first row of the Mueller matrix for a VLA S-band primary beam model, generated using PLUMBER (Sekhar et al., 2022) is shown in Figure 2.4. This software uses Zernike polynomials to model the antenna aperture illumination patterns based on holography measurements. The figure illustrates that the leakage responses are asymmetrical, and therefore highly time-dependent in comparison to the Stokes I primary beam (approximately rotationally symmetric within the FWHM). *On-axis* polarisation leakage (i.e. at the pointing centre) is generally time-independent and corrected for during standard calibration (Section 2.1.2). For example, the on-axis

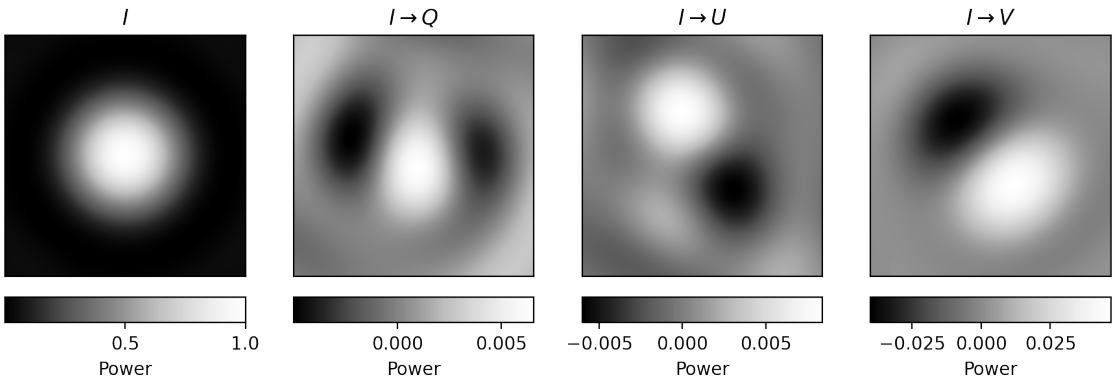

Figure 2.4: The first row of the Mueller matrix for the VLA S-band primary beam models. The first panel shows the primary beam response for Stokes I, while the following panels shown the leakage of the total intensity into Stokes Q, U and V respectively. The models have beem generated using the `plumber` software (Sekhar et al., 2022).

leakage of the VLA is constrained to less than 5% (Perley, 2010). The correction for this effect is done by observing a known, unpolarised source at the pointing centre and assuming that all detected polarisation is instrumental.

For our ATCA observations in Chapter 3, we only observe sources on axis, so this correction is sufficient. Constraining *off-axis* leakage (i.e. away from the pointing centre) is an on-going field of research. A-projection (Bhatnagar et al., 2008; Bhatnagar et al., 2013) is the most well-known algorithm to account for this. This requires a well-defined full-Stokes primary beam model, which is applied directly to the visibilities during the gridding step in the imaging process. However, this is extremely computationally expensive, and not often used in practice. In Chapter 4, we produce wide-field Stokes Q and U images from VLA observations, and account for the off-axis leakage by modelling the leakage percentage across the field. We use this to constrain the effect of leakage on our detected sources and exclude spurious detections. Without any correction, off-axis leakage increases up to e.g. 3% with the VLA (Cotton, 1994). In Chapter 4, we also discuss the effect of leakage on observables such as fractional polarisation and RM, and how it can be minimised through observation setup (see also Chapter 6).

As I will detail in Section 2.2.2, λ-dependent depolarisation is an important observable for inferring the magnetic field ordering and turbulence in the direct source vicinity or along the line-of-sight. However, there are some instrumental depolarisation effects, that if not correctly quantified, can misinform our interpretation of the polarisation measurements. We define beam depolarisation and bandwidth depolarisation below.

Beam depolarisation is a λ-independent effect that can cause a reduction in the polarised signal if there are multiple discrete polarised components within a beam, i.e. the individual components cannot be spatially distinguished within the angular resolution of the observations. Considering the vector representation of complex polarisation $\mathbf{P}$ (Equation 2.17), the addition of multiple non-zero complex

polarisation vectors will always be smaller than the sum of their polarised intensities P e.g.,

$$\sum_{0}^{i} |\mathbf{P}_i| \geq \left| \sum_{0}^{i} \mathbf{P}_i \right|, \tag{2.20}$$

unless their polarisation angles are equal. As we will show in Chapter 4, the beam depolarisation effect can only be circumvented by observing at higher angular resolutions.

Bandwidth depolarisation is another instrumental depolarisation effect. Similar to beam depolarisation, this reduction of polarised intensity is caused by the bandwidth averaging when generating an MFS image, or due to the frequency averaging within a channel when creating spectral image cubes. This is caused by Faraday rotation, i.e. the change of polarisation angle with a given channel. The degree of bandwidth depolarisation p_b can be described as

$$p_b = \left| \frac{\sin \Delta\Theta}{\Delta\Theta} \right|, \tag{2.21}$$

with

$$\Delta\Theta = \frac{2\mathrm{RM}c^2\Delta\nu}{\nu^3}, \tag{2.22}$$

where $\Delta\nu$ is the channel width and ν is the central frequency (Gardner and Whiteoak, 1966; Gaensler et al., 2001). For example, a source with an RM of +200 rad m^{-2} will be depolarised by 50% for channel width of $\Delta\nu$ = 125 MHz, but only by 10% for a bandwidth of $\Delta\nu$ = 50 MHz. Figure 2.5 shows an example of p_b as a function of $\Delta\nu$ for a range of |RM| values. The effect of bandwidth depolarisation increases with higher |RM|, larger channel width and lower observing frequency. While it is apparent that we could mitigate this effect with high channel resolution, it is also important to take into account that the per-channel S/N for a source increases with larger channel widths. Sufficient per-channel S/N is essential for the spectro-polarimetric analysis done in this thesis. This is discussed in detail in each chapter, where we use the above equations to optimally select the appropriate channel width for the respective science cases.

2.2 Techniques in broadband polarimetry

Broadband radio observations (see Table 2.1) offer a unique advantage for the polarisation studies of the Milky Way as well as extragalactic sources. Observing over a large λ^2 range allows for better characterisation of the linearly polarised sources, their local magneto-ionic medium as well as intervening media along the line-of-sight. Methods such as *RM synthesis* (Section 2.2.1) enable a more accurate computation of RMs, eliminating the $n\pi$-ambiguity. This method can also be used to identify multiple sources of linear polarisation or turbulent screens along the line of sight and/or in the plane of the sky (i.e. *Faraday complexity*, see Section 2.2.3). Moreover, with *QU-fitting* (fitting physical models to the Stokes Q and U spectra, see Section 2.2.2), we can accurately model the λ-dependent behaviour of these spectra (e.g. Faraday rotation and depolarisation) and diagnose any complexities. The caveat regarding QU-fitting is that we require appropriate physical models, for which selecting the correct model is a key part of the analysis, in contrast to RM synthesis which is model-independent. Below, I will explain these broadband analysis methods in detail and their importance in this thesis.

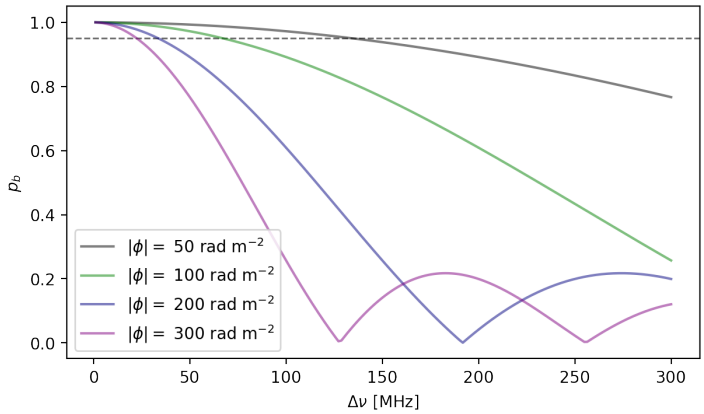

Figure 2.5: The degree of bandwidth depolarisation p_b, given by Equation 2.21, as a function of channel bandwidth $\Delta\nu$. Here, the central frequency is $\nu = 1.3$ GHz. Each colour represent a different |RM| values as indicated in the legend. The dashed horizontal line shows $p_b = 0.95$, which is considered the limit for a reasonable degree of bandwidth depolarisation.

2.2.1 RM synthesis

In Chapter 1, we introduce Faraday depth ϕ, a more generalised description of RM. RM synthesis (Brentjens and de Bruyn, 2005) is a method that utilises the Fourier-like nature of complex polarisation $\mathbf{P}(\lambda^2)$ to evaluate the observed polarisation as a function of Faraday depth ϕ. This relationship is described by the Faraday dispersion function (FDF, also called the *Faraday spectrum*) $\mathbf{F}(\phi)$ (Burn, 1966),

$$\mathbf{P}(\lambda^2) = \int_{-\infty}^{+\infty} \mathbf{F}(\phi)\, e^{2i\phi\lambda^2}\, \mathrm{d}\phi. \tag{2.23}$$

This equation is similar to an inverse Fourier transform, with an important exception that $\mathbf{P}$ is unphysical for $\lambda^2 < 0$. An added complication is that even for $\lambda^2 > 0$ we do not have continuous λ^2 coverage for real observations. Brentjens and de Bruyn (2005) draw an analogy between Equation 2.23 and the incomplete uv-plane sampling in aperture synthesis (Section 2.1.2), from which they devise a weighting function $W(\lambda^2)$ to address the λ^2 limitations mentioned above:

$$\tilde{\mathbf{P}}(\lambda^2) = W(\lambda^2)\mathbf{P}(\lambda^2) = W(\lambda^2) \int_{-\infty}^{+\infty} \mathbf{F}(\phi)\, e^{2i\phi\lambda^2}\, \mathrm{d}\phi. \tag{2.24}$$

Here, $\tilde{\mathbf{P}}(\lambda^2)$ is the observed complex polarisation, as sampled by $W(\lambda^2)$. By taking the inverse Fourier transform, we obtain the observed FDF $\tilde{\mathbf{F}}$, or *dirty FDF*,

$$\tilde{\mathbf{F}}(\phi) = \mathbf{F}(\phi) \circledast \mathbf{R}(\phi). \tag{2.25}$$

$\mathbf{R}(\phi)$ is the *Rotation Measure Spread Function* (RMSF), and is analogous to the PSF described in Section 2.1.2 (e.g. contributes sidelobe artefacts that corrupt the true signal). In the ideal case of a uniform, continuous λ^2 coverage, the sampling function is a top-hat distribution, for which the Fourier transform is a sinc function with predictable sidelobes. However, as discussed above, the λ^2-coverage

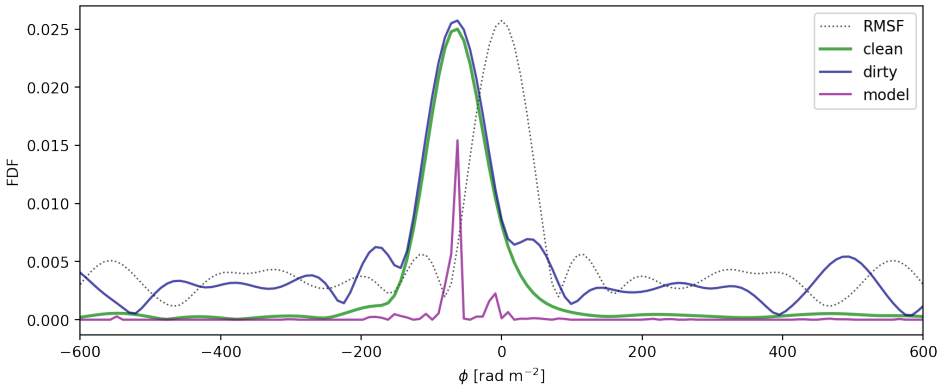

Figure 2.6: An example of the dirty FDF (of Faraday spectrum $\tilde{\mathbf{F}}(\phi)$) for source NVSS J161021–395858 (Chapter 3) shown in blue. The cleaned Faraday spectrum $\mathbf{F}(\phi)$ is plotted in green with the corresponding clean components in purple. The RMSF $\mathbf{F}(\phi)$ is indicated by the dotted line.

cannot be continuous and is limited by the channelisation of the data that is typically defined in ν-space, and therefore non-uniform in λ^2-space, as well as frequency chunks that have been removed due to RFI contamination. This results is larger sidelobes, or "shoulders" to the RMSF primary lobe. To combat this, we can obtain the clean FDF $\mathbf{F}(\phi)$, through deconvolution using the CLEAN algorithm (Heald, 2009, similar to the imaging process). Figure 2.6 shown an example of a $\mathbf{R}(\phi)$, $\mathbf{F}(\phi)$, $\tilde{\mathbf{F}}(\phi)$ and the *clean components* (cf. model image) for source NVSS J161021–395858, observed with ATCA as part of Chapter 3. As indicated in Figure 2.6, the FDF peaks at the RM of the source. The amplitude of this peak corresponds to the polarised intensity with that RM. We can use this Fourier decomposition of polarised intensity to identify if an observed source contains multiple emitting polarised components, and measure the polarised intensity of the respective components, as well as the amount of Faraday rotation they undergo. This can be observed as multiple peaks in the FDF and is an example of Faraday complexity, which will be detailed in Section 2.2.3. Other physical conditions resulting in Faraday complexity may manifest as a broadening and flattening of the FDF. Our sensitivity to detecting such complexities in the Faraday depth domain is fundamentally linked to the λ^2-coverage, and can be described by three parameters, which we define below.

Just as the PSF determines the angular resolution of images, the RMSF determines the Faraday depth resolution $\delta\phi$ (Brentjens and de Bruyn, 2005). Assuming the ideal top-hat λ^2 sampling function, $\delta\phi$ can be described by the FWHM of the main lobe of the RMSF, with

$$\delta\phi \approx \frac{2\sqrt{3}}{\Delta\lambda^2}. \tag{2.26}$$

The Faraday depth resolution can be maximised by observing over a large bandwidth, particularly at lower frequencies. For example, for the VLA S-band bandwidth described in Table 2.1, we would expect $\delta\phi \approx 200$ rad m^{-2}, in contrast to observations with the LOw Frequency ARray (LOFAR, $120 < \nu < 168$ MHz) with an expected $\delta\phi \approx 1$ rad m^{-2}. Another key parameter, the largest detectable scale in Faraday depth space, at which the sensitivity remains greater than 50%, is also determined by

the λ^2-coverage, as

$$\text{max-scale} \approx \frac{\pi}{\lambda^2_{\text{min}}}, \tag{2.27}$$

where λ^2_{min} is the minimum sampled λ^2 (i.e. upper end of the frequency band). Broad *Faraday thick* structures in Faraday depth spanning a range wider than the max-scale cannot be accurately recovered through RM synthesis, and can appear as multiple discrete peaks. For example, at 3 GHz, we would expect a max-scale ≈ 315 rad m^{-2}, which can be resolved under the $\delta\phi$ described for the VLA S-band above. Finally, the maximum Faraday depth to which we are sensitive above 50%, ϕ_{max}, is determined by the channel resolution, $\delta\lambda^2$, and is a limitation imposed by bandwidth depolarisation. This is given by

$$|\phi_{\text{max}}| \approx \frac{\sqrt{3}}{\delta\lambda^2}. \tag{2.28}$$

At S-band frequencies, this is typically $> 10^4$ rad m^{-2}, although such extreme values of ϕ are only found in compact regions (e.g. AGN cores), or regions of dense plasma (e.g. the Galactic centre). While I have defined the FDF in terms of polarised intensity here, typically we divide the Stokes Q and U spectra by the Stokes I spectrum (assuming that all intensity is associated with synchrotron emissison), and use the fractional q and u spectra in this method. This removes any spectral effects of Stokes I, e.g. spectral index, spectral turnover, that might result in an incorrect interpretation of the FDF. In this thesis, we use RM synthesis and the related parameters in Chapters 3 and 4 to determine polarised intensity, fractional polarisation and Faraday depth. In Chapter 3, our lower frequency observations (Table 2.1) allow for a high Faraday depth resolution. Here, alongside QU-fitting, we use the Faraday depth spectra to identify and analyse Faraday complexity. In Chapter 4, we have comparatively low resolution Faraday spectra, and cannot use this for complexity analysis. However, by performing RM synthesis on all candidate sources, we utilise the Faraday spectra to perform source finding of linearly polarised sources in the Faraday depth domain. The effect of limited λ^2 coverage on both the QU-spectra and Faraday spectrum in the context of the observations used in this thesis is illustrated through modelled spectra in Figures 2.7 and 2.8.

2.2.2 Stokes QU-fitting

Stokes QU-fitting (e.g. Farnsworth et al., 2011; O'Sullivan et al., 2012) is a method that can be used to understand the physical origins of the Faraday rotation and depolarisation associated with observed polarised emission. With this method, we simultaneously fit the fractional Stokes Q and U spectra as the real and imaginary components of the complex (fractional) polarised intensity (i.e. $\mathbf{p}(\lambda^2) = q(\lambda^2) + iu(\lambda^2)$) using physical models that describe the magneto-ionic environment. These models do not only describe the direct source environment, but also any synchrotron-emitting or Faraday-rotating media along the line-of-sight. Because the line-of-sight is not infinitely thin, we refer to the detected polarised signal "within the beam volume". Below, I will introduce the physical models used in this thesis. These models can be combined linearly with n polarised components, as

$$\mathbf{p}(\lambda^2) = \sum_j^n \mathbf{p}_j(\lambda^2). \tag{2.29}$$

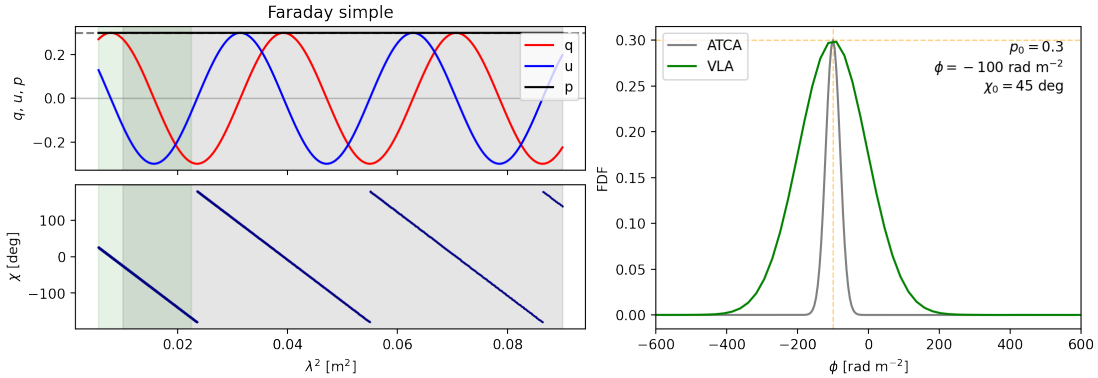

Figure 2.7: The spectra for a modelled Faraday simple source (Faraday thin). This model (Equation 2.30) describes a synchrotron-emitting source with a Faraday-rotating foreground. *Top left:* Fraction Stokes q (red) and u (blue) spectra with fractional polarisation p (black). The grey dashed line indicates the intrinsic fractional polarisation p_0 of the model. *Bottom left:* polarisation angle χ as a function of λ^2. The green and grey shaded regions indicate the λ^2 coverage for the VLA S-band observations (Chapter 4) and the ATCA 16 cm band observations (Chapter 3), respectively. *Right:* Modelled Faraday spectra for the λ^2 ranges indicated in green and grey on the left panels. The model parameters are listed on the plot, and indicated by the yellow dashed lines.

This is usually required when there are multiple synchrotron emitting components in the plane of the sky. Through QU-fitting we can recover important parameters that describe both the intrinsic source properties and external features affecting the observed fractional polarisation.

The Faraday simple model (similar to Equation 2.17) is described as a purely synchrotron emitting source with an external Faraday rotating screen, with

$$\mathbf{p}(\lambda^2) = p_0 e^{2i(\chi_0 + \phi\lambda^2)}, \tag{2.30}$$

where p_0 is the intrinsic fractional polarisation at the source, χ_0 is the intrinsic polarisation angle, and ϕ is the RM corresponding to the emitting component. When all of the polarised emission is subjected to a single RM only, this is sometimes referred to as a *Faraday thin* source. An example of the QU spectra and the Faraday spectrum for this model is shown in top left and right panels of Figure 2.7, respectively. An astrophysical example of this model is a synchrotron-emitting radio galaxy with the Milky Way as a foreground Faraday rotating screen. In Chapter 3, we use a modified version of this model (Schnitzeler et al., 2015), which we derive in Appendix A of Ranchod et al. (2024) (presented in Appendix D of this thesis),

$$\mathbf{p}(\lambda^2) = p_0 \left(\frac{\lambda^2}{\lambda^2_{\rm ref}} \right)^{-\delta\alpha/2} e^{2i(\chi_0 + \phi\lambda^2)}. \tag{2.31}$$

Here, in the case of multiple emitting components, as described above, we assume that dividing by Stokes I does not fully compensate for the spectral indices of individual components. The parameter $\delta\alpha$ captures any deviation from the net spectral index on a per-component basis, and $\lambda_{\rm ref}$ is a given frequency for which the spectral index is measured. An example of this model for two emitting components is

shown in the first row of Figure 2.8.

Depolarisation is the reduction of the fractional polarisation with respect to the intrinsic polarisation of the source. In Section 2.1.3, we describe bandwidth and beam depolarisation caused by instrumental effects. Below, we detail astrophysical causes of depolarisation by introducing QU-fitting models that include λ-dependent depolarisation, which occurs when the magneto-ionic medium becomes relatively less ordered within the beam volume, e.g. turbulence, or in the case of differential Faraday rotation along the line of sight. The *Burn slab model* describes a simultaneously synchrotron-emitting and Faraday-rotating volume. This model represents a Faraday thick source (i.e. emitting over a continuous range of Faraday depths), as the emission from the side that is further from the observer experiences more Faraday rotation than the near side as it passes through the volume. This results in differential Faraday rotation, dispersing the signal over a range of ϕ. Typically, this model also includes a homogeneous Faraday rotating foreground screen, i.e. The Milky Way ISM. This model is given by,

$$\mathbf{p}(\lambda^2) = p_0 \frac{\sin(\phi_{\rm diff}\lambda^2)}{\phi_{\rm diff}\lambda^2} e^{2i[\chi_0 + (\frac{1}{2}\phi_{\rm diff} + \phi)\lambda^2]}, \tag{2.32}$$

where ϕ is the foreground Faraday rotation and $\phi_{\rm diff}$ is the differential Faraday rotation within the source. This is plotted in Figure 2.8, which shows a decrease in fractional polarisation, as well as a "top-hat" broadening of the FDF. Another important source of depolarisation is turbulence in the magneto-ionised medium, both in the foreground and in the direct source environment. As we introduce in Chapter 3, this turbulence is due to spatial fluctuations in the magnetic field and/or the electron density and can be described by *Faraday dispersion*. Assuming the simplest model, this is an effect of Gaussian turbulence (i.e., the probability density function of the thermal electron density and/or magnetic fields are Gaussian), whereby there exists a significant number of turbulent cells within the beam volume. Various lines of sight within the beam volume might pass through different turbulent cells and therefore experience a different amount of Faraday rotation. The net signal is combined due to the telescope resolution limit, causing a dispersion in the FDF as well as depolarisation (Figure 2.8). This model is called *external Faraday dispersion* and is given by,

$$\mathbf{p}(\lambda^2) = p_0 e^{-2\sigma_\phi \lambda^4} e^{2i(\chi_0 + \phi\lambda^2)}, \tag{2.33}$$

where σ_ϕ is the Faraday dispersion. Finally, we use an *internal Faraday dispersion* model. This is similar to the Burn slab scenario where we have a simultaneously synchrotron-emitting and Faraday-rotating source. However, in addition to this, the Faraday-rotating medium is also turbulent. This is given by,

$$\mathbf{p}(\lambda^2) = p_0 e^{2i\chi_0} \left(\frac{1 - e^{i\phi\lambda^2 - 2\sigma_\phi^2\lambda^4}}{2\sigma_\phi^2\lambda^4 - i\phi\lambda^2} \right). \tag{2.34}$$

In Chapter 4, we use Equations 2.30, 2.32, 2.33 and 2.34 to fit the QU spectra of the extragalactic polarised sources in the COSMOS field. In both Chapters 3 and 4, we fit multiple models to the spectra and select the model with the best fit using the Bayesian information criterion (BIC) and log Bayesian evidence $\log(Z)$ for the respective studies.

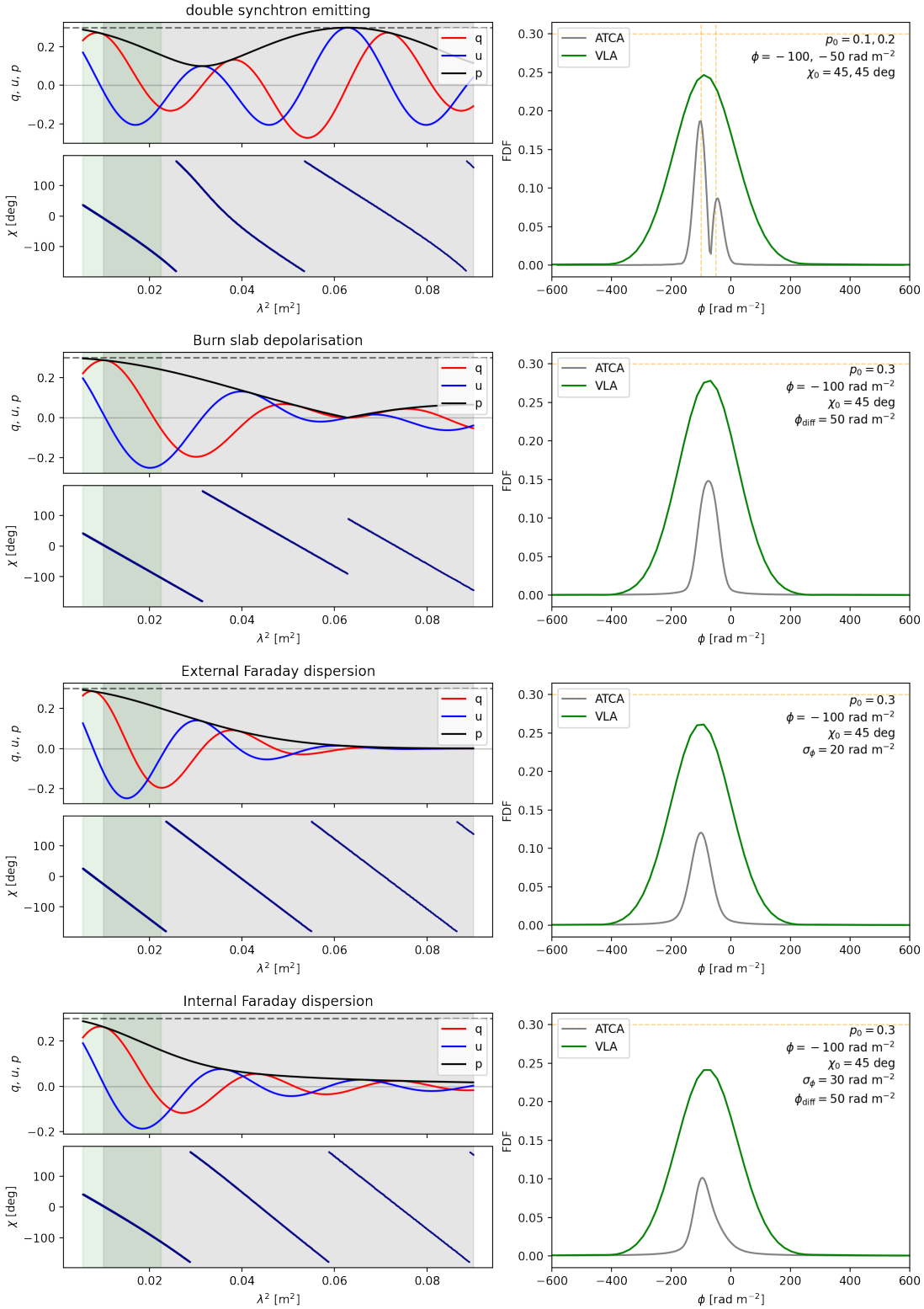

Figure 2.8: Fractional Stokes *qu* spectra, fractional polarisation, polarisation angles and Faraday spectra, as in Figure 2.7, illustrated for various Faraday complex models. From top to bottom, we have the double Faraday synchrotron-emitting model, the Burn slab depolarisation model, the external Faraday dispersion model and the internal Faraday dispersion model.

2.2.3 Faraday complexity

Faraday complexity is a key characteristic of the broadband λ^2 behaviour of a polarised source, and an important definition in the context of this thesis. This designator describes whether a source is Faraday simple or Faraday complex. It is important to note that Faraday complexity is an observational classification and can be affected by various observational parameters, such as angular resolution, frequency, and telescope sensitivity, as I will detail below. First, we define *Faraday simple*. This is when all of the polarised emission within the beam volume is subjected to a single ϕ only (i.e. a single Faraday thin component). An example of a Faraday simple source is shown in Figure 2.7. In Faraday depth, such a source would appear as a delta function convolved with the RMSF (Equation 2.25). Faraday simple sources also exhibit a linear $\Delta\chi$ as a function of λ^2, which can be described by the classical definition $\Delta\chi = \phi\lambda^2$. In terms of the complex polarisation, Faraday simple sources are best fit by Equation 2.30 or Equation 2.31 (with $\delta\alpha = 0$) for a single synchrotron-emitting component only (i.e. $n = 1$ as defined in Equation 2.29). Additionally, these sources do not exhibit λ-dependent depolarisation and have constant $p(\lambda^2)$. This is illustrated in the right panel of Figure 2.7, where the ATCA and VLA observations sample different ranges of λ^2, and as a result the VLA observations have a much lower Faraday depth resolution, hence the broader FDF peak. Despite this, both example Faraday spectra have the sample amplitude, indicating no depolarisation.

In contrast, a *Faraday complex* source has emission that is subjected to a range of ϕ within the beam volume. This may be a case where there are multiple emitting components within the beam volume (e.g. multiple radio lobes in an FRII galaxy, intervening galaxies or intercluster medium and foreground Galactic emission) or if a single source of emission has a range of ϕ due to differential Faraday rotation or turbulence. Regarding the QU-fitting models, Equations 2.32–2.34 describe Faraday complex sources, as well as Equations 2.30 and 2.31 if $n > 1$. Figure 2.8 illustrates examples of Faraday complex sources. As shown in the right-hand panels of the figure, these sources typically have a more complex Faraday spectrum, with multiple peaks or broadened peaks. However, these features cannot be distinguished with limited Faraday depth resolution, and can sometimes be modelled through more detailed QU-fitting. This is also illustrated in Figure 2.8, where the lower frequency ATCA models show complex structures in the Faraday spectra, however, these are not resolved in the lower resolution VLA Faraday spectra. For Faraday complex sources, the $\Delta\chi$ is also often non-linear as function of λ^2. Another important observed feature of Faraday complex sources is depolarisation. Figure 2.8 shows a clear overall decrease in $p(\lambda^2)$ for the internal and external Faraday dispersion models, while the double synchrotron emitting and the Burn slab depolarisation models have $p(\lambda^2)$ variablilty that results in a net depolarisation effect. This is illustrated in the corresponding Faraday spectra, where all examples peak with lower p than the intrinsic value of $p_0 = 0.3$. This depolarisation is more pronounced for the lower frequency ATCA observations due to the λ^2 dependence of Faraday rotation, emphasising the advantage of polarised observations at higher frequencies. Some examples of properties used to identify Faraday simple and complex sources are summarised in Table 2.2, however the interpretation of Faraday complexity is currently an active field of research, including in this thesis, and careful considerations should be taken when classifying sources.

With the emergence of broadband, large-area polarisation surveys in the pre-SKA era, e.g. POlarisation Sky Survey of the Universe's Magnetism (POSSUM; Gaensler et al., 2025), LOFAR Two-metre Sky Survey (LoTSS; Shimwell et al., 2022) and the MPIfR MeerKAT Galactic Plane Survey (MMGPS; Padmanabh et al., 2023), more automated methods for identifying Faraday complexity are currently

Table 2.2: Identifying features of Faraday simple and Faraday complex sources*

	Faraday simple	Faraday complex
ϕ	single discrete	multiple discrete or continuous range
FDF	one peak	multiple peaks or broadening
$\chi(\lambda^2)$	linear	typically non-linear
$p(\lambda^2)$	constant	variable or depolarisation

*As detailed in the text, the sensitivity to detecting Faraday complexity is highly dependent on the observation setup and sensitivity. This table serves as a simplified visual guide, under the assumption that we are able to detect complexity.

under development to allow for the systematic processing of a large number of sources. While these methods are not used in this thesis, I will briefly summarise a few below. The FDF second moment M_2 (e.g. Anderson et al., 2015; Livingston et al., 2021) is a single value used to quantify the complexity of a Faraday spectrum. This is computed by weighting various peaks in the FDF by their amplitude and difference in ϕ from the mean ϕ of the source. This quantification can be particularly useful when comparing the degree of complexity across a sample. A similar method is the $\sigma_{\rm add}$ complexity metric (e.g. Vanderwoude et al., 2024). This method subtracts the q and u spectra for a given source from modelled Faraday simple q and u spectra, where ϕ, χ and p_0 are determined from RM synthesis. Here, the Faraday complexity is quantified by the residuals between the observed spectrum and the simple model.

Investigations into Faraday complexity are important for understanding the physical magneto-ionic properties of radio galaxies (both SFG and AGN), as well as complex structures in the Galactic magneto-ionic foreground. This is on-going field of research, with recent complexity studies done to study star-forming galaxies (e.g. Mao et al., 2015; Basu et al., 2017; Legodi et al., 2021), AGN (e.g. O'Sullivan et al., 2017; Pasetto et al., 2018) and the extragalactic source population in general (e.g. Anderson et al., 2015; Schnitzeler et al., 2019). Other recent works have used Faraday complexity to probe small scale turbulence or ionisation fronts in the Milky Way (e.g. Anderson et al., 2015; Livingston et al., 2021; Ma et al., 2025). In Chapter 3 we investigate the effect of angular resolution on complexity classification, and the extent to which large scale Galactic polarised emission can cause a misinterpretation of Faraday complexity when measuring small-scale turbulence in the Galactic plane. In Chapter 4, we also classify sources according to their best-fit QU-fitting models to assess the prevalence of depolarisation in an unbiased extragalactic sample to investigate how this affects the polarised source counts at higher frequencies.

CHAPTER 3

The Galactic latitude dependency of Faraday complexity

The Galactic latitude dependency of Faraday complexity in the S-PASS/ATCA RM Catalogue
S. Ranchod, S. A. Mao, R. Deane, S. S. Sridhar, A. Damas-Segovia, J. D. Livingston, and Y. K. Ma
Astronomy & Astrophysics, 686, A104 (2024)

This chapter serves as a summary of the paper "The Galactic latitude dependency of Faraday complexity in the S-PASS/ATCA RM Catalogue", Ranchod et al. (2024), originally published in Astronomy & Astrophysics. The full paper is presented in its original form in Appendix D.

3.1 Paper summary

The Faraday rotation measure (RM) of extragalactic polarised sources (i.e. the variation of polarisation angle as a function of λ^2) is an essential observational tool for probing the structure of the Galactic magneto-ionic foreground. The broadband receivers of modern radio telescopes allow for the measurement of complex λ^2 behaviour (Faraday complexity) to characterise the magneto-ionic properties of both extragalactic sources and their Galactic foregrounds along the line-of-sight. While Faraday complexity is a key physical descriptor, this classification can be affected by various observational factors, and it is crucial to understand how parameters such as angular resolution and telescope sensitivity can bias this classification scheme. In this chapter, and the associated publication, we address the systematic trends in the SPASS/ATCA RM catalogue (Schnitzeler et al., 2019, hereafter S19), the most extensive broadband RM catalogue in the southern sky. Quantifying such trends in legacy RM catalogues is an important step for developing analysis methods and optimising synergy with these catalogues in the pre-SKA and SKA eras.

In the analysis of the S19 catalogue, we report an increase of Faraday complexity towards the Galactic plane, accompanied by a deficit of Faraday simple sources near the plane. Here, the complexity is quantified by the number of fitted polarised components in the Stokes Q and U spectra. We propose that this increase is Galactic in origin and aim to investigate if it is caused by contamination in the SPASS/ATCA spectra from diffuse Galactic synchrotron emission, or if this is an effect of small-scale magneto-ionic turbulence in the Milky Way.

To investigate this, we carry out higher angular resolution observations using the Australia Telescope Compact Array (ATCA) of 105 bright sources in the SPASS/ATCA catalogue close to the Galactic plane. We calibrate (primary- and self-calibration) and flag the data for RFI. Each source is then imaged as spectral cubes in Stokes I, Q and U. We perform QU-fitting with models describing the sum of up to 5 polarised components and select the best model for each source using the Bayesian information criterion, with the given number of components n quantifying the Faraday complexity.

As a verification of the SPASS/ATCA catalogue, we compared flux density measurements. We found a 5% offset in total intensity, and significant offsets ($> 3\sigma$) for 19% sources in polarised intensity. We find 94% of sources have consistent RM with SPASS/ATCA. The most striking result of this work is that only 42% of our observed sources are Faraday complex ($n > 1$), in contrast to 90% of the same sample in SPASS/ATCA. We also no longer observe an increase of complexity towards the Galactic plane, and find a mean difference in number of components per latitude bin of $|\Delta n| = 1.1$. This provides evidence that the increase of Faraday complexity in SPASS/ATCA is caused by contaminating diffuse synchrotron emission, with the assumption that the polarised intensity of the diffuse foreground is approximately constant.

We discuss the various physical scenarios that contribute to Faraday complexity, and how this is affected by the observation set up. We emphasise that correctly removing the diffuse foreground emission is crucial for an accurate measure of small-scale magneto-ionic turbulence in the Galactic plane. Finally, we discuss the origin of Faraday complexity in the remaining complex sources by analysing their Faraday spectra. Considering the Galactic longitude of the complex sources, we find a fair correlation $\rho = 0.65$ between the positions of the complex sources and the spiral arm tangents, the first time such a relation has been reported. This suggests an effect of small-scale magneto-ionic ISM turbulence in the spiral arm regions, which we resolve out (i.e. do not detect) in the interarm regions, at scales consistent with those established through RM structure function analysis in the literature. This is another key finding from this paper, and is the first instance of the Faraday complexity of background extragalactic sources being used to probe turbulent scales in the Galactic spiral arm tangents.

This work was originally published as *The Galactic latitude dependency of Faraday complexity in the S-PASS/ATCA RM Catalogue*, Ranchod et al. (2024) in Astronomy & Astrophysics. As the leading author of this paper, I wrote the entire manuscript. I conducted the observations with the Australia Telescope Compact Array in January and February 2022, with assistance from the PI, Y. K. Ma. I developed the calibration and imaging pipelines to process the data, and conducted the spectro-polarimetric analysis. I conducted the QU-fitting analysis using self-modified software originally developed by A. Basu. I conducted remainder of the analysis and produced all figures, as well as the catalogue that was released with this work.

CHAPTER 4

Unveiling the μJy polarised source population in the VLA-COSMOS 3 GHz survey

4.1 Introduction

As introduced in Chapter 1, magnetic fields have a crucial active role in galaxy evolution, influencing physical source properties, such as star-formation and the feedback processes of active galactic nuclei (AGN). The strength and ordering of magnetic fields in synchrotron-emitting sources can be directly observed through the linear polarisation of this emission. Furthermore, the Faraday rotation of the polarised emission from an extragalactic background source as it propagates towards the observer can reveal the physical conditions of the foreground Galactic magneto-ionic medium or the local environment of the source. To fully understand the role of magnetic fields in galaxy evolution, how this varies with source characteristics and develops over cosmic time, we require statistically large samples of polarised extragalactic sources. In particular, we require source detections over a range of polarised intensities, to probe various sub-populations, such as low-luminosity AGN and star-forming galaxies. As such, deep polarisation surveys are an important tool for understanding both the faint extragalactic source population and the intervening Galactic magneto-ionic field medium.

Historically, blind extragalactic polarisation surveys have been limited to the bright source population ($P_{1.4\,\mathrm{GHz}} > 0.5$ mJy). Investigations into the number counts of polarised sources have found that the dominant source of polarised emission in current surveys is from AGN (Taylor et al., 2007), likely from the extended lobes of Fanaroff-Riley (FR; Fanaroff and Riley, 1974) radio galaxies (Grant et al., 2010). Other polarisation surveys in this era reported an anti-correlation between the total intensity or luminosity of radio sources and their fractional polarisation (e.g. Mesa et al., 2002; Tucci et al., 2004; Taylor et al., 2007; Grant et al., 2010). The cause of this anti-correlation is still an open question, and since fractional polarisation is both a probe of the direct source environment (e.g. interstellar medium, or some cases, intracluster medium) and the magnetic field ordering within the sources, it is important to understand the physical processes that are driving this trend. Modern, deeper polarisation surveys (Hales et al., 2014; Rudnick and Owen, 2014; Berger et al., 2021) have argued against the physical origin of the anti-correlation, attributing it rather to selection bias and spurious detections at low flux densities. On the contrary, a targeted study of separate extragalactic populations (Banfield et al., 2014), i.e. quiescent vs quasar-like polarised sources identified using infrared colours, found a higher fractional

polarisation for low luminosity (quiescent) sources with respect to high luminosity sources (quasar-like). This suggested that the anti-correlation is an effect of the change in source population as a function of luminosity. Further evidence for this dichotomy was provided by O'Sullivan et al. (2015) and O'Sullivan et al. (2017), who find a difference in the intrinsic fractional polarisation of radio galaxies based on their host accretion state (i.e. jet-mode vs radiative-mode), where lower luminosity jet-mode sources possess a higher intrinsic fractional polarisation.

Over the past decade, we have begun to probe the fainter polarised population, with Rudnick and Owen (2014) (hereafter, RO14) pioneering the investigation into the μJy regime. Their deep survey of the GOODS-N field with the Karl G. Jansky Very Large Array (VLA), down to $P_{1.4\,\mathrm{GHz}} > 30\ \mu\mathrm{Jy\,beam}^{-1}$, revealed a flattening in the cumulative polarised source counts for $P_{1.4\,\mathrm{GHz}} < 1$ mJy, with respect to previous works with brighter sources (Subrahmanyan et al., 2010; Grant et al., 2010). This slope transition has also been observed by Eyles et al. (2020) and Berger et al. (2025). While RO14 attribute this flattening to a change in population between FRI (core-dominated) and FRII (lobe-dominated) sources (e.g. O'Sullivan et al., 2008), no modern surveys have had both the angular resolution for morphological source classification (e.g. Berger et al., 2021), and the depth and area for a statistically large number of detections to confirm this trend. More recently, the Square Kilometre Array (SKA) precursor telescopes have given rise to sensitive polarisation surveys that readily detect the sub-mJy polarised population, producing unprecedented rotation measure (RM) densities for RM grid experiments. These catalogues can be used to map the foreground Galactic magnetic field (e.g. Brown et al., 2007; Schnitzeler et al., 2019; Ma et al., 2020), nearby galaxies (e.g. Mao et al., 2008; Livingston et al., 2022) and galaxy clusters (e.g. Anderson et al., 2021; Loi et al., 2025). The early science results from the Polarisation Sky Survey of the Universe's Magnetism (POSSUM; Gaensler et al., 2010) with the Australian SKA Pathfinder (ASKAP) have produced RM densities of $> 30\ \mathrm{deg}^{-2}$ (Vanderwoude et al., 2024), and will eventually cover 20 000 deg^2 of the southern sky to a sensitivity of $\sim 25\ \mu\mathrm{Jy\,beam}^{-1}$. The MPIfR MeerKAT Galactic Plane Survey (MMGPS; Padmanabh et al., 2023) is set to produce an RM density of $\sim 40\ \mathrm{deg}^{-2}$ around the southern Galactic plane to a sensitivity of $\sim 9\ \mu\mathrm{Jy\,beam}^{-1}$. While these surveys are actively ongoing, there remains much to be understood about observational biases that may effect these RM grid experiments (Chapter 3). Moreover, there are many unknowns about about the physical nature of the faint polarised population, such as the prevalence of AGN with various radiative modes, how magnetic field ordering is related to AGN morphology and the environment of the host galaxy, and also the role of magnetic fields in the evolution of star-forming galaxies (SFGs; Crutcher, 2012). These can all be addressed through deep extragalactic polarisation surveys. To date, the deepest are the MeerKAT International GHz Extragalactic Exploration (MIGHTEE; Taylor et al., 2024) with $P_{1.4\,\mathrm{GHz}} > 16.5\ \mu\mathrm{Jy\,beam}^{-1}$ and the MeerKAT Fornax Survey (Loi et al., 2025) with $P_{1.4\,\mathrm{GHz}} > 9\ \mu\mathrm{Jy\,beam}^{-1}$. Despite the depths of these surveys, all polarised sources are classified as AGN, and it is not well constrained to which depth we require to readily detect the SFG population (e.g. O'Sullivan et al., 2008).

While the majority of the blind extragalactic surveys discussed here were conducted at 1.4 GHz (L-band), higher frequencies can offer a new perspective. The resulting higher angular resolution can better mitigate beam depolarisation and enable the morphological classification of radio sources. Given the λ^2-dependence of depolarisation (due to turbulent screens or internal effects, see Chapter 2), at 3 GHz, we are less affected by depolarisation, and can possibly detect sources that are otherwise depolarised at lower frequencies. Through simulations, Stil et al. (2009) show that unresolved SFGs

are expected to have an increased rest-frame fractional polarisation up 20% at 4.8 GHz as opposed to only 10% (in extreme cases) at 1.4 GHz. In a simulation of Milky Way-like SFGs, Sun and Reich (2012) found a similar frequency dependence, with the distribution of integrated fractional polarisation peaking at 4.2% at 4.8 GHz and dropping to a peak of 0.8% at 1.4 GHz. In a review of available polarisation surveys at the time, Tucci and Toffolatti (2012) show an increase in the median fractional polarisation from 1.5% at 1.4 GHz to ~3% at > 10 GHz for steep- and flat-spectrum AGN. However, the frequency-dependence of polarised source counts is relatively unexplored in the literature. Detailed modelling of the frequency dependence of observed source counts for various source classifications can characterise the spectral index and depolarisation behaviour (e.g. Lamee et al., 2016) of the polarised source population as a whole. Moreover, this is a necessary step in the planning of SKA-era surveys, to maximise the number of detected sources for RM grid experiments (e.g. Heald et al., 2020).

To study the faint polarised sky at 3 GHz, we use the VLA-COSMOS 3 GHz Large Project (Smolčić et al., 2017a, hereafter, S17), which is a deep ($\sim$ 2.3 μJy beam^{-1}), high resolution (0.75”), broad bandwidth (2–4 GHz) survey with the VLA, over 2 deg^2 in the COSMOS field. This region has broad multi-wavelength coverage, which combined with the radio catalogue has produced new insights into the far-infrared-radio correlation (Delhaize et al., 2017), the redshift evolution of the AGN dichotomy (Delvecchio et al., 2017) and the cosmic star-formation rate history (Novak et al., 2017; Leslie et al., 2020). In this chapter, we reprocess this survey to include polarisation calibration and Stokes Q and U imaging to investigate the polarised source population in the COSMOS field. We aim to provide a comprehensive characterisation of the sub-100 μJy polarised source population in terms of intrinsic fractional polarisation, radio morphology and radiative mode of host galaxy. Furthermore, through spectral modelling, we will investigate the dominant depolarisation mechanisms for the detected sources. This will characterise the faint polarised source population over an unexplored parameter space, due to the combined depth, resolution, bandwidth and multi-wavelength coverage of this survey and produce the largest sample of sub-100 μJy sources at 3 GHz to date. In addition, we will compute the polarised source counts at 3 GHz to investigate their frequency dependence with respect to legacy L-band surveys (e.g. RO14).

This chapter is organised as follows: In Section 4.2, we detail the data processing, including calibration, imaging, source finding, and spectral analysis. We present the polarised source counts in Section 4.3. In Section 4.4, we present the fractional polarisation analysis based on the source classification, the results of the Stokes QU-fitting and RM synthesis. In Section 4.5, we discuss the frequency evolution of the polarised source counts and the biases regarding source detectability at 3 GHz. We summarise and conclude in Section 4.6.

4.2 VLA-COSMOS 3 GHz Large Project

The VLA-COSMOS 3 GHz large project (S17) is a broadband full-Stokes survey of the 2 deg^2 COSMOS field (centred at RA=10:00:28.6, Dec=+02:12:21.0) with the VLA, a 27-dish radio interferometer located in New Mexico, USA. This survey observes the COSMOS field in the S-band (2–4 GHz), an important contribution to the wealth of already-available multi-wavelength data for this legacy extragalactic field. The continuum (Stokes I) data release produced a total intensity mosaic image with a median rms of $\sigma = 2.3\,\mu$Jy beam^{-1}, and a high angular resolution of 0.75".

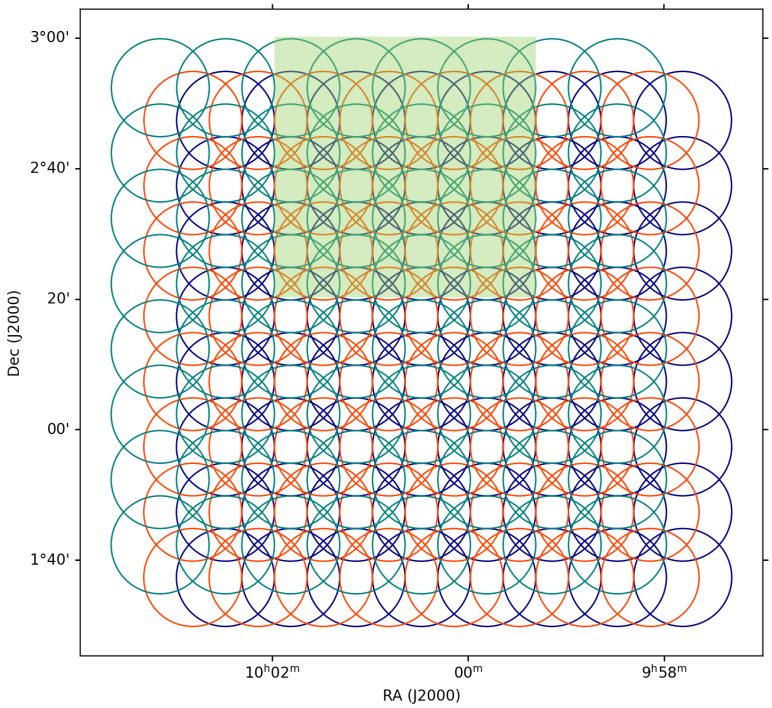

Figure 4.1: Pointing configuration for the VLA-COSMOS 3 GHz survey. The offset 8×8 grids are indicated in orange, blue and teal, respectively. Each circle represents the primary beam at the central frequency (3 GHz), with a half-power beam width (HPBW) of 15'. The HPBW is frequency dependent and scales by a factor of 2 between the high and low ends of the band. This tight configuration ensures significant overlap between pointings, even at the high end of the band. The shaded green area indicates the "subgrid" region used for the initial data verification.

A total of 384 hours were observed on this field from November 2012 to May 2014 with the VLA A-array (324 hours) and C-array (60 hours) configurations. The survey is comprised of 192 pointings, arranged in three grids of 64 (8×8), with a 10' separation in RA and Dec within a given grid. This separation corresponds to two thirds of the full-width half-maximum (FWHM) of the primary beam at the central frequency of 3 GHz. The second (third) grid was separated from the initial grid by 5' in RA and Dec (–5' in RA only), resulting in a dense pointing configuration designed to achieve a uniform rms over the field. A diagram of the pointing configuration is shown in Figure 4.1. A given observation observed all pointings in one of the 64-pointing grids either once (twice) over a 3 (5) hour observing block, maximising the uv-coverage for each pointing. In each observation, J1331+3030 (3C 286) was observed for flux, bandpass and polarisation calibration with a 3–5 min scan and J0713+4349 for 5 min as a polarisation leakage calibrator. The complex gain calibrator J1024–0052 was observed every 30 min over each observation. Further information on the calibrator duty-cycle and observing conditions is available in S17.

4.2.1 Data processing and imaging

In the continuum data release, the data were calibrated using the Astronomical Image Processing System (AIPS). In this work, we recalibrate the data to allow for a robust verification of the polarisation calibration, which was not regarded in the continuum data release. Moreover, given the technical advancements in the handling of big radio interferometric data in the pre-SKA era, particularly the development of new software and pipelines, it is feasible to reprocess from scratch.

The uncalibrated data were retrieved from the VLA archive, under the Legacy ID AS1163, as 113 separate schedule blocks and processed using the VLA CASA pipeline (McMullin et al., 2007) version 2022.2.0.64 in CASA version 6.4.1. We note that S17 use an early version of the VLA CASA pipeline as a comparison to the tailored AIPS pipeline, and find no significant difference in the output. In brief, the VLA CASA pipeline primary calibration consists of the application of flags based on instrumental limitations (i.e. band edges) and flux calibration. It then iteratively performs initial bandpass, delay and gain (phase) calibration while identifying and flagging radio frequency interference (RFI). The initial calibration is then applied and a second round of RFI flagging is performed on the calibrator sources. This is followed by a final bandpass, delay and gain calibration, the application of the solutions and flags to the target data, and a final round of RFI flagging on the target data. We modify the standard version of the pipeline to include polarisation calibration, using the polarisation leakage calibrator J0713+4349 and the polarisation angle calibrator J1331+3030 (3C286; Perley and Butler, 2017). This is done by enabling `hifv_circfeedpolcal`, which performs cross-hand delay, leakage and polarisation angle calibration before solutions are applied to the target and the final round of RFI flagging.

We assess the quality of the calibration through the diagnostic plots that are produced by the pipeline. Of the 113 observations, six are discarded due to corruption of the data in the archiving process. Inspecting the phase calibrator for each observation, we find an average flagged percentage of 67.4%, 61.9% and 61.5% for the three pointing grids respectively. As described in S17, spectral windows 2 and 3 have high levels of RFI corruption, and were 100% flagged in the S17 calibration. Due to the robust automated flagging methods `tfcrop` and `rflag` in CASA's `flagdata`, in this work we flag as little as 70% in these spectral windows (SPW) for some observations, with the majority of observations flagged at 100%. Similarly, we have high RFI contamination at the higher frequency end of the band (SPW 14–16). This contamination is worse in the C-array pointings, due to less RFI decorrelation in the more compact configuration, for which we have at least 90% flagged.

As a check for the success of the polarisation calibration, we plot the corrected amplitude and phase of the polarisation leakage calibrator and the polarisation angle calibrator as a function of frequency. Examples of such plots are shown in Appendix A. We found a consistent amplitude and phase with the expected values for both calibrator sources across all observations. As a further check, we concatenate one third of the observations of the leakage calibrator and the polarisation angle calibrator into single measurement sets (MS) to image together. We then image both calibrator sources as full-Stokes spectral cubes using WSClean (Offringa et al., 2014) with a spectral resolution of 16 MHz (128 channels). To assess the polarisation angle calibration, we perform RM synthesis on the polarisation angle calibrator using the RMtools package from CIRADA Tools (Purcell et al., 2020). We obtain a polarisation angle χ of $\chi = 31.92 \pm 0.02$ deg and a Faraday depth of $\phi = 0.36 \pm 0.06$ rad m^{-2}, which is consistent with what we expect from the literature (Perley and Butler, 2013). In this section, we only discuss on-axis leakage

quantification. An in-depth off-axis leakage quantification can be found in Section 4.2.3. To quantify the residual on-axis leakage, we measure the linear p_L and circular p_V polarisation fraction of the leakage calibrator J0713+4349, which is unpolarised. We find $p_L = 0.027\%$ and $p_V = 0.35\%$, and take these to be the upper limit for leakage in the respective polarisations.

Following calibration, the data were prepared for imaging and mosaicking. The calibrated data were split out of each observation, and combined into separate MSs according to their pointing positions, using CASA tasks `split` and `mstransform`. This resulted in 192 MSs, that each consisted of ~ 30 individual observations, combining A-array and C-array observations. From here, each pointing was processed separately.

Self-calibration

In S17, phase-only self-calibration was performed on pointings that contained sources brighter than 5 mJy beam^{-1}. From the inspection of our initial images, we find that the artefacts caused by gain phase and amplitude errors around the bright sources are less severe than that shown in Figure 5 of S17. In addition, the total intensity data release has produced high quality Stokes I MFS images, that we can use for fractional polarisation analysis. For the Stokes Q and U images, we do not expect any emission above 5 mJy beam^{-1} that would be greatly affected by these artefacts. Furthermore, any such artefacts would not be visible above the noise, as evident from the initial image cubes.

Spectral cube imaging

After splitting the data into separate MSs for individual pointings, we imaged each pointing as multi-channel spectral cubes for Stokes I, Q and U and as multi-frequency synthesis images (MFS) for Stokes I. In this work, we are only interesting in detect linearly polarised sources, so we do not image the Stokes V, in which we would detect circularly polarised sources. To assess various imaging methods and select suitable parameters, we first imaged a sub-sample of 27 pointings. This was comprised of 9 (3×3) pointings from each of the observing grids, covering an area of 0.56 deg^2 ($45' \times 45'$). This region (referred to as 'subgrid' hereafter) was centred on an arbitrarily chosen position of RA =10:00:38.6, Dec = +02:39:50.95, towards the north-centre of the full field (see Figure 4.1). The selected imaging parameters are detailed below.

For spectral cube imaging, we have to carefully select the optimal number of frequency channels and the channel width $\Delta\nu$, particularly regarding the expected per-channel sensitivity and bandwidth depolarisation effects (see Chapter 2). The channel width also affects the maximum Faraday depth ϕ we are sensitive to after RM synthesis. In addition, we are limited by computational time and disk capacity for large volumes of data. Following Gaensler et al. (2001), the degree of bandwidth depolarisation p_b is given by

$$p_b = \left| \frac{\sin \Delta\Theta}{\Delta\Theta} \right|, \tag{4.1}$$

where

$$\Delta\Theta = \frac{2\phi c^2 \Delta\nu}{\nu^3}. \tag{4.2}$$

Assuming a range of $5 < |\phi| < 400$ rad m^{-2}, which is typical for extragalactic point sources at ~arcsec resolution at high Galactic latitude (O'Sullivan et al., 2017; Taylor et al., 2024), we calculate p_b for channel widths between $0 < \Delta\nu < 100$ MHz. We assume a reasonable bandwidth depolarisation limit of $p_b > 95\%$, and can achieve this for $\Delta\nu < 70$ MHz over the given range of ϕ. We opt for 64 channels with $\Delta\nu = 32$ MHz. This allows for an expected per-channel sensitivity of 18 μJy beam^{-1} for mosaicked channels, assuming natural weighting and uniform flagging across the band, and results in a sufficient number of channels for RM synthesis.

Imaging was carried out using WSClean, for 8000×8000 pixel images, and a pixel size of 0.2". First, we created a deconvolution mask, using the Stokes I mosaicked image from S17. This was done by selecting pixels above 8σ, with respect to the local root-mean-square (rms) noise and performing two rounds of binary dilation. This mask was then cropped and centred to create individual masks for each pointing. Since the lower frequency channels have a field of view larger than their counterparts in the S17 mosaic, we manually create masks for pointings at the edge of the mosaic. First, we created a shallow image with 100 iterations, and created a 6σ mask from this, as described above. This mask was then combined with the mask from the S17 image. We selected a Briggs (Briggs, 1995) weighting of 0.7 (CASA convention) and cleaned to a threshold of 0.3σ, based on the local rms. We also use the `join-channels` parameter, and do not apply multi-scale cleaning. This would be too time consuming and computationally expensive with this channel resolution. Furthermore, we do not expect to detect the larger-scale faint emission at the sensitivity of the individual channel maps, and explore this in more detail in the producing of the MFS images (Section 4.2.1). Using this method, we imaged 64 frequency channels for Stokes I, Q and U for all 192 pointings, resulting in 36 864 images.

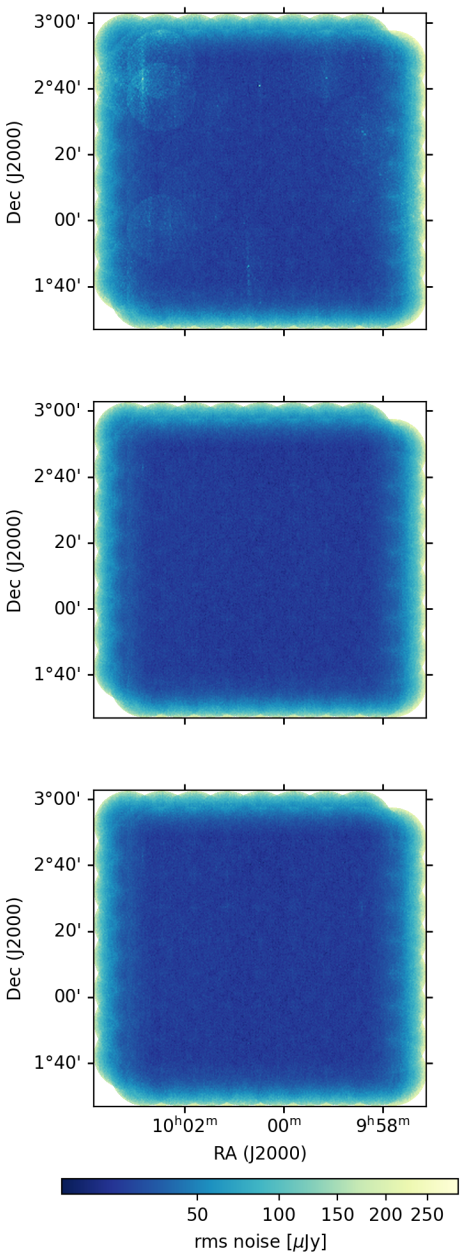

Figure 4.2: RMS noise maps for the central frequency (ν = 3002 MHz) of the mosaicked images. Stokes I is shown at the top, Stokes Q in the centre and Stokes U at the bottom. The colour stretch of the maps is in square-root scale to highlight outliers.

To achieve a uniform angular resolution across the band, we smoothed each channel map, such that the resulting angular resolution was larger than or equal to the angular resolution at the lowest

frequency. We selected a target angular resolution of $\theta = 1.5''$, which is roughly two times worse than the angular resolution of the MFS image in S17 ($\theta = 0.75''$). This was followed by primary beam correction. We created primary beam models for each frequency channel, and for Stokes I, Q and U using the CASA task `tclean`. The primary beam correction was applied to all channel maps using the task `pbcor`. We find that 20% of pointings have large restoring beams with extreme ellipticity for one or more channels between 2129 MHz $< \nu <$ 2349 MHz due to the large flagged percentage at these frequencies (SPWs 2 and 3). For such cases, we exclude the channel map in the mosaicked image. These areas in the mosaic are still fully covered by adjacent pointings. As we will discuss in further sections, excluding these channels from RM synthesis would have a minimal impact on derived parameters and uncertainties, as the affected channels are localised over a small frequency range.

Following primary beam correction, we group images by channel rather than pointing position in preparation for mosaicking. We create a mosaic for each channel in Stokes I, Q and U using MONTAGE[1], where each image is weighted by the square of the primary beam model. On average, each channel mosaic has an rms of 22 μJy beam^{-1} in Stokes I, Q and U. We produce rms maps for each mosaic using PYBDSF (Mohan and Rafferty, 2015) to map the spatial variation of noise per channel and across the mosaicked area. PYBDSF computes these images using a sliding box of 100 pix $\times$ 100 pix. The resultant rms maps (Stokes I, Q, U) for the central frequency, (ν = 3002) MHz are shown in Figure 4.2. We note that there are regions with increased rms in the Stokes I noise map. This is attributed to increased artefacts surrounding bright sources, and is typically confined to individual pointings containing those sources. The increased noise is not present in the corresponding pointings in the Stokes Q and U maps, as these sources are significantly fainter or undetected in polarisation. We do not combine the separate channel maps into a cube due to the impracticalities of handling a file of this size. The median rms noise as a function of frequency is shown in Figure 4.3. We have increased noise at $\nu < 2.4$ GHz and $\nu > 3.6$ GHz due a larger flagged percentage at those frequencies.

Multi-frequency synthesis imaging

We produce a multi-frequency synthesis (MFS) image in Stokes I, to allow for a comparison to S17, which is detailed in Appendix A. Here, we use the same pixel scale, image size, Briggs weighting and masks as in Section 4.2.1, while also enabling multi-scale cleaning. We employ multi-scale cleaning here, as the larger SPWs allow for deeper cleaning and better recovery of diffuse, extended emission. The MFS images also require significantly less computing time with respect to the spectral cube images, for which it would be too time- and resource-consuming to image with multi-scale cleaning. Here, we do not specify scales used, and following imaging tests, allow for WSCLEAN to select scales automatically. For imaging, we divide the bandwidth into eight SPWs ($\Delta\nu$ = 256 MHz) which are combined into a MFS image with weights determined by WSCLEAN. As above, and as in S17, joint decovolution is not possible due to the large data volumes, and we therefore image each pointing individually, and mosaic after. Similar to the spectral cube imaging, we smooth all MFS images to an angular resolution of 1.5" and apply primary beam correction. To account for the variation in the primary beam response across the band, we create primary beam model that is produced using the same spectral weighting as the MFS images. We produce primary beam models corresponding to the central frequency of each spectral window using `tclean` and combine the models using the same per-SPW weights as for the MFS image.

[1] http://montage.ipac.caltech.edu/

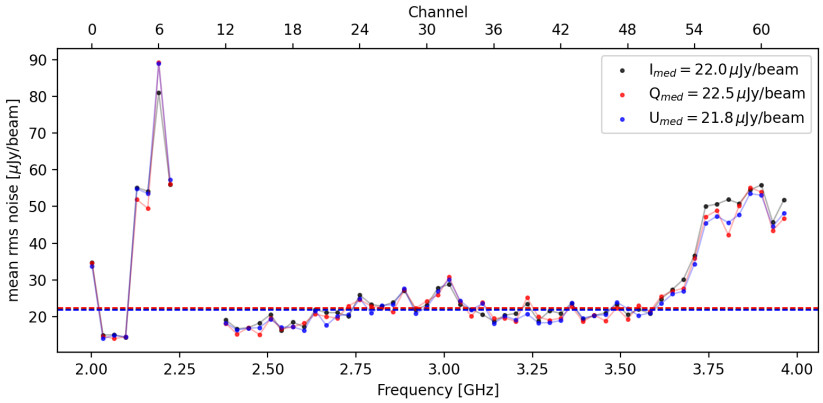

Figure 4.3: Mean rms noise per frequency channel for Stokes I (black), Q (red) and U (blue). The dashed lines indicate the median per-channel rms across the band, as displayed in the legend.

This wideband primary beam correction is applied to all pointings, after which they are cropped at 40% of the primary beam power, corresponding to an angular radius of 7.8'. As above, the 192 pointings are mosaicked using MONTAGE, weighted by the square of the primary beam. A typical rms of an individual pointing is 7 μJy beam^{-1} and 4 μJy beam^{-1} for the mosaicked image. This rms for the smoothed mosaic is consistent with what is reported at this resolution for the convolved VLA-COSMOS 3 GHz mosaic in Delhaize et al. (2017).

4.2.2 Source detection

Due to the positive bias introduced when using traditional source finding algorithms, (e.g. PYBDSF) on polarised intensity images due to the Ricean noise distribution (e.g. Hales et al., 2012), we elect not to use this for source detection in this field, and instead adopt the statistical approach described in RO14.

Candidate selection

Since the radio source population of the COSMOS field has been well defined in Stokes I, down to 10 μJy in S17, we can use this catalogue as a prior when searching for polarised sources. We do not use MFS Stokes Q and U images to create a polarised intensity map, as this might result in the bandwidth depolarisation of sources with large ϕ (e.g. $\phi > 400$ rad m^{-2}). To avoid this, we perform RM synthesis to measure the peak polarised intensity at each pixel. This is described in detail below. We are limited in computing resources due to the large data volume of the full-mosaic Q and U channel maps, so instead create cutouts around all candidate sources from the S17 catalogue, which we select for below.

We select candidate sources such that each source falls within the mosaic area in all frequency channels, to ensure that all source cutouts sample the same λ^2 coverage for RM synthesis. We do this by inspecting the rms map at channel 63 (3.96 GHz), as it has the smallest mosaic area. We limit the extent of the S17 to the area that has the lowest 20% of rms in the 3.96 GHz mosaic. This area has an angular size of 80.43' $\times$ 77.86' and covers 1.74 deg^2. This candidate catalogue contains 9253 of the total 10830 sources in the original catalogue.

In preparation for RM synthesis, we create cutouts in all 64 channels and in Stokes I, Q and U for each source. The cutout fits files are then combined to generate spectral cubelets for each source. By default, each cutout is 100×100 pixels (20"×20"). Special cases are made for sources that are classified as "multi-component" or sources containing more than 100 pixels, as defined by S17. There were 55 sources that met these criteria, for which we manually selected regions from which to extract the cutouts, based on the spatial extent of the sources in the MFS image.

RM synthesis

The complex polarised intensity can be expressed as a function of Faraday depth ϕ,

$$P(\lambda^2) = Q(\lambda^2) + iU(\lambda^2) = \int_{-\infty}^{\infty} F(\phi) \exp(2i\phi\lambda^2) \mathrm{d}\phi. \tag{4.3}$$

Here $F(\phi)$ is the Faraday spectrum, or Faraday dispersion function, which is the complex polarised intensity at a given Faraday depth (Burn, 1966; Brentjens and de Bruyn, 2005). Through RM synthesis, we can obtain the observed Faraday spectrum, which is convolved with a sampling function of the λ^2 domain (RMSF). Through deconvolution, we can compute the true Faraday spectrum (see Chapter 2 for more details). We perform RM synthesis to obtain the polarised intensity and RM for each candidate using the `RM-tools` package (Version 1.1.1, Purcell et al., 2020) from the Canadian Initiative for Radio Astronomy Data Analysis (CIRADA) tools. We use `RMsynth3D` to run RM synthesis on every pixel in a given cutout cubelet, and `RMclean3D` to deconvolve these spectra. The spectra are cleaned to an absolute threshold of 27 μJy beam^{-1} . Considering the sampled λ^2 range, the resulting Faraday depth resolution, largest Faraday scale (where sensitivity has dropped by 50%) and maximum Faraday depth (for which we are up 50% sensitive) are as follows (Brentjens and de Bruyn, 2005):

$$\delta\phi = \frac{2\sqrt{3}}{\Delta\lambda^2} = 206 \text{ rad m}^{-2} \tag{4.4}$$

$$\text{max} - \text{scale} = \frac{\pi}{\lambda^2_{\text{min}}} = 550 \text{ rad m}^{-2} \tag{4.5}$$

$$|\phi_{\text{max}}| = \frac{\sqrt{3}}{\delta\lambda^2} = 15576 \text{ rad m}^{-2} \tag{4.6}$$

An example of the RMSF is shown in Figure 4.4. Each cleaned spectrum is then fitted with a parabola, resulting in a peak polarised intensity P_{peak} map, RM map and a mean absolute deviation (MAD) noise map for each candidate source. This method allows for a better estimate for polarised intensity images, and to mitigate biases introduced through wide-band MFS imaging for polarised source counts (e.g. bandwidth depolarisation). In addition, the P_{peak} maps are corrected for polarisation bias, using the method described in George et al. (2012) as implemented in the `RM-tools` software.

Detection threshold

As indicated above, we only search for polarised emission at the location of sources detected in total intensity, which have been well defined in S17. However, we cannot simply use the rms in the P_{peak} images, as their noise is non-Gaussian. We therefore make use of an adaptation of the empirical method used in RO14, using a control sample. Firstly, for all candidates that are classified as point sources in

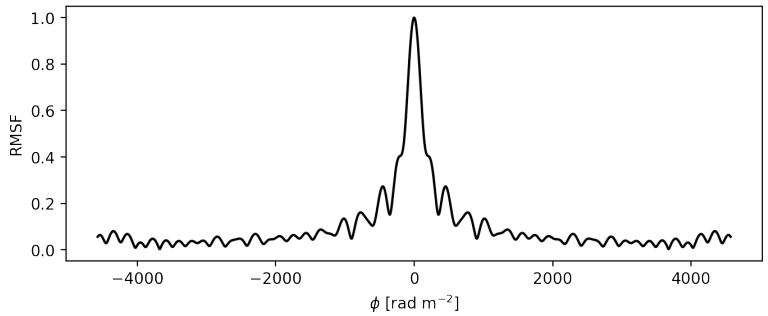

Figure 4.4: The typical RMSF obtained through RM synthesis for the λ^2 range in these data.

the S17 sample ($\sim$ 9000), we record the $P_{\rm peak}$ at the position of the brightest total intensity emission and determine the signal-to-noise ratio (S/N) in the Faraday spectrum at that point, by dividing by the MAD. In addition, we record the $P_{\rm peak}$/MAD at four off-source positions at 6" distance (4 beams) from the source as the control sample. Here, we considered $P_{\rm peak}$ across the full Faraday depth range $-2280 < \phi < 2280$ rad m^{-2}. In Figure 4.5, we plot the cumulative distributions for both the sources and the control sample. We define our detection threshold, at the $P_{\rm peak}$/MAD value for which we can expect 5% of sources to be false detections, i.e. beyond which the 5% of detected sources would be from the control sample. This results in detection threshold of 10.7σ in the Faraday depth domain.

In our source-finding routine we search the full spatial extent of the total intensity maps above 10.7σ. A source is detected if any pixels within this region have a peak in the Faraday depth spectrum above this threshold. Of the 9253 candidate sources, we detect 65 polarised sources above this threshold, with 89 separate components. Sources typically have 1 or 2 componets, with the exception being 3 distinct components (two lobes and a core) for particularly large soures. This yields an RM grid density of 51 deg^{-2}. The median MAD across all candidate sources is 2.6 μJy beam^{-1}, and the faintest detected source has a peak polarised intensity of 23.4 μJy beam^{-1}. Of the 65 sources, 55 are extended sources and 10 are point sources. This source finding routine is followed by a manual inspection of both images and Faraday cubes, after which we do not find spurious detections caused by noise peaks (e.g. extreme Faraday depths $|\phi| > 1000$ rad m^{-2}, typically characteristic of false detections (RO14)). We discuss the completeness of the sample in Section 4.3.1.

Total polarised intensity

The total polarised intensity of an extended source is non-trivial to measure, as it is difficult to define the extent of the polarised region due to the positive noise bias in polarised intensity maps. Modern, large-scale polarisation surveys either only report the peak polarised intensity – a more practical quantity, or do not have the angular resolution to detect large samples of extended polarised sources (e.g. O'Sullivan et al., 2023; Vanderwoude et al., 2024; Taylor et al., 2024). Here, however, we require the total polarised intensity to compute the Euclidean-normalised source counts. RO14 have high angular resolution polarised source detections at 1.6″, and smooth sources to 10″ to measure their total polarised intensity. As many of our sources have angular size much larger than 10″, we do not employ this method. To measure the integrated polarised intensity, we consider the extent of the source (for which we can expect

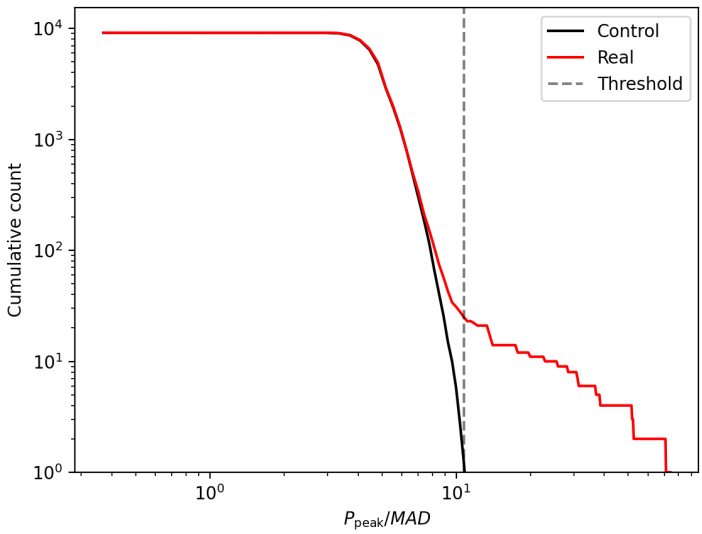

Figure 4.5: The cumulative distribution of the P_{peak}/MAD ratios at the brightest pixel for all total intensity detections (red), and the cumulative distribution of the control (off-source) sample of P_{peak}/MAD (black). The selected source-finding threshold is indicated by the dashed line at 10.7σ.

to detect polarised emission) to be above 12σ in the Stokes I MFS image, as determined through iterative testing and comparison. We then mask all pixels with peaks lower than 7σ in their Faraday depth spectra. To mitigate the inclusion of noise peaks, we apply this mask to the RM map, and further mask all pixels beyond 5σ from the mean RM (i.e. significant outliers), where σ is the determined by a Gaussian fit to the unmasked RMs. Finally, we integrate over the unmasked region. Here, we assume that polarised components of all sources are unresolved in the Faraday depth domain, such that the total polarised intensity for a given pixel has units of Jy beam^{-1}, rather than Jy beam^{-1} RMSF^{-1}. Similarly, this applies for peak polarised intensity. This is a fair assumption, given the low resolution of our Faraday spectra. Image cutouts of Stokes I and polarised intensity maps for all sources are displayed in Appendix B.

4.2.3 Off-axis leakage quantification

To identify spurious polarised detections due to instrumental polarisation, i.e. leakage of Stokes I emission into Stokes Q and U, it is essential to quantify this effect (see Chapter 2). We need to account for two forms of instrumental polarisation, on-axis and off-axis. On-axis leakage is caused by imperfections in the individual antennas responses, and we are able to correct for this during polarisation calibration, which we discuss and quantify to be 0.027% in Section 4.2.1.

Similar to on-axis leakage, off-axis leakage is caused by imperfections in the antenna response, but is much more difficult to correct for, as it is dependent on position with respect to the pointing centre, frequency, and parallactic angle coverage. The sky brightness distribution rotates with respect to the antenna response as a function of parallactic angle χ (see Chapter 2 for details). This effect can be mitigated through A-projection imaging (Bhatnagar et al., 2008; Bhatnagar et al., 2013), however method this is extremely computationally expensive as each position, frequency and time-stamp needs to be individually corrected, and is not yet implemented in WSClean for the VLA. Jagannathan et al.

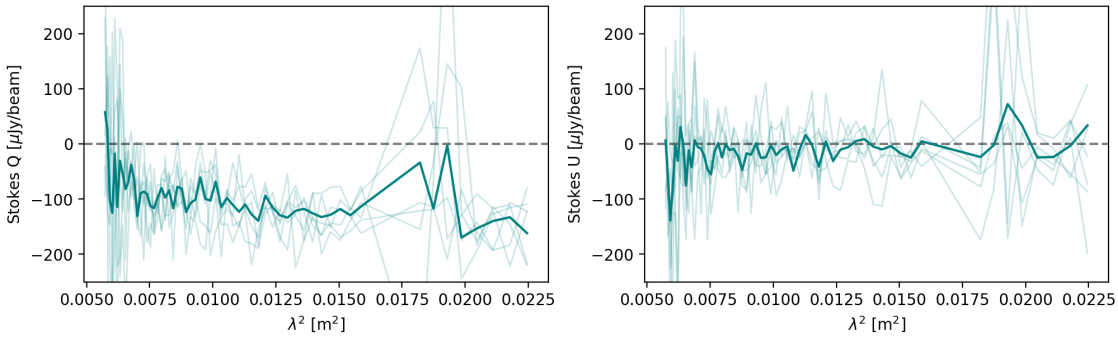

Figure 4.6: Example Stokes Q (left) and U (right) spectra for source ID 66. The spectra from the various individual pointings are shown by the light line weight, and the spectrum extracted from the mosaic is shown by the heavier line. Although for this example there is not a strong spectral variation in Stokes U, it is clear from the Stokes Q spectra that all pointings, as well as the mosaic, show consistent spectral dependence.

(2017) show how leakage can introduce errors in both polarised intensity and RM. However, they find that this effect is reduced through long observations sampling a significant range of parallactic angles, and becomes negligible for $\Delta\chi \sim 180$ deg. In this section, we conduct tests to estimate the degree to which off-axis leakage affects our observations.

Due to the dense pointing configuration of the survey, each source appears in on average 9 pointings. We select four of the brightest polarised point sources identified in the subgrid to measure the variation in fractional polarisation $p_{\rm peak}$ as a function of position in a given pointing. Firstly, we select pointings for which the sources are present at all frequencies. The source IDs and the number of associated pointings are summarised in Table 4.1. We create Stokes I, Q and U cubelets from each pointing and run `rmsynth3D` and `rmclean3d`, as described in Section 4.2.2. We then compare the Faraday spectra, Stokes Q and U spectra, as well as the $p_{\rm peak}$ between pointings. An example for source 66 is plotted in Figure 4.6. We find that across the various pointings, we have consistent measured RM, and this is not affected by the position of the source with respect to the pointing centre. In the Faraday spectra, there is a polarised intensity offset from pointing to pointing and the measured $p_{\rm peak}$ from the mosaic is consistent with the mean $p_{\rm peak}$ across all individual pointings. We plot the $p_{\rm peak}$ as a function of separation from the pointing centre, and as a function of parallactic angle coverage over all observations for a given pointing (Figure 4.7). There are no clear trends for either of these parameters, but we find on average, the offset between various pointings is $\sim 3\%$ in $p_{\rm peak}$, within uncertainty of the mosaic measurement. For source ID 160, we find an instrumentally enhanced fractional polarisation for sources further than 0.1 degrees from the pointing centre and with $\Delta\chi < 80$ deg, though it is unclear which effect dominates. Further investigation into this is beyond the scope of this thesis.

To better quantify the off-axis leakage, and to estimate the expected percentage leakage for spurious detections, we create a leakage mosaicked map. Using `plumber` (Sekhar et al., 2022), we generate models for the off-diagonal elements of the Mueller matrix, representing the leakage between various Stokes parameters (e.g. $I \rightarrow Q$, $I \rightarrow U$). This software uses Zernike polynomials to model the antenna aperture illumination patterns based on holography measurements. Across all observations, we have a parallactic angle coverage of $\chi = [-60; +60]$ deg. We generate rotated beam responses over this

Table 4.1: Summary of sources used in the leakage analysis, and the number of points for each source. The source ID is defined as in S17.

Source ID	Number of pointings
33	3
66	6
80	5
160	6

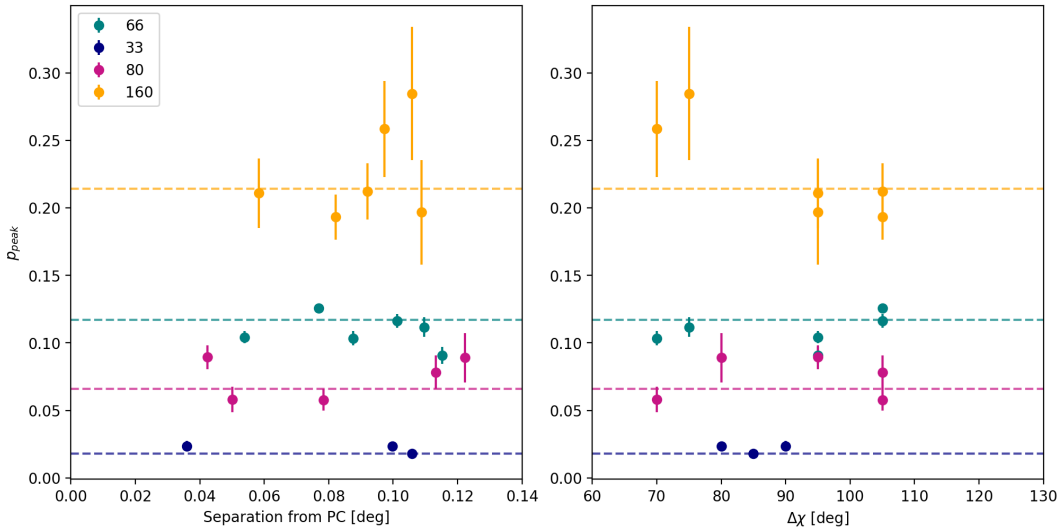

Figure 4.7: Fractional polarisation of test sources (Table 4.1) as a function of separation from pointing centre (left) and range of parallactic angle (right) as observed in various pointings. The dashed lines show the fractional polarisation as measured in the mosaic.

range in increments of $\Delta\chi = 10$ deg for the $I \rightarrow Q$ and $I \rightarrow U$ elements of the Mueller matrix. We then create an averaged beam response for each pointing, weighted by its parallactic angle distribution. The $I \rightarrow Q$ and $I \rightarrow U$ beam responses are then mosiacked to produce leakage maps of the entire survey area for Stokes Q and U. We add the absolute on-axis leakage to the Stokes Q and U maps respectively, and combine them in quadrature to produce a linear polarisation leakage map $P_{\rm leak}$ (e.g. Hales et al., 2014). A cumulative distribution of the percentage leakage in linear polarisation, normalised by survey area, is plotted in Figure 4.8. The maximum off-axis leakage is 0.5%, while half of the mosaic has leakage of $< 0.1\%$. The long 'tail', where $\sim 15\%$ of the area has leakage ranging from $0.2 - 0.4\%$ corresponds to the pointings around the edge of the mosaic, which do not have as many overlapping pointings as those in the centre of the mosaic, and therefore a higher leakage percentage. We have not considered the frequency dependence of leakage for this map, as it indicates a low leakage percentage in general, and we can exclude possible spurious sources with the upper limit of $p = 0.5\%$.

As a final verification for the off-axis leakage limit, we attempt to detect spurious polarised emission from the brightest sources detected in total intensity within the area of the subgrid. Source ID 3

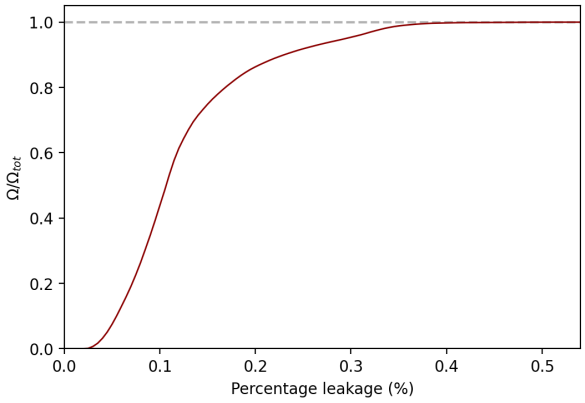

Figure 4.8: Cumulative distribution of the percentage leakage as determined from the leakage map. The distribution is normalised by the total survey area.

has a peak total intensity of 11 mJy beam^{-1}. For the corresponding position in the $P_{\rm peak}$ map produced from RM synthesis, we measure a fractional polarisation of 0.25%, consistent with our model. This measurement has S/N = 4, and was not detected above our source finding threshold. From inspection, there are no apparent peaks at $\phi = 0$ rad m^{-2} in the Faraday spectrum. It is therefore unlikely that we will detect any spurious sources caused by instrumental polarisation.

4.2.4 Spectro-polarimetric analysis

As introduced in Chapter 2, there are numerous advantages to broadband measurements of polarised sources. This includes more accurate RM measurements when breaking the $n\pi$ ambiguity, and detailed spectral modelling to characterise Faraday complexity and depolarisation within the beam volume (e.g. along the line-of-sight within the resolution limit of the observations). For each detected source, we extract Stokes I, Q and U spectra at the pixel with peak polarised intensity to perform spectro-polarimetric fitting. An example of the extracted spectra, their relevant fitted models and the corresponding Faraday spectra are show in Figure 4.9.

Spectral fitting

We calculated the in-band spectral index α, by fitting a power law to the total intensity spectrum as $S(\nu) \propto \nu^{\alpha}$. In general, the total intensity spectra are well fit by a single power law, with no spectral turnovers or complex structures present in the sample. Similarly, we fit the fractional polarisation as a function of λ to measure the depolarisation index β, introduced by Farnes et al. (2014) as $p(\lambda) \propto \lambda^{\beta}$. Sources with $\beta < 0$ are depolarised, likely due to internal or external Faraday dispersion, media with disordered magnetic fields, or magneto-ionic turbulence within the beam volume (e.g. Ranchod et al., 2024). Ahead of fitting, we flag the band edges and all channels with extreme uncertainties, e.g. greater than 100%. The resulting α and β distributions are discussed in Section 4.4.3.

Stokes QU fitting

We use QU-fitting (e.g. Farnsworth et al., 2011) to characterise the magneto-ionic environment of the sources, as well as any potential intervening magnetised media. By fitting physical models, we can retrieve the RM (or peak Faraday depth ϕ), polarisation angle χ, intrinsic fractional polarisation p_0 and other parameters in the Faraday complex case. We fit four different models to each source using `RMTools`, where the complex polarisation fraction is comprised of the real q and imaginary u components as

$$\mathbf{p}(\lambda^2) = q(\lambda^2) + iu(\lambda^2). \tag{4.7}$$

The physical interpretation of all models is detailed in Chapter 2, and we summarise them briefly here:

(i) A simple Faraday thin source,

$$\mathbf{p}(\lambda^2) = p_0 e^{2i\chi_0 + \phi\lambda^2}. \tag{4.8}$$

(ii) A single Faraday component with external Faraday dispersion (Burn, 1966),

$$\mathbf{p}(\lambda^2) = p_0 e^{-2\sigma_{\rm RM}^2\lambda^4} e^{2i(\chi_0+\phi\lambda^2)}, \tag{4.9}$$

where $\sigma_{\rm RM}$ is dispersion in Faraday depth due to a turbulent screen.
(iii) Burn slab with foreground screen (Sokoloff et al., 1998),

$$\mathbf{p}(\lambda^2) = p_0 \frac{\sin(\phi_{\rm diff}\lambda^2)}{\phi_{\rm diff}\lambda^2} e^{2i[\chi_0+(\frac{1}{2}\phi_{\rm diff}+\phi)\lambda^2]}, \tag{4.10}$$

a simultaneously synchrotron-emitting and Faraday-rotating "thick" volume, resulting in differential Faraday rotation along with line-of-sight, within the beam volume. This model contains an additional foreground screen resulting in extra Faraday rotation ϕ.
(iv) Internal Faraday dispersion (Burn, 1966),

$$\mathbf{p}(\lambda^2) = p_0 e^{2i\chi_0+\phi\lambda^2} \left(\frac{1 - e^{i\phi_{\rm diff}\lambda^2 - 2\sigma_{\rm RM}^2\lambda^4}}{2\sigma^2\lambda^4 - i\phi_{\rm diff}\lambda^2} \right), \tag{4.11}$$

which is similar to the Burn slab model with an additional turbulent component, as well as the Faraday-rotating foreground screen. By inspection of the Faraday spectra of the detected sources, we find that no sources exhibit multiple peaks in Faraday depth. We therefore do not fit models with multiple emitting components. Furthermore, at high angular resolution, we do not expect multiple polarised components or diffuse foreground polarised emission within the beam volume. In addition, the multi-component models have significantly more degrees of freedom, which will likely result in over-fitting the spectra with low S/N. `RMtools` uses nested sampling for model fitting, with the python packages `bilby` (Ashton et al., 2019) and `dynesty` (Speagle, 2020). We select the best fitting model by comparing the log Bayesian evidence $\log(Z)$. An example of a fitted spectra is shown in Figure 4.9, and the fits for the full sample are in Appendix B.

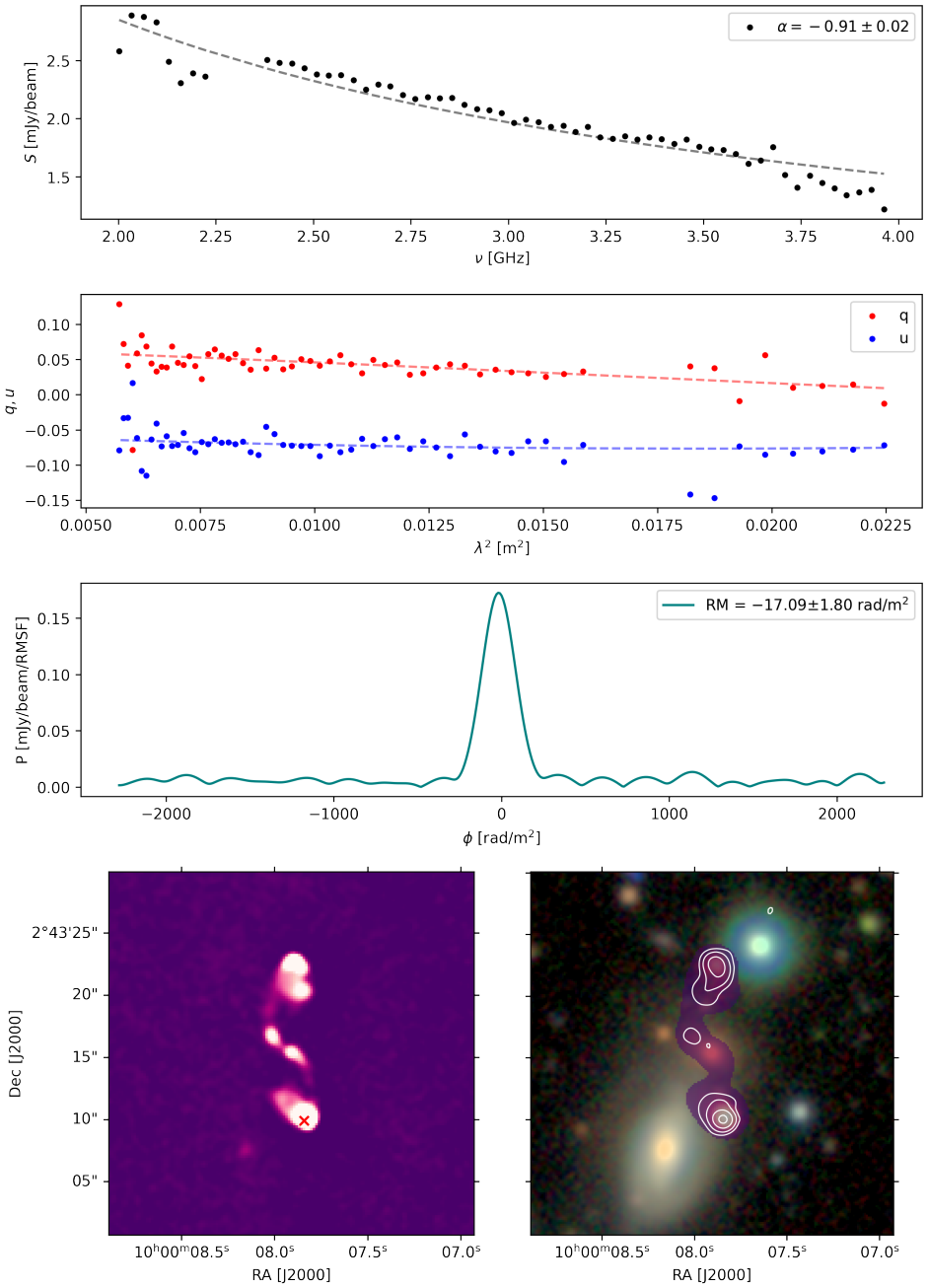

Figure 4.9: Example of extracted spectra and images for source ID 10909, which we classify as an FRII galaxy. *Top:* Total intensity spectrum, with the spectral index α indicated on the plot. *Second:* Fractional Stokes Q and U spectra, where $q = Q/I$ and $u = U/I$. The dashed lines show the best QU model fit, which in this case is the Burn slab depolarisation model (Equation 4.10). *Third:* The cleaned Faraday spectrum, with the resultant RM indicated on the plot. *Bottom left:* Total intensity image from S17 ($\theta = 0.75''$). The red cross shows the position at which the spectra are extracted, corresponding to the position of brightest polarised intensity. *Bottom right:* The total intensity MFS image from this work ($\theta = 1.5''$, purple) and the polarised intensity contours plotted on an RGB optical image. The RGB image is composed of the UltraVISTA (McCracken et al., 2012) *Ks*, *J* and *H* bands. The polarised intensity contour levels correspond to [22, 45, 90, 150] μJy beam^{-1}. The host is an elliptical galaxy, centred on the image, while the other bright sources are likely not associated.

Fractional polarisation

Using `RMsynth3D`, we produce fractional polarisation maps for each source. To avoid propagating artefacts from the total intensity cubes into the fractional polarisation, we fit a polynomial to each pixel in the Stokes I cubes, returning Stokes I model cubes. We then create fractional q and u cubes by dividing through by the model I cube, and process the fractional cubes through `RMsynth3D`, with the same parameters described in Section 4.2.2. The fractional polarisation at the position corresponding to the peak polarised intensity is catalogued.

4.2.5 Ancillary catalogues

As introduced in Section 4.1, the COSMOS field is covered by a wide range of multi-wavelength surveys. These have been exploited to characterise the radio source population presented in the S17 catalogue, in particular the AGN sub-populations and identifying star-forming galaxies (SFGs). Smolčić et al. (2017b) find counterparts for $\sim 93\%$ of the radio catalogue in optical, near-infrared, mid-infrared and/or X-ray. Through these data, they classify sources as SFGs, moderate-to-high radiative luminosity AGN (HLAGN) and low-to-moderate radiative luminosity AGN (MLAGN) (Delvecchio et al., 2017). To summarise, HLAGN were identified based on X-ray, MIR colour-colour and SED-fitting criteria, as well as their radio excess with respect to the star-formation rate of the host galaxies ($\log[L_{1.4\,\mathrm{GHz}}/\mathrm{SFR}_{\mathrm{IR}}]$). Star-forming galaxies were identified based on their dust-extinction-corrected rest-frame colour and the absence of radio excess. "Radio excess MLAGN" were identified as remaining sources with radio excess after the removal of HLAGN, and "quiescent MLAGN" were selected based on radio excess and their rest-frame colour. We discuss this classification in more detail in Section 4.4.2. The Smolčić et al. (2017b) catalogue also contains e.g. source spectroscopic redshifts, rest frame luminosity and star-formation rate, where available.

For this work, we present the polarised source catalogue, which includes the peak and total polarised intensities for all detected sources, as well as an upper limit of the peak polarised intensity for non-detected candidates. For the detected sources, we present the results of the spectral index fitting, QU fitting and RM synthesis, as well as notes on the morphological classification of each source. The final catalogue is cross-matched with the total intensity catalogue from S17, as well as the ancillary catalogue described above (Smolčić et al., 2017b). An example of the catalogue and further descriptions are presented in Appendix C.

4.3 Polarised source counts

In this section, we present both the cumulative source counts and the Euclidean-normalised differential source counts. Both source counts are corrected for the completeness of the sample, which we determine below.

4.3.1 Completeness

To measure the completeness of the survey, and understand the efficacy of our source finding method, we produced mock image cubes with 300 modelled polarised point sources. The polarised flux density for each source was sampled from a uniform distribution ranging from $2 < P < 200$ μJy across 9

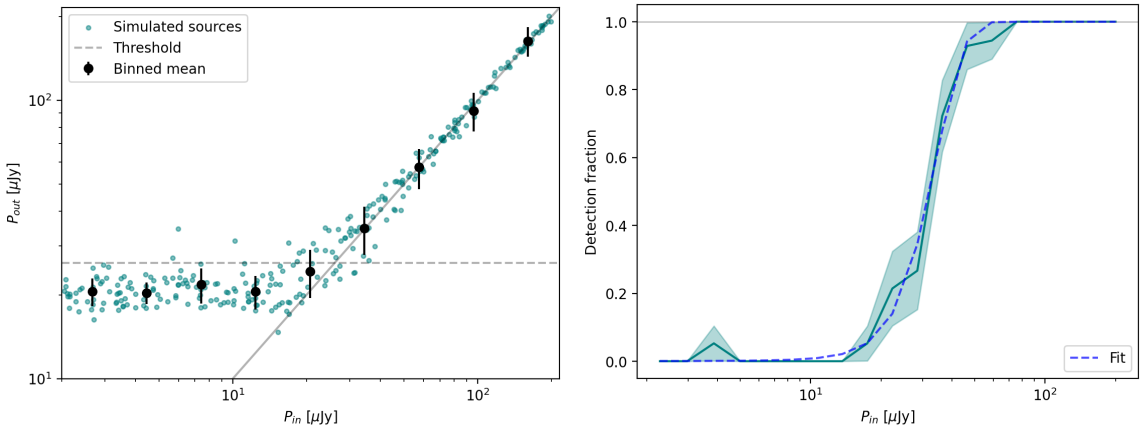

Figure 4.10: *Left:* The injected $P_{\rm in}$ vs recovered $P_{\rm out}$ polarised intensity for the sources in the simulated cubes (cyan, Section 4.3.1). The binned data, in log space is shown in black. The grey solid line is the 1-to-1 line, and the dashed grey line is an indicative threshold of 27 μJy beam^{-1}. *Right:* The detection fraction of sources per $P_{\rm in}$ bin (teal), with their associated binomial uncertainties. The fitted normalised cumulative distribution is indicated by the blue dashed line. The horizontal grey line shows 100% completeness.

logarithmically spaced bins. The lower limit is selected as the MAD noise in Faraday depth, and the upper limit corresponds to the brightest detected source. We assumed the RM of all sources to be $\phi = 0$ rad m^{-2}, which is the mean expected Faraday depth for a high Galactic latitude extragalactic sample, and a polarisation angle of $\chi = 45$ deg. The sources are injected into the QU channel maps at random positions, with the exception that sources should have at minimum a three beam (4.5") separation from any known total intensity sources in the field.

For a given injected source, the Stokes $Q(\lambda^2)$ and $U(\lambda^2)$ spectra are first generated. We assume Faraday simple sources, i.e. single component and without depolarisation, and no spectral index effect, i.e., $\alpha = 0$.:

$$Q(\lambda^2) = P\cos[2(\chi + \mathrm{RM}\lambda^2)] \tag{4.12}$$

$$U(\lambda^2) = P\sin[2(\chi + \mathrm{RM}\lambda^2)]. \tag{4.13}$$

The spectra are then convolved with the restoring beam in the image plane, and inserted into the Q and U mosaicked channel maps. We then extract Q and U spectral image cutout cubes for each source. These cubes are processed with `rmsynth3D`, as described in Section 4.2.2. We then recover the polarised intensity and MAD noise at the position of all mock sources. The injected polarised intensity is plotted against the recovered polarised intensity in Figure 4.10. We find good agreement between these measurements down to 27 μJy beam^{-1}. This is consistent with a 10.7σ detection threshold for an average MAD of 2.6 μJy beam^{-1}, as found in Section 4.2.2. In Figure 4.10, we also show the fraction of recovered sources as a function of polarised intensity, which can be fit with a normalised cumulative distribution. We are 100% complete at 75 μJy beam^{-1} and do not recover sources below 14 μJy beam^{-1}. The errorbars shown here are binomial uncertainties.

4.3.2 Cumulative polarised source counts

In Figure 4.11, we present the cumulative counts for peak polarised intensity. The cumulative counts have been corrected for completeness using the completeness curve in Figure 4.10, and the uncertainties are estimated through bootstrap resampling. The peak cumulative counts are particularly useful for characterising the polarised flux density distribution for deep surveys and for predicting the number of polarised sources in future observations. To investigate the frequency dependence of the cumulative counts, we compare to RO14, who present cumulative counts at 1.4 GHz with comparable angular resolution ($\theta = 1.4''$), also with the VLA but over a smaller area of 0.3 deg^2 in the GOODS-N field. While they detect only 11 polarised sources in this small region with good certainty, their work has produced the most well-constrained analytical expressions for cumulative source counts due to their care regarding the correction of systematic effects, and is most widely used in the literature. Here, we aim to update this expression to be suitable for 3 GHz, and with a larger sample size. RO14 find a flattening in the cumulative distribution below 1 mJy beam^{-1}, which they attribute to the change in source population at fainter polarised intensities. This flattening has subsequently been reported for shallower surveys using the Australia Telescope Compact Array (ATCA; Eyles et al., 2020) and the Westerbork Synthesis Radio Telescope (WSRT; Berger et al., 2025). We find that we are consistent with RO14 at low flux density $P < 0.14$ mJy beam^{-1} within the bootstrap uncertainties, but appear to have a steeper slope at higher flux densities. We note that the bootstrap uncertainties used here are consistent with Poisson uncertainties on the source counts.

To understand if the change in slope is statistically significant, we perform Bayesian model selection, assuming a Poisson likelihood function. We use nested sampling to evaluate the evidence $\log(Z)$ with the PYTHON package `bilby` and the `dynesty` sampler. For all parameters, we define uniform priors. We assess the Bayesian evidence ratio between a power law (model A),

$$N(>p) = N_0 \left(\frac{P}{P_0}\right)^{\alpha_1}, \tag{4.14}$$

and a broken power law

$$N(>p) = \begin{cases} N_0 \left(\dfrac{P}{P_0}\right)^{\alpha_2} & \text{if } P \leq P_{\rm break} \\ N_0 \left(\dfrac{P_{\rm break}}{P_0}\right)^{\alpha_2-\alpha_1} \left(\dfrac{P}{P_0}\right)^{\alpha_1} & \text{if } P > P_{\rm break}, \end{cases} \tag{4.15}$$

considering options where $P_{\rm break}$ is either fixed at 0.2 mJy beam^{-1} (model B), or is a free parameter (model C). As our motivation here is to determine the statistical significance of our perceived slope break, model B is defined by the visual identification of the break in Figure 4.11. Above, N_0 is a normalisation constant, and α_1 and α_2 are the slopes of the distribution below and above the break, respectively. $P_{\rm break}$ is the polarised intensity at which the break occurs, and P_0 is the polarised intensity of the faintest source in the sample. Model A has two free parameters, model B has three and model C has four. For the broken power law with free $P_{\rm break}$, we find a Bayes factor of 0.162 with respect to the power law. With fixed $P_{\rm break} = 0.20$ mJy beam^{-1}, we find a Bayes factor of 0.517 with respect to the power law. While this does not *strongly* favour the power law model, we select the power law, as it is the simplest model. Furthermore, the best fit for $P_{\rm break}$ is $\log(P_{\rm break}/\,\text{Jy beam}^{-1}) = -3.18^{+0.81}_{-1.06}$, above which we only have

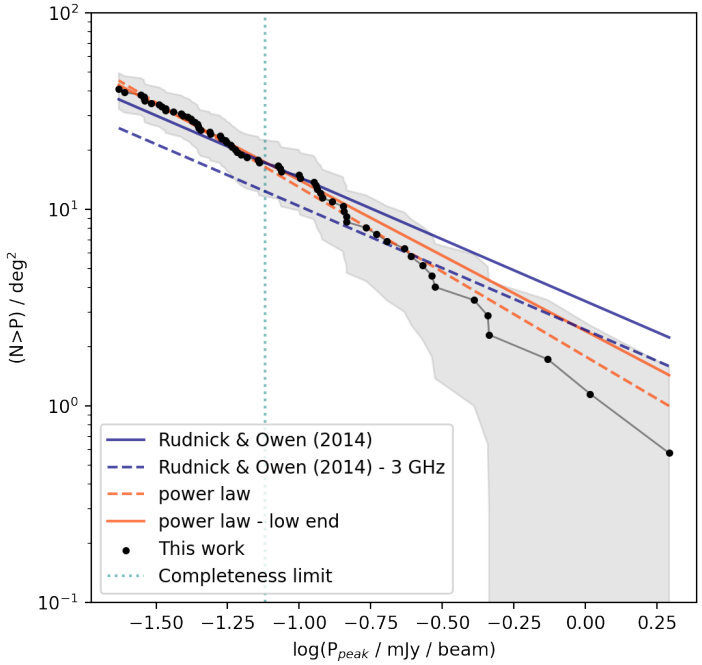

Figure 4.11: Cumulative source counts based on the peak polarised intensity of detected sources (black). These counts have been corrected for completeness. The uncertainties are indicated in grey and are estimated through bootstrap resampling. The blue solid line shows the counts from RO14 at 1.4 GHz, and extrapolated to 3 GHz (blue dashed line). The orange line is a power law fit (Equation 4.14) to the full sample (solid line) and to only the low frequencies (dashed line). The limit above which we are 100% complete is indicated by the dotted cyan line.

one data point. A break here would be consistent with the change of slope found in the literature. As an additional test for the perceived changed in slope, we perform a bootstrapping experiment where we select 65 sources (with replacement) from our sample and construct 10^4 realisations of the cumulative source counts (shaded grey region). From this we can conclude that the perceived change of slope is not statistically significant, and is likely an effect of small number statistics, particularly for higher polarised flux densities, where only 25% sources are above 0.14 mJy beam^{-1}. This is not unexpected, as in total intensity it is well established that few bright sources are detected in the COSMOS field, an effect of the small sky area due to cosmic variance (e.g. Heywood et al., 2013). We therefore limit the power law fit to the lower flux densities with $P < 0.14$ mJy beam^{-1}. The resulting power law fit is

$$N(>P) = 42.89 \pm 0.37 \left(\frac{P}{23\,\mu\text{Jy beam}^{-1}} \right)^{-0.77\pm0.01} . \tag{4.16}$$

From Figure 4.11, we find that we have consistent cumulative source counts with RO14. This consistency is interesting, as we expect sources to be fainter at higher frequencies due to the spectral index effect (typically $\alpha = -0.7$ for radio galaxies). In Figure 4.11 we plot the RO14 extrapolated to 3 GHz, assuming $\alpha = -0.7$. The frequency dependence materialises as a shift in the x-axis to lower flux densities. The inconsistency of our data with this relation at 3 GHz suggests the spectral index does not fully describe the frequency dependence of the cumulative counts. Through an analysis of the polarised sources in

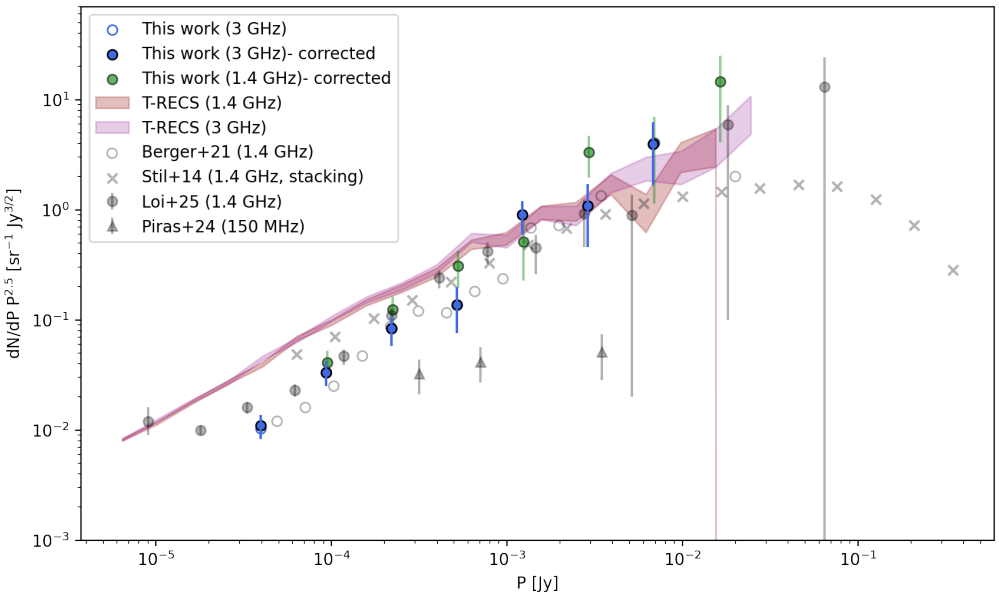

Figure 4.12: Euclidean normalised differential source counts for the polarised source population in the VLA-COSMOS 3 GHz survey. The counts without completeness correction are indicated by the open blue circles. The completeness corrected counts are plotted as filled circles at 3 GHz (blue) and extrapolated to 1.4 GHz (green). In grey, we plot the source counts from recent deep surveys: Lockman Hole field (Berger et al., 2021, open circles), MeerKAT Fornax Survey (Loi et al., 2025, filled circles), ELAIS-N1 (Piras et al., 2024, triangles), and stacking of NVSS sources (Stil et al., 2014, crosses). The polarised source counts computed from the T-RECS simulation (Bonaldi et al., 2019) for 1.4 GHz (brown) and 3 GHz (purple) are also plotted.

the S-PASS survey (2.3 GHz) in comparison to the NVSS polarisation catalogue (1.4 GHz), Lamee et al. (2016) suggest that number counts may be consistent between 2.3 GHz and 1.4 GHz for bright sources ($P_{2.3\ \mathrm{GHz}} > 230$ mJy) at low angular resolution (~ 9 arcsec). They attribute this to the increase of polarised intensity at 2.3 GHz in their sample, an effect of λ^2-dependent depolarisation. We present our depolarisation results in Section 4.4.3 and further discuss the frequency-dependence of the polarised source counts in Section 4.5.1.

4.3.3 Euclidean normalised counts

As introduced in Chapter 1, Euclidean-normalised differential source counts are a standard depiction of source counts in the literature (Condon, 1984), assuming a static, Euclidean Universe. This representation has historically been used for total intensity (e.g. Smolčić et al., 2017a; Matthews et al., 2021b) and polarised intensity (e.g. Hales et al., 2014; Berger et al., 2021) counts. Typically, any deviation from a monotonic decrease towards lower flux densities is indicative of a change in source population, e.g. the emergence of the star-forming galaxy population as observed in total intensity (Matthews et al., 2021b). However this regime has not yet been observed in polarised intensity, with the exception of Loi et al. (2025) who find an increase at $P < 10$ μJy, for which they suggest that they are sensitive to the radio-quiet quasar population. This Euclidean normalisation also allows for a more direct comparison with other surveys in the literature. In Figure 4.12, we present the Euclidean-normalised differential polarised source counts for the VLA-COSMOS 3 GHz survey. These source counts are computed

Table 4.2: Euclidean-normalised differential polarised source counts

$P_{3\,\mathrm{GHz}}$ [mJy]	$\Delta P_{3\,\mathrm{GHz}}$ [mJy]	N	N_{corr}	$\mathrm{d}N/\mathrm{d}P\,P^{2.5}$ [$\mathrm{Jy}^{1.5}\mathrm{sr}^{-1}$]
0.039	0.023–0.055	18	19	0.041±0.021
0.093	0.055–0.131	16	16	0.124 ± 0.075
0.219	0.131–0.308	11	11	0.31 ± 0.22
0.517	0.308–0.728	5	5	0.51 ± 0.55
1.222	0.728–1.717	9	9	3.3 ± 2.7
2.885	1.717–4.054	3	3	4.0 ± 5.5
6.812	4.054–9.570	3	3	14 ± 20

using P_{tot}, in contrast to P_{peak} used above. This is an important distinction as the majority of detected sources are resolved. We also display the source counts extrapolated to 1.4 GHz to compare with the literature, assuming $\alpha = -0.7$. We calculate Poisson uncertainties for the number of sources detected in each bin. Similar to Section 4.3.2, we correct the source counts for completeness, as calculated in Section 4.3.1, and plot the corrected and uncorrected counts. Due to the binning, we only have one bin below our completeness limit of 75 μJy beam^{-1} . We note that although the completeness simulations consider an injected P_{peak} rather than P_{total}, this correction is still applicable for the Euclidean counts, as the simulated sources were all unresolved. In Figure 4.12, we also plot the source counts from other sub-mJy polarised source count studies: The Lockman Hole field at 1.4 GHz with the WSRT (Berger et al., 2021), ELAIS-N1 at 150 MHz observed with the LOw Frequency ARray (LOFAR; Piras et al., 2024), the MeerKAT Fornax Survey at 1.4 GHz with MeerKAT (Loi et al., 2025), and the result of source stacking in NVSS at 1.4 GHz (Stil et al., 2014). The source counts presented in this work are the deepest polarised source counts at $\nu > 2$ GHz, and the second deepest overall (cf. Loi et al., 2025, at 1.4 GHz as the deepest polarised counts). For the first time, we are probing the sub-mJy regime at higher frequencies over a significant area. In Table 4.2 we indicate the polarised intensity bins, the number of sources per bin (with and without completeness correction), as well at the Euclidean normalised counts (with completeness correction).

From Figure 4.12, our source counts show the expected monotonic decrease towards low flux densities. At 3 GHz, we are consistent with Loi et al. (2025), within uncertainties, with the exception of the bin at 0.517 mJy. In this bin, we have relatively fewer sources (an offset of -0.3 dex in the source counts). This bin indicates the transition range between resolved and unresolved sources in our sample (see Figure 4.13), and this dearth may be related to the limited surface brightness sensitivity of our observations, i.e. missing faint, diffuse emission in the flux integration across a given source. It may also be an effect of the binning with low number statistics. Further investigations are beyond the scope of this work, as we are still consistent within uncertainties with the counts from Stil et al. (2014) within this bin. In general, our source counts are compatible with Stil et al. (2014) at higher polarised intensities until 0.131 mJy, below which our counts are lower by a discrepancy of 0.5 dex. We also show general agreement with the source counts from Berger et al. (2021), however, a subsequent paper from these authors (Berger et al., 2025) acknowledge that certain corrections were not taken into account here, so we do not compare further. Finally, for completeness, we include the counts from Piras et al. (2024), as

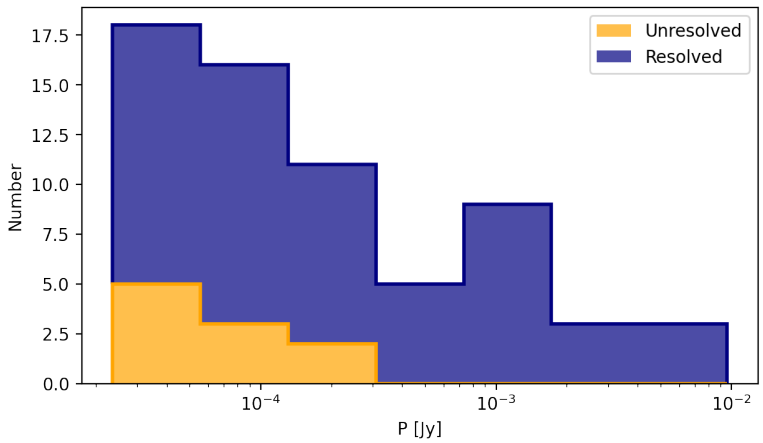

Figure 4.13: Histogram of the integrated polarised intensity P for detected sources. The resolved sources are indicated in blue and the unresolved sources in orange.

these are the only sub-mJy counts at MHz frequencies. However, a spectral extrapolation to 100 MHz is non-trivial, due to the more pronounced λ-dependent depolarisation effects at $\nu < 1$ GHz.

With the extrapolated source counts at 1.4 GHz, we also find consistency with the literature. These counts have both higher flux densities and Euclidean-normalised values than at 3 GHz, as expected from Figure 4.11. Given the modest number of detections in our sample, and the large-per bin uncertainties, this increase is not statistically significant, and we find that cumulative counts are a more appropriate measure for a frequency-dependent comparison.

Finally, we compare the polarised source counts to those from the Tiered Radio Extragalactic Continuum Simulations (T-RECS; Bonaldi et al., 2019). This is a set of simulated catalogues of the radio continuum sky (150 MHz $< \nu <$ 20 GHz), including both the AGN and SFG population, designed for predicting results of deep radio surveys with the SKA. This catalogue is unique in its inclusion of polarisation information for all sources, which were not included in previous iterations due to the lack of available data. In this work we made use of the T-RECS medium catalogue, which covers a 25 deg^2 area down to a depth of $S_{1.4\ \mathrm{GHz}} < 10$ nJy. In Figure 4.12, we plot the 1σ uncertainty range of the Euclidean-normalised source counts from T-RECS at 1.4 GHz and 3 GHz from 5 μJy $< P <$ 0.1 Jy. Here, we only include AGN population from the T-RECS catalogue. The source counts and their uncertainties are calculated as above. We find that there is no significant difference between the source counts at 1.4 GHz and 3 GHz, and that these simulated counts show good agreement with our measurements and those from the literature for $P > 500$ μJy. At fainter polarised intensities, we find that the simulated source counts are significantly overestimated. We note that Bonaldi et al. (2019) assumed the fractional polarisation distribution from Hales et al. (2014), which was derived from source counts with $P_{1.4\ \mathrm{GHz}} > 200$ μJy, and at the time, source counts below this limit were not readily available. Moreover, the fractional polarisation for flat spectrum sources was determined from a sample selected at 20 GHz with $P_{20\ \mathrm{GHz}} > 200$ μJy (Galluzzi et al., 2018), which may introduce a bias in the extrapolation down to 3 GHz. In general, this highlights the necessity for deep polarised source counts, as presented in this work, over a large range of frequencies to inform and update simulations of the faint source population ahead of the SKA era.

4.4 Properties of the faint polarised source population

In this section, we present the characterisation of the faint source population, with a focus on results regarding the RM, fractional polarisation, frequency-dependent depolarisation, and a classification of the sources based on their spatial morphology, multi-wavelength properties and source component with the brightest polarised intensity (e.g. lobe, core), from which the spectra are extracted.

4.4.1 Rotation measure

In Section 4.2.2, we compute the RM or peak Faraday depth ϕ for each source[2]. The RM is describes the magnetic field strength $\mathbf{B}_{||}$ and electron density n_e along the line of sight L:

$$\phi(L) = 0.812 \int_{l=0}^{l=L} n_e \mathbf{B}_{||} dl, \tag{4.17}$$

and can inform us about the properties of the immediate source environment or any foreground Faraday screens (e.g. magneto-ionic medium of the Milky Way). In Figure 4.14, we plot a histogram of the RMs at the peak pixel of our detected sources, as determined through RM synthesis. We note that although we produce RM maps through `rmsynth3D` for the spatially resolved sources, we do not discuss them here, and we find, in general, that the sources have very little RM variation across the source. This is an effect of the low Faraday depth resolution (Equation 4.4) in these observations, with which we are not sensitive to variations smaller than $\sim$40 rad m^{-2}. We report a median Faraday depth of $+1.60 \pm 3.51$ rad m^{-2}. The RM values follow a Gaussian distribution, as expected for an extragalactic field (e.g. Rudnick and Owen, 2014; Taylor et al., 2024), with the majority of the RM contribution attributed to the Milky Way foreground. The median RM reported here is consistent with $+1.03 \pm 6.60$ in Taylor et al. (2024) for a subregion of the same field observed with the MeerKAT MIGHTEE-POL survey, an L-band survey centred at 1.1 GHz. This survey has a similar, albeit slightly higher sensitivity (detection threshold of 16 μJy beam^{-1}) to VLA-COSMOS, but with a lower angular resolution of 7". Although the Milky Way is a significant contributor to the RMs of extragalactic sources, we can assume that any significant outliers with respect to the Galactic RM grid may be intrinsic to the source or its local environment (e.g. Pandhi et al., 2025). Therefore, we require an accurate Galactic RM model to identify such cases. Figure 4.15 shows the spatial variation of the RMs across the survey area. In this visual representation, there are clear regions of either negative or positive RM. We compare this RM grid to the Galactic foreground RM map from Hutschenreuter et al. (2022). These authors produced an interpolated all-sky map from the available catalogues at the time, with an RM density of $\sim$ 1 deg^{-2}. We note that no sources from this catalogue coincide with the COSMOS field. This low RM density and the associated large statistical and astrophysical uncertainties are a limitation of this map, and can be improved by deep observations with higher RM density. The Hutschenreuter et al. (2022) mean and standard deviation maps σ are plotted in Figure 4.15. While the mean map shows a similar structure as in the COSMOS RM grid, it is on average more negative, with a mean of -61.78 ± 4.46 rad m^{-2}. Due to the sparse coverage of this field in the compiled catalogue used by Hutschenreuter et al. (2022), the σ values over this region are also high, with an average of 39.22 ± 4.93 rad m^{-2}. Taylor et al. (2024) show that for the COSMOS field, the Galactic RM structure as reported in their catalogue converges to that of the Hutschenreuter et al. (2022) map at scales of $\sim$ 15 arcmin. This implies smaller scale RM structure present in the Galactic foreground, only

[2] We note that in this chapter, RM and ϕ are used interchangeably.

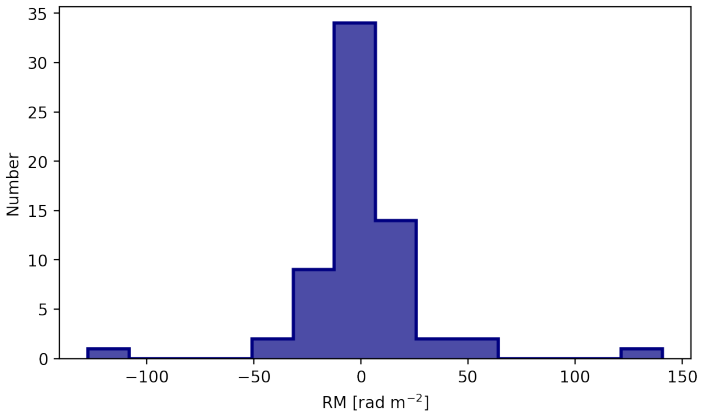

Figure 4.14: Histogram showing the RM distribution of the detected polarised sources.

detectable at sub-mJy sensitivity, which is further substantiated by our results. To understand the spatial variations of this deviation, from the Hutschenreuter et al. (2022) map, we compute Δ, where

$$\Delta = \frac{\phi - \phi_{\rm H22}}{\sigma_{\rm H22}}. \tag{4.18}$$

We find 68% of sources have $\Delta < 2$, i.e. have RMs within 2σ of the Hutschenreuter et al. (2022) map, and 29% of sources have $2 < \Delta < 3$. The latter are situated in the north-west of the field, corresponding to the grouping of positive RM sources in this region. A clear outlier, with $\Delta = 6$ is source ID 101, with $\phi = 145.7 \pm 7.3$ rad m^{-2}. This is a point source, which also has extreme Faraday dispersion (Section 4.4.3). Upon consulting the Chandra/XMM-Newton catalogue of X-ray identified galaxy groups (Gozaliasl et al., 2019), we find that the line-of-sight of this source ($z = 0.79$) passes through a large foreground galaxy group at $z = 0.12$. This galaxy group has a radius of $R_{200} = 0.099$ deg and an X-ray luminosity of $\log(L_X) = 42.81$ erg s^{-1}. The enhanced RM for this source is likely not Galactic in origin, and rather a result of the intervening magnetised intra-group medium.

The COSMOS field is centred at Galactic coordinates $l = 236^\circ46'02''$, $b = 42^\circ08'17''$. We find an RM standard deviation of 28.34 rad m^{-2} over the full sample, and 16.05 rad m^{-2}, excluding the outliers (i.e. the two extremes with $|\mathrm{RM}| > 100$ rad m^{-2}). While a detailed RM structure function analysis will be done in a future paper, we find that this is consistent with the RM standard deviation of sources detected at $b \sim 42^\circ$ in the NVSS RM catalogue (Schnitzeler, 2010), which has been corrected for large-scale fluctuations $> 10^\circ$. This is a further indication that the dominant contribution to the RM fluctuations at $b \sim 42^\circ$ is Galactic in origin at scales $< 10^\circ$.

4.4.2 Source classification

The high angular resolution of this survey enables a morphological classification of the detected polarised sources. While this has already been done in previous works for resolved sources in the VLA-COSMOS continuum catalogue ($\theta = 0.75''$) (Vardoulaki et al., 2021), we redo the classification here, including both the polarised intensity maps, and the lower resolution MIGHTEE Early Science continuum maps ($\theta = 8''$ Heywood et al., 2022), for better sensitivity to diffuse emission. By visual inspection, we

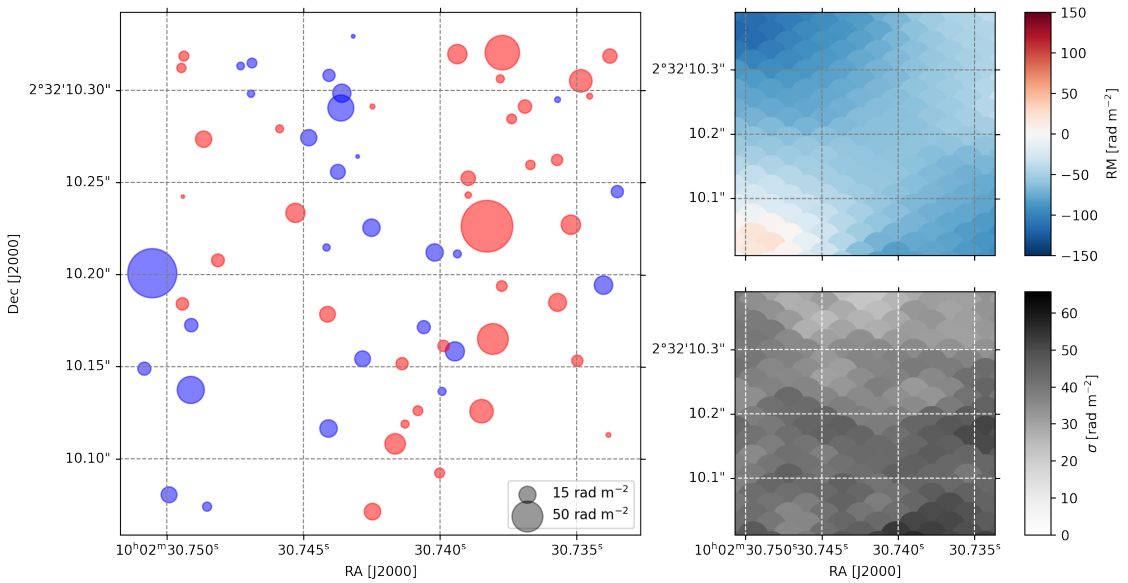

Figure 4.15: *Left:* Spatial distribution of detected polarised sources. The marker size is indicative of its |RM| value, as shown in the legend, and the colour represents a positive (red) or negative (blue) RM. *Top right:* Hutschenreuter et al. (2022) RM map over the region of this survey. *Bottom right:* Corresponding uncertainty for the Hutschenreuter et al. (2022) RM map.

classify the sources by their Fanaroff-Riley type (i.e. FRI, FRII), where this is predominantly based on whether resolved sources are lobe or core dominated. We find that 12 (18%) sources are FRI, 33 (50%) are FRII, 10 (15%) sources are compact (i.e. unresolved at $\theta = 0.75''$) and we classify 10 (15%) sources as extended, where they have irregular morphologies that do not correspond to the FR classes. Examples of sources belonging to each morphology class is shown in Figure 4.16.

We further classify sources based on their host galaxy properties. As introduced in Section 4.2.5, we use the classification of star-forming galaxies (SFG), moderate-to-high luminosity AGN (HLAGN) and low-to-moderate luminosity AGN (MLAGN), introduced by Smolčić et al. (2017b) and Delvecchio et al. (2017). This classification scheme was designed to be analogous to the high-excitation radio galaxy (HERG) and low-excitation radio galaxy (LERG) classification, also known as radiative-mode and jet-mode galaxies. The key difference between these populations are the different modes of super-massive blackhole accretion – HERGs radiate efficiently across a large range frequencies, while the emission from LERGs corresponding to AGN feedback is only brighter than that of the host galaxy at radio frequencies (for a review, see Heckman and Best, 2014). The luminosity properties of the HLAGN/MLAGN populations have been found to be consistent with that from HERGs/LERGs (Delvecchio et al., 2017). Furthermore, Whittam et al. (2022) classify the sources detected in the MIGHTEE Early Science COSMOS field into HERGs and LERGs. While this only covers a portion of our sky area (20 matches with the polarised detections presented in this work), they make a detailed comparison for $\sim$ 3000 common sources (i.e. identified in both surveys and verified to be the same source) in total intensity, and between the respective classification methods, SFGs are 82% consistent, HLAGN/HERGs are 97% consistent and MLAGN/LERGs are 57% consistent between their detections and Smolčić et al. (2017b).

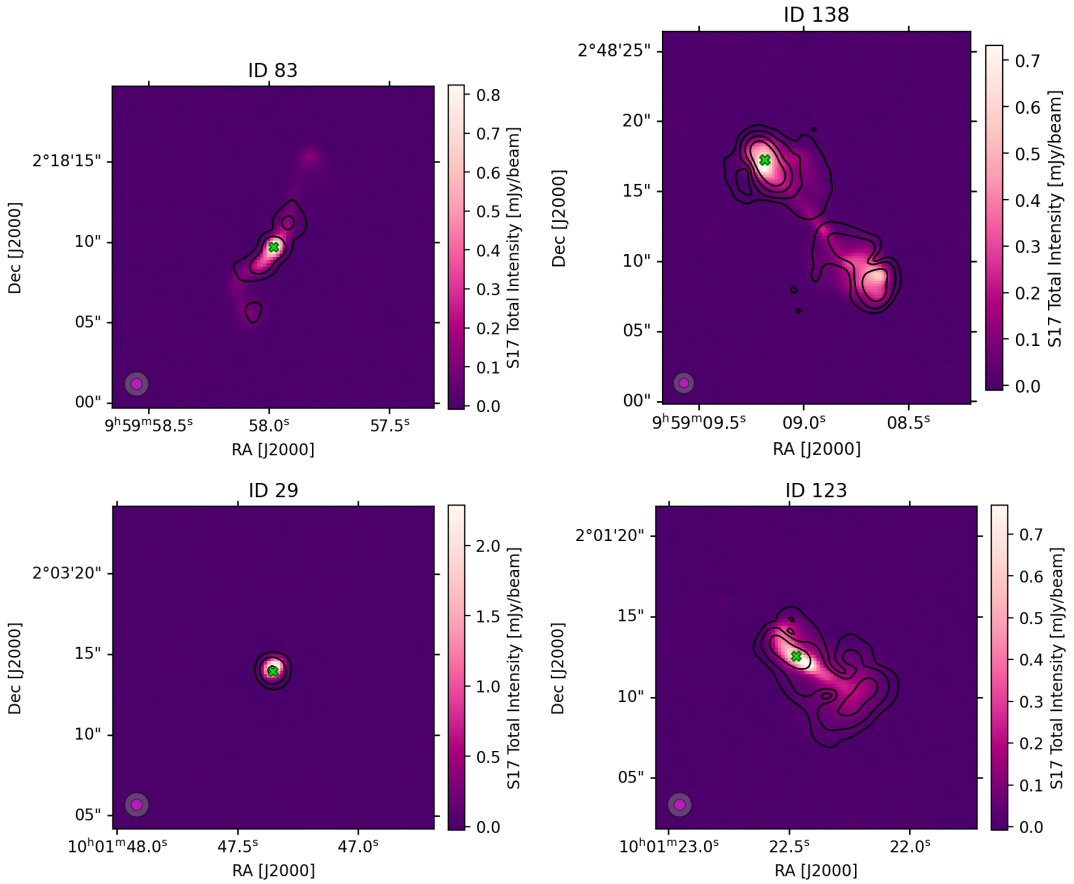

Figure 4.16: Examples of sources morphologically classified as FRI (top left), FRII (top right), compact (bottom left) and extended (bottom right). The total intensity image from S17 are plotted and overlayed with the polarised intensity contours from this work. The contours correspond to P = [22, 45, 90, 150] μJy beam^{-1} . The restoring beams for the total intensity (magenta) and polarised intensity (grey) images are shown in the bottom left corner. The green cross indicates the position at which the Stokes Q and U spectra are extracted for QU-fitting.

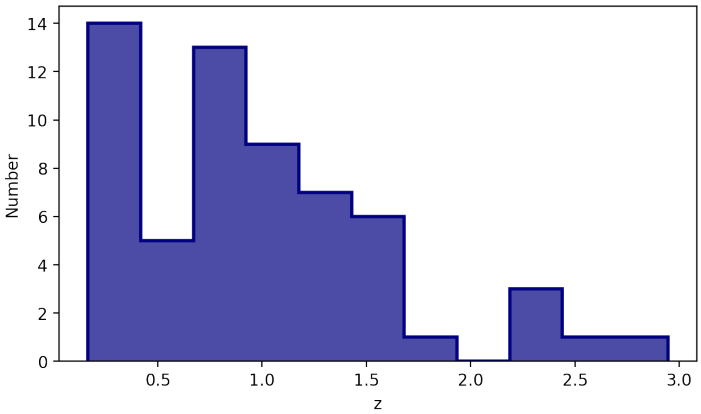

Figure 4.17: Redshift distribution of detected polarised sources, as obtained from the Smolčić et al. (2017b) catalogue.

While it may appear that there is a large discrepancy for the MLAGN/LERG classification, this is rather that the Whittam et al. (2022) LERGs are 32% Smolčić et al. (2017b) SFG and 7% Smolčić et al. (2017b) HLAGN. If we consider the converse, 70% of the MLAGN are classified as LERGS, which is significantly better. Throughout this work, we therefore use these classifications interchangeably, bearing in mind the lower degree of consistency for the MLAGN/LERG classification.

Of the 65 polarised sources, 60 have a multi-wavelength counterpart. These sources also have an associated redshift. The redshift distribution of detected sources is plotted in Figure 4.17 and discussed further in Section 4.5.2. All of these sources are classified as AGN, and we do not detect any star-forming galaxies in polarisation. This is unexpected given the depth of the survey and the decreased λ-dependent and beam-dependent depolarisation effects at 3 GHz. This is discussed in detail in Section 4.5.2. Of our detected sources we find 30 HLAGN, 29 MLAGN and one AGN without a reliable further classification. This, along with the five sources without a multi-wavelength counterpart are excluded from further analyses regarding this classification. In Figure 4.18, we show the total intensity Euclidean-normalised differential source counts from Smolčić et al. (2017b), separated into HLAGN, MLAGN and SFG. Alongside this, we plot the polarised source counts, also separated into HLAGN and MLAGN. The dotted vertical line indicates the lowest total intensity to which we detect polarised sources at $S_{3\,\mathrm{GHz}} = 0.52$ mJy. In the domain above this limit, we only cover the brightest of the star-forming regime, for which the sources are rare. For the two AGN classes, we find a general consistency in the dominance of HLAGN at higher (polarised) flux densities. The transition to the MLAGN dominating flux densities at $S_{3\,\mathrm{GHz}} < 2.5$ mJy in total intensity is mirrored by the change in dominant population at $P_{3\,\mathrm{GHz}} < 0.2$ mJy for polarised intensity. This suggests a similar fractional polarisation p for both AGN types. We discuss this further in Section 4.4.4.

4.4.3 Spectral index and depolarisation

In Section 4.2.4, we introduced the various models that we use to interpret the wavelength-dependent behaviour of the Q and U spectra, as well as the spectral index α in total intensity. While the broadband characterisation of polarised sources is currently an active field of research for both the interpretation of

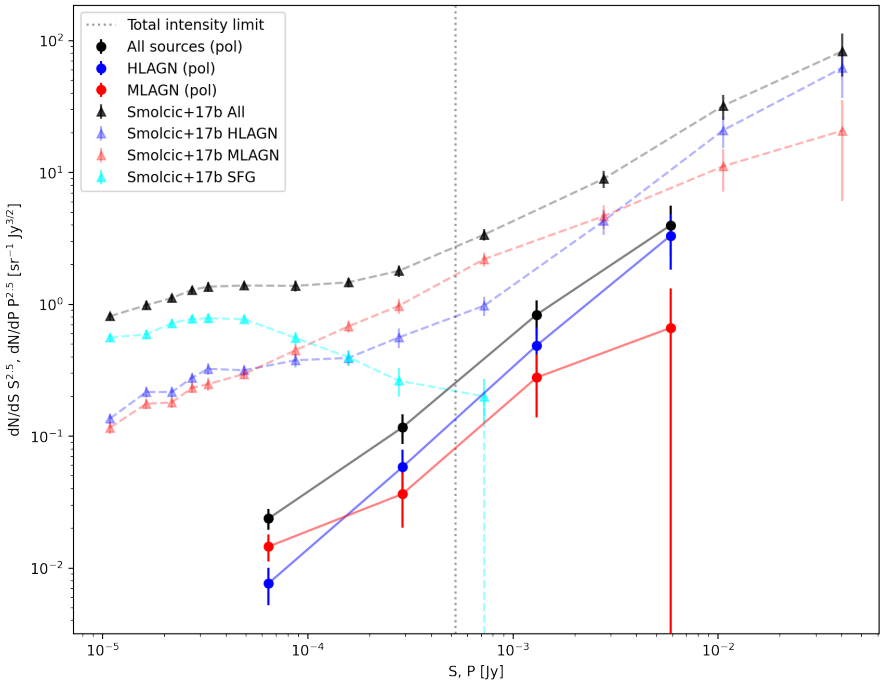

Figure 4.18: The polarised Euclidean-normalised differential source counts $\mathrm{d}N/\mathrm{d}P\,P^{2.5}$, as in Figure 4.12, are plotted below (circles with solid line) for all sources (black), HLAGN (blue) and MLAGN (red). This is shown in comparison to the Euclidean-normalised differential source counts in total intensity $\mathrm{d}N/\mathrm{d}S\,S^{2.5}$ from Smolčić et al. (2017b) (triangles with dashed line) with the same colouration, as well as SFGs in cyan. The dotted vertical line indicates the lowest total intensity to which we detect polarised sources. Here, we elect for fewer bins than in Figure 4.12, due to the smaller sample sizes for the respective AGN classifications.

the Galactic foreground (e.g. Anderson et al., 2015; Ma et al., 2020; Ranchod et al., 2024) as well as the physical properties of radio galaxies (e.g. Farnes et al., 2014; O'Sullivan et al., 2017; Pasetto et al., 2018), to date this has been limited to the bright polarised population, typically with $P > 1$ mJy. Here, we aim to provide a broadband characterisation of the sub-mJy polarised sky, an important step into understanding the properties of these faint polarised sources. Additionally, the λ^2 range which we sample at 3 GHz is less susceptible to λ-dependent depolarisation, allowing us to better anchor the intrinsic fractional polarisation of the source, and understand which source populations would be undetected at lower frequencies due to strong depolarisation effects.

In Figure 4.19 we present the distribution of the total intensity spectral index α and depolarisation index β, as defined in Section 4.2.4. These values and their uncertainties are presented in the catalogue associated with this work (Appendix C). The α measurements have typical errors of $\sim 10\%$ and the β fits typically have larger errors of $\sim 50\%$, due to the low S/N and the complex nature of the spectra. The α distribution is as expected for S-band frequencies (e.g. Smolčić et al., 2017b; Ranchod et al., 2025); a bimodal distribution peaking at $\alpha_{\mathrm{med}} = -0.8$, with the secondary peak for flat spectrum sources, centred at $\alpha \approx -0.4$. In terms of radio-AGN, flat spectra ($\alpha > -0.5$) usually indicate core-dominated sources, i.e. the optically thick region at the base of the jets, while steep spectra are dominated by the optically thin jet or core. Since the majority of sources are spatially resolved in total intensity, we can

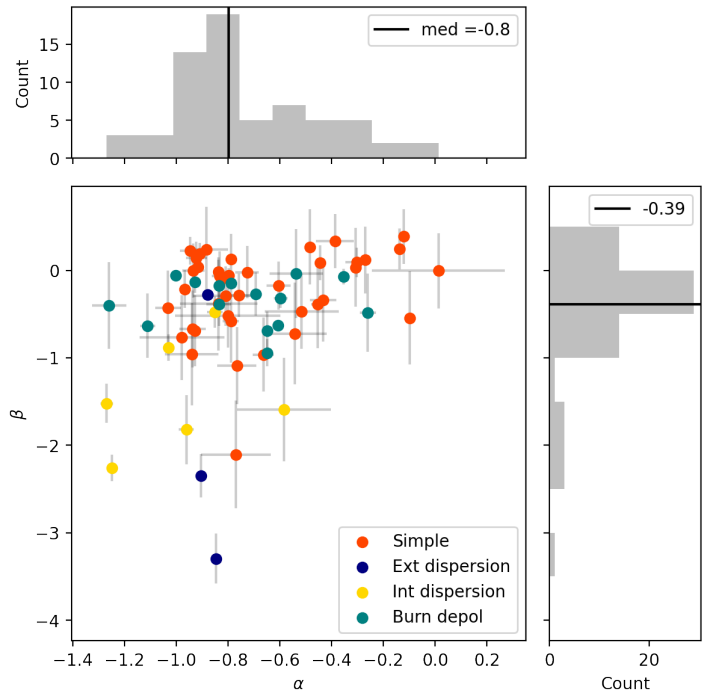

Figure 4.19: Spectral index α against depolarisation index β for P_{peak} of all sources. The markers are colourised according to their best fit depolarisation model, with Faraday simple (Equation 4.8) in orange, external Faraday dispersion (Equation 4.9) in blue, internal Faraday dispersion (Equation 4.11) in yellow and Burn slab depolarisation (Equation 4.10) in green. Histograms of the α and β distributions are shown on the top and right, respectively. The black solid lines indicate their median values, as shown in the legend.

visually identify which part of the source the peak spectrum is extracted from. In the case of the flat spectrum sources in this sample, all except one (ID 145) are either compact sources, or the P_{peak} is at the AGN core. In the special case of ID 145 (see Appendix B), a resolved FRII galaxy, the P_{peak} pixel is not associated with the core or the total intensity hotspots on the lobes, but is rather located towards the edge of the source. This is characteristic of the classical increased polarisation fraction at the edge of radio lobes due to magnetic field alignment after interaction with the intergalactic medium, as determined through observations (e.g. Baidoo et al., 2023) and numerical simulations (e.g. Stimpson et al., 2025). Therefore, the total intensity spectrum for this position has insufficient S/N for a reliable measurement of α.

The relationship of $\alpha - \beta$ seen in this work is consistent with that from Farnes et al. (2014), where the authors characterised the broadband polarisation properties of $\sim 10^3$ bright sources ($P_{1.4\text{ GHz}} > 3$ mJy) from 400 MHz to 100 GHz using narrowband observations from a range of different surveys. This distribution of sources signifies that depolarisation is an intrinsic property of the source, rather an external effect. As in Farnes et al. (2014), there is a clear separation between flat- and steep-spectrum sources. Steep spectrum sources show a moderate ($\beta > -1$) or high depolarisation ($\beta < -1$), while flat-spectrum sources have a β distribution symmetric about $\beta = 0$. This includes measurements of $\beta > 0$, or "repolarisation", which is caused by the more complex total intensity spectral behaviour of

an optically thick, core-dominated source (e.g. synchrotron self-absorption), or fractional polarisation models that have sinc-like variation with λ^2 (e.g. Burn slab). Our results show that repolarisation is observed for flat-spectrum sources, even with a limited frequency range, consistent with Taylor et al. (2024). This consistency with Farnes et al. (2014) and Taylor et al. (2024) despite the smaller λ^2 coverage suggests that the $\sim 1-4$ GHz range may be the most relevant when characterising the broadband behaviour of polarised extragalactic sources.

Next, we identified the dominating depolarisation mechanism for these sources, by fitting physical models to the Stokes Q and U spectra, as described in Section 4.2.4. The best-fit model is indicated by colour on Figure 4.19. We find 41 sources are Faraday simple (Equation 4.8), which is 63% of the sample. It is difficult to compare source Faraday complexity fractions with those in the literature, as this is highly dependent on bandwidth, angular resolution and complexity metric. The complexity can be based on either QU-fitting (e.g. Ranchod et al., 2024), or based on resolving the complexity in the Faraday spectra (see Chapters 2 and 3 for details). The latter is highly dependent on $\delta\phi$ and max-scale of the observations. We have a consistent complexity fraction with Livingston et al. (2022), with 37%, in a study of polarised sources behind the Small Magellanic Cloud. For observations with the same bandwidth of 2–4 GHz for a range of extragalactic fields, Pandhi et al. (2025) found 21% complexity, based on the Faraday spectra. Similarly, over a small frequency range in the POSSUM pilot obserations, Vanderwoude et al. (2024) found a complexity fraction of 22% at $b \sim 50^\circ$, whereas for $|b| > 20^\circ$, O'Sullivan et al. (2017) found a complexity fraction of 55% for broadband ($1-3$ GHz) ATCA observations of extragalactic sources. Considering the Faraday complex sources, 3 sources are best fit with the external Faraday dispersion model (Equation 4.9), 6 sources with internal Faraday dispersion (Equation 4.11) and 15 sources with Burn slab depolarisation (Equation 4.10). Values of $\sigma_{\rm RM}$ range between $13 < \sigma_{\rm RM} < 88$ rad m^{-2} and for $\phi_{\rm diff}$, we have $12 < \phi_{\rm diff} < 84$ rad m^{-2}. The Burn slab and internal dispersion models also have a foreground RM component. For the internal dispersion model this is consistent within the uncertainties of the RM measured from RM synthesis, with the exception of source ID 101, which is the positive outlier in Figure 4.14, with an RM of 140 ± 6 rad m^{-2}, as determined from RM synthesis. From QU-fitting, we have $\phi = 78 \pm 10$ rad m^{-2}, suggesting that a significant contribution to the RM is internal to the source. In general, sources best fit by Burn slab depolarisation have a mean offset of foreground ϕ with respect to that determined from RM synthesis of 24 rad m^{-2}. While this is still within limitation of the $\delta\phi$ for the sampled λ^2 and the large uncertainties of the Hutschenreuter et al. (2022) RM map (Section 4.4.1), it emphasises the importance of QU fitting for determining accurate RMs when probing the foreground Galactic magnetic field. Another intriguing result is the large fraction of sources with Burn slab depolarisation. This is not typically the best fitting depolarisation model for studies of bright polarised sources in the literature (e.g. Anderson et al., 2015; O'Sullivan et al., 2017). However, we have a previously unexplored perspective here with such high resolution and sensitivity. All of the sources showing Burn slab depolarisation are resolved and 9 of the 15 correspond to the lobes of FRII galaxies. Broadband studies ($1-12$ GHz) of nearby, extended radio lobes Cygnus A (Sebokolodi et al., 2020) and Hydra A (Baidoo et al., 2023), find that > 60% of sightlines show sinc-like depolarisation or more complex behaviour. This is consistent with what we find in our sample, suggesting that Burn slab depolarisation may be a common characteristic of resolved radio lobes when observed with sufficient sensitivity and λ^2 coverage.

As evident in Figure 4.19, the various depolarisation models are grouped in specific areas of the $\alpha - \beta$ parameter space, with external and internal Faraday dispersion having the strongest depolarisation.

The Faraday simple sources and those with Burn slab depolarisation occupy a similar region, with the Faraday simple sources closer to $\beta = 0$, as expected. The Faraday simple model is also preferred for flat spectrum sources, including those that show repolarisation, as none of the models account for repolarisation. Of the Faraday complex models, the most commonly selected is the Burn slab depolarisation. For all steep spectrum sources, this corresponds to spectra extracted from radio lobes. While a detailed redshift analysis is beyond the scope of this work, and will be addressed in a future paper, we find that all sources best fit with Burn depolarisation, and the majority (>90%) of the Faraday simple sources have $z < 2$. Of the sample, we there are 5 sources with $2 < z < 3$, three of which are best fit with external Faraday dispersion. We note that the Faraday simple sources that show depolarisation with β typically have high uncertainties in polarised intensity, i.e. they are detected with relatively lower significance. This is likely due to the bias for higher S/N sources be Faraday complex (e.g. Anderson et al., 2015; Ranchod et al., 2024), as we are not sensitivity to the Faraday complexities in the QU-spectra above the noise level for faint sources. The majority of sources occupy the parameter space where, within uncertainties, $\alpha \approx \beta$, which may contribute to the absence of frequency dependence in the sources counts presented in Section 4.3. This relation between depolarisation and source counts will be discussed in detail in Section 4.5.1.

We briefly discuss the properties of the sources that are both Faraday complex and show large degrees of β depolarisation. Of the five sources, three are compact (IDs 16, 29, 101), and two are FRII galaxies where the brightest polarised component is selected from the lobes (IDs 10901, 10915). Both sources with external Faraday dispersion are compact and these sources, along with ID 10901 are some of the brightest of the sample $P > 100$ μJy beam^{-1}. Both sources showing internal Faraday dispersion and ID 16 also have some of the highest redshifts of the sample with $z > 2$. While this suggests that compact and higher redshift sources are preferentially depolarised, we require a much larger sample to draw meaningful conclusions. This work can be expanded on by obtaining $\sim$ 100 MHz – 2 GHz broadband observations of such sources in the sub-mJy regime to better characterise their wavelength-dependent behaviour. Such datasets will become readily available with future surveys with the SKA, with the possibility of coordinated SKA-low and SKA-mid surveys covering the same sky areas.

4.4.4 Fractional polarisation

In this section, we discuss both the observed fractional polarisation p of the detected sources, as well as the intrinsic fractional polarisation p_0. The former can inform us on the depolarisation effects in the environment of the source, or foreground Faraday screens, i.e. as determined through QU-fitting, while the latter describes the intrinsic magnetic field ordering within the source. The distribution of fractional polarisation for the full sample is shown in Figure 4.22. This histogram follows a log-normal distribution with $\mu = 0.11$ and $\sigma = 1.29$, where μ and σ are the median and standard deviation of the log-normal distribution.

As we are limited by the small number statistics of our detected sample, we require a more complete measure to include sources depolarised beyond our detection threshold as well as the full extent of the polarised source counts. To account for this, we derive a probability density distribution for the fractional polarisation (e.g. Tucci and Toffolatti, 2012; Piras et al., 2024). To differentiate between this derived distribution and our observed values, we refer to fractional polarisation as Π rather than p . This

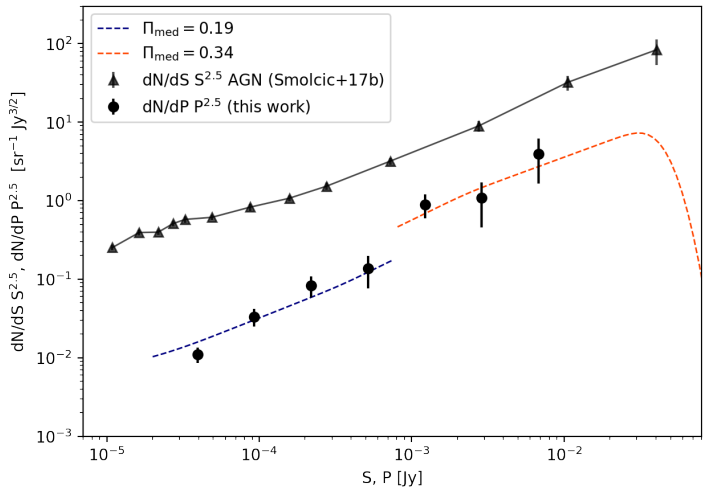

Figure 4.20: Euclidean-normalised differential source counts for the AGN population of Smolčić et al. (2017b) (black triangles). The Euclidean-normalised differential polarised source counts from this work are shown with black circles. Here, we plot two illustrative models (Equation 4.20) with Π_{med} = 19% (blue) and Π_{med} = 34% (orange).

probability density distribution can be described as log-normal function $\mathcal{P}(\Pi)$,

$$\mathcal{P}(\Pi) = \frac{1}{\sqrt{2\pi\sigma^2}\Pi} \exp\left(-\frac{\left[\log \Pi/\Pi_{med}\right]^2}{2\sigma^2}\right), \tag{4.19}$$

where Π_{med} is the median of the distribution and $\sigma^2 = \frac{1}{2}\log\left(\langle\Pi^2\rangle/\Pi^2_{med}\right)$. By convolving the differential total intensity source counts $n(S)$ with this probability distribution, we can obtain the differential polarised counts $n(P)$:

$$n(P) = \int_{S_0=P}^{\infty} \mathcal{P}\left(\Pi = \frac{P}{S}\right) n(S) \frac{\mathrm{d}S}{S}, \tag{4.20}$$

and constrain $\mathcal{P}(\Pi)$ by comparing with our data. As we are restricted by the large uncertainties of the binned counts, we do not fit the modelled $n(P)$, but rather discuss the results for various input Π. These models are plotted in comparison to the data in Figure 4.20. We find the best suited model to the data is Π_{med} = 19% for $P < 1$ mJy and Π_{med} = 34% for $P > 1$ mJy. There is a disparity between the fractional polarisation for high polarised intensity sources and low polarised intensity sources. As we will discuss in Section 4.5.2, the brightest sources in the sample are large, extended AGN. With the resolved nature of these sources we can expect to have higher fractional polarisation (e.g. Grant et al., 2010; Adebahr et al., 2022). While the majority of the unresolved sources show strong depolarisation within the band, this is likely an effect of both intrinsic source properties and a bias caused by beam depolarisation, i.e. a net depolarisation due to the averaging of a range of polarisation angles within a beam element. For example, the average source size in the highest polarised intensity bin is 145 beams, in comparison to 7 beams in the lowest bin. Comparing to other studies at $\sim$ 3 GHz, Lamee et al. (2016), have a significantly lower average fractional polarisation of 2%, and

a maximum observed fractional polarisation of 12% for an angular resolution of 45" (S-PASS at 2.3 GHz).

Previous studies involving polarised Euclidean-normalised source counts are at a factor of > 5 lower angular resolution (e.g. Hales et al., 2014; Berger et al., 2021) and are not affected by the bias of non-uniformly resolved sources. While a clear strategy to mitigate this bias would be to convolve the spectral cubes to lower resolution, this becomes largely self-defeating for sources of angular size $> 45''$ because of the poor brightness temperature sensitivity of the VLA A-array at these spatial scales. In the context of future polarisation surveys, e.g. MeerKAT+ S-band Legacy Survey (Chapter 6), VLASS (Lacy et al., 2020), and the SKA, the similar $\sim 1''$ resolutions can reveal new insights into the structure and magnetic field ordering of polarised radio galaxies for statistically large samples and should be preserved. This discrepancy in fractional polarisation shows a clear effect in the source counts, which without careful quantification can be interpreted as a change in slope or source population. Therefore, due to this additional factor of beam depolarisation, it is worth mentioning the limited interpretation of polarised Euclidean-normalised source counts at such high angular resolution, in comparison to those in total intensity.

Intrinsic fractional polarisation of FRI and FRII

In Figure 4.21, we show a comparison between p_0 for the FRI and FRII galaxies in our sample. On average, FRII sources show a higher intrinsic fractional polarisation, with a median $p_0 = 15.1\%$, while FRI sources have a median $p_0 = 6.7\%$. We note that these p_0 values are derived only for the brightest pixel of polarised intensity per source. Since our source classification here is based on radio morphology, this distinction can also represent that of radio cores (FRI) and lobes or hotspots (FRII). An outlier is the FRI source ID 247 with the highest fractional polarisation of $p_0 = 50.3\%$, for which the brightest pixel spectrum is extracted from the lobe.

In recent 150 MHz surveys with LOFAR, it has been reported for both the LOFAR Two-Metre Sky Survey (LoTSS; Mahatma et al., 2021) and the LOFAR Deep Field ELIAS-N (Piras et al., 2025) that FRII sources have a higher polarisation detection rate at 150 MHz than FRI sources. Furthermore, Mahatma et al. (2021) report a statistically higher polarisation fraction for FRII sources compared to FRI, which they attribute to the bright FRII hotspots dominating the sample. Piras et al. (2025) suggest that their lower detection rate of FRI galaxies is caused by these sources residing in denser magneto-ionic environments and therefore being more susceptible to depolarisation. Our results show that while environmental effects are also at play, the polarised core regions of FRI galaxies are also dominated by a more disordered magnetic field structure, as evident by their lower p_0, in comparison to the lobes of FRII galaxies. Figure 4.19 also shows lower depolarisation for flat-spectrum sources, typically associated with AGN cores which also suggests that this is an intrinsic source property rather than an environmental effect. Our interpretation of more ordered magnetic fields in radio lobes is consistent with detailed studies of individual sources (e.g. Guidetti et al., 2011; O'Sullivan et al., 2012; Baidoo et al., 2023). However, this interpretation is limited by the bandwidth of our data, the uncertainties on the p_0, and the significance of the polarised intensity detections. A more accurate measurement for p_0 can be derived over a larger frequency range as well as considering more complex QU-fitting models.

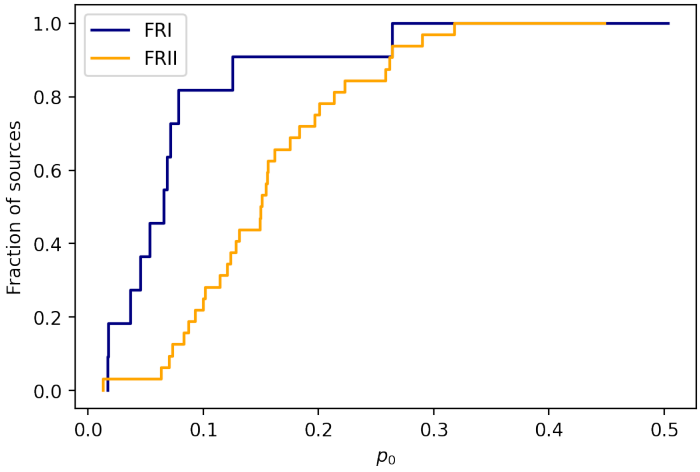

Figure 4.21: Cumulative distributions of the intrinsic polarisation fraction p_0 for FRI (blue) and FRII (yellow) sources.

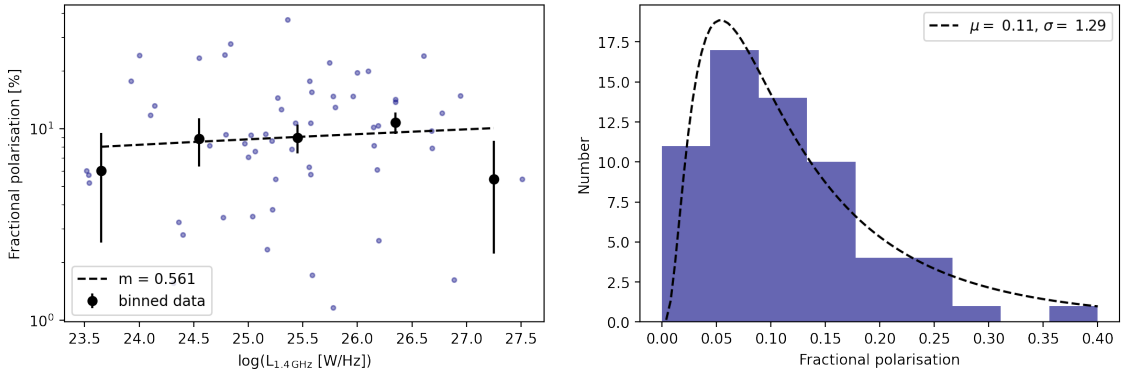

Figure 4.22: *Left:* fractional polarisation as a function of 1.4 GHz luminosity. The data for individual sources are shown in blue and the binned measurements in black. A linear fit is indicated by the dashed line, with a slope of $m = 0.56 \pm 1.00$. *Right:* Histogram of fractional polarisation p of detected source (blue). The log-normal fit is indicated by the dashed line with fit parameters in the legend.

Intrinsic fractional polarisation of HLAGN and MLAGN

In this section, we compare the p_0 for sources classified as HLAGN and MLAGN. As we discuss in Section 4.4.2, we use this classification as a proxy for jet-mode (LERG) and radiative-mode (HERG) sources. Previous studies have shown an anti-correlation of fractional polarisation with total intensity (Mesa et al., 2002; Tucci et al., 2004; Taylor et al., 2007; Subrahmanyan et al., 2010; Stil et al., 2014). To explain this anti-correlation, more detailed studies classified sources based on their physical properties and found a similar anti-correlation with source luminosity. Banfield et al. (2014) classified sources into quiescent and quasar-mode galaxies, another proxy for jet-mode and radiative mode. They suggested that the anti-correlation was driven by lower luminosity sources (i.e. quiescent mode) which they find have intrinsically higher fractional polarisations. A similar result was found by O'Sullivan et al. (2015) who report an increased fractional polarisation for jet-mode sources and O'Sullivan et al. (2017), who after

Table 4.3: Median μ and standard deviation σ as determined from the log-normal fits to the HLAGN and MLAGN intrinsic fractional polarisation p_0 distributions.

	μ	σ
HLAGN	0.17	1.59
MLAGN	0.13	0.87

broadband observations and QU-fitting find that jet-mode sources also have an increased p_0 with respect to the higher luminosity radiative mode sources. These detailed classifications were done mostly using targeted surveys of bright radio sources $P > 2$ mJy. More recent blind surveys covering lower polarised flux densities have disputed the fractional polarisation anti-correlation as a systematic effect caused by spurious detections and selection bias (Hales et al., 2014; Berger et al., 2021). In Figure 4.22, we show that we do not observe this anti-correlation as a function of total intensity or luminosity, consistent with what was found for the faint source population. To assess the correlation of the data, fit a linear function to the fractional polarisation as a function of luminosity, and find a slope of $m = 0.56 \pm 1.00$, showing that fractional polarisation is approximately constant with luminosity. In addition, we compute the Pearson correlation coefficient r and find $r = 0.0032$ and a $p = 0.81$. This implies that there is no statistically significant linear correlation. Similar to Hales et al. (2014) and Berger et al. (2021), the observed constant polarisation fraction can be due to our careful quantification of systematics in the data and the unbiased nature of a blind survey. Below, we further investigate this in the context of source classification.

In Figure 4.23, we plot the distribution of p_0 for HLAGN and MLAGN. We fit log-normal functions to the distributions and summarise the fit parameters in Table 4.3. This plot suggests that there is not a clear difference between the respective populations regarding intrinsic fractional polarisation. We perform the two-sample Kolmogorov-Smirnov (KS) test to understand if these values are drawn from the same distribution. We find a KS statistic of 0.0039 and a p-value of 1, suggesting that the HLAGN and MLAGN distributions are not statistically different in this survey. While this appears to be in contradiction with the targeted studies of Banfield et al. (2014) and O'Sullivan et al. (2017), we note that the range of luminosities $L_{1.4\,\mathrm{GHz}}$ for the polarised sources is much smaller in comparison, and covers the range where the two populations overlap in the targeted studies. This comparison is plotted in Figure 4.23, where $L_{1.4\,\mathrm{GHz}}$ is obtained from the Smolčić et al. (2017b) catalogue. We note that Delvecchio et al. (2017) emphasise that the naming convention for HLAGN/MLAGN sources implies an overlap in the respective classifications and that the small area of the VLA-COSMOS survey may limit our sensitivity to a large range of $L_{1.4\,\mathrm{GHz}}$, as extreme cases are rare due to cosmic variance. The selection bias and limitations of small-area blind surveys are discussed in Section 4.5.2.

4.5 Discussion

In the following section, we discuss the drivers behind the consistent source counts between 1.4 GHz and 3 GHz, as well as the limitations of source detectability for deep, high resolution polarisation surveys.

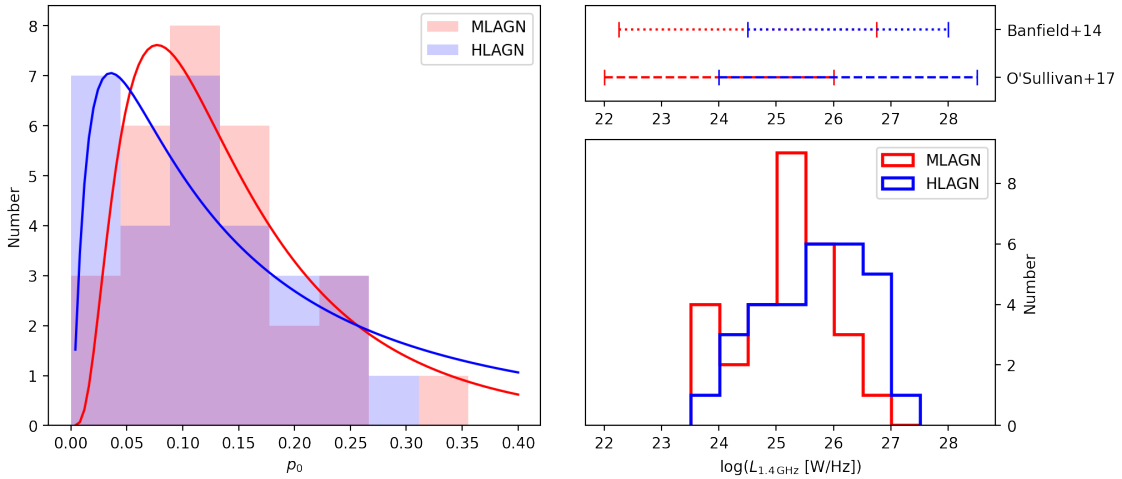

Figure 4.23: *Left:* Distribution of intrinsic fractional polarisation p_0 for HLAGN (blue) and MLAGN (red) and their respective log-normal fits (Table 4.3). *Right:* 1.4 GHz luminosities $L_{1.4\,\mathrm{GHz}}$ of the polarised HLAGN (blue) and MLAGN (red) populations in this work. The corresponding $L_{1.4\,\mathrm{GHz}}$ ranges for the quiescent (MLAGN)/quasar-like (HLAGN) classifications from Banfield et al. (2014) and the jet-mode (MLAGN)/radiative-mode (HLAGN) classifications from O'Sullivan et al. (2017) are also plotted.

4.5.1 Frequency evolution of polarised source counts

Given the λ-dependence of depolarisation, one might expect an increased polarised source count at higher frequencies, as we might detect sources that would otherwise be depolarised at lower frequencies. In Section 4.3.2, we presented the cumulative source counts for the COSMOS field at 3 GHz, and found consistency with the source counts of Rudnick and Owen (2014) at 1.4 GHz. With these observations, we can confirm the prediction by Lamee et al. (2016) that source counts with VLASS (i.e. at the same frequency range and angular resolution of this work) would be consistent with those at 1.4 GHz. Their prediction was based on the comparison between the polarised source detections in the S-PASS (2.3 GHz) and NVSS (1.4 GHz) surveys for $P > 230$ mJy, where they investigated the spectral index and depolarisation ratio $P_{2.3\,\mathrm{GHz}}/P_{1.4\,\mathrm{GHz}}$. To further understand the interplay between spectral index and depolarisation for the sub-mJy population, we model the effect of these parameters on the polarised intensities at 3 GHz and the detected source counts below.

The polarised intensity, as a function of frequency ν can be expressed as

$$P(\nu) = S(\nu)p(\nu). \tag{4.21}$$

For total intensity S, the ν-dependence is the effect of spectral index α, $S(\nu) \propto \nu^{\alpha}$. As introduced in Section 4.2.4, there are multiple models that can describe the fractional polarisation $p(\nu)$. We adopt the Burn slab model (Equation 4.10) to demonstrate the ν-dependence, as is the most commonly selected model for Faraday complex sources. Here, we simplify this equation to include only the amplitude of the

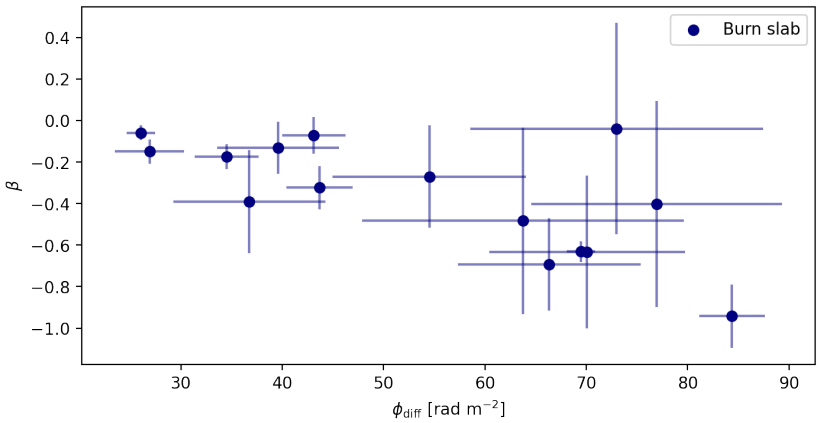

Figure 4.24: Differential RM $\phi_{\rm diff}$, as obtained from Equation 4.10 vs. the depolarisation index β.

complex depolarisation, and rewrite it as a function of ν

$$p(\nu) = p_0 \frac{\sin(\phi_{\rm diff}(c/\nu)^2)}{\phi_{\rm diff}(c/\nu)^2}. \tag{4.22}$$

The $\alpha - \beta$ parameter space that this model occupies is dominant across the sample (Figure 4.19) and also in the literature (e.g. Farnes et al., 2014; Taylor et al., 2024). To investigate the frequency evolution of this model, we simulate a source population with the same properties as the detected sources. Firstly, we fit a double Gaussian to the α distribution (top panel of Figure 4.19). As discussed in Section 4.4.3, we treat the flat- and steep-spectrum sources separately, due to their different β distributions. We fit a double Gaussian to the β distribution with $\alpha < -0.5$, and a single Gaussian to the β distribution for flat-spectrum sources. We then sample 10^4 sources from the α distribution and the corresponding β distribution. To characterise the depolarisation of the simulated sources in more physical parameters, we examine the relationship between β and the $\phi_{\rm diff}$, the differential Faraday rotation measure in the Burn slab model. In Figure 4.24, we show the moderate to strong correlation between these quantities, with a Pearson correlation coefficient of $r = -0.69$ and a p-value of $p = 0.0044$. We generate a $\phi_{\rm diff}$ measurement for each simulated β by interpolating over this relation.

With respect to a reference frequency $\nu = 1.4$ GHz, Equation 4.21 can be written as

$$P(\nu) = P_{1.4\,\rm GHz} \left(\frac{\nu}{1.4\,\rm GHz}\right)^{\alpha} \frac{\sin(\phi_{\rm diff}(c/\nu)^2)}{\phi_{\rm diff}(c/\nu)^2} \frac{\phi_{\rm diff}(c/1.4\,\rm GHz)^2}{\sin(\phi_{\rm diff}(c/1.4\,\rm GHz)^2)}. \tag{4.23}$$

We evaluate the 10^4 simulated sources through this model over a frequency range of $1 < \nu < 4$ GHz, as displayed in Figure 4.25, where the colourmap indicates the point density. This plot shows a constant ratio up to $\nu = 2$ GHz, after which the dispersion of $P_\nu / P_{1.4\ \rm GHz}$ increases, and the peak ratio decreases, i.e. spectral index dominates over depolarisation effects. For $\nu > 2.3$ GHz, a secondary peak emerges with $P_{3\ \rm GHz}/P_{1.4\ \rm GHz} \sim 2.5$, corresponding to the population with extreme depolarisation (e.g. $\beta < -1$). The right subplot shows a normalised cross-section at $\nu = 3$ GHz. This probability density distribution is best described by a double Gaussian, where the peak is at $P_{3\ \rm GHz}/P_{1.4\ \rm GHz} = 0.72$, and a ratio

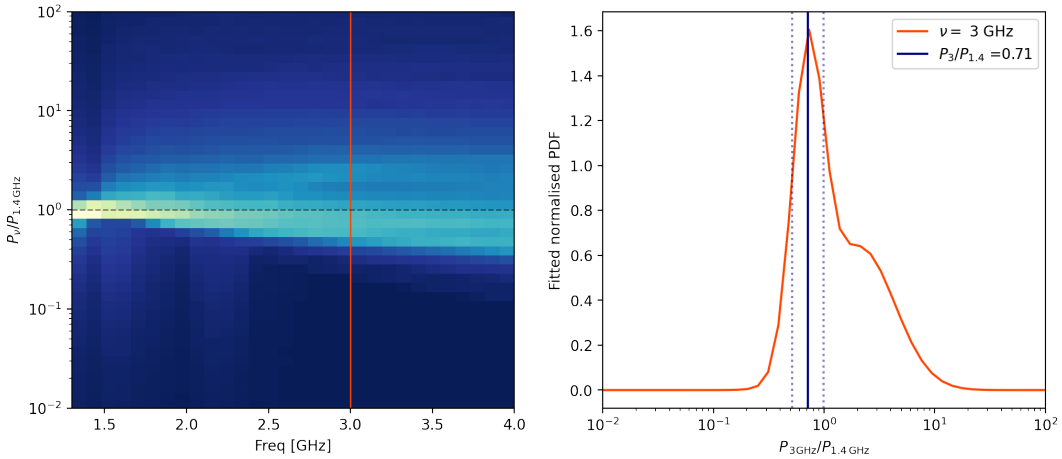

Figure 4.25: *Left:* Normalised density plot for the ratio between the polarised intensity at a given frequency ν and at ν = 1.4 GHz. The grey dashed line is where $P_\nu = P_{1.4\,\mathrm{GHz}}$. The orange line indicates the cross section from which the distribution in the right subplot is taken. *Right:* The probability density distribution for the ratio of polarised intensity at 3 and 1.4 GHz. The peak of the distribution is indicated by the blue solid line, and the 1σ range is shown by the dotted blue line.

of $P_{3\ \mathrm{GHz}}/P_{1.4\ \mathrm{GHz}} = 1$ is within 1σ. The secondary peak of the distribution indicates a significant population with larger polarised intensities at 3 GHz, where depolarisation dominates over spectral index.

We further investigate this frequency dependence of polarised intensity in the context of source counts. Assuming that there is no polarised intensity dependence on the α and β parameters, we sample 10 000 simulated sources from the RO14 distribution as $P_{1.4\,\mathrm{GHz}}$ and assign α and ϕ_{diff} parameters as above (Model 1). We then compute $P_{3\,\mathrm{GHz}}$ from Equation 4.23. The resulting cumulative counts are shown in Figure 4.26. Alongside this, we show cumulative counts that only assume the median α and β values rather than the full distribution (Model 2). We find that Model 1 overestimates the source counts by approximately 10%. We make assumptions in the model that may account for the overestimation, most likely the handling of sources with extreme depolarisation, and the resulting increased probability for sources with these properties. Model 2 describes only the median α and β values and without the extreme cases, and we find that we produce more consistent source counts, both with RO14 and this work.

We briefly discuss the effect of observation bandwidth in the context of frequency dependence. Although we do detect Faraday complexity in our sample, the low Faraday depth resolution from 2–4 GHz limits our sensitivity to model depolarisation within this λ^2 range (Brentjens and de Bruyn, 2005). While we have the advantage of obtaining p closer to the intrinsic value, the more severe depolarisation effects are more prevalent at $\nu < 2$ GHz, and the observed frequency range is a limitation for accurately modelling the frequency dependence down to 1.4 GHz. A more detailed modelling of the frequency dependence of source counts will be addressed with future multi-band surveys with a more statistically significant number of detections, e.g. POSSUM combined with MeerKAT+ S-band Legacy Survey. Observations over large bandwidths are crucial for a more accurate modelling of depolarisation and spectral index.

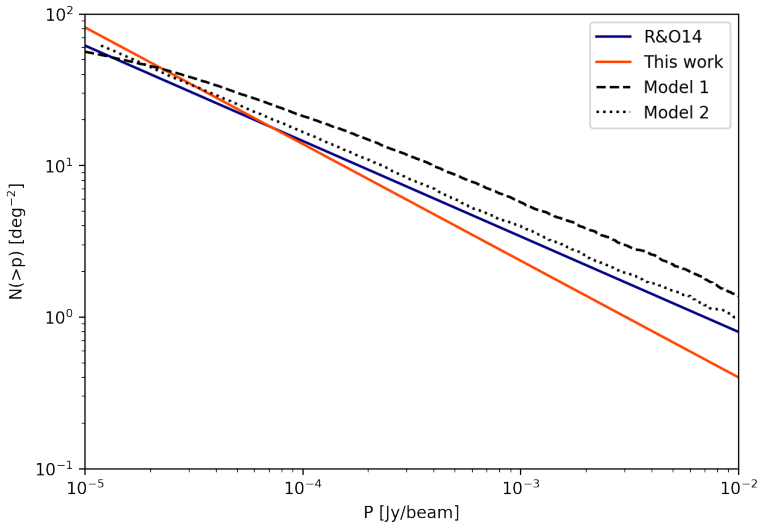

Figure 4.26: Modelled cumulative source counts, as in Figure 4.11. The blue and orange solid lines show the analytical expressions for source counts from Rudnick and Owen (2014) and this work (Equation 4.16), respectively. Model 1 and 2, as described in the text, are plotted as dashed and dotted lines, respectively.

However, within the limitations of our model and the S-band frequency range, we can confirm that the combination of depolarisation effects due to differential Faraday rotation (Burn slab) in radio lobes and the spectral index of these regions account for the consistency of source counts between 1.4 GHz and 3 GHz in an extragalactic field.

An important implication of this work is the assessment of whether S-band or L-band observations are more optimal for maximising the polarised source counts for future surveys. Both bands have their advantages, e.g. higher angular resolution at S-band and higher Faraday depth resolution and larger field of view at L-band. The band selection should rather be based on these properties, as the source count is unlikely to be effected between L- and S-band. This is valid for extragalactic fields only, as we expect the fraction of depolarised sources to increase drastically towards the Galactic plane (e.g. Ranchod et al., 2024). We emphasise that broadband observations are essential for a full characterisation of the depolarisation mechanisms affecting the polarised extragalactic population and in turn, the magnetic field structure of AGN, their various components and their interactions with their surrounding environments.

4.5.2 Nature of the faint polarised source population

In Section 4.4.2, we show that all detected polarised sources are AGN. To understand the limitations of this survey in terms of source detectability for various populations, we investigate the difference between the sources detected and not detected in polarisation. Figure 4.27 shows the peak total intensity against the number of pixels (in total intensity) for each source in the S17 catalogue. At the beam size of $\sim$ 75 pixels, there is a tight correlation from the clustering of point sources, above which sources can be considered resolved. From here it is apparent that the detected sources are of the brightest and largest of the catalogue. In fact, we detect all sources with more than $\sim$ 1200 pixels (17 beams) in polarisation. Similarly, all extended sources with $S_{\rm peak} > 1$ mJy are also detected in polarisation. These

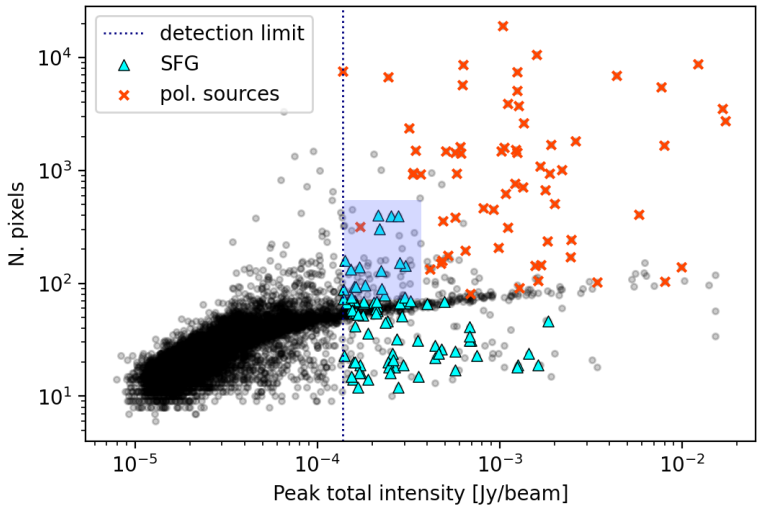

Figure 4.27: Peak total intensity plotted against the number of pixels as detected in the total intensity catalogue from S17 (black). The sources detected in polarisation are indicated by orange crosses, and the polarisation detection limit from this work is shown by the dotted vertical line. The cyan triangles are the star-forming galaxies above the detection threshold and the blue shaded regions indicates the parameter space for which we have resolved star-forming galaxies above the detection threshold.

highly extended sources are in the minority compared to the full sample of mostly point sources. This trend of preferentially detecting extended sources in polarisation is consistent with what was found in RO14, for their sample of 11 sources, also at arcsec resolution. We note that the redshift distribution is statistically consistent between detected and non-detected sources, with a KS statistic of 0.097 and $p = 0.60$. This implies that the extended, polarised sources are not only larger in angular size, but also physically larger. This trend in detectability does not follow for point sources, where the polarised point sources are not necessarily the brightest, and numerous bright point sources are not detected in polarisation. This is in accordance with our observation that compact sources have higher depolarisation indices and p_0. While the detectability of radio sources is linked to their fractional polarisation, an observable for magnetic field ordering, this does not necessarily imply that larger, brighter sources have more ordered magnetic fields. It may also be an effect of beam depolarisation, and that small sources become depolarised below the detection threshold even at arcsecond resolutions. This can be further explored through high angular resolution observations of resolved polarised AGN.

As presented in Section 4.4.2, we do not detect any SFGs within the survey area. This is likely a combination of observational effects and the physical properties of SFG. Various observations and simulations have shown that SFGs have significantly lower integrated fractional polarisations than AGN (Stil et al., 2009; Beck, 2015). As a result, only the magnetic field properties of nearby, resolved star-forming galaxies have been studied in detail, and such sources are rare and not present in the limited area of the COSMOS survey[3]. For example, Kierdorf et al. (2020) present broadband observations

[3] For the following paragraph, we note that we compare our results to nearby $z = 0$ galaxies or simulated populations, and for a fair comparison, consider the rest-frame frequencies of our sample. Assuming an average redshift of $z = 1$, the rest frame frequencies of the polarised sources in VLA COSMOS are 4 – 8 GHz.

of the nearby face-on SFG M51, and report fractional polarisations averaging at $p \sim 15\%$ at 3 GHz, and $p \sim 25\%$ at 4.85 GHz (VLA C-band). For unresolved galaxies, Stil et al. (2009) and Sun and Reich (2012) show that the detection of SFGs is highly dependent on the inclination angle of the galaxy, and as such there is a low probability of detecting unresolved SFGs due to geometrical (beam) depolarisation and Faraday effects. SFGs are more susceptible to this effect in comparison to AGN, as their large-scale magnetic fields vary azimuthally, following the orientation of the spiral arms (Beck, 2015), resulting in a large range of polarisation angles, and thus higher beam depolarisation. Sun and Reich (2012) investigate the frequency dependence of the inclination angle-dependence using 3D emission models of Milky Way-like galaxies, including the regular disk field, the regular halo field and the random magnetic field. Their results show a strong increase of fractional polarisation with inclination angle at frequencies $\nu > 2.7$ GHz. They find for $\nu = 4.8$ GHz, this peaks at 70° with a fractional polarisation of 4.3%, significantly lower than found in resolved nearby galaxies. In terms of observational effects, the array configuration selected for the VLA-COSMOS survey favours higher angular resolution over sensitivity to diffuse emission. As such, we may resolve out diffuse emission from extended star-forming galaxies. Delhaize et al. (2017) convolve the S17 total intensity mosaic to various angular resolutions larger than the native 0.75", up to a maximum of 3" to investigate this effect. From this, they detect 455 additional star-forming galaxies based on prior positions determined from infrared data, which are not accounted for in the S17 catalogue. While this illustrates the resolution bias in these data, their newly detected sources do not exceed $S_{3\,\mathrm{GHz}} = 45\ \mu\mathrm{Jy\,beam^{-1}}$, and therefore would require extreme fractional polarisations of $p > 30\%$ to be detected in polarisation. Based on our non-detection of SFGs, we can determine an upper limit on the density of polarised star-forming galaxies at 3 GHz. We find a polarised SFG density of $< 0.58\ \mathrm{deg^{-2}}$ at $P_{3\,\mathrm{GHz}} > 15\ \mu\mathrm{Jy\,beam^{-1}}$ for a high Galactic latitude field. In Figure 4.27, we indicate the SFGs with a peak total intensity above the minimum peak total intensity of the polarised sources. The majority of these galaxies are unresolved. The blue shaded region highlights the resolved SFGs above the detection threshold. For these sources, we calculate an upper limit on their polarisation fraction to be a maximum of $p < 8\%$, based on the pixel of peak total intensity. Although we can not directly compare to the simulations from Sun and Reich (2012), as they model only unresolved galaxies, this upper limit is consistent with what they found for $\nu = 4.8$ GHz, as mentioned above. This consistency supports the assumptions made in Sun and Reich (2012) concerning the presence of field reversals in the regular disk field, and that various random field components within the disk also contribute increased depolarisation for disk galaxies. Our results substantiate the understanding that the star-forming source population does not contribute to the polarised source counts, even at sub-mJy flux densities (O'Sullivan et al., 2008). Future SKA-era surveys will require observations much deeper than $2.6\ \mu\mathrm{Jy\,beam^{-1}}$ to readily detect the SFG population in polarisation.

In Section 4.4.4, we introduce the dichotomy between the fractional polarisation properties of MLAGN and HLAGN (i.e. jet-mode and radiative-mode AGN), which has been suggested to be the driver of the anti-correlation between luminosity and fractional polarisation (Banfield et al., 2014). Our results show no significant anti-correlation, and support the evidence that it is a systematic rather than physical effect (e.g. Hales et al., 2014; Berger et al., 2021). Moreover, we do not observe a statistically significant difference between the p_0 of HLAGN and MLAGN, which we attribute to the large overlap in luminosity between these populations. Here, we discuss the difference in detected source populations in deep, blind surveys and shallow, large area surveys (or similarly, targeted observations of bright sources). As shown in Figure 4.23, the targeted studies that observed this dichotomy (Banfield et al., 2014; O'Sullivan et al., 2017) include sources over a larger luminosity range. The selection of sources in both of these works

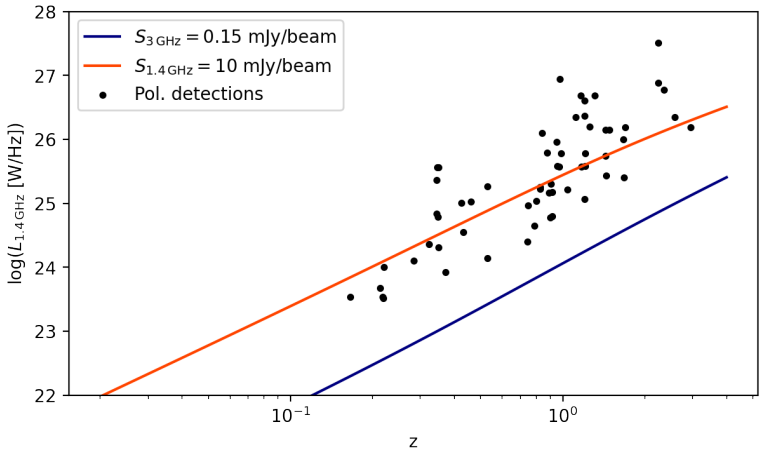

Figure 4.28: Luminosity $L_{1.4\,\mathrm{GHz}}$ as a function of redshift for a survey with a minimum total intensity corresponding to a polarised detection of $S_{1.4\,\mathrm{GHz}} = 10$ mJy beam^{-1} (e.g. NVSS, blue) and $S_{1.4\,\mathrm{GHz}} = 0.15$ mJy beam^{-1} (e.g. VLA-COSMOS, orange). The detected polarised sources are shown in black.

were based on the NVSS RM catalogue (Taylor et al., 2009), covering the entire northern sky (Dec $\geq -40^{\circ}$) down to a total intensity sensitivity of ~ 11 mJy beam^{-1}. The same catalogue was used for other analyses that reported the anti-correlation between total intensity and fractional polarisation (Tucci et al., 2004; Stil et al., 2014). In Figure 4.28, we plot the luminosity $L_{1.4\,\mathrm{GHz}}$ as a function of redshift for a representative sensitivity of NVSS-like surveys as

$$L_{\nu} = 4\pi D_L^2 S_{\nu} (1+z)^{-1}. \tag{4.24}$$

This figure shows that at $S_{1.4\,\mathrm{GHz}} > 10$ mJy, we can detect the low-luminosity source population, but only at low redshifts ($z < 0.1$). These relatively rare sources are still readily detected due to the large area coverage of the survey. While for sources at the peak of our redshift distribution ($z \sim 1$), we are limited to high luminosities $L_{1.4\,\mathrm{GHz}} > 10^{26}$ W/Hz. This reflects the luminosity distributions for the respective source populations in Banfield et al. (2014) and O'Sullivan et al. (2017). On the other hand, as illustrated in Figure 4.28, we are sensitive to a larger range of the redshift-luminosity space for a deep survey (i.e. this work) of $S_{3\,\mathrm{GHz}} > 0.15$ mJy. As shown for our detected polarised sources, we do not detect AGN at low redshifts ($z < 0.1$) due to the limited sky area of the survey, and the majority of sources are at $z \sim 1$ in the intermediate luminosity range. We suggest that this selection bias accounts for why we do not observe a clear dichotomy in the fractional polarisation for HLAGN and MLAGN. While systematic effects may still be at play, this selection bias may also explain why the anti-correlation is not observed in this work, and other similar deep, small area surveys (Hales et al., 2014; Berger et al., 2021). This bias can be confirmed with future polarisation surveys that simultaneously cover a large area and also have high sensitivities ($\sigma \sim 15\,\mu$Jy beam^{-1}), such as the POSSUM and the MeerKAT+ S-band Legacy Survey.

Finally, we discuss the effect of the different source populations on the sub-mJy source counts. As introduced in Section 4.3.2, RO14 report a flattening in the cumulative polarised source counts, attributed to the change in population between FRII and FRI sources. From our VLA-COSMOS catalogue, we also find a flattened cumulative count across the detected polarised intensity range. While

limited by small number statistics, we find 50% of sources are FRII and only 18% are FRI, indicating that even in the sub-mJy regime, the polarised source counts are still dominated by FRII sources. We suggest that this is unlikely to be the dominant cause of the flattening, and it could rather be due to an increased count of low-redshift (jet-mode) MLAGN with a higher fractional polarisation at $P > 1$ mJy, as detected in wide-area surveys. A detailed modelling of this effect is beyond the scope of this thesis and will be addressed in a future work.

4.6 Conclusion

In this chapter, we present the polarisation component of the VLA-COSMOS 3 GHz survey, covering the 1.74 deg^{-2} central region of the continuum survey (Smolčić et al., 2017a). By producing Stokes Q and U cubes and performing RM synthesis, we achieve a sensitivity of 2.6 μJy beam^{-1} in Faraday depth space. With a 10.7σ detection threshold, we detect 65 polarised sources, all of which can be classified as AGN, according to their multi-wavelength properties. Despite the depth and frequency band of this survey, we do not detect any SFG in polarisation. This work provides the deepest polarised source counts at 3 GHz to date, and is the first detailed study of the sub-mJy polarised source population at higher frequencies.

We find a consistent polarised cumulative source counts with Rudnick and Owen (2014) at 1.4 GHz, despite the spectral index effect. By fitting models to the Stokes Q and U spectra, we find that differential Faraday rotation (Burn slab model) in the lobes of the polarised sources is the dominant cause of depolarisation of this sample. While Burn slab depolarisation has been associated to detailed studies of radio lobes with large angular extent, this is not commonly found for bright, unresolved sources. The source count consistency with 1.4 GHz can be described by a combination of this depolarisation effect and spectral index. We derive an analytical model that can be used to predict polarised source counts for future S-band surveys, with a slope of $\alpha = -0.77$. We also find that the Euclidean-normalised counts are consistent with those in the literature, and that the T-RECS simulated catalogue of polarised sources returns a higher source count than we observe in this work, highlighting the necessity for deep polarised source counts across a large frequency range to constrain population models ahead of the SKA era.

In analysing the spatial variation of RM across the sample, we report a median RM = +1.60 ± 3.51, consistent with what was reported in a subregion of the COSMOS field with MeerKAT (Taylor et al., 2024). By comparing to the Hutschenreuter et al. (2022) all sky RM map, we find that the majority of the RM contribution of this sample is attributed to the Galactic foreground, while our increased RM density reveals smaller scale Galactic RM structures. We find that a $> 3\sigma$ deviation from the Hutschenreuter et al. (2022) map indicates an extragalactic RM contribution, in this case from an intervening galaxy group.

In our analysis of the fractional polarisation p and intrinsic fractional polarisation p_0, we present the following results:

(i) By convolving the total intensity counts with a probability density distribution of p, we find an increased total fractional polarisation for large, extended sources. This discrepancy may be an effect of the reduced beam depolarisation at 1.5" angular resolution.

(ii) We classify 50% of our sample as FRII and 18% as FRI sources, and find on average a higher p_0 for the former. By identifying the dominant source component, we find that this traces an

increased p_0 for the radio lobes in comparison to the AGN cores, where magnetic fields are more disordered. This further substantiates the understanding that large-scale coherent magnetic fields are present in radio lobes.

(iii) The high fraction of FRII galaxies in this sample suggests that a change in population between FRII to FRI may not be the driver of the flattening of cumulative source counts at $P < 1$ mJy, as suggested by RO14.

(iv) In contrast with what has been found in targeted surveys of bright sources, we do not find a dichotomy in the p_0 of HLAGN and MLAGN, and a corresponding large overlap in luminosity between the classifications. This is likely a selection bias due to the small-area of the survey. We suggest that large-area, deep surveys are essential to fully explore the this relation down to low polarised intensities.

(v) We find no significant anti-correlation of fractional polarisation with total intensity or luminosity, consistent with other deep, narrow surveys (Hales et al., 2014; Berger et al., 2021). These results support both the claim that anti-correlation is a systematic bias, and also that it is driven by the different fractional polarisation for high- and low-luminosity AGN, for which we are not sensitive to, as stated above.

As we detect no SFGs in polarisation in the VLA-COSMOS, we derive an upper limit of the density of polarised SFGs to be < 0.58 deg^{-2} at $P_{3\,\mathrm{GHz}} > 15$ μJy beam^{-1} , and suggest that survey sensitivities of much less than 2.6 μJy beam^{-1} will be required to readily detect these sources in the SKA era.

These results imply that despite the advantages of high frequency ($\sim$ 3 GHz) polarisation surveys, and the consistent observed source counts at low polarised intensities, we require broad multi-band observations over, e.g. L- and S-band to fully characterise the depolarisation properties of faint extragalactic AGN. This will be possible by combining large-area pre-SKA polarisation surveys, such as POSSUM and the MeerKAT+ S-band Legacy survey, and with common multi-band observations with SKA-mid and SKA-low.

CHAPTER 5

A first glimpse at the MeerKAT DEEP2 field at S-band

A first glimpse at the MeerKAT DEEP2 field at S-band
S. Ranchod, J. D. Wagenveld, H.-R. Klöckner, O. Wucknitz, R. P. Deane, S. S. Sridhar, E. Barr, S. Buchner, F. Camilo, A. Damas-Segovia, C. Kasemann, M. Kramer, L. S. Legodi, S. A. Mao, K. Menten, I. Rammala, M. R. Rugel and G. Wieching
Monthly Notices of the Royal Astronomical Society, 536, 3647 (2025)

This chapter serves as a summary of the paper "A first glimpse at the MeerKAT DEEP2 field at S-band", Ranchod et al. (2025), originally published in Monthly Notices of the Royal Astronomical Society. The full paper is presented in its original form in Appendix E.

5.1 Paper summary

As demonstrated throughout this thesis, observations at S-band frequencies are have numerous advantages for both Galactic and extragalactic science. In 2023, S-band receivers built and designed at MPIfR were integrated into the MeerKAT telescope, the SKA-mid precursor array in the Northern Cape, South Africa. Over the past 7 years, MeerKAT has produced unprecedented results in L-band (875–1750 MHz) continuum imaging, due to its high surface brightness sensitivity and imaging fidelity, as well as its wide field-of-view. This has resulted in numerous discoveries in the structures and morphologies of radio galaxies (e.g. Ramatsoku et al., 2020; Cotton et al., 2020; Delhaize et al., 2021) and the statistical study of radio source populations (e.g. Matthews et al., 2021b; Hale et al., 2023). S-band frequencies (1750–3500 MHz) with MeerKAT offer a higher-resolution view of this, which not only allows for detailed studies of morphologically interesting individual galaxies and more reliable multi-wavelength counterpart cross-matching, but also has a significantly lower confusion limit than L-band, allowing for deeper observations (e.g. Mauch et al., 2020). In this chapter, we present MeerKAT S-band observations of the DEEP2 field, a radio-selected "empty" deep field. Due to the local sparcity of bright sources, this has been historically used as the optimal pilot field for MeerKAT commissioning. We present the first extragalactic deep field image with the S-band receivers, and in this chapter aim to demonstrate the performance of the MeerKAT S-band in the context of extragalactic wide-field imaging, and produce a catalogue of sources in the DEEP2 field at S-band.

We obtain observations of the DEEP2 field in the MeerKAT S1 (1968.75 - 2843.75 MHz) and S4 (2625.00 - 3500.00 MHz) subbands for $\sim$ 70 min on source integration time, respectively. We calibrate (primary- and self-calibration) and flag the data for RFI. After conducting an evaluation for the optimal Briggs robust weighting parameter R (Appendix B of this paper), we combine the S1 and S4 observations to produce a high resolution ($R = -0.5$) and lower resolution ($R = 0.3$) image with respective sensitivities of 7.5 and 4.7 μJy beam^{-1}. We note that the spectral windows above 3 GHz in the S4 band should be flagged for optimal image quality due to the primary beam squint effects at these frequencies.

After performing automated source-finding with PyBDSF, we detect 1199 sources in the $R = 0.3$ image, of which we find 1097 have matches in the L-band catalogue (Matthews et al., 2021b) with good astrometric accuracy. We compute the spectral indices of sources above 10σ, and find a median spectral index of $\alpha = -0.6$, as expected in the literature. We assess the completeness and purity of the catalogue by injecting simulated sources into our image and measuring the fraction of recovered sources. We are 99% complete for point sources above 5×10^{-5} Jy for $R = 0.3$ and 1×10^{-4} Jy for $R = -0.5$.

We provide some examples of extended sources resolved in our observations, in comparison to the L-band image. This illustrates that the higher resolution of S-band can better resolve AGN into multiple components, but does not recover diffuse emission as efficiently as at L-band, particularly with $R = -0.5$. However, we do successfully resolve diffuse emission in extended SFGs with $R = 0.3$.

As an assessment for the accuracy of MeerKAT S-band measurements in comparison to surveys in the literature, we compute the Euclidean-normalised differential source counts. Our source counts are consistent with both MeerKAT L-band counts, as well as deep S-band counts from the VLA-COSMOS 3 GHz survey. Furthermore, we use image-plane stacking to probe the undetected source population. By comparing the stacked flux densities to the expected flux density from L-band measurements, we derive lower limits for the source counts down to 10 μJy, which we find to also be consistent with the literature. These observations demonstrate that only a fraction of integration time is needed for comparable results with legacy S-band surveys, highlighting the potential for deep S-band surveys with MeerKAT and MeerKAT+.

This work was originally published as *A first glimpse at the MeerKAT DEEP2 field at S-band*, Ranchod et al. (2025) in Monthly Notices of the Royal Astronomical Society. This work was highly collaborative, with large fractions done by myself, J. D. Wagenveld and H.-R. Klöckner. As leading author of the paper, I wrote the majority of the manuscript. My contribution is as follows: cross-matching with L-band, and the discussion surrounding sources without matches (Section 3.2, Fig. 3), computing the multi-band spectral indices (Section 3.3.1, Fig. 4), examples of resolved sources (second half of Section 3.3.2, Fig 5.), completeness simulations (Section 4.1, Fig 7.), purity assessment (Section 4.2) and the stacking analysis (Section 4.3, Table 3).

CHAPTER 6

The MeerKAT+ S-band Legacy Survey

6.1 Introduction

The MeerKAT radio interferometer (Jonas and MeerKAT Team, 2016) is the South African mid-frequency precursor to the Square Kilometre Array (SKA), and will eventually be integrated into the SKA-MID AA4 (Sridhar et al., 2025). Since its first light in 2018, MeerKAT has produced unprecedented results across continuum imaging, spectral line and time-domain science areas, as highlighted in Chapter 5. A natural intermediary step between the exceptional standard set by MeerKAT and the next-generation SKA-MID, is the extension of MeerKAT into MeerKAT+.

MeerKAT+ began construction in 2023 and had its first light[1] in 2025. This expansion includes the addition of fourteen 15 m dishes to the MeerKAT array. The new dishes are jointly funded by the South African Radio Astronomy Observatory (SARAO), the Max Planck Society (MPG) and the Istituto Nazionale di Astrofisica (INAF). The MeerKAT+ extension, with a maximum baseline of 16 km, will return a factor of 2 higher angular resolution than MeerKAT, as well as a significant boost of sensitivity ($\sim 40\%$), improving calibration and image fidelity. This, in turn, will open up significant new science capabilities for MeerKAT+.

The MeerKAT+ partners will take part in a joint legacy programme, whereby 10% of the MeerKAT+ observing time will be reserved for legacy surveys, for which the data will be available to all partners. Criteria for such a legacy survey include the following: (i) considerations for the uncertain time available with MK+ before transitioning into SKA-MID, (ii) minimising the impact on existing MeerKAT projects, (iii) a matched scientific interest of South African, German and Italian communities, (iv) a legacy value that continues into the SKA-MID era, (v) science goals beyond what is possible with only MeerKAT.

In collaboration with the South African and Italian partners, we proposed the MeerKAT+ S-band Full Stokes Legacy Survey, a high-resolution, large-area, 15 μJy beam^{-1} of the southern sky. After the proposal submission in January 2024, our survey was officially selected as the favoured survey in August 2025, and observations will begin within the next two years. This chapter will serve as a summary of our submitted proposal (written in collaboration with S. A. Mao, R. P. Deane, H.-R. Klöckner and A.

[1] An initial image using the MeerKAT array and one additional SKA dish,

Ingallinera), as well as a detailed description of the calculations and simulations that I contributed in the writing of the proposal. My role in this project was to lead the preparation of the revised proposal, collating science contributions from the community to develop the science case. Calculations in this chapter were in part reproduced from an early iteration of the proposal (circa 2019) prepared by S. A. Mao and R. P. Deane, which I have updated in this work with the latest values and assumptions. Section 6.2 is an abridged science justification for the survey and in Section 6.3 we detail the survey design.

6.2 Science goals

This total intensity and polarisation survey will cover the southern sky at Dec $< -40^{\circ}$, corresponding to 7368 deg^2, making this one of the largest contiguous area survey conducted with MeerKAT or MeerKAT+. Through this, we aim to maximise the number of sources detected in total intensity and polarisation, allowing for robust statistical studies, as well as maximising the detection of sources in rare and exotic radio galaxy classes. The large area will enable a broad range of science possibilities covering areas such as magnetism, active galactic nuclei (AGN), galaxy evolution, large-scale structure and Galactic science. The higher angular resolution ($\theta \sim 1 - 2''$) and survey speed of MeerKAT+ provides a unique opportunity for a detailed view of the southern radio sky in S-band, that has not previously been possible with current interferometers and will not be surpassed by planned future interferometers, including SKAO. Figure 6.1 shows a comparison of this survey to other legacy and pre-SKA surveys, in terms of sensitivity σ, survey area and frequency band. This survey lies in the intermediary parameter space between the small area, deep-drilling surveys e.g. VLA-COSMOS (Smolčić et al., 2017a), MIGHTEE (Jarvis et al., 2016) and the shallow $\sigma \geq 100$ μJy beam^{-1} all-sky surveys e.g. NVSS (Condon et al., 1998), VLASS (Lacy et al., 2020). This large area, $\sigma \sim 10$ μJy beam^{-1} parameter space is also occupied by other SKA precursor surveys, while the MeerKAT+ S-band Legacy Survey stands to be the only extragalactic survey at S-band frequencies.

This survey will address a large range of science goals in total intensity and polarisation, across Galactic and extragalactic science area. Here, I will summarise only those that are relevant to the work in this thesis, and highlight how this survey can build on the results presented in Chapters 3, 4 and 5.

As introduced in Chapter 1, the extragalactic continuum sky at 10 μJy beam^{-1} sensitivity and S-band frequencies is dominated by the optically-thin synchrotron emission from star-forming galaxies, and a smaller percentage is made up of the synchrotron emission of active galactic nuclei (AGN) (e.g. Condon, 2015). There remain many unanswered questions surrounding evolution of AGN, particularly concerning the duty cycle of AGN, and characterising the different evolutionary phases of radio galaxies (e.g. Sabater et al., 2019; Bruni et al., 2020). The combined sensitivity and large area coverage of this survey will allow for a more complete census of AGN, including measuring the prevalence of less common sources, (e.g. giant radio galaxies, X- and S-shaped radio galaxies, compact steep spectrum sources, and GHz peaked-spectrum sources) and uncovering their evolutionary history (e.g. Collier et al., 2018). The proposed bandwidth of 875 MHz will provide broadband spectral energy distributions for extragalactic sources, allowing for a more accurate determination of spectral indices (Norris et al., 2013). We expect to detect 3.4×10^6 sources above 5σ in total intensity (see Section 6.3). We predict 20% of the detected population in total intensity to be (unresolved) star-forming galaxies, the most extreme of

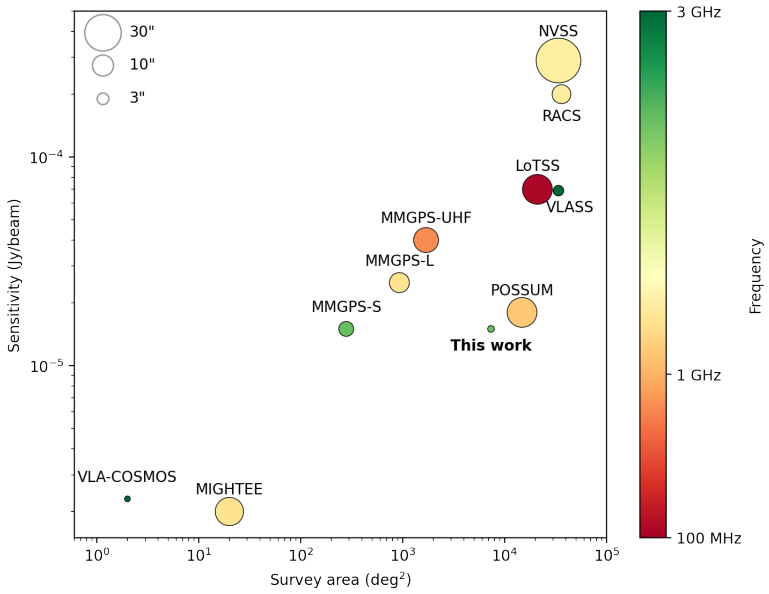

Figure 6.1: MeerKAT+ S-band Legacy Survey (bold) in comparison to other SKA-precursor surveys, in terms of area coverage and sensitivity. The markers are coloured according to the central frequency of the survey, and their sizes correspond to the angular resolution of the respective surveys.

which would extend out to redshifts of $z \sim 4$ (i.e. beyond the peak cosmic epoch of AGN/SF activity), with AGN up to $z \sim 10$. The redshift distributions of the AGN and star-forming populations are plotted in Figure 6.2, as determined from the SKA Design Study simulated skies (SKADS; Wilman et al., 2008). This legacy dataset will be further enhanced when combined with lower frequency broadband data from other MeerKAT and ASKAP surveys, enabling a detailed characterisation of broadband spectral energy distributions spanning up to 2 GHz, and the identification of complex features such as spectral curvatures and turnovers. Systematically classifying these sources based on their spectral properties will be a key diagnostic of the physical mechanisms of radio emission and developing more advanced K-correction methods, particularly since continuum radio observations can probe higher redshifts than in optical or infrared. Well-sampled radio spectral energy distributions significantly enhance easier identification of high-redshift sources, to be confirmed with follow-up spectroscopy. The high angular resolution of this survey opens a parameter space not available to existing MeerKAT surveys. This will improve our understanding of the duty cycle of AGN, and the formation of morphologically unusual galaxies (Cotton et al., 2020). High angular resolution is essential to probe small-scale structures in AGN jets, e.g. collimated synchrotron threads (Ramatsoku et al., 2020), wisps, and filamentary structures (Velović et al., 2023).

A key advantage of this survey is its unique perspective on cosmic magnetism. The high resolution and broadband S-band receiver allows for the exploration of polarised media that are otherwise undetectable (e.g. Arshakian and Beck, 2011). As I show in Chapter 4, the high resolution of the VLA-COSMOS survey favours the detection of resolved polarised sources, a result of mitigating the effect of beam depolarisation. In this sense, a high-resolution full-Stokes survey is important for maximising the polarised source counts. Furthermore, higher frequencies allow for the detection of polarised sources that would be depolarised by λ-dependent effects at lower frequencies, and will produce the largest

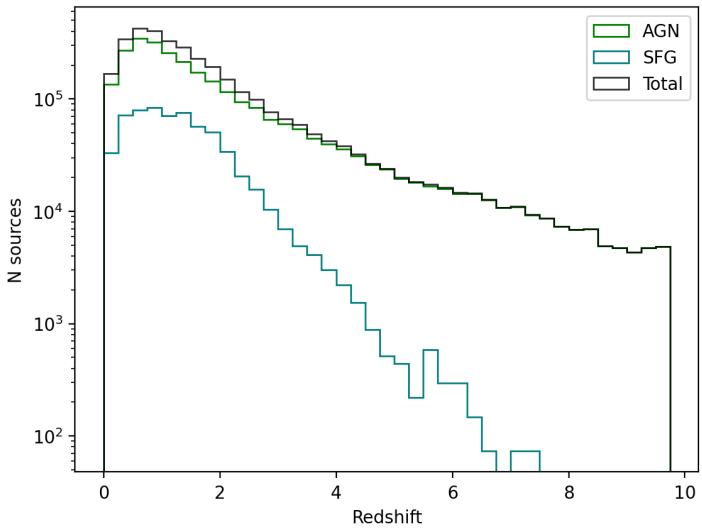

Figure 6.2: The redshift distribution of AGN and star-forming galaxies detectable at 5σ over the full survey area, as predicted from the SKADS simulations (Wilman et al., 2008).

broadband S-band polarisation catalogue of the southern sky. This new parameter space will include extremely turbulent astrophysical environments or sources that have extended structures in Faraday depth (scales < 263 rad m^{-2}), e.g. inner regions of jets, interiors of massive galaxy clusters. As shown throughout this thesis, the advent of broadband receivers in radio interferometers has transformed the field of cosmic magnetism, and has allowed for the better physical characterisation of polarised sources through methods such as QU-fitting and RM synthesis (see Chapter 2). The large predicted sample of $\sim 1.6 \times 10^5$ broadband Stokes Q and U spectra will allow for the direct classification of sources based on their observed Stokes QU spectra alone and to improve how $Q(\lambda^2)$ and $U(\lambda^2)$ have been modelled/fitted to date. This will provide a better understanding of the intrinsic properties of the polarised source population which will, in turn, allow for more refined RM grid experiments, e.g. constrained to only include Faraday simple sources, resulting a more accurate measure of foreground magnetised media. Observations at S-band frequencies also enable targeted RM grid experiments through extremely turbulent foreground screens (e.g. Milky Way, nearby galaxies and galaxy clusters). With complementary multi-wavelength data, we can build on the polarised source population characterisation in Chapter 4. As discussed, we require the detection of polarised sources over a large sky area for a statistically significant constraint on the dichotomy in fractional polarisation of radiative-mode and jet-mode sources. Furthermore, with a comparable angular resolution to the VLA-COSMOS, we will similarly be able to classify sources based on their Fanaroff-Riley morphology, but with comparably better sensitivity to diffuse emission due to MeerKAT+'s enhanced surface brightness sensitivity. Having a detailed source characterisation for such a large sample (more than three orders of magnitude larger than the VLA-COSMOS) will provide new insights into the driver of the flattening of cumulative source counts originally reported by Rudnick and Owen (2014). As described above for the continuum science case, this survey will be highly complemented by lower frequency observations of the same sky area. The POlarization Sky Survey of the Universe's Magnetism (POSSUM; Gaensler et al., 2025) will return Stokes Q and U spectra at ~ 1.2 GHz for the majority of detected sources. Jointly analysing these data will allow for a more detailed modelling of the frequency dependence of polarised sources for which we

laid the groundwork in Chapter 4. Constraining this frequency-dependence of polarised source counts in extragalactic fields, positions us to characterise the global depolarisation across statistically large samples of polarised sources, and investigate key turbulence scale in e.g. the Galactic plane and the intracluster medium of galaxy clusters.

As with the continuum science drivers, the high angular resolution of MeerKAT+ ($\theta \sim 1 - 2''$ at S-band) will give an unique view of polarisation in radio galaxies, revealing the physical processes driving the evolution and formation of features in the lobes and jets of AGN (e.g. Anderson et al., 2018; Baidoo et al., 2023), including the role of magnetic fields in AGN feedback, circular polarisation in AGN jets. Most polarised sources exhibit complex Stokes Q and U behaviours as a function of λ^2 which encode information on gas densities, magnetic fields and turbulence of the medium probed (see Chapter 2). As demonstrated in Chapter 4, since S-band data is less affected by λ-dependent depolarisation effects and is more sensitive to extended Faraday depth structures than L-band data, it serves as a superior anchor to the intrinsic polarisation properties of radio sources (e.g., intrinsic polarisation fraction, amount of internal depolarisation, number of unresolved polarised components, etc.). There are a plethora of important questions to be addressed with the MK+ S-band legacy survey data, including the characterisation of AGN feedback, interaction of radio lobes and their environments, and entrainment by modelling the spatially-resolved broadband polarisation behaviours of extragalactic radio sources. We note that published studies to date have focused mainly on the integrated polarisation properties of a few radio galaxies. The next major step, which this survey will accomplish, is a dramatic increase in the sample-size of spatially-resolved radio sources. As we show in Chapter 4, almost all spatially resolved sources were detected in polarised intensity, demonstrating that higher angular resolution is an effective strategy for mitigating beam depolarisation.

With the survey footprint covering a large region of the southern sky, it will naturally include a portion of the southern Galactic Plane ($260^\circ < l < 350^\circ$), a region that has not been studied in the same detail at GHz frequencies as its northern counterpart. The high resolution of the MeerKAT+ S-band legacy survey will enable a large range of Milky Way science in both total intensity and polarisation. This will facilitate the detailed mapping of discrete Galactic objects, such as supernova remnants, HII regions, pulsar wind nebulae, planetary nebulae. It will also allow for the search for faint polarised point sources, that can be targeted as pulsar candidates (e.g. Frail et al., 2024). We can use the broad bandwidth for more constrained spectral index and rotation measure maps of such objects to better understand the local plasma conditions their spatial variations across these objects.

We aim to exploit the MeerKAT+ sensitivity for detailed modelling of the large- and small-scale Galactic disk and halo magnetic fields, introduced in Chapter 1. As discussed in the previous section, the Galactic RM grid density will be significantly improved with this survey, and can be used to enable a better understanding of the foreground Galactic Faraday screen, particularly for characterising Faraday thick structures. The increased density and quality of the RM values through the Milky Way can contribute to the global mapping and statistical analysis of the Galactic magnetic field with information field theoretical methods (e.g. Hutschenreuter et al., 2023). With the survey's sensitivity to extreme Faraday depths, one can also hunt for extreme Faraday depths produced in the Milky Way and better understand their origin (e.g. Shanahan et al., 2019), with the improved statistics this survey will provide. At S-band, we can observe turbulent regions of the Galactic plane that are completely depolarised at L-band frequencies, to understand the small-scale structure and turbulent scales within the plane,

through the computation of the RM structure function and via the depolarisation effects of individual sources to probe even smaller scales of turbulence (e.g. Livingston et al., 2021). This survey will cover almost the entire Galactic longitude range observed in Chapter 3, including the Norma, Inner Perseus and Inner Sagittarius spiral arm tangents (Vallée, 2014). With a factor of 6 times better sensitivity, we expect to detect 1.8×10^4 polarised sources within this Galactic plane area alone (see Section 6.3). By conducting the Faraday complexity analysis presented in Chapter 3 for this large background sample, we can constrain the physical extent of the turbulent magnetic field within the spiral arms. Similar analyses can be used to study other prominent Galactic features, e.g. the Gum Nebula, the southern extension of the Fermi bubbles (Planck Collaboration et al., 2016), leading to the development of advanced methods for characterising Galactic magnetic field turbulence.

6.3 Survey design

In this section, we outline the survey design and provide a motivation for the selected survey sky coverage and frequency band (Section 6.3.1) to maximise the legacy survey goals. As discussed in Section 6.1, the conditions of the Legacy survey programme require the survey to be flexible in its design, and have guaranteed scientific output regardless of its completion. With MeerKAT+ still under commissioning, and at the time of this proposal, still under construction, a number of assumptions are required with regards to the performance of the heterogeneous array. Here, we derive possible survey design parameters of the MK+ S-band legacy survey. We make the following assumptions in these calculations:

- There are 13 SKA dishes of 15.8 m diameter, with 60 MeerKAT dishes in the case of the “all-80", and 51 MeerKAT for the “any-64" correlator. Note, that since these calculations were made, the number of SKA dishes has been increased to 14.
- We assume 3000 hours of on-source time will be available for the legacy project, with 500 hours per year. This is as specified in the White paper[2], with the optimistic assumption that MeerKAT+ will be online for 6 years before being incorporated into the SKA.
- All calculations are made for the S1 sub-band 1968.75 – 2843.75 MHz.
- 16% flagging in the S1 band due to RFI, as found in our science verification observations of the DEEP2 field with the MeerKAT S1-band presented in Chapter 5. We argue that this assumption is conservative given the tendency of RFI to de-correlate on longer baselines.
- We include an additional 10% overhead for antenna settling time and slewing time, and potential data corruption/capture issues.
- We assume natural weighting, corresponding to a penalty factor of one for all sensitivity calculations.
- We assume an array efficiency of 75%.

A given limitation for the early operating period is the 64-dish correlator. For an uncertain period, the array will make use of the MeerKAT correlator (“any-64”), that can only correlate the response of up to 64 dishes. However, this can include any combination of dishes, including the SKA dishes. Throughout

[2] https://www.meerkatplus.tel/documents/

this section, we will calculate all relevant quantities for both the “any-64” or “all-80”[3] setups.

The system equivalent flux density (SEFD) of the heterogeneous MK+ array is calculated as specified in the recipe on the MeerKAT+ website[4]. The SEFD of the MeerKAT S-band is 426 Jy, and the SEFD of the MeerKAT+ S-band is 312 Jy. We determine the average SEFD, weighted by the number of baselines containing MeerKAT antenna pairs, SKA antenna pairs or MeerKAT-SKA pairs. The average SEFD is 402 Jy for the “any-64" correlator and 405 Jy for the “all-80" correlator (cf. SEFD ∼ 450 Jy for MeerKAT S1).

The survey area will be covered using a standard hexagonal mosaic pattern with pointing separation $\theta_{\rm hex}$,

$$\theta_{\rm hex} = f\theta_{\rm PB}, \tag{6.1}$$

where $\theta_{\rm PB}$ is the primary beam FWHM and f is the separation factor. In this section, we will conduct simulations to optimise f in terms of integration time, sensitivity and number of pointings. The effective mosaic beam size Ω_B is computed as,

$$\Omega_B = \pi\theta_{\rm PB}^2 \ / \ 8\ln 2. \tag{6.2}$$

We assume the $\theta_{\rm PB}$ for the high-frequency end of the band, for a more conservative estimate of the sensitivity. Here, we take the maximum frequency to be 2.75 GHz, as band edges will be flagged above a threshold SEFD. The variability of the MeerKAT S-band SEFD is addressed in Chapter 5, and illustrated in Figure A1 in Appendix E. We emphasise that this is a conservative estimate and with a more uniform bandpass, we can expect a fractionally larger usable bandwidth. We assume the primary beam of the MeerKAT+ array to be smaller than that of MeerKAT, due to the response of the larger diameter SKA dishes. We therefore optimise our survey design based on the SKA-mid prototype dish primary beam response, rather than a weighted averaged between MeerKAT and SKA dishes, consistent with the conservative approach taken throughout. From measurements with the SKA-MPI prototype dish (F. Jünemann, priv. comm.), we expect a primary beam with FWHM = 0.501 deg and a diameter of 1.004 deg at 5% of the primary beam power, measured at 2.75 GHz. The total survey area $A_{\rm survey}$ that can be covered in T hours is:

$$A_{\rm survey} = \left(\frac{12\sqrt{3}\ln 2}{\pi}\right) 2^{\frac{-8f^2}{3}} f^2 T\Omega_B \ / \ t_{\rm eff}\ {\rm deg}^2, \tag{6.3}$$

where each mosaic pointing has an effective integration time of $t_{\rm eff}$. Therefore, given a fixed area to cover for the survey and a fixed total time of T hours, one can determine the effective integration time (not to be confused with the actual integration time per discrete mosaic pointing) using the above equation. Here, T takes into account the increase of sensitivity achieved from the overlap of adjacent pointings in a

[3] At the time of writing, it was not confirmed exactly how many additional dishes would be part of the MeerKAT+ array. The “all-80” assumption was assumed based on the briefing the the Legacy Survey programme. As of October 2025, there will be 78 dishes in total. Please note that all “all-80” calculations assume 80 dishes.

[4] https://www.meerkatplus.tel/

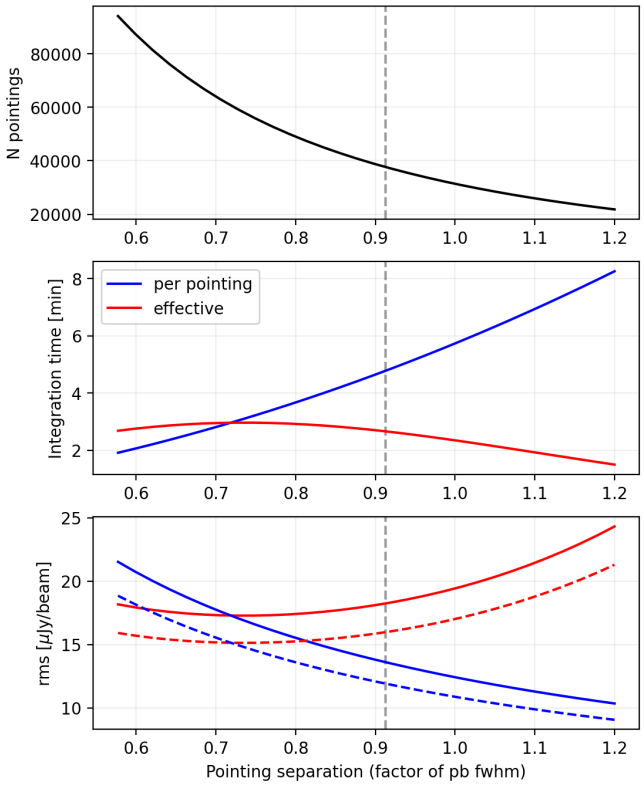

Figure 6.3: The predicted number of pointings (top), integration time (centre) and sensitivity (bottom) as a function of pointing separation factor f. The effective integration time and sensitivity is shown in red and the per pointing integration time and sensitivity is shown in blue. The dashed lines in the sensitivity plot assume the "all-80" correlator and the solid lines assume "any-64". The dashed vertical line shows the separation factor of $f = 0.913$.

mosaic. We calculate the sensitivity of the survey σ as the thermal noise, given as

$$\sigma = \mathrm{SEFD}_{\mathrm{MK+}} \,/\, A_{\mathrm{eff}} \sqrt{N_{\mathrm{pol}} N_{\mathrm{tot}} (N_{\mathrm{tot}} - 1) \Delta\nu t_{\mathrm{eff}}}, \tag{6.4}$$

where A_{eff} is the array efficiency, N_{pol} is the number of polarisations, N_{tot} is the total number of baselines, $\Delta\nu$ is the bandwidth and $\mathrm{SEFD}_{\mathrm{MK+}}$ is the SEFD of the heterogenous array, as described above. We conservatively assume that only 77% of the recorded visibilities are usable due to RFI excision or integration time lost due to antenna settling, and we assume an array efficiency of 0.75. The N_{pol} is two and the bandwidth of the S1 subband is 875 MHz.

Given that the primary beam area is smaller for the heterogeneous MeerKAT+ array than for MeerKAT, it will be less effective in survey speed. We therefore consider a range of separation factors f to minimise the number of pointings while still achieving a reasonable integration time per pointing and achieving our sensitivity goals. For the full sky area of 7368 deg^2, we determine the effective number of pointings as

$$N_{\mathrm{eff}} = A_{\mathrm{survey}} \,/\, \Omega_B = 55405. \tag{6.5}$$

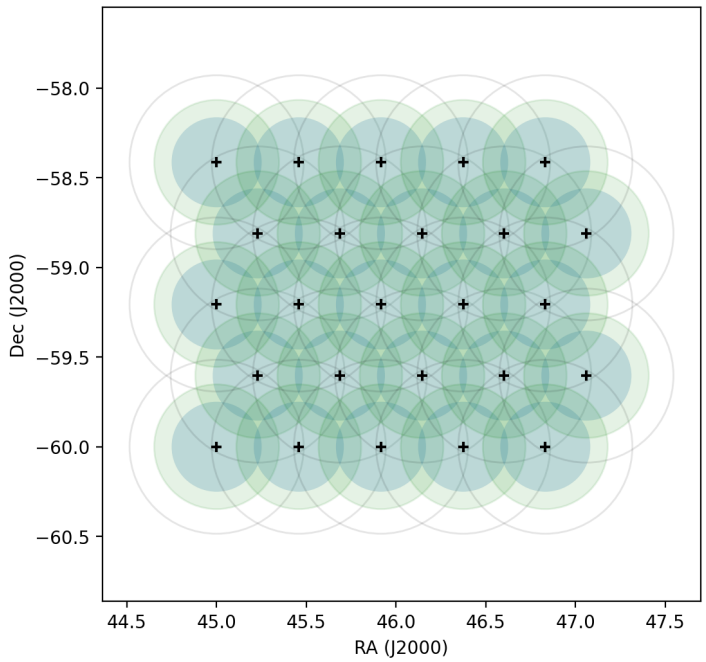

Figure 6.4: An example of the pointing layout for the S-band Legacy survey. The pointing centres are indicated with black crosses, the light blue circles show the region within the FWHM of the primary beam at 2.75 GHz, the light green circles show the region within the FWHM at 1.98 GHz, and the grey unshaded circles show the 5% power of the primary beam at 2.75 GHz.

Figure 6.3 shows an estimate for the number of pointings, the integration time and sensitivity as a function of the pointing separation factor f. Prioritising uniform sensitivity across the survey would require a smaller separation between pointings, e.g. $f = 1/\sqrt{3}$ (lower limit of Figure 6.3), however, a per-pointing integration time of ~ 2 minutes becomes less efficient when considering telescope settling time and slew time. Considering the relevant trade-offs, we opt for a larger pointing separation to prioritise per-pointing integration time and uv-coverage, setting a lower limit for integration time at 4.5 min. This results in a separation factor of $f = 0.913$. An example of the pointing gird is shown in Figure 6.4. With this pointing configuration we require ~ 6 pointings per square degree. This configuration allows for full area coverage within the primary beam FWHM up to a frequency of 2.65 GHz. The limitations of the pointing configuration will be discussed in Section 6.3.1. All survey parameters defined in this section and calculated for the above pointing configuration are summarised in Table 6.1. The survey parameters calculated here were an estimate required for the approval of the proposal, and will be a first step towards a more concrete survey design once telescope commissioning has completed. Given the conservative nature of the assumptions described above, we expect to fine-tune these parameters based on real data and its achieved performance following test observations.

We then estimated the expected total intensity source counts for different source populations and their redshift distribution using the SKADS simulation (Wilman et al., 2008). Considering our predicted effective sensitivity for the “any-64" correlator, i.e. $\sim 18\ \mu\mathrm{Jy\,beam}^{-1}$ and $T_b = 0.95$ K, we expect to detect $\sim 3.4\times10^6$ sources above 5σ in total intensity. For a conservative estimate, we assume only point

Table 6.1: Survey design parameters

Total integration time (per year)	3000 (500) hours
Effective integration time	2.66 min
Effective sensitivity - “any-64"	18.2 μJy/beam
Effective sensitivity - “all-80"	15.1 μJy/beam
Per-pointing sensitivity - “any-64"	14.5 μJy/beam
Per-pointing sensitivity - “all-80"	12.7 μJy/beam
Number pointings (per year)	42881 (7147)
Integration time per pointing	5.04 min
Distance between pointings	0.44 deg

source SFGs, and both point source and extended AGN. We further estimate the expected polarised source density and source count by assuming the L-band polarised source count in the literature. In doing so, we implicitly assume that, when extrapolating the polarised flux from L- to S-band, spectral index effects are fully compensated by the reduction in λ-dependent depolarisation effects going from lower to higher frequencies[5]. The total number of polarised sources N_P for L-band (Rudnick and Owen, 2014) above a detection threshold ($\geq 5\sigma$) expected for a survey covering $A_{\rm survey}$ deg^2 with a sensitivity of σ Jy is,

$$N_P = A_{\rm survey} \times 45.0 \left(\frac{5.0 \times 10^6 \sigma}{30.0} \right)^{-0.6} . \tag{6.6}$$

Based on the above, we expect a total number of $\sim 1.6 \times 10^5$ polarised sources for a 7368 deg^2. This yields an RM density of 23 deg^{-2}.

6.3.1 Sky coverage and frequency selection

A key motivation of this Legacy survey is to maximise the number of detected sources by maximising the sky coverage. This, in turn, maximises the discovery potential, the synergy with multi-wavelength catalogues and community engagement. A wide, shallow survey is favourable over a medium-area, medium-depth survey, e.g. a 3000-hour survey over 7368 deg^2 will yield a factor ~ 3.5 increased number counts than a survey with the same total integration time over 1000 deg^2.

To maximise the survey area, a sparse pointing coverage is required, which raises the following limitations. Figure 6.5 shows the RMS map of our MeerKAT S1-band observations of the DEEP2 field, presented in Chapter 5. This map has been primary-beam-corrected, and cropped at 5% of the primary beam power response. The RMS at the pointing centre is $\sigma = 10$ μJy beam^{-1}, representative of the approximate RMS of our survey observations. The lower panel shows a cross-section of the RMS map, scaled to the dimensions of the primary beam model from the SKA-MPI dish at 2.8 GHz. The lighter shaded regions correspond to the maximum radius to the adjacent pointing, given the pointing

[5] We note that these calculation were done before the results from Chapter 4 were obtained, and we therefore did not use the source counts expression presented in that chapter for an updated prediction at S-band frequencies. Following the consistency between our results in Chapter 4, and the source counts from Rudnick and Owen (2014), computed at 1.4 GHz, our assumption here holds for the purpose of this chapter.

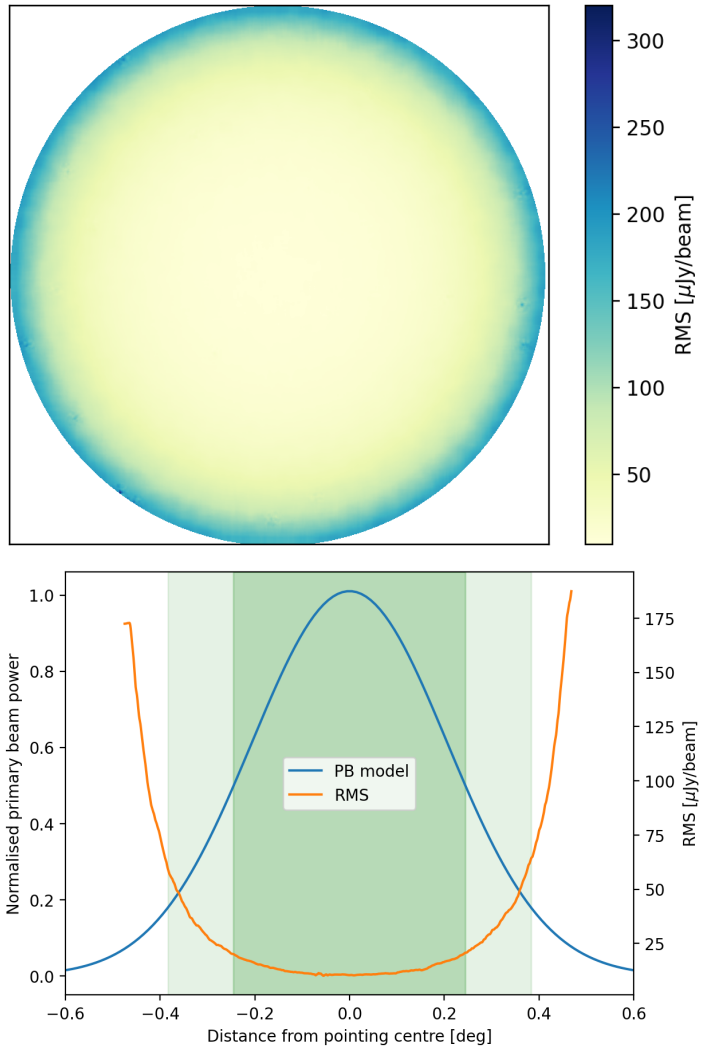

Figure 6.5: Top: An RMS map for the primary-beam-corrected image of the DEEP2 field with the MeerKAT S1 band. Bottom: A cross section of the DEEP2 RMS map (orange), scaled to, and plotted with the primary beam model from the SKA-MPI dish at 2.8 GHz (blue). The darker shaded region shows the FWHM of the primary beam, and the lighter shaded regions correspond to the maximum radius to the adjacent pointing, given the pointing configuration in Figure 6.4.

configuration in Figure 6.4. As shown, the RMS increases rapidly at this radius. Considering the overlap, we would expect an effective sensitivity of ~ 37 μJy beam^{-1}. The increased RMS in these regions (i.e. beyond this radius), will hamper the uniformity of the survey, and decrease survey completeness. By prioritising the survey area coverage, we will have a lower sensitivity at the high frequency end of the band. However, at the low-frequency end of the band, we have $f \sim 1/\sqrt{2}$, which is sufficient for near-uniform coverage. This limitation, and the associated systematic effects will be taken into account when assessing completeness and creating catalogues, e.g. an upper frequency limit for polarisation products. To compensate for these limitations, the individual pointings will also be made available for all data products for science areas that require deeper observations. As introduced in Chapter 5, the MeerKAT S-band consists of five overlapping frequency sub-bands, each with an instantaneous bandwidth of $\Delta\nu$ = 875 MHz. Another key aspect of the survey design, was the selection of which sub-band to conduct the survey with. As previously stated, the survey will be conducted in the S1 sub-band (1968.75 – 2843.75 MHz). This will maximise the overlap between pointings due to the increased field-of-view. It will also ensure higher complementarity with SKA-MID band 2 surveys, as well as precursor L-band surveys with MeerKAT and POSSUM, ensuring a more continuous frequency coverage with these instruments. This is essential for polarimetric studies, reducing artefacts and sidelobes in Faraday spectra produced combining both frequency bands.

6.4 Conclusion

In this chapter, we present a summary of the proposal for the recently accepted MeerKAT+ S-band Full Stokes Legacy Survey. This will be a large area Galactic and extragalactic survey of the southern sky at Dec $\leq$-40° with the upgraded MeerKAT array. With the combination of the 15 μJy beam^{-1} sensitivity, 1 arcsec resolution and enhanced imaging fidelity of MeerKAT+, we aim to provide a definitive census of this relatively unexplored part of the sky. This will result in transformative statistical insights and individual discoveries from within our Galaxy to the distant Universe, addressing a broad range of science cases including, but not limited to, galaxy evolution and cosmic magnetism.

CHAPTER 7

Conclusion

In this final chapter, I will summarise the results presented in Chapters 3, 4 and 5, and place them in context of the broader research area introduced in Chapter 1. Here, I will also discuss the important technical takeaways found throughout this thesis work. In Section 7.2, I will outline how the research presented here can be continued in the following years, particularly regarding modern radio surveys in the pre-SKA era. Lastly, I will conclude in Section 7.3 with final remarks.

7.1 Summary

Magnetic fields permeate the Universe at all scales, fundamentally influencing the evolution of galaxies. Their role in star-formation, cosmic-ray propagation and galaxy kinematics has been an active field of research over the past half-century, for which radio astronomy has facilitated significant advancements. The observation of linearly polarised, synchrotron-emitting sources at radio frequencies can be used to study the magneto-ionic properties of both the emitting source (typically AGN) and any intervening media (e.g. the Milky Way ISM). By maximising the number of detected polarised sources across a sky region, we can conduct RM grid experiments to map out the strength and geometry of the foreground magnetic field.

As the μJy radio sky becomes readily more accessible with new generation radio interferometers, the number counts of polarised EGSs will increase, expanding to include fainter AGN populations, and begin exploring star-forming galaxies at cosmologically significant distances. As such, it is essential to characterise the faint polarised source population, in terms of both their physical properties, and their associated Faraday complexities to accurately constrain models of the foreground Milky Way magnetic field. In turn, accurate, high resolution Galactic RM models are required for subtracting the foreground Faraday depth component when studying the intrinsic magnetic field properties of external galaxies. In this thesis, I address both of these factors: a) a characterisation of the polarised extragalactic source population, as well as b) an investigation into the Faraday complexities present when probing the Milky Way magnetic field, and how this can be used to quantify small-scale magneto-ionic turbulence in the Milky Way.

In Chapter 3, we reported an increase in the Faraday complexity of polarised EGS towards the

Galactic plane (i.e. $b = 0^\circ$) in the S-band Polarisation All Sky Survey (SPASS/ATCA) RM catalogue (Schnitzeler et al., 2019). Given the important legacy value of this catalogue, particularly its dominance in the Galactic Faraday Sky reconstruction (Hutschenreuter et al., 2022) at Dec $\leq -40^\circ$, it is essential to characterise this systematic trend to understand and rectify any biases that it may contribute. To investigate this, we conducted new, higher resolution, broadband (1.1–3.1 GHz) observations of 105 SPASS/ATCA sources surrounding the Galactic plane with the ATCA. Through these observations, we aimed to filter out the smoothly-varying, large-scale polarised emission from the Galactic plane, and investigate if contamination from this emission is the sole contributor to the Galactic latitude dependence of Faraday complexity, or if this is rather a physical effect introduced by small-scale turbulence in the Galactic ISM. By conducting QU-fitting on the spectra, we quantified the complexity as done in S19 (i.e. by the number of emitting components n within the beam volume), and found an overall decrease in Faraday complexity in our follow-up observations, with an average $|\Delta n| = 1.1$. In our observations, we found that we no longer observed the increase in complexity at $|b| < 10^\circ$, but rather a constant degree of complexity at up to $|b| > 2^\circ$, clear evidence that this increase was attributed to contamination by diffuse Galactic emission in S19. While this indicates a limitation of the S19 catalogue (as well as important technical implications regarding the filtering of diffuse emission, which I will discuss in Section 7.1.1), we find that 94% of RMs (or peak Faraday depths) reported in the S19 catalogue are reliable, confirmed through RM synthesis. We conduct further analysis into the origin of Faraday complexity in our sources that show $n > 1$. While we cannot confirm if this complexity is extragalactic in origin due to small number statistics, we report a relative increase of Faraday complex sources surrounding the Crux-Centaurus, Norma, Inner Perseus and Inner Sagittarius spiral arm tangents, as well within $\Delta l \leq 5^\circ$ of the Galactic centre. We suggest that this is attributed to small-scale turbulence (2.4 pc at a 4 kpc distance) in the Galactic ISM, consistent with the structure function results of Haverkorn et al. (2008, see Section 7.2.2), or small-scale patchy polarised synchrotron emission in the spiral arm regions. These results present the first indication of small-scale structure in the Milky Way spiral arms revealed through Faraday complexity, highlighting the importance of broadband spectro-polarimetric observations to fully characterise small-scale and/or turbulent structures in the Galactic magnetic field.

From an extragalactic perspective, in Chapter 4 I present the linear polarisation component of the VLA-COSMOS 3 GHz Large Project (Smolčić et al., 2017a). The source population in this field has been extremely well characterised in total intensity due to the combined depth and angular resolution of the observations, and its rich multi-wavelength coverage. In this work, I reprocessed the data, including polarisation calibration and imaging, to produce the linear polarisation data release of this survey and conduct a comprehensive study into the polarised source population. With a sensitivity of 2.6 μJy beam^{-1} in the Faraday depth domain, and an empirically determined detection threshold, I detected 65 polarised sources. While this chapter contains a broad range of results concerning polarised source counts and the nature of the faint polarised population, here I will summarise three findings that address prominent open questions in the literature: (i) Despite the advantages of polarisation studies at 3 GHz, as highlighted throughout this thesis, this parameter space has been relatively unexplored, and the expected polarised source counts at 3 GHz is therefore unconstrained. In this work, I produce the deepest polarised source counts at 3 GHz, down to $P_{3\ \mathrm{GHz}} = 15\ \mu$Jy beam^{-1}, and the second deepest overall (cf. Loi et al., 2025). My key finding is that the faint polarised source counts at 3 GHz are consistent with those at 1.4 GHz, an effect of the λ-dependent depolarisation counteracting the ν-dependent spectral index. Through QU-fitting, I establish that the dominant cause of depolarisation in this case is differential Faraday rotation (i.e. Burn slab depolarisation) in the radio lobes of AGN, as found in 28% of polarised

sources. An important implication of these results is that S-band (∼3 GHz) surveys are as effective as L-band (∼1.4 GHz) in computing the RM grids in extragalactic deep fields in terms of expected source counts, with the caveat of slower survey speed. (ii) Simulations predict that SFGs have higher expected fractional polarisations at higher frequencies, and therefore with this deep 3 GHz survey I attempt to uncover the previously undetected faint polarised SFG population. Based on their multi-wavelength properties, I found that all detected polarised sources are classified as AGN and that we do not detect any SFGs down to $P_{3\ \mathrm{GHz}} \geq 15\ \mu\mathrm{Jy\ beam}^{-1}$. From this, I compute an upper limit on the density of polarised SFGs to be $< 0.58\ \mathrm{deg}^{-2}$, with the unfavourable implication that surveys much deeper than 2.6 μJy beam^{-1} are required to readily detect polarised SFG sources, even at S-band frequencies. This conclusion is associated with the caveat of the lower surface brightness sensitivity of VLA A-array observations in comparison to SKA precursor telescopes. (iii) While the dichotomy between the intrinsic fractional polarisation of radiative-mode and jet-mode AGN has been established in the literature, and has been suggested as a driver of the anti-correlation between total intensity and fractional polarisation, this has been limited to targeted studies of bright polarised sources $P > 2$ mJy. Although this anti-correlation has been disputed by other deep polarisation surveys, it has not been investigated regarding the AGN dichotomy. In this work, I did not find a clear dichotomy in the fractional polarisation between these AGN populations, and similarly, find no anti-correlation. I suggest that this is a selection bias of deep surveys, due to their typically small sky areas. This highlights the requirement for deeper, large area surveys to fully understand this trend.

Chapter 5 describes a science demonstrator project of the recently installed S-band receivers on MeerKAT. Here, we present the first extragalactic deep field image with the MeerKAT S-band receivers to demonstrate the performance of this new instrumentation in the context of extragalactic wide-field imaging. With only a combined 140 min on-source integration time across the S1 and S4 sub-bands, we achieve a sensitivity of 4.7 μJy beam^{-1}, combining both sub-bands. Our results show consistent Euclidean-normalised source counts with those in the literature, including the total intensity source counts in the VLA-COSMOS 3 GHz survey (Smolčić et al., 2017a). These observations demonstrate that only a fraction of integration time is needed for comparable results with legacy S-band surveys, highlighting the potential for deep S-band surveys with MeerKAT and MeerKAT+.

7.1.1 Technical comments

In addition to the scientific results summarised above, I would like to highlight key technical insights from this thesis as recommendations for future work.

Firstly, regarding the contamination of diffuse emission in Faraday complexity studies. In Chapter 3, we attempt to filter out large-scale, diffuse polarised emission through higher angular resolution observations. With the 6 km configuration of the ATCA, not only do our observations have higher angular resolution, but we are also sensitive to a smaller maximum angular scale of emission. An important conclusion from this work is that it is essential to remove the foreground diffuse emission for polarisation studies, particularly regarding the study of polarised EGSs. While the effect of such contamination will be less pronounced for interferometric arrays with low surface brightness sensitivity and less compact configurations (e.g. ATCA 6 km, VLA A-array), we emphasise that this needs to be carefully handled for observations with SKA precursor telescopes MeerKAT and ASKAP, where their surface brightness sensitivities have been optimised in their design (e.g the compact core of MeerKAT's array configuration).

Recently, the early science polarisation data release for the MeerKAT MIGHTEE survey (Taylor et al., 2024) has shown large-scale diffuse polarised emission across the XMM-LSS field ($b \sim -59^\circ$), which they perceive to be Galactic in origin, emphasising that the contamination of diffuse Galactic emission needs to be considered, even at high Galactic latitudes. Similar results have recently been reported in POSSUM early science (Vanderwoude et al., 2024, see Section 7.2.1) and targeted VLA D-array configuration observations (Ma et al., 2025), where they effectively subtract the diffuse foreground using a median filter and as approximated within an annulus around the target source, respectively.

In Chapter 4, we find that we preferentially detect large, extended sources in polarisation, even with respect to point sources with higher peak polarised intensities. Although this has previously been noted in the literature for smaller areas (e.g. Grant et al., 2010; Rudnick and Owen, 2014), I emphasise the advantage of high angular resolution $\theta \leq 2''$ observations to maximise faint polarised source detection. While this is naturally an effect of beam depolarisation in unresolved sources, Grant et al. (2010) also attribute this to angular structure of polarised emission in radio lobes being typically of $1''$ scale. In addition, our results demonstrate difficulties in reconciling the integrated polarised intensity between resolved and unresolved sources due to the difference in degree of beam depolarisation. Given the high angular resolution of future pre-SKA surveys, particularly the MeerKAT+ S-band Legacy survey, I recommend that further investigation into these biases is required for a more meaningful interpretation of polarised source counts.

7.2 Outlook

7.2.1 New generation radio surveys

In Chapter 6, I introduce the MeerKAT+ S-band Legacy survey, which stands to be a transformational addition in the study of cosmic magnetism as we transition into the SKA era. In addition to this, three ongoing pre-SKA surveys, the POlarisation Sky Survey of the Universe's Magnetism (POSSUM; Gaensler et al., 2025), Spectra and Polarisation in Cutouts of Extragalactic sources in the Rapid ASKAP Continuum Survey (SPICE-RACS; Thomson et al., 2023) and the MPIfR MeerKAT Galactic Plane Survey (MMGPS; Padmanabh et al., 2023) will dramatically increase the density of RMs in the southern sky, a contribution that will revolutionise our view of the Galactic magnetic field. As I will detail in this section, these surveys are being observed using modern broadband receivers, allowing for robust characterisation of the Milky Way magnetic field through Faraday complexity analyses. Below, I will detail the specifications of the MMGPS, POSSUM and SPICE-RACS surveys (summarised in Table 7.1), and in the following sections I will discuss how these surveys can be used to further the research presented in this thesis.

The MMGPS is a $\sim$ 3000 hour full-Stokes MeerKAT survey conducted over UHF- (554–1088 MHz), L- (856–1712 MHz) and S1- (1968–2844 MHz) bands. The area coverage of the respective bands is plotted in Figure 7.1. This survey also consists of a Galactic centre component, where 200 hours are dedicated to observing the Galactic centre at the S4-band (1969–3500 MHz), with the primary goal of detecting a pulsar in the vicinity of Sagittarius A*. This survey is currently achieving sensitivities on par with its theoretical predictions, i.e. 22, 14, and 9 μJy beam^{-1} for UHF-, L- and S-band respectively. It is set to produce an RM density of $\sim$ 40 deg^{-2} in the dense, turbulent near-plane ($|b| < 2^\circ$) region covered by the S-band (priv. comm. A. Basu), and detect of order 25 000 background RMs overall. This

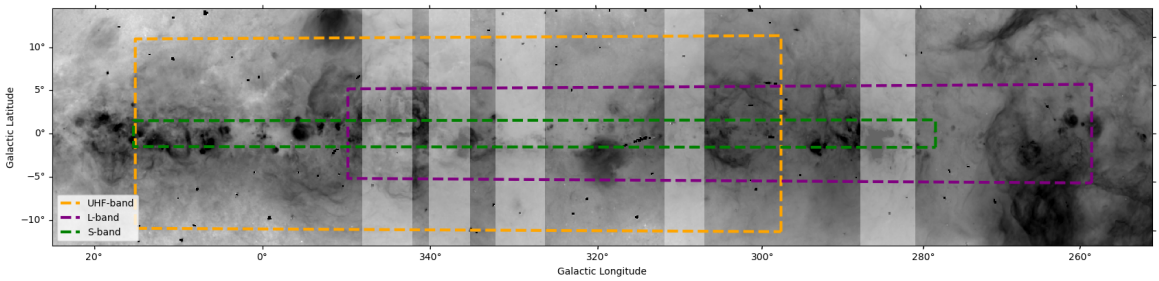

Figure 7.1: Sky coverage of the MMGPS survey, overplotted on the Southern H-Alpha Sky Survey Atlas (SHASSA; Gaustad et al., 2001) Hα map. The UHF-band (orange), L-band (purple) and S-band (green) are indicated by the dashed outlines. The white horizontal stripes show the spiral arm tangents. Image credit: Y. K. Ma.

quasi-continuous bandwidth from 554–2844 MHz ($\Delta\nu$ = 2290 MHz) in the southern Galactic plane is a totally unexplored parameter space, and will benefit from both the high Faraday depth resolution afforded by the low frequency domain, as well as the sensitivity to Faraday thick structures and regions associated with strong foreground depolarisation at the high frequency end. While a key aim of the survey is to map out the Galactic magnetic field, particularly in the fourth Galactic quadrant ($270^\circ < l < 360^\circ$), it will address other prominent questions in the field of Galactic magnetism, such as the origin of extreme RMs in the spiral arm tangents, and the extent of field reversals in the Galactic plane. This survey will also provide a census of the HII regions and supernova remnants in the southern Galactic plane to inform future electron density models (e.g. Ocker et al., 2024), required to disentangle the magnetic field contribution from RM values.

POSSUM is an ongoing large area (20 630 deg^2) Stokes I, Q and U survey of the entire southern sky (Dec $\leq 0^\circ$) using ASKAP. This survey is being conducted at L-band (800–1088 MHz and 1296–1440 MHz) down to a target sensitivity of 18 μJy beam^{-1} and an angular resolution of $\theta = 20''$. With the primary aim of providing a dense, wide-area RM grid with high Faraday depth resolution (~ 1 rad m^{-2}), this survey expects to detect of order 1 million linearly polarised sources in the southern sky. While this survey will revolutionise our understanding of the Galactic magnetic field structure, similar to as described above for MMGPS, its large-area coverage will also enable individual and statistical studies of the extragalactic source population. This dense RM grid will illuminate the foreground magnetic field structures of resolved nearby star-forming galaxies, the Magellanic clouds, the intergalactic medium of galaxy groups, clusters and cosmic web filaments, the latter of which have previously been limited to statistical stacking approaches. The high-resolution mapping of such structure will address key open questions in extragalactic magnetism, such as the origin of galaxy cluster magnetic fields, the geometry and extent of galaxy magnetic fields into the circumgalactic medium, and provide new constraints on the plasma conditions in magneto-hydrodynamical simulations.

SPICE-RACS is the other major polarisation survey with ASKAP. With a similar angular resolution to POSSUM ($\theta = 20''$), this survey aims to cover a larger sky area of 36 000 deg^2 (87% of the sky) down to a comparatively lower sensitivity of ~ 100 μJy beam^{-1}. The primary aim of this survey is to produce an all-sky RM grid, with a density of 7 deg^{-2} (see Figure 7.2), a factor of 7 denser than what

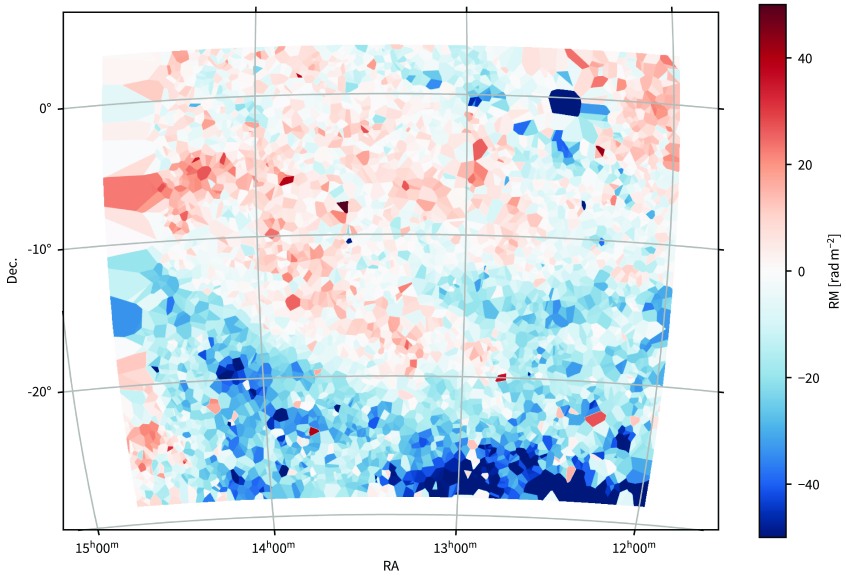

Figure 7.2: The RM grid of the Spica Nebula region, directly reproduced from the SPICE-RACS DR1 paper (Thomson et al., 2023). The authors produce this continuous map using a nearest-neighbour interpolation.

is currently available (Van Eck et al., 2023). While not as deep as the above-mentioned surveys, this survey has the advantage of faster observations and processing speed (e.g. less integration time and data volume). With the the next data release expected in 2025, it will already be the next step in improving our understanding of the large-scale Galactic magnetic field structure.

In contrast to the work presented in this thesis, which we conduct at S-band frequencies, POSSUM and SPICE-RACS are L-band surveys. Our results in Chapter 4 show that we expect consistent source counts between L-band and S-band surveys in extragalactic fields. However L-band offers the particular advantage of higher angular resolution in Faraday depth. To produce the maximum scientific output from these surveys, I reiterate a key takeaway from Chapters 4 and 6; L-band and S-band QU-spectra should be jointly analysed to best constrain both intrinsic fractional polarisation and depolarisation parameters. The $\sim$ 7000 deg^2 sky area of the MeerKAT+ S-band Legacy Survey overlaps entirely with POSSUM to a comparable sensitivity, effectively allowing for joint analysis of $\sim 1.6 \times 10^5$ polarised sources. Furthermore, the higher Faraday depth resolution of POSSUM ($\sim$ 1 rad m^{-2}) coupled with the higher angular resolution in the S-band survey ($\sim 1''$), will maximise the analysis of extragalactic sources and their foregrounds in both datasets, particularly in understanding and interpreting the physical origin of Faraday complexity.

7.2.2 Small-scale Galactic magnetic fields

While the RM grid can effectively map the large-scale magnetic field of the Milky Way, we require more advanced methods to probe small-scale Galactic magnetic fields, linked to the turbulent nature of the ISM. The RM structure function (SF), introduced in Chapter 3 can be used to statistically measure the RM fluctuations between pairs of polarised sources as a function of their separation, cf. turbulent power spectrum. SF analysis can accurately measure the outer scale of turbulence, limited by the minimum

Table 7.1: Summary of key survey parameters of the large-area SKA precursor polarisation surveys. In the case of multiple frequency bands, the maximum sensitivities and minimum angular resolutions are listed.

Survey	Telescope	Area [deg^2]	Frequency [MHz]	Min. θ [arcsec]	Max. sensitivity [μJy beam^{-1}]	Reference
MMGPS	MeerKAT	$\sim$ 2000	544–2844	6	9	Padmanabh et al. (2023)
MK+ Legacy	MeerKAT+	7368	1969–2843	1	13	Chapter 6
POSSUM	ASKAP	20 630	800–1440	20	18	Gaensler et al. (2025)
SPICE-RACS	ASKAP	36 000	800–1800	20	100	Thomson et al. (2023)

separation between pairs. In Chapter 3, we smooth our image cubes to a common angular resolution of θ = 15", but show that 24% of sources have multiple spatial components (in total intensity) when inspected at the high frequency end of the cube. This close angular separation of 15" is sensitive to scales of $\sim$ 0.3 pc in the foreground Galactic plane (at a distance of 4 kpc), smaller than has been probed in the literature. Although the extraction of separate spectra for individual components is non-trivial, further investigation into the structure function of this sample will certainly be beneficial in constraining the outer scale of turbulence in this Galactic plane region. In this chapter, we also demonstrate how Faraday complexity can be used to characterise the small-scale Galactic magnetic field at angular scales even smaller than the beam. Combining the SF and Faraday complexity approaches can provide a more complete view of RM fluctuations across a large range of angular and physical scales. The combination of these methods has recently been explored by Ma et al. (2025), who find evidence of turbulent injection smaller than that of the supernova-driven turbulent magnetic field in the northern Galactic plane.

The combined RM density and broadband coverage of the surveys introduced in Section 7.2.1 will enable robust studies into small-scale Galactic magnetic fields. In particular, the ultra-broadband coverage of MMGPS will allow for extremely detailed modelling of Faraday dispersion and differential Faraday rotation via QU-fitting, to expand our knowledge on the structure, scale, strength and distribution of small-scale magnetic fields. This will in turn, enable further investigation into the drivers of such RM fluctuations, e.g. stellar feedback (Livingston et al., 2021), which are relatively unknown on these scales. Observations of extended magnetised Galactic objects (e.g. HII regions) with well-characterised electron densities and distances will open up the parameter space to even smaller turbulent scales, i.e. close to the magnetic dissipation scales (Haverkorn and Spangler, 2013). We have proposed MeerKAT observations[1] of the nearby (160 pc) HII region, Sharpless 2–27, for which using the above methods will provide insight into the magneto-ionic turbulent scales at 360 AU, the smallest scales probed yet.

7.2.3 Towards a consolidated Faraday complexity metric

In Chapter 3, we highlight the observational nature of Faraday complexity. The complexity classification of polarised EGSs is dependent on factors such as angular resolution, maximum angular scale, signal-to-noise ratio (in Faraday depth), frequency band and bandwidth. Detailed Faraday complexity analysis has only become accessible over the past decade with the advent of broadband receivers, and as of now, analyses have been limited to targeted samples of order 100 sources. In this thesis, we emphasise the importance of Faraday complexity as a means to detect both the small-scale magneto-ionic structure in the Milky Way as well as internal depolarisation within radio galaxies, or external depolarisation

[1] A collaboration between S. Ranchod, S. A. Mao, A. Basu, Y. K. Ma and J. D. Livingston

from their local environment. As we present in Chapter 3 and 4, even for small samples, it becomes difficult to draw meaningful comparisons to other works regarding Faraday complexity if they have a) a different observational setup and b) a different Faraday complexity classification scheme. In this work, we predominantly use QU-fitting to characterise Faraday complexity and note that a particular limitation in this the lack of a single parameter that quantifies the degree of complexity between different QU-fitting models and their best fit parameters. Recently, Ma et al. (2025) defined "FD spread" [rad m^{-2}], a new parameter that encompasses multiple Faraday depth and Faraday dispersion measurements from complex QU-fitting models into a single value. While this parameter is extremely useful for comparison within one dataset, it once again becomes difficult to compare to other works if QU-fitting was not performed. In Chapter 2, I describe more automated methods currently being developed to process and classify the upcoming large samples of polarised sources with surveys such as POSSUM and SPICE-RACS. The M_2 and $\sigma_{\rm add}$ methods introduced here are both based on the Faraday spectra alone, and will still be inconsistent between observations at different bands and angular resolutions.

This situation poses a need for a consolidated Faraday complexity metric that takes both spectral behaviour or complexities as well as observational parameters into account. This will be particularly necessary when comparing and combining catalogues from these new generation surveys, given their range of bandwidths and angular resolutions. This will also be important when comparing Faraday depth or QU-spectra within a survey, if e.g. the various bands in POSSUM and MMGPS are processed separately. The need for a uniform approach for interferometric spectro-polarimetric analysis has already been addressed by Van Eck et al. (2023) in their creation of RMTable2023, a standard for producing catalogues of polarised radio sources. I suggest that a similar approach is required for Faraday complexity to maximise the scientific output of these new generation pre-SKA polarisation surveys. For example, $\sigma_{\rm add}$ is particularly useful as it is easy to produce for any Faraday spectrum. This could be weighted by parameters describing the angular resolution and bandwidth of the observations. An alternative suggestion would be to have a simplified rubric or scale involving e.g. fractional bandwidth and uv-coverage to compare between surveys in a more robust manner.

7.2.4 Characterisation of the polarised source population

The magnetic field geometry and depolarisation properties of radio galaxies is still largely unexplored, a research area where e.g. POSSUM and the MeerKAT+ S-band Legacy Survey will contribute significantly. In previous studies, a major limitation was the angular resolution (for morphological classification) or the availability of multi-wavelength data, both of which are available in the VLA-COSMOS data set. With the polarisation data products produced in this thesis, this survey will continue to be a goldmine in terms of polarised source characterisation beyond what is presented in this work. In this section, I will propose further avenues in which this dataset can be explored.

Recent results from LOFAR surveys ($\nu \sim 100$ MHz) have reported an increased fractional polarisation for sources with larger projected sizes (e.g. O'Sullivan et al., 2023; Piras et al., 2025). This has been attributed to an effect of the local source environment, where large radio galaxies expand further out of the direct source environment, and are therefore less depolarised by said environment. The highest resolution at which this was observed was at $\theta = 6''$ for a sample of only 33 sources in the ELAIS-N1 field (Piras et al., 2025). With the high resolution and higher frequency of the VLA-COSMOS survey, we can investigate this in more detail, considering the variation of fractional polarisation across the

radio lobes with respect to the extent and mass of the host galaxy. This can be further supplemented by QU-fitting spectra extracted at multiple pixels across a given source to constrain the magnetic field ordering and dominant depolarisation mechanisms as a function of projected distance from host galaxy. Another compelling topic of current research is the anti-correlation between fractional polarisation and redshift (e.g. Carretti et al., 2022). This is a signature of intergalactic magnetic fields in cosmic web filaments, and has been detected at both low frequencies (144 MHz; Carretti et al., 2022) and higher frequencies (1.4 GHz; Berger et al., 2021). While larger statistical samples are favourable for such a detection, the 3 GHz perspective can contribute to a holistic view of this depolarisation trend, particularly in the COSMOS field, which has a well-constrained cosmic web structure (e.g. Darvish et al., 2017).

Two important questions investigated in Chapter 4 are the origin of the flattening of cumulative source counts at $P < 1$ mJy as well as the frequency-dependence of polarised source counts. While this thesis provides important first steps in addressing these via morphological classification and depolarisation characterisation, even larger statistical samples are required for a deeper insight into these trends. Since high-resolution and large sky areas are essential for such an investigation, the MeerKAT+ S-band Legacy Survey will be able to provide statistically significant constraints and further understanding regarding these questions.

7.2.5 Polarised SFG population: a statistical approach

Star-forming galaxies dominate the μJy radio sky, but due to their low fractional polarisations, have not been readily detected in polarised intensity, despite the increased sensitivities of modern radio interferometers. As introduced in Chapter 4, it remains unclear the level of sensitivity required to detect this faint and/or distant SFG population. The detection of this population with statistically significant number counts will not only considerably increase the density of the all-sky RM grid, but also provide a window into the evolution of magnetic fields in spiral galaxies over cosmic time. The upper limit obtained in Chapter 4 concerning the density of polarised star-forming galaxies shows that observations more sensitive than 2.6 μJy beam^{-1} in the Faraday depth domain will be required to directly detect these sources, and it will therefore likely not be possible with the new generation of pre-SKA surveys. This highlights the need for a statistical approach for the detection of large samples of polarised star-forming galaxies. As introduced in Chapter 5, stacking is a statistical technique that can provide an aggregate measurement of a selected sample of sources that cannot be measured individually due to sensitivity limitations. In polarisation, stacking has been used to probe the diffuse Galactic ISM (Šnidarić et al., 2023) and intergalactic medium of cosmic filaments (Vernstrom et al., 2021). It has also been used to measure polarisation properties of point source populations identified in total intensity in NVSS (Stil et al., 2014) and the LOFAR deep fields (Piras et al., 2024). However these works do not achieve the sub-μJy stacked sensitivity levels required to detect the star-forming population. Ancillary multi-wavelength data is essential to meaningfully constrain e.g. the fractional polarisation (a tracer of magnetic field geometry) over cosmic time. These data should be used to a) specifically select for star-forming galaxies via optical cross-matching or the FIR-radio correlation, and b) divide sources into sub-samples according to their redshift. The VLA-COSMOS survey is a well-suited sample for this investigation, as the catalogue includes approximately ~ 4300 star-forming galaxies with available redshifts ($z < 5.6$, see Figure 7.3), which after stacking the full sample can reduce the noise in Stokes Q and U by a factor of ~ 65. Furthermore, the high angular resolution of the survey can mitigate potential error-inducing source confusion and blending effects. As originally suggested by Stil and Keller (2015),

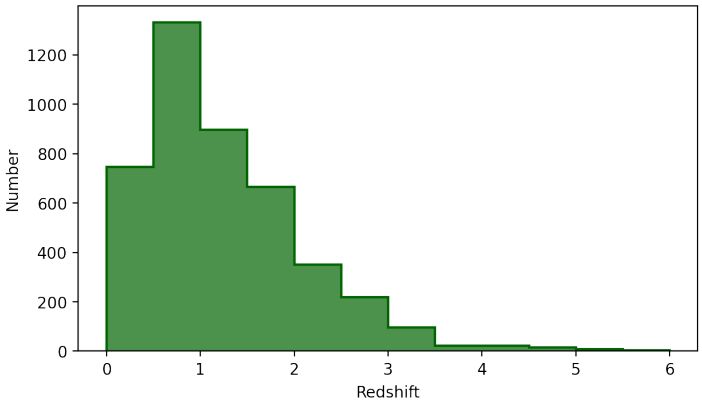

Figure 7.3: Redshift distribution of star-forming galaxies within the VLA-COSMOS 3 GHz polarisation footprint (Chapter 4). This distribution only includes sources confirmed as star-forming galaxies as cross-matched with multi-wavelength catalogues.

one can further benefit from broadband spectro-polarimetry in this sense, by stacking in the Faraday depth domain, which is model independent and does not require assumptions regarding the polarisation angle of sources. This methodology has not yet been implemented for real data, and requires a careful quantification of the noise properties, instrumental polarisation (i.e. leakage) and polarisation bias via simulated catalogues, for which the VLA-COSMOS image cubes can be particularly instructive. In addition to the redshift dependence, stacking can be used to probe the polarisation properties of SFGs as a function e.g. environment, star-formation rate, merger history etc.

7.3 Final remarks

The next generation of large-area polarisation surveys will usher in a prosperous new era in the field of cosmic magnetism. As I present in this thesis, a comprehensive understanding of the physical properties of the extragalactic polarised source population, as well as any contributions of Faraday complexity within these sources is essential to fully exploit the scientific potential of these surveys, particularly in the context of a detailed mapping of the RM sky. Furthermore, I have shown that in-depth Faraday complexity analysis, enabled by the broadband receivers of modern telescopes, is an important tool for studying the small-scale structure of the Galactic magnetic field. Our advancement into the SKA era, expanding to larger samples and higher angular resolutions provides an exciting opportunity to revolutionise our understanding of cosmic magnetic fields from the ISM of our own Galaxy, to the large scale structure of the Universe.

APPENDIX A

Calibration verification in the VLA-COSMOS

A.1 Polarisation calibration verification

In Section 4.2.1, we describe the calibration pipeline used for processing the VLA-COSMOS data in Chapter 4. To assess the success of the polarisation calibration, we plot the following diagnostic plots, examples of which are shown in Figure A.1. Firstly, we show the corrected amplitude (all correlations) as a function of frequency for the polarisation leakage calibrator J0713+4349. The data points corresponding to total intensity are clustered around an amplitude of 1.9, consistent with the model[1]. The points clustered around an amplitude of zero correspond to Stokes I, Q and U indicating that the sources is unpolarised, as expected.

In Figure A.2 we plot the Faraday spectrum and the polarisation angle χ of the polarisation angle calibrator J1331+3030 (3C 286). We have a consistent peak Faraday depth with the model value of RM = 0 rad m^{-2} , and also closely matched to the model polarisation angle of $\chi = 33^{\circ}$ (Perley and Butler, 2013). The $\sim$ 1 degree offset is a sufficient consistency for the science applications in this work. For completeness, we note the updated model for 3C 286 (Hugo and Perley, 2023). While this new model shows an approximate $\sim$ 1 degree offset from the Perley and Butler (2013) model and may explain our observed offset, it was published after the calibration of these data. The update model shows a more significant discrepancy at $\nu < 1$ GHz, and since we do not use the polarisation angle parameter in our analysis, we do not expect any change in results had we used the updated Hugo and Perley (2023) model.

A.2 Comparison to S17

Although we no not use the MFS image produced in Section 4.2.1 for science applications, we require it for visual inspection and verification. In this section, we compare the total intensity flux density measurements obtained from our MFS image to those in the the S17 catalogue. We produce a catalogue from our image using the `PyBDSF` source finding software. Here, we use the default parameters, with a 5σ detection threshold (where σ is the local rms), and detect 5977 sources within the survey area. After cross matching with the S17 catalogue with a 1" maximum separation, we find counterparts for 5364 sources. In Figure A.3 we plot the integrated total intensity per source against that from the

[1] https://www.vla.nrao.edu/astro/calib/vlacal/cal_mon/last/0713+4349.html

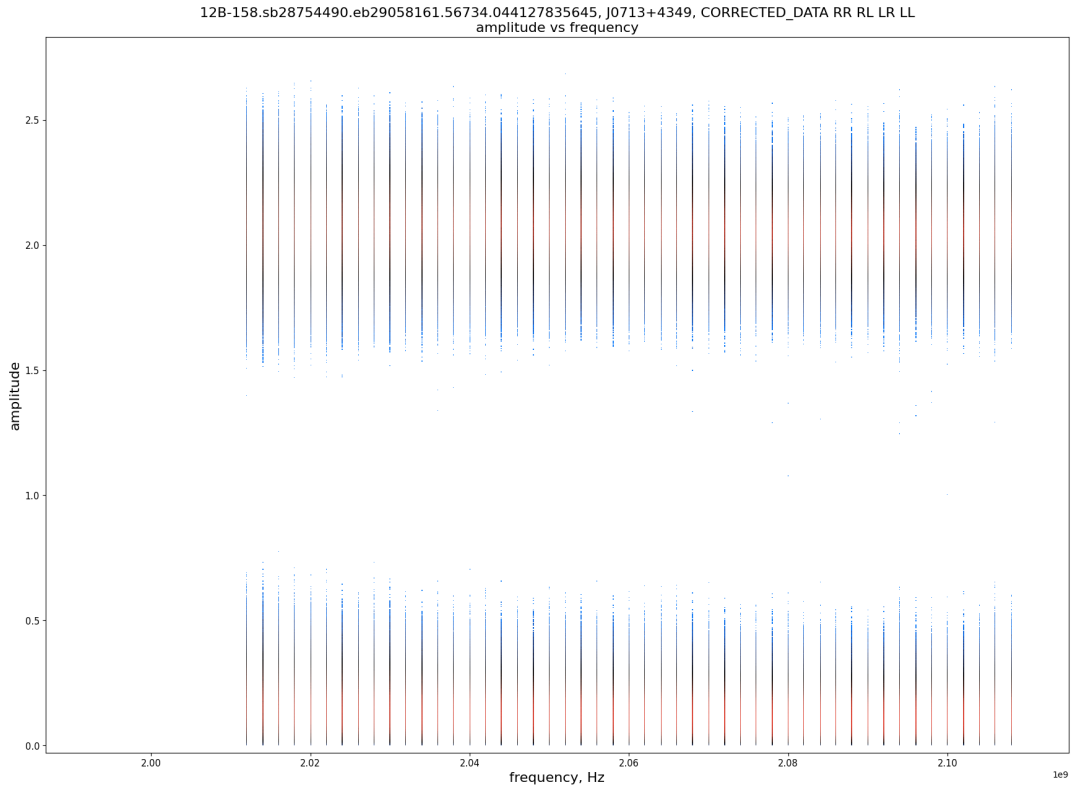

Figure A.1: Corrected amplitude vs frequency plots for the polarisation leakage calibrator J0713+4349. The colouration indicates point density, where red shows high density and blue shows low density. This plot shows all correlations, RR, RL, LR and LL (see Chapter 2).

S17 catalogue where the points were colourised according the number of associated pixels in the S17 MFS image. This plot shows good agreement between the two measurements, with an approximately 10% offset. This offset is consistent with the discrepancy expected with the imaging is done with the WSClean software in comparison to casa's `tclean` task. We note that some of the bright sources have underestimated flux densities in our catalogue. These correspond to the cases where all components of a multi-component source are not correctly associated to the same catalogue entry. As this catalogue is produced purely for this flux density comparison, we do not manually combine these components.

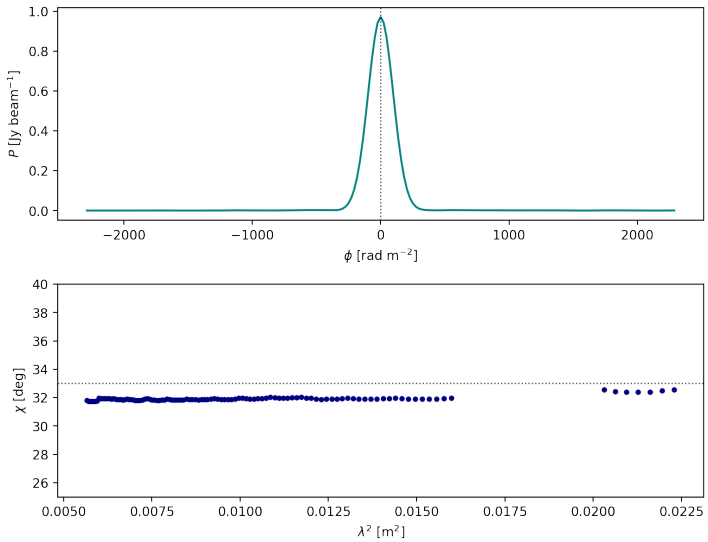

Figure A.2: Top: Faraday spectrum of polarisation angle calibrator J1331+3030 (3C 286). The peak Faraday depth is centred at the model RM= 0 rad m^{-2}, as indicated by the dotted line. Bottom: The polarisation angle of 3C 286 as a function of λ^2. Here we have a minimal 1 deg offset from the model values of $\chi = 33^\circ$ (Perley and Butler, 2013).

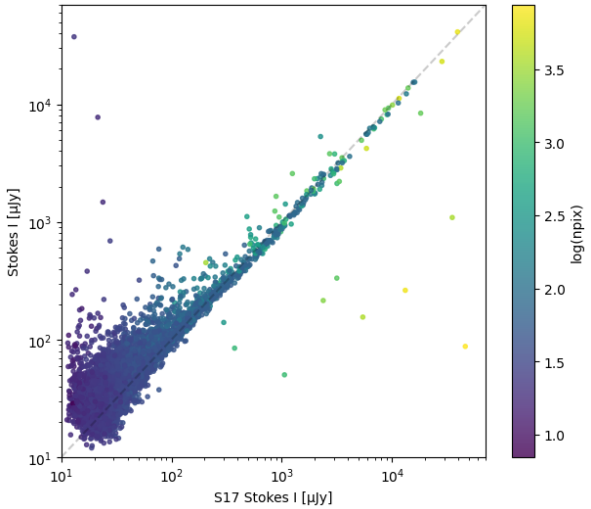

Figure A.3: Comparison between the integrated total intensity flux density of sources detected in the S17 MFS image and the corresponding source in the Stokes I MFS image produced in this work. The data points are colourised according to the number of pixels in a source, based on the S17 catalogue. The 1-to-1 line is indicated by the dashed grey line.

APPENDIX B

Source maps and spectra from the VLA-COSMOS

We present images of detected polarised sources, as well as their fractional Stokes Q and U spectra. Figure B.1 shows the total intensity images from S17, with contours on the polarised intensity from this work. Here, we also indicate the position at which we extract the Stokes Q and U spectra for further analysis. Figure B.2 shows the fractional Stokes q and u spectra with their best fit physical model, as described in Section 4.2.4.

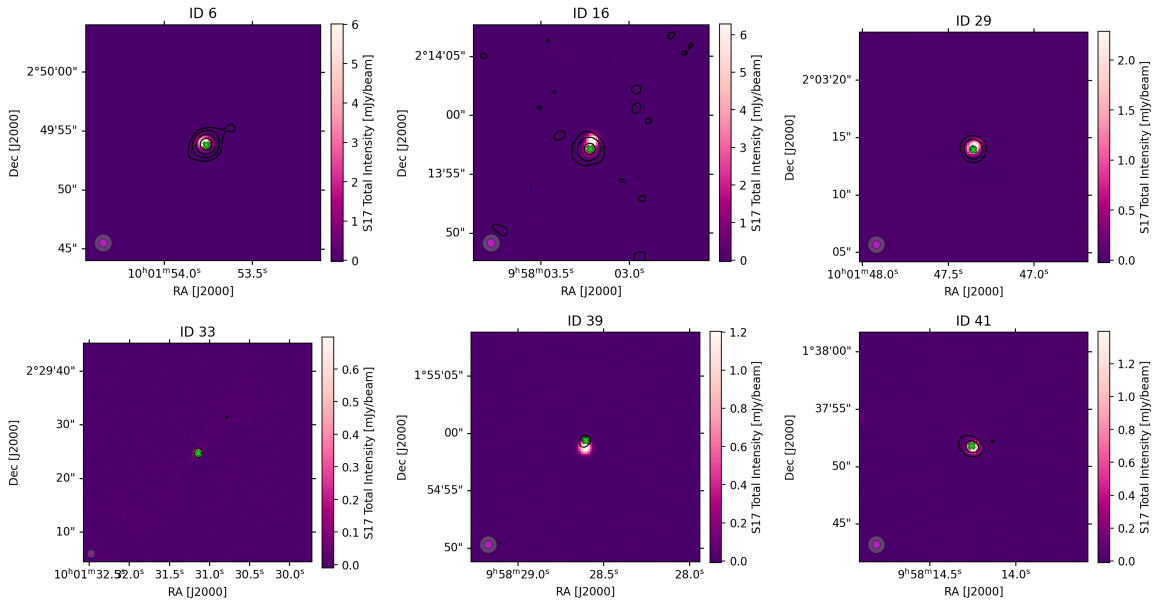

Figure B.1: The total intensity images from S17, overlayed with the polarised intensity contours from this work. The contours correspond to P = [22, 45, 90, 150] μJy beam^{-1}. The restoring beams for the total intensity (magenta) and polarised intensity (grey) images are shown in the bottom left corner. The green cross indicates the position at which the Stokes Q and U spectra are extracted for QU-fitting.

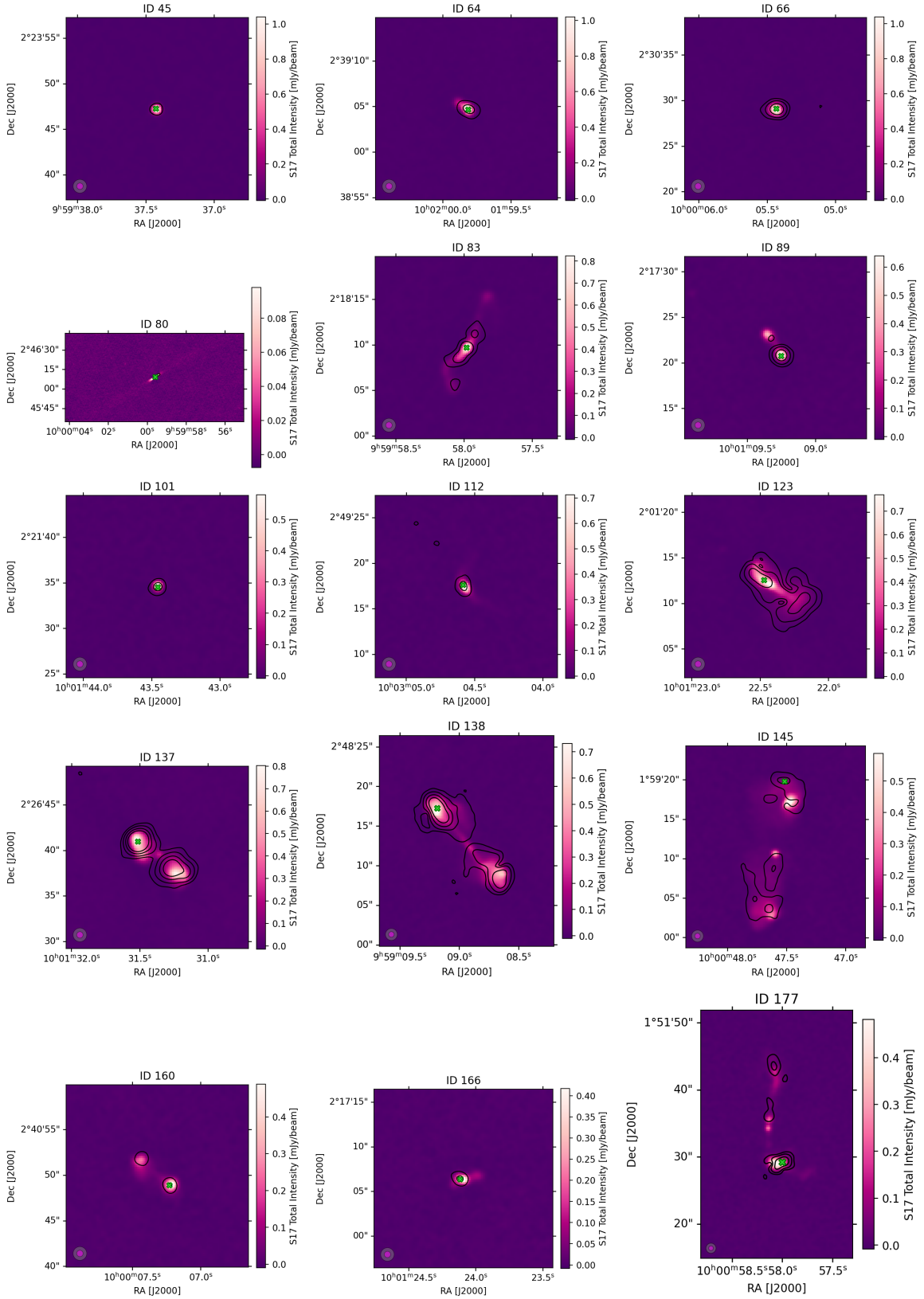

Figure B.1: The total intensity images from S17, overlayed with the polarised intensity contours from this work, continued.

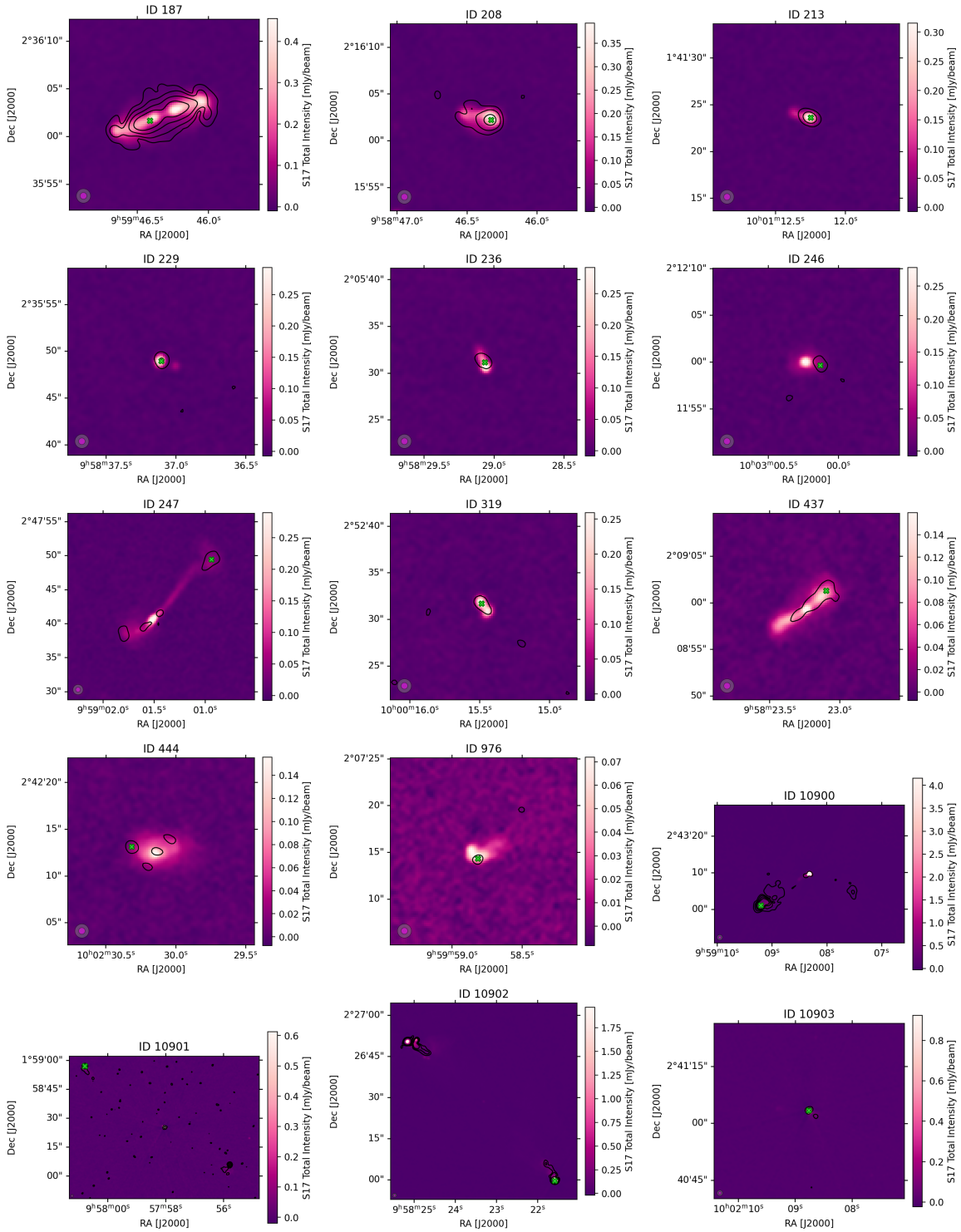

Figure B.1: The total intensity images from S17, overlayed with the polarised intensity contours from this work, continued.

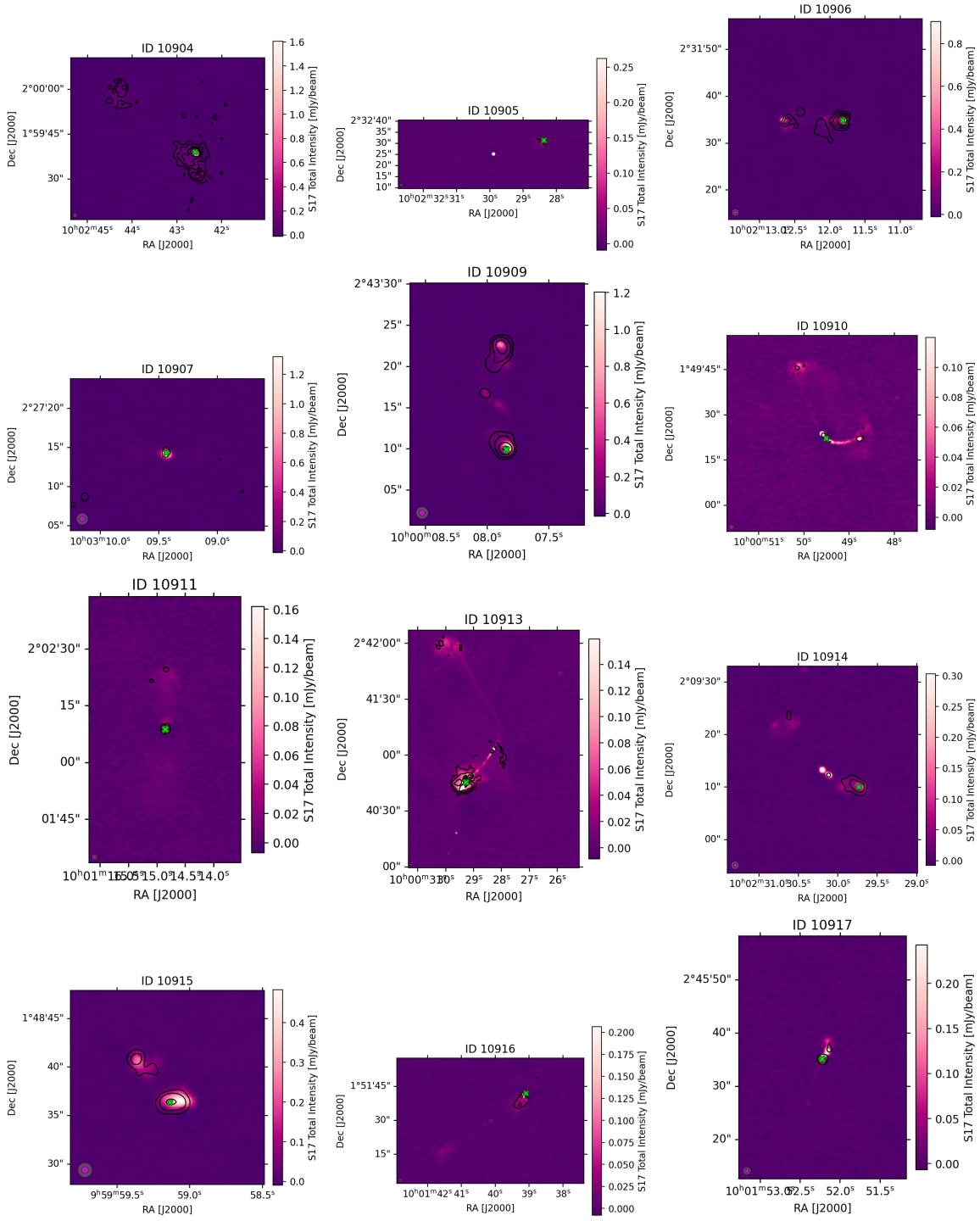

Figure B.1: The total intensity images from S17, overlayed with the polarised intensity contours from this work, continued.

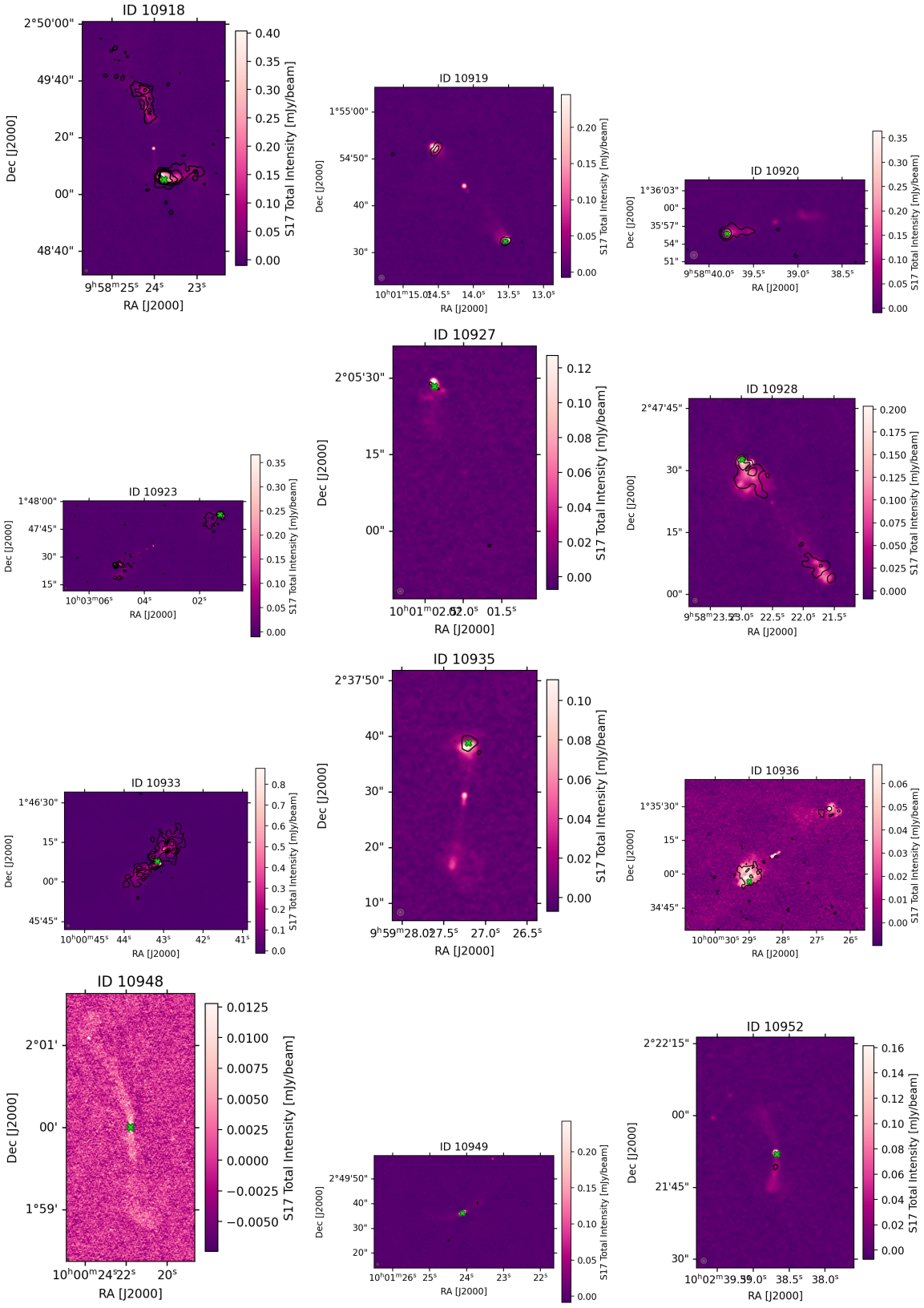

Figure B.1: The total intensity images from S17, overlayed with the polarised intensity contours from this work, continued.

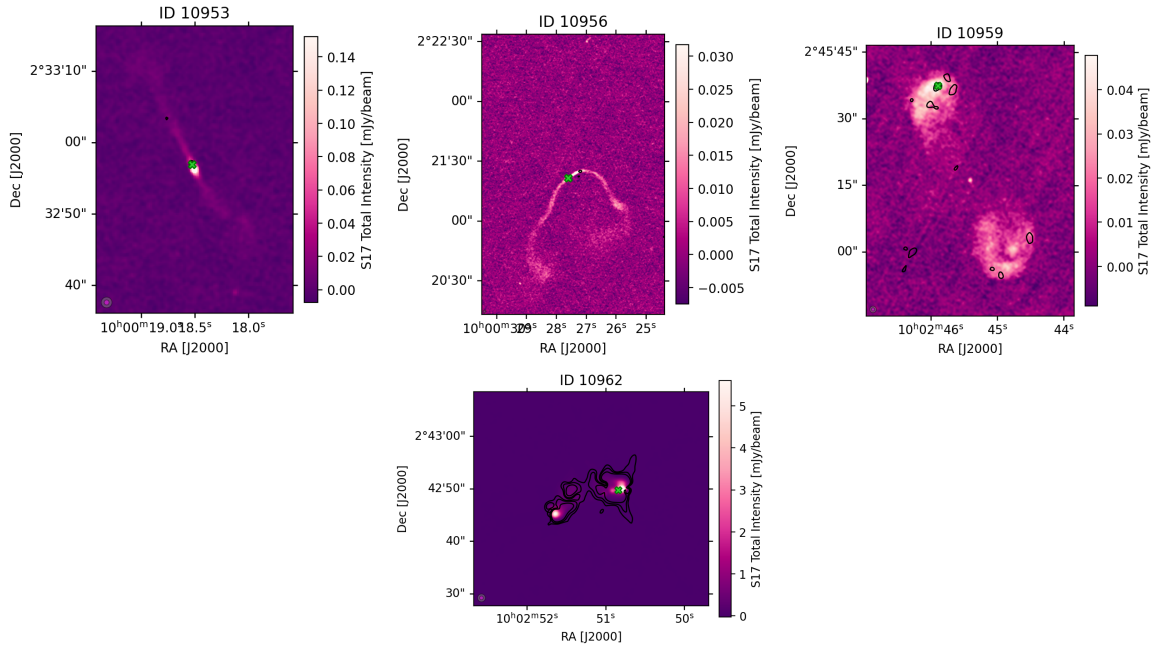

Figure B.1: The total intensity images from S17, overlayed with the polarised intensity contours from this work, continued.

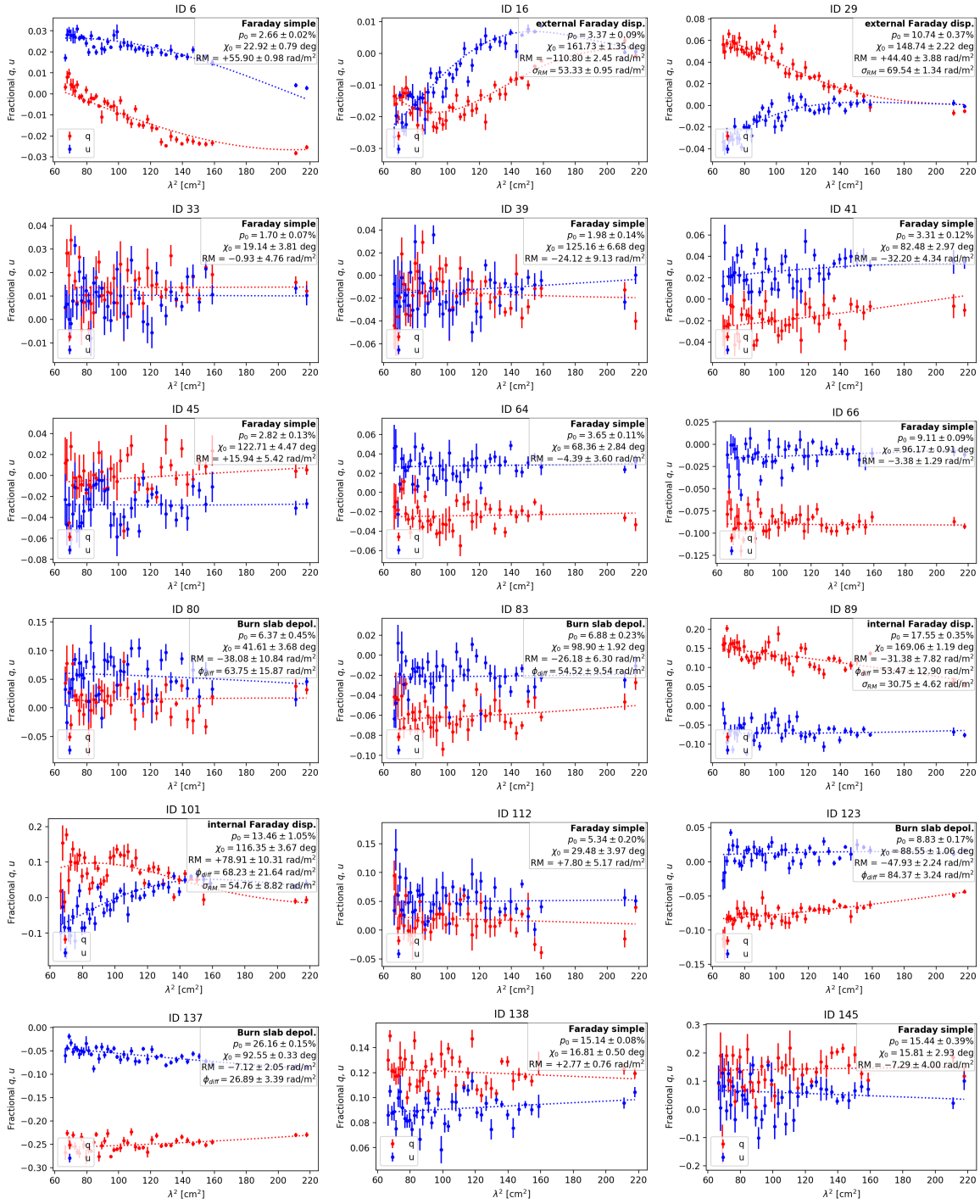

Figure B.2: The fractional Stokes q and u spectra for each source, plotted with the corresponding best fit depolarisation model, as defined in Section 4.2.4. The fit parameters are also listed on the figure.

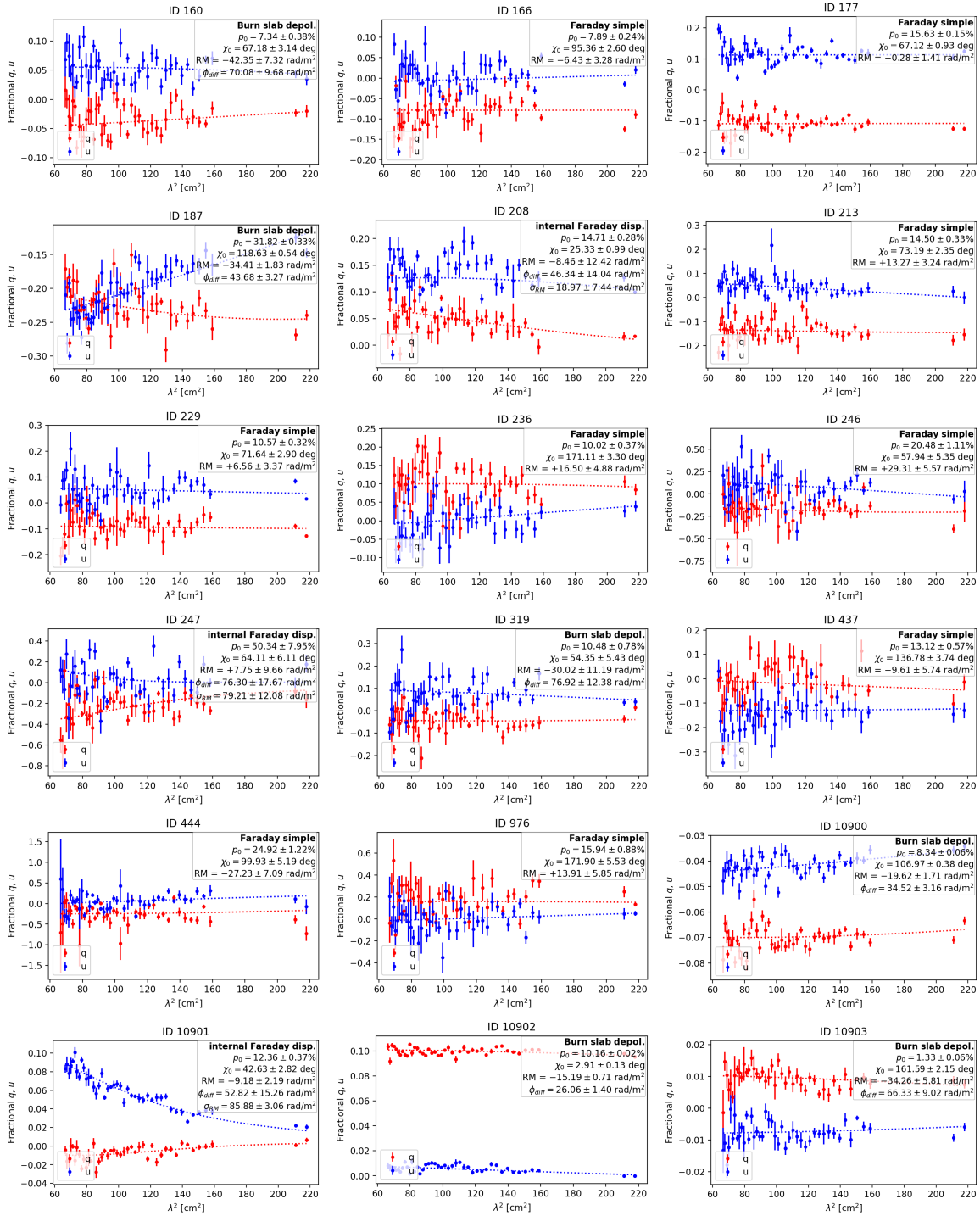

Figure B.2: The fractional Stokes q and u spectra for each source, plotted with the corresponding best fit depolarisation model, continued.

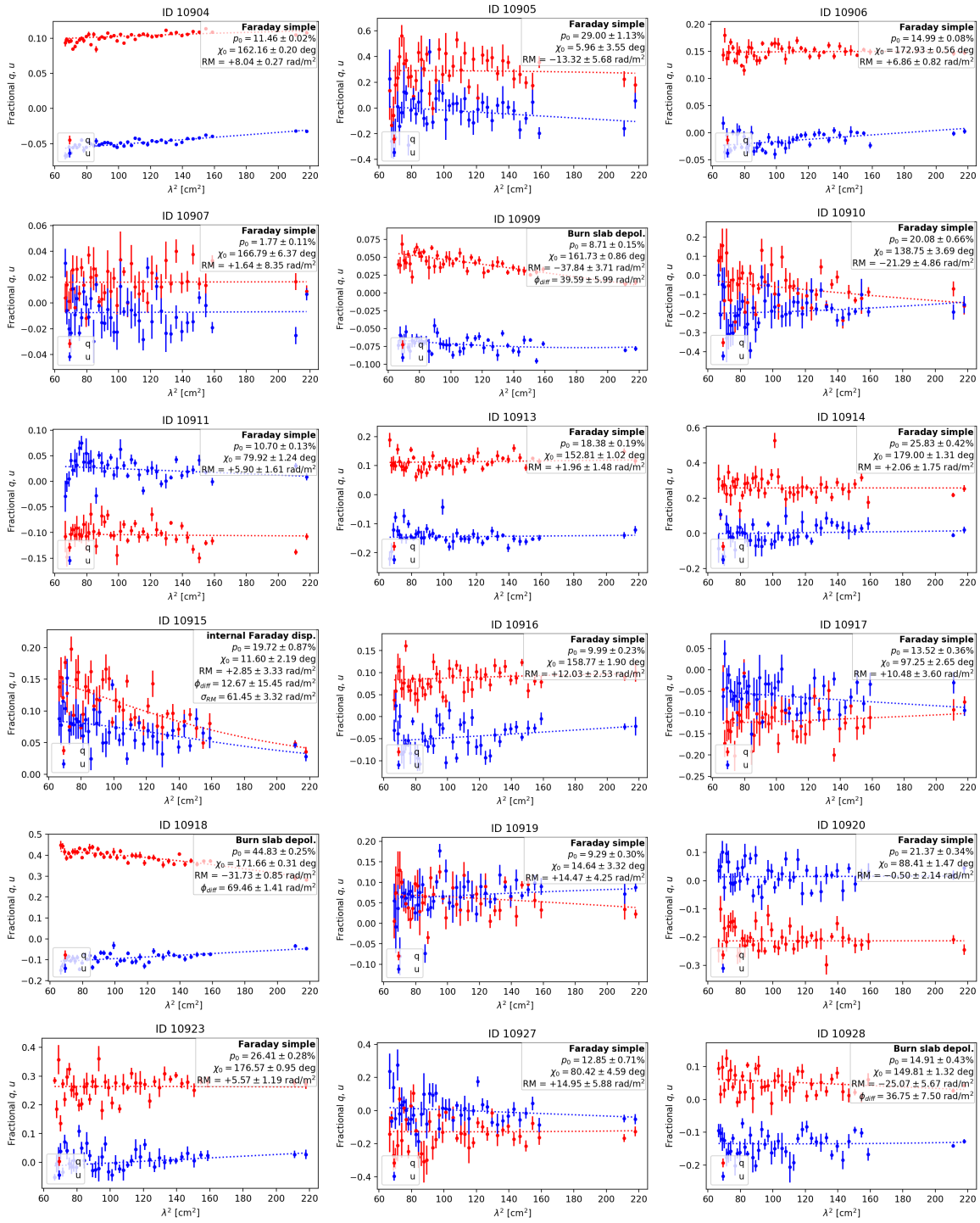

Figure B.2: The fractional Stokes q and u spectra for each source, plotted with the corresponding best fit depolarisation model, continued.

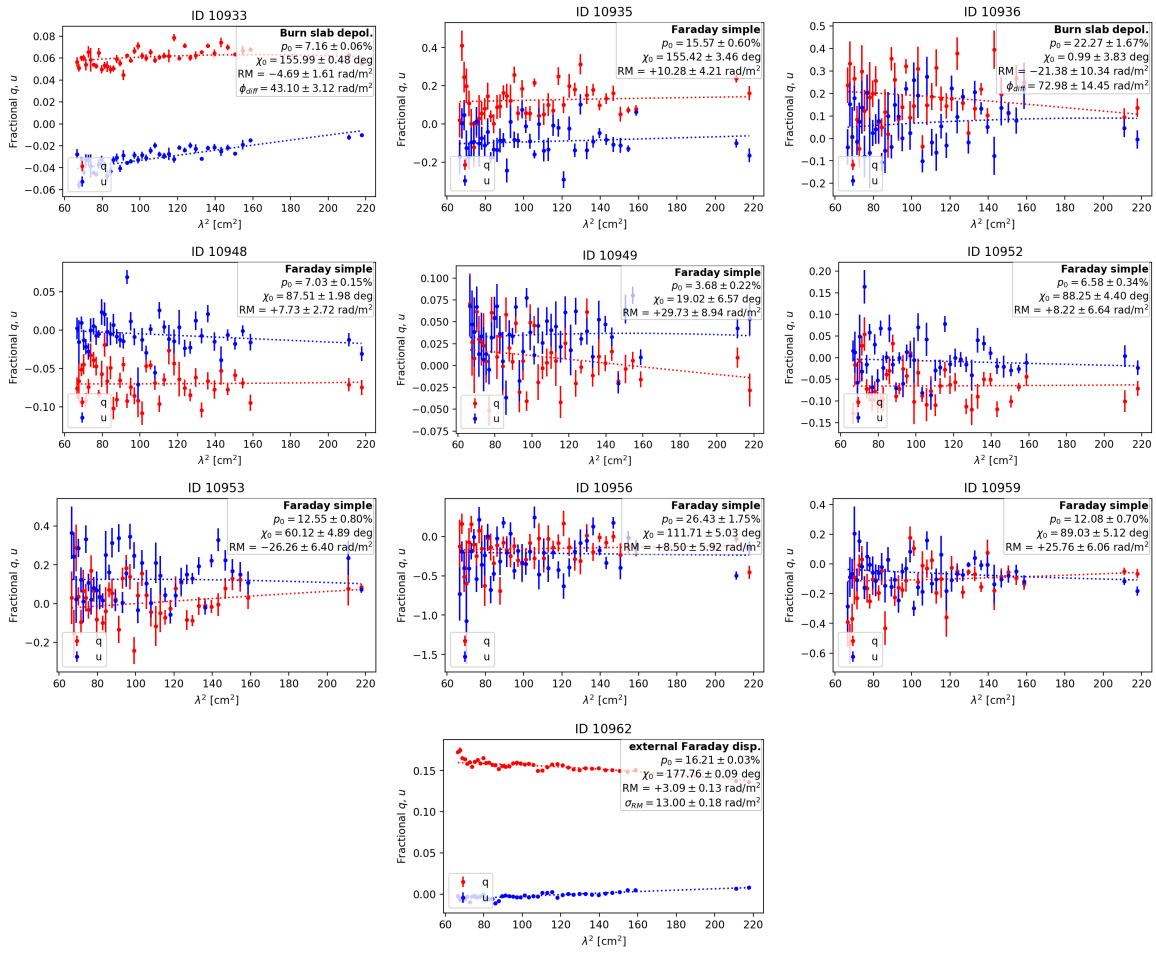

Figure B.2: The fractional Stokes q and u spectra for each source, plotted with the corresponding best fit depolarisation model, continued.

APPENDIX C

VLA-COSMOS sample catalogue of polarised sources

C.1 Catalogue sample

Table C.1: Polarisation properties and source classifications of the detected polarised sources. The ID used in column 1 corresponds to that in the S17 catalogue.

ID	RA (J2000)	Dec (J2000)	$P_{\rm peak}$ [μJy beam^{-1}]	$P_{\rm total}$ [μJy]	RM [rad m^{-2}]	p %	S/N	AGN class	FR class	pol comp
6	10:01:54	+2:49:54.0	202.71 ± 2.86	206.63 ± 4.67	+62.63 ± 1.89	2.62	53.8	HLAGN	C	compact
16	9:58:03	+2:13:57.6	114.23 ± 4.48	120.23 ± 4.48	−127.37 ± 4.54	1.63	25.2	HLAGN	C	compact
26	10:01:53	+2:11:52.6	112.45 ± 2.88	109.20 ± 2.88	+5.56 ± 3.09	4.69	38.7	–	FRI	core
29	10:01:47	+2:03:14.2	100.68 ± 3.03	76.02 ± 3.03	+49.65 ± 3.39	3.25	33.4	HLAGN	C	compact
33	10:01:31	+2:29:24.7	39.37 ± 3.84	39.37 ± 3.84	+10.56 ± 9.63	1.56	13.7	HLAGN	FRI	core
39	9:58:29	+1:54:58.8	28.87 ± 2.35	28.87 ± 2.35	−38.42 ± 10.42	2.34	11.2	MLAGN	C	compact
41	9:58:14	+1:37:51.8	62.61 ± 2.02	45.60 ± 2.02	−12.83 ± 4.48	3.44	29.8	HLAGN	C	compact
45	9:59:37	+2:23:47.2	38.71 ± 2.89	38.71 ± 2.89	+19.08 ± 8.66	2.81	13.5	HLAGN	C	compact
64	10:02:00	+2:39:04.8	57.45 ± 2.47	63.07 ± 2.47	+4.51 ± 4.99	3.48	27.1	MLAGN	C	compact
66	10:00:05	+2:30:29.0	146.37 ± 3.03	152.81 ± 4.71	−11.19 ± 2.28	8.35	52.1	MLAGN	C	compact
80	10:00:00	+2:46:08.9	41.75 ± 2.53	87.06 ± 4.55	−7.34 ± 6.83	5.72	16.3	MLAGN	FRII	core
83	9:59:58	+2:18:09.7	84.58 ± 1.73	206.63 ± 4.02	−2.28 ± 2.58	6.12	53.5	MLAGN	FRI	core
89	10:01:09	+2:17:21.7	142.26 ± 2.55	145.28 ± 4.21	−15.39 ± 2.21	13.78	49.3	MLAGN	FRII	lobe
101	10:01:43	+2:21:34.6	58.13 ± 2.86	43.84 ± 2.86	+140.68 ± 6.18	8.18	16.0	HLAGN	C	compact
112	10:03:05	+2:49:17.4	55.11 ± 3.52	47.48 ± 3.52	+10.27 ± 7.15	5.21	19.5	–	FRI	core
123	10:01:22	+2:01:11.8	130.16 ± 2.65	897.00 ± 10.00	−18.86 ± 2.31	7.13	50.3	HLAGN	E	core?
137	10:01:31	+2:26:39.2	460.36 ± 4.30	1263.32 ± 14.15	+1.60 ± 1.06	24.23	119.7	MLAGN	FRII	lobe
138	9:59:09	+2:48:13.0	291.02 ± 4.72	1516.91 ± 22.11	−4.50 ± 1.73	14.19	100.5	MLAGN	FRII	lobe
145	10:00:48	+1:59:11.5	53.49 ± 2.59	569.49 ± 10.95	+7.35 ± 5.96	–	–	–	FRII	lobe
160	10:00:07	+2:40:49.9	48.64 ± 2.63	56.33 ± 2.63	−35.39 ± 6.77	5.79	21.9	MLAGN	FRII	lobe
166	10:01:24	+2:17:06.4	52.96 ± 3.09	52.96 ± 3.09	−2.76 ± 7.16	7.83	18.7	MLAGN	FRI	core
177	10:00:58	+1:51:33.4	146.17 ± 3.48	397.81 ± 10.13	+4.54 ± 2.86	15.05	51.2	–	FRII	lobe/jet
187	9:59:46	+2:36:02.2	245.85 ± 3.59	1520.29 ± 15.14	−13.42 ± 1.72	27.81	67.7	MLAGN	FRII	jet
208	9:58:46	+2:16:02.4	118.90 ± 3.89	194.13 ± 6.98	+8.21 ± 3.48	12.63	41.0	HLAGN	E	lobe?
213	10:01:12	+1:41:23.7	72.44 ± 4.36	61.37 ± 4.36	+4.69 ± 6.80	13.18	17.5	MLAGN	E	lobe?
229	9:58:37	+2:35:48.9	48.97 ± 3.40	48.97 ± 3.40	+13.56 ± 8.20	10.35	15.0	HLAGN	C	compact
236	9:58:29	+2:05:31.1	40.78 ± 2.28	40.78 ± 2.28	−8.95 ± 7.95	7.63	13.7	MLAGN	E	lobe
246	10:03:00	+2:12:00.0	34.04 ± 2.54	34.04 ± 2.54	−17.63 ± 9.71	17.78	9.3	HLAGN	E	lobe
247	9:59:01	+2:47:42.5	36.26 ± 2.65	128.34 ± 5.77	−2.60 ± 7.93	–	–	–	FRI	lobe
319	10:00:15	+2:52:31.4	44.25 ± 4.32	44.25 ± 4.32	−0.22 ± 11.15	8.65	13.2	MLAGN	E	lobe
437	9:58:23	+2:08:59.5	42.20 ± 2.74	91.45 ± 4.86	+7.72 ± 8.35	11.74	9.6	MLAGN	FRII	lobe
444	10:02:30	+2:42:12.7	30.33 ± 2.69	62.33 ± 4.39	−1.29 ± 10.05	–	–	MLAGN	E	none
976	9:59:59	+2:07:15.1	28.70 ± 2.23	28.70 ± 2.23	+12.61 ± 9.75	15.67	10.4	–	E	core?
10900	9:59:08	+2:43:09.6	408.28 ± 3.91	1352.59 ± 18.68	−2.32 ± 1.11	7.94	98.1	HLAGN	FRII	lobe
10901	9:57:58	+1:58:25.1	233.10 ± 3.42	551.42 ± 10.88	−8.53 ± 1.74	5.45	42.2	HLAGN	FRII	lobes
10902	9:58:23	+2:26:28.5	1038.49 ± 4.91	5454.30 ± 41.03	+0.11 ± 0.63	9.72	168.9	HLAGN	FRII	lobes
10903	10:02:09	+2:41:03.3	65.55 ± 2.41	64.91 ± 2.41	+9.00 ± 4.73	1.17	25.2	HLAGN	FRII	core
10904	10:02:43	+1:59:43.4	738.82 ± 7.06	3663.45 ± 52.24	+6.20 ± 1.14	10.76	94.8	HLAGN	FRII	lobe
10905	10:02:30	+2:32:25.1	45.21 ± 2.02	78.26 ± 3.29	+6.14 ± 6.36	23.46	11.6	HLAGN	FRII	lobe
10906	10:02:12	+2:31:35.0	298.18 ± 3.47	840.70 ± 13.20	+4.17 ± 1.34	14.80	98.6	HLAGN	FRII	lobe
10907	10:03:09	+2:27:14.1	34.16 ± 2.29	34.16 ± 2.29	−7.46 ± 9.31	1.72	13.4	MLAGN	FRI	core
10909	10:00:08	+2:43:15.4	171.35 ± 2.61	480.42 ± 7.62	−17.09 ± 1.80	8.16	70.5	HLAGN	FRII	lobe
10910	10:00:50	+1:49:23.7	44.59 ± 3.46	133.74 ± 7.61	+2.91 ± 8.72	14.50	7.5	HLAGN	FRII	core
10911	10:01:15	+2:02:08.7	120.25 ± 2.44	168.30 ± 5.04	+6.42 ± 2.58	10.74	53.1	HLAGN	E	core
10913	10:00:28	+2:41:03.4	143.42 ± 1.82	4239.94 ± 17.11	+0.82 ± 1.41	17.68	81.5	MLAGN	FRII	lobe
10914	10:02:30	+2:09:13.3	85.58 ± 3.65	251.78 ± 9.28	+16.45 ± 4.75	22.09	25.9	HLAGN	FRII	lobe
10915	10:00:00	+1:48:37.8	99.75 ± 3.18	214.76 ± 6.74	−15.60 ± 3.89	12.10	32.9	MLAGN	FRII	lobe
10916	10:01:40	+1:51:29.7	71.91 ± 2.66	470.95 ± 9.25	+28.57 ± 4.35	9.29	24.5	MLAGN	FRII	lobe
10917	10:01:52	+2:45:35.3	55.86 ± 2.93	69.62 ± 4.49	+2.92 ± 6.38	10.74	18.4	MLAGN	E	core
10918	9:58:24	+2:49:16.2	455.75 ± 4.45	3907.63 ± 35.57	+4.71 ± 1.13	37.09	125.7	HLAGN	FRII	lobe
10919	10:01:14	+1:54:44.2	59.64 ± 3.16	141.10 ± 6.54	−2.90 ± 6.64	10.18	19.6	HLAGN	FRII	lobe
10920	9:58:39	+1:35:57.7	115.72 ± 3.34	156.07 ± 6.43	−3.87 ± 3.35	19.56	37.4	HLAGN	FRII	lobe
10923	10:03:04	+1:47:36.0	186.19 ± 3.72	1377.35 ± 20.85	+0.66 ± 2.19	23.95	62.9	HLAGN	FRII	lobe
10927	10:01:02	+2:05:11.5	24.50 ± 2.61	24.50 ± 2.61	−8.55 ± 13.61	9.33	8.8	MLAGN	FRII	none
10928	9:58:22	+2:47:22.2	86.53 ± 3.61	999.79 ± 19.14	+4.01 ± 4.51	12.93	21.7	MLAGN	FRII	lobe
10933	10:00:43	+1:46:07.9	269.40 ± 5.09	3676.22 ± 41.57	+21.72 ± 2.15	6.33	53.0	HLAGN	FRI	core
10935	9:59:27	+2:37:29.4	43.28 ± 3.66	95.21 ± 6.62	+2.78 ± 10.06	15.57	12.8	MLAGN	FRII	lobe
10936	10:00:28	+1:35:08.6	44.17 ± 2.00	877.33 ± 10.52	+14.01 ± 5.44	20.05	19.0	HLAGN	FRII	lobe
10948	10:00:22	+2:00:00.0	60.84 ± 3.84	52.01 ± 3.84	−12.67 ± 6.79	6.03	20.3	MLAGN	FRII	core
10949	10:01:24	+2:49:36.7	32.40 ± 2.03	40.06 ± 2.03	+19.23 ± 8.16	3.79	13.2	HLAGN	FRI	core
10952	10:02:39	+2:21:52.2	28.77 ± 2.34	28.77 ± 2.34	+19.33 ± 10.99	5.46	9.1	MLAGN	FRI	core
10953	10:00:19	+2:32:56.3	23.43 ± 3.01	23.43 ± 3.01	−0.19 ± 14.56	9.38	5.8	MLAGN	FRI	jet
10956	10:00:27	+2:21:23.3	27.92 ± 2.62	87.56 ± 5.35	−15.52 ± 10.06	24.18	11.2	MLAGN	FRI	core
10959	10:02:45	+2:45:16.1	33.13 ± 2.89	104.49 ± 6.05	+26.49 ± 9.73	14.73	9.8	MLAGN	FRII	lobe
10962	10:02:51	+2:42:48.1	1958.71 ± 9.40	9570.27 ± 60.01	+1.34 ± 0.54	14.88	172.8	HLAGN	FRII	lobe

Table C.2: Spectral fit (QU-fitting, spectral index and depolarisation index) parameters for the detected polarised sources.

ID	p_0 %	χ_0 [deg]	RM [rad m^{-2}]	$\sigma_{\rm RM}$ [rad m^{-2}]	$\phi_{\rm diff}$ [rad m^{-2}]	α	β
6	2.66 ± 0.02	22.9 ± 0.8	+55.90 ± 0.98	–	–	−0.91 ± 0.01	0.19 ± 0.12
16	3.37 ± 0.09	161.7 ± 1.3	−110.80 ± 2.45	53.3 ± 0.9	–	−0.90 ± 0.01	−2.35 ± 0.25
26	4.55 ± 0.06	72.1 ± 1.3	+6.82 ± 1.65	–	–	−0.14 ± 0.01	0.25 ± 0.24
29	10.74 ± 0.37	148.7 ± 2.2	+44.40 ± 3.88	69.5 ± 1.3	–	−0.85 ± 0.01	−3.29 ± 0.28
33	1.70 ± 0.07	19.1 ± 3.8	−0.93 ± 4.76	–	–	−0.31 ± 0.02	0.03 ± 0.45
39	1.98 ± 0.14	125.2 ± 6.7	−24.12 ± 9.13	–	–	−0.93 ± 0.02	−0.69 ± 0.41
41	3.31 ± 0.12	82.5 ± 3.0	−32.20 ± 4.34	–	–	−0.27 ± 0.02	0.12 ± 0.38
45	2.82 ± 0.13	122.7 ± 4.5	+15.94 ± 5.42	–	–	−0.10 ± 0.02	−0.54 ± 0.53
64	3.65 ± 0.11	68.4 ± 2.8	−4.39 ± 3.60	–	–	−0.79 ± 0.01	0.13 ± 0.29
66	9.11 ± 0.09	96.2 ± 0.9	−3.38 ± 1.29	–	–	−0.84 ± 0.01	−0.02 ± 0.14
80	6.37 ± 0.45	41.6 ± 3.7	−38.08 ± 10.84	–	63.7 ± 15.9	−0.26 ± 0.03	−0.48 ± 0.45
83	6.88 ± 0.23	98.9 ± 1.9	−26.18 ± 6.30	–	54.5 ± 9.5	−0.69 ± 0.02	−0.27 ± 0.25
89	17.55 ± 0.35	169.1 ± 1.2	−31.38 ± 7.82	30.7 ± 4.6	53.5 ± 12.9	−1.03 ± 0.02	−0.88 ± 0.15
101	13.46 ± 1.05	116.3 ± 3.7	+78.91 ± 10.31	54.8 ± 8.8	68.2 ± 21.6	−0.96 ± 0.03	−1.82 ± 0.40
112	5.34 ± 0.20	29.5 ± 4.0	+7.80 ± 5.17	–	–	−0.79 ± 0.03	−0.58 ± 0.48
123	8.83 ± 0.17	88.5 ± 1.1	−47.93 ± 2.24	–	84.4 ± 3.2	−0.65 ± 0.02	−0.94 ± 0.15
137	26.16 ± 0.15	92.5 ± 0.3	−7.12 ± 2.05	–	26.9 ± 3.4	−0.79 ± 0.02	−0.15 ± 0.06
138	15.14 ± 0.08	16.8 ± 0.5	+2.77 ± 0.76	–	–	−0.82 ± 0.01	−0.10 ± 0.09
145	15.44 ± 0.39	15.8 ± 2.9	−7.29 ± 4.00	–	–	−0.39 ± 0.07	0.33 ± 0.31
160	7.34 ± 0.38	67.2 ± 3.1	−42.35 ± 7.32	–	70.1 ± 9.7	−1.11 ± 0.03	−0.63 ± 0.37
166	7.89 ± 0.24	95.4 ± 2.6	−6.43 ± 3.28	–	–	−0.66 ± 0.04	−0.96 ± 0.42
177	15.63 ± 0.15	67.1 ± 0.9	−0.28 ± 1.41	–	–	−0.97 ± 0.02	−0.21 ± 0.22
187	31.82 ± 0.33	118.6 ± 0.5	−34.41 ± 1.83	–	43.7 ± 3.3	−0.60 ± 0.03	−0.32 ± 0.10
208	14.71 ± 0.28	25.3 ± 1.0	−8.46 ± 12.42	19.0 ± 7.4	46.3 ± 14.0	−0.85 ± 0.03	−0.48 ± 0.18
213	14.50 ± 0.33	73.2 ± 2.4	+13.27 ± 3.24	–	–	−0.60 ± 0.05	−0.17 ± 0.27
229	10.57 ± 0.32	71.6 ± 2.9	+6.56 ± 3.37	–	–	−1.03 ± 0.05	−0.43 ± 0.43
236	10.02 ± 0.37	171.1 ± 3.3	+16.50 ± 4.88	–	–	−0.94 ± 0.05	−0.67 ± 0.44
246	20.48 ± 1.11	57.9 ± 5.3	+29.31 ± 5.57	–	–	−0.80 ± 0.20	−0.52 ± 0.37
247	50.34 ± 7.95	64.1 ± 6.1	+7.75 ± 9.66	79.2 ± 12.1	76.3 ± 17.7	−0.58 ± 0.18	−1.59 ± 0.59
319	10.48 ± 0.78	54.4 ± 5.4	−30.02 ± 11.19	–	76.9 ± 12.4	−1.26 ± 0.07	−0.40 ± 0.49
437	13.12 ± 0.57	136.8 ± 3.7	−9.61 ± 5.74	–	–	−0.77 ± 0.08	−1.09 ± 0.44
444	24.92 ± 1.22	99.9 ± 5.2	−27.23 ± 7.09	–	–	0.01 ± 0.26	−0.01 ± 0.43
976	15.94 ± 0.88	171.9 ± 5.5	+13.91 ± 5.85	–	–	−0.84 ± 0.15	−0.38 ± 0.53
10900	8.34 ± 0.06	107.0 ± 0.4	−19.62 ± 1.71	–	34.5 ± 3.2	−0.83 ± 0.01	−0.17 ± 0.06
10901	12.36 ± 0.37	42.6 ± 2.8	−9.18 ± 2.19	85.9 ± 3.1	52.8 ± 15.3	−1.25 ± 0.01	−2.26 ± 0.15
10902	10.16 ± 0.02	2.9 ± 0.1	−15.19 ± 0.71	–	26.1 ± 1.4	−1.00 ± 0.01	−0.06 ± 0.04
10903	1.33 ± 0.06	161.6 ± 2.2	−34.26 ± 5.81	–	66.3 ± 9.0	−0.65 ± 0.01	−0.69 ± 0.22
10904	11.46 ± 0.02	162.2 ± 0.2	+8.04 ± 0.27	–	–	−0.92 ± 0.01	0.04 ± 0.04
10905	29.00 ± 1.13	6.0 ± 3.6	−13.32 ± 5.68	–	–	−0.52 ± 0.14	−0.47 ± 0.43
10906	14.99 ± 0.08	172.9 ± 0.6	+6.86 ± 0.82	–	–	−0.80 ± 0.02	−0.06 ± 0.08
10907	1.77 ± 0.11	166.8 ± 6.4	+1.64 ± 8.35	–	–	−0.48 ± 0.02	0.27 ± 0.43
10909	8.71 ± 0.15	161.7 ± 0.9	−37.84 ± 3.71	–	39.6 ± 6.0	−0.93 ± 0.01	−0.13 ± 0.12
10910	20.08 ± 0.66	138.8 ± 3.7	−21.29 ± 4.86	–	–	−0.81 ± 0.13	−0.29 ± 0.34
10911	10.70 ± 0.13	79.9 ± 1.2	+5.90 ± 1.61	–	–	−0.44 ± 0.02	0.09 ± 0.20
10913	18.38 ± 0.19	152.8 ± 1.0	+1.96 ± 1.48	–	–	−0.30 ± 0.04	0.09 ± 0.17
10914	25.83 ± 0.42	179.0 ± 1.3	+2.06 ± 1.75	–	–	−0.76 ± 0.06	−0.29 ± 0.25
10915	19.72 ± 0.87	11.6 ± 2.2	+2.85 ± 3.33	61.4 ± 3.3	12.7 ± 15.4	−1.27 ± 0.02	−1.52 ± 0.22
10916	9.99 ± 0.23	158.8 ± 1.9	+12.03 ± 2.53	–	–	−0.83 ± 0.03	−0.06 ± 0.28
10917	13.52 ± 0.36	97.3 ± 2.6	+10.48 ± 3.60	–	–	−0.73 ± 0.05	−0.02 ± 0.30
10918	44.83 ± 0.25	171.7 ± 0.3	−31.73 ± 0.85	–	69.5 ± 1.4	−0.61 ± 0.02	−0.63 ± 0.05
10919	9.29 ± 0.30	14.6 ± 3.3	+14.47 ± 4.25	–	–	−0.93 ± 0.04	0.00 ± 0.31
10920	21.37 ± 0.34	88.4 ± 1.5	−0.50 ± 2.14	–	–	−0.92 ± 0.04	0.14 ± 0.19
10923	26.41 ± 0.28	176.6 ± 1.0	+5.57 ± 1.19	–	–	−0.95 ± 0.04	0.22 ± 0.16
10927	12.85 ± 0.71	80.4 ± 4.6	+14.95 ± 5.88	–	–	−0.94 ± 0.10	−0.96 ± 0.59
10928	14.91 ± 0.43	149.8 ± 1.3	−25.07 ± 5.67	–	36.8 ± 7.5	−0.84 ± 0.05	−0.39 ± 0.25
10933	7.16 ± 0.06	156.0 ± 0.5	−4.69 ± 1.61	–	43.1 ± 3.1	−0.35 ± 0.01	−0.07 ± 0.09
10935	15.57 ± 0.60	155.4 ± 3.5	+10.28 ± 4.21	–	–	−0.88 ± 0.08	0.24 ± 0.49
10936	22.27 ± 1.67	1.0 ± 3.8	−21.38 ± 10.34	–	73.0 ± 14.4	−0.54 ± 0.10	−0.04 ± 0.51
10948	7.03 ± 0.15	87.5 ± 2.0	+7.73 ± 2.72	–	–	−0.12 ± 0.02	0.39 ± 0.31
10949	3.68 ± 0.22	19.0 ± 6.6	+29.73 ± 8.94	–	–	−0.45 ± 0.03	−0.39 ± 0.51
10952	6.58 ± 0.34	88.3 ± 4.4	+8.22 ± 6.64	–	–	−0.43 ± 0.05	−0.34 ± 0.47
10953	12.55 ± 0.80	60.1 ± 4.9	−26.26 ± 6.40	–	–	−0.54 ± 0.12	−0.72 ± 0.58
10956	26.43 ± 1.75	111.7 ± 5.0	+8.50 ± 5.92	–	–	−0.98 ± 0.16	−0.77 ± 0.48
10959	12.08 ± 0.70	89.0 ± 5.1	+25.76 ± 6.06	–	–	−0.77 ± 0.13	−2.10 ± 0.61
10962	16.21 ± 0.03	177.8 ± 0.1	+3.09 ± 0.13	13.0 ± 0.2	–	−0.88 ± 0.01	−0.27 ± 0.04

APPENDIX D

Paper: The Galactic latitude dependency of Faraday complexity in the S-PASS/ATCA RM catalogue

A&A, 686, A104 (2024)
https://doi.org/10.1051/0004-6361/202348993

Astronomy & Astrophysics

The Galactic latitude dependency of Faraday complexity in the S-PASS/ATCA RM catalogue

S. Ranchod[1], S. A. Mao[1], R. Deane[2,3], S. S. Sridhar[4], A. Damas-Segovia[1], J. D. Livingston[1], and Y. K. Ma[5]

[1] Max-Planck-Institut für Radioastronomie, Auf dem Hügel 69, 53121 Bonn, Germany
e-mail: sranchod@mpifr-bonn.mpg.de
[2] Wits Centre for Astrophysics, School of Physics, University of the Witwatersrand, 1 Jan Smuts Avenue, Johannesburg 2000, South Africa
[3] Department of Physics, University of Pretoria, Private Bag X20, Pretoria 0028, South Africa
[4] SKA Observatory, Jodrell Bank, Lower Withington, Macclesfield SK11 9FT, UK
[5] Research School of Astronomy & Astrophysics, Australian National University, Canberra, ACT 2611, Australia

Received 18 December 2023 / Accepted 14 March 2024

ABSTRACT

The *S*-band Polarisation All Sky Survey (SPASS/ATCA) rotation measure (RM) catalogue is the largest broadband RM catalogue to date, increasing the RM density in the sparse southern sky. Through analysis of this catalogue, we report a latitude dependency of the Faraday complexity of polarised sources in this catalogue within 10° of the Galactic plane towards the inner Galaxy. In this study, we aim to investigate this trend with follow-up observations using the Australia Telescope Compact Array (ATCA). We observe 95 polarised sources from the SPASS/ATCA RM catalogue at 1.1–3.1 GHz with ATCA's 6 km configuration. We present Stokes *QU* fitting results and a comparative analysis with the SPASS/ATCA catalogue. We find an overall decrease in complexity in these sources with the higher angular resolution observations, with a complexity fraction of 42%, establishing that the majority of the complexity in the SPASS/ATCA sample is due to the mixing-in of diffuse Galactic emission at scales $\theta > 2.8'$. Furthermore, we find a correlation between our observed small-scale complexity $\theta < 2.8'$ and the Galactic spiral arms, which we interpret to be due to Galactic turbulence or small-scale polarised emission. These results emphasise the importance of considering the maximum angular scale to which the observations are sensitive in the classification of Faraday complexity; the effect of which can be more carefully investigated with SKA-precursor and pathfinder arrays (e.g. MeerKAT and ASKAP).

Key words. polarization – techniques: polarimetric – Galaxy: general – radio continuum: galaxies

1. Introduction

Magnetic fields have an essential dynamic role in galaxy evolution, particularly in influencing the distribution of cold and ionised gas and the formation of stars (for a review, see Beck 2015). It is therefore important to fully understand the structure and strength of magnetic fields in galaxies. For example, there remain unanswered questions concerning the role of magneto-ionic turbulence in galaxy evolution and the correlation length of turbulence in the interstellar medium (ISM). A primary observational tool for probing magnetic fields in galaxies is the Faraday rotation of linearly polarised synchrotron emission from a background source as it passes through an intervening magneto-ionic medium (e.g. Lamee et al. 2016; Ma et al. 2020; Eyles et al. 2020). This background synchrotron radiation is typically from active galactic nuclei (AGN) and is parameterised by the Faraday rotation measure (RM) or, in the general case, characterised by the Faraday depth ϕ (Burn 1966),

$$\phi(L) = 0.812 \int_{s=0}^{L} n_{\rm e} \boldsymbol{B} \cdot {\rm d}\boldsymbol{s} \ {\rm rad\,m^{-2}}, \tag{1}$$

where $n_{\rm e}$ and $\boldsymbol{B}$ are, respectively, the electron density and magnetic field of intervening media along the line of sight $\boldsymbol{s}$, from the source to the observer L. A linearly polarised synchrotron-emitting source is considered Faraday simple when the entire source is subjected to a single ϕ only (i.e. a single Faraday thin polarised component is detected). Meanwhile, Faraday complex sources are composed of multiple polarisation components, each experiencing a different amount of Faraday rotation due to the distribution of the magneto-ionic medium between them (e.g. Farnsworth et al. 2011; Anderson et al. 2015). Such changes can either occur in the medium within or surrounding those sources, or in the Galactic foreground. In Faraday complex cases, the Faraday depth parameter allows for the characterisation of emitting Faraday components or magnetised sources through techniques such as RM synthesis (Brentjens & de Bruyn 2005) and Stokes *QU* fitting (Farnsworth et al. 2011; O'Sullivan et al. 2012). Faraday complexity is an observational classification and can be affected by various observational parameters, such as angular resolution, frequency, and telescope sensitivity (e.g. Sun et al. 2015).

Extragalactic sources (EGSs) exhibit a variation in complex Stokes Q and U spectra as a function of λ^2, which encode the physical magnetic field properties of the emitting sources and intervening Faraday screens (e.g. Farnsworth et al. 2011; O'Sullivan et al. 2012). With the advent of broadband receivers and backends in centimetre-wavelength radio telescopes – for example, the Australia Telescope Compact Array (ATCA), *Karl G. Jansky* Very Large Array (VLA), Australian Square Kilometre Array Pathfinder (ASKAP), and MeerKAT – we are, in principle, able to disentangle the various contributions in the polarised emission of Faraday complex sources by fitting multi-component physical models

to broadband Q and U spectra. This reveals rich properties of the magneto-ionic medium that were previously inaccessible with narrow-band data (e.g. O'Sullivan et al. 2017; Pasetto et al. 2018; Ma et al. 2019a). Methods such as QU fitting (Farnsworth et al. 2011; O'Sullivan et al. 2012) and RM synthesis (Brentjens & de Bruyn 2005) enable a good characterisation of Faraday complexity in EGSs; however, the field is still developing and there are open questions as to how the classification of Faraday complexities can be integrated into a physical model (e.g. Alger et al. 2021).

Previous studies have reported trends in Faraday complexity due to various foreground screens. Livingston et al. (2021) found that a large percentage (95%) of their sample of EGSs in the Galactic centre region are Faraday complex, which is attributed to small-scale (∼3 pc) turbulence in the Galactic foreground screen driven by stellar feedback. Anderson et al. (2015) analysed the environment of 14 Faraday complex sources at an arcminute resolution and identified several possible contributors to complexity, including foreground magneto-ionic galaxy clusters and an association of complexity with ionisation fronts near neutral hydrogen structures in the ISM.

As this paper subsequently demonstrates, it is crucial to consider observations at various angular scales to fully interpret the physical scale of the Faraday complexity. In principle, interferometric observations using long baselines can filter out the smoothly varying large-scale polarised emission (e.g. from the Galactic plane) to better disentangle the contributions of small-scale Faraday components in Faraday complex sources. Such components can be associated with small-scale magneto-ionic turbulence using the RM structure function (SF; Haverkorn et al. 2008; Stil et al. 2011). The SF can be used to reveal the outer scale of turbulent cells and how this changes with angular scale, as was done for the Galactic plane (Haverkorn et al. 2008; Livingston et al. 2021), the Milky Way at high Galactic latitudes (e.g. Mao et al. 2010), and Magellanic Clouds (e.g. Mao et al. 2012). This method can also improve our understanding of turbulence within nearby galaxies and the EGSs themselves (Anderson et al. 2015, 2016; O'Sullivan et al. 2017).

RM grids allow us to understand the variation of magnetic fields on various scales and in different cosmic environments, for example, nearby galaxies (e.g. Gaensler et al. 2005; Mao et al. 2008; Livingston et al. 2022), galaxy clusters (e.g. Anderson et al. 2021) or the Milky Way (Brown et al. 2007; Haverkorn et al. 2008; Hutschenreuter et al. 2022), dependent on the density of polarised background sources. This can be constrained by more sensitive, large-area polarised intensity surveys. Modern large area polarisation surveys at lower frequencies (≤1.1 GHz) include the LOFAR Two-metre Sky Survey (LoTSS, O'Sullivan et al. 2023) and Spectral and Polarisation in Cutouts of Extragalactic sources from the Rapid ASKAP Continuum Survey (SPICE-RACS, Thomson et al. 2023), with 2461 and 5818 sources respectively. The Taylor et al. (2009) catalogue derived from NRAO VLA Sky Survey is the largest RM catalogue to date, containing ∼40 000 sources at Dec > −40°, observed with two narrow bands (42 MHz) at ∼1.4 GHz. However, due to the limitations of narrow-band spectropoliametry, this catalogue contains inaccurate RMs due to the $n\pi$ ambiguity (Ma et al. 2019a), and increased RM uncertainties from off-axis instrumental polarisation (Ma et al. 2019b). The SPASS/ATCA RM catalogue (Schnitzeler et al. 2019, hereafter S19) is currently the most extensive large-area broadband catalogue at cm-wavelengths, with ∼4500 sources at Dec < 0°, covering 1–3 GHz. This catalogue has contributed to improving the Galactic Faraday sky reconstruction, by increasing the RM density to 1 RM per 5 deg^2 in the "southern hole" (Hutschenreuter et al. 2022). This unique catalogue will continue to have legacy value into the SKA-era, due to its polarised source density, sky coverage and, most importantly its broad bandwidth. It is therefore important to fully understand any systematic trends observed. However, the SPASS/ATCA catalogue has several limitations, particularly its low angular resolution, short integration time and the spectra-extraction methods used. Follow-up observations can help us better characterise these limitations to optimise the synergy and scientific output of this catalogue in the pre-SKA and SKA eras.

In this paper, we present a study of the polarisation properties of a subset of 95 sources from the SPASS/ATCA catalogue with follow-up observations from the ATCA. We investigate the dependence of Faraday complexity with Galactic latitude and how this dependency changes with higher angular resolution data. Furthermore, through the QU fitting and the analysis of Faraday spectra, we aim to discern whether this dependence is caused by mixed-in diffuse Galactic emission or small-scale turbulence in the Galactic Plane.

This paper is organised as follows; in Sect. 2, we detail the systematics we uncovered in the SPASS/ATCA catalogue and describe our observations and data calibration methods. Section 3 describes our methods of extracting and analysing the spectro-polarimetric data. Section 4 presents the results from RM synthesis, QU fitting and Faraday complexity classification. In Sect. 5, we discuss the physical origin of Faraday complex sources, how observational constraints affect the perception of complexity and resulting caveats regarding the SPASS/ATCA catalogue. We summarise and conclude in Sect. 6.

2. Data

2.1. The SPASS/ATCA RM catalogue

The SPASS/ATCA RM catalogue (S19) contains ∼4500 polarised sources at Dec ≤ 0 deg. The survey was observed using an unconventional snapshot mode (∼36 s on source integration time) with the ATCA in the 16 cm (1.1–3.1 GHz) band. S19 used the hybrid ATCA configuration H168 (excluding antenna 6) with baselines between 61–192 m. This configuration was chosen to maximise uv-coverage for equatorial sources, and corresponds to an angular scale of $2.8' < \theta < 9.0'$, and a reported angular resolution of $1' \times 2'$. The spectra were extracted directly from the visibilities without forming spectral image cubes to reduce processing time and the required storage space. The Stokes Q and U spectra were then fit iteratively for up to 5 Faraday-thin (simple) polarised components using the `FIRESTARTER` (Schnitzeler & Lee 2017) fitting algorithm. Here, sources are considered Faraday simple if they are best fit by a single polarised component and Faraday complex if they are best fit by multiple polarised components. The details of this classification and fitting methods used are elaborated on in Sect. 3.2.

The spatial distribution of Faraday simple and Faraday complex source density is shown in Fig. 1. In this plot, we find an increase in the number of sources with multiple fitted polarised components (Faraday complex) towards the Galactic plane, as well as a decrease in the number of sources with only one fitted polarised component (Faraday simple) towards the plane. This systematic trend was not previously noted in the literature. A reduction in Faraday simple source density and a corresponding increase in Faraday complex source density is seen above and below the Galactic plane. It is more pronounced towards the inner Galaxy in Q1 and Q4 ($30° > l > 0°$, $360° > l > 270°$). We

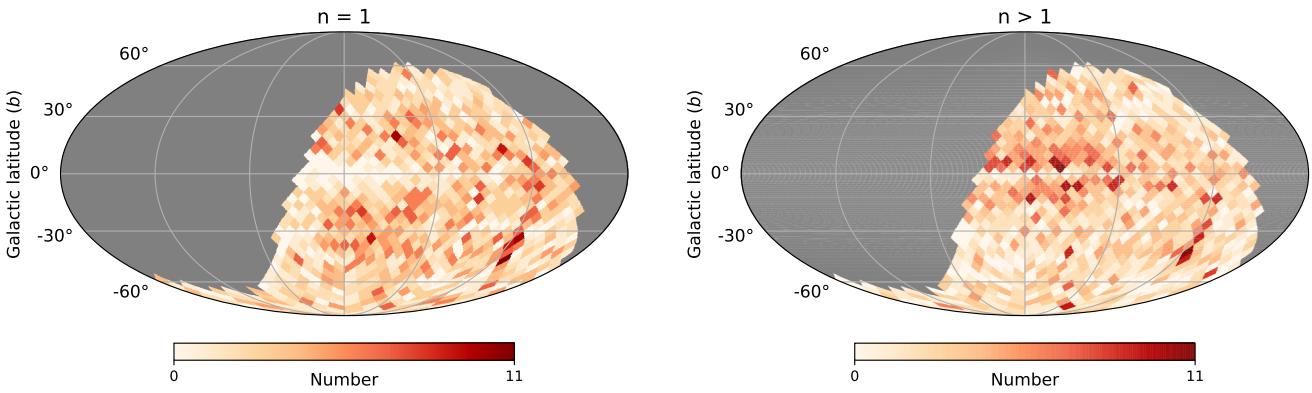

Fig. 1. Sky source density distribution for Faraday simple ($n = 1$, left) and Faraday complex ($n > 1$, right) polarised sources from the SPASS/ATCA catalogue in Galactic Mollweide projection. The colour bar indicates the number of sources per bin.

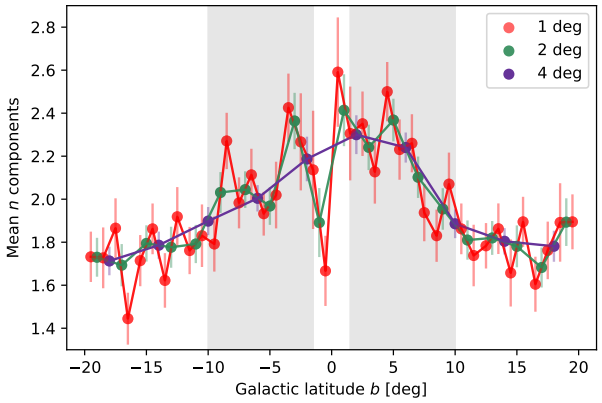

Fig. 2. Mean number of fitted polarised components for sources in the SPASS/ATCA RM catalogue, as a function of Galactic latitude. The different colours indicate different latitude bins. The grey, shaded regions indicate the latitude range of our observations.

also observe a deficit of Faraday simple sources at $b \sim 0°, l \sim 280°$, which is likely produced by the Gum Nebula (e.g. Stil et al. 2011; Purcell et al. 2015). The gap in Faraday complex sources that are very close to the Galactic plane ($|b| < 1.5°$), in the right panel of Fig. 1, is a selection effect from S19.

We further demonstrate this trend of increased complexity in Fig. 2, with the increase in the mean number of fitted polarised components (i.e. the Faraday complexity) as a function of Galactic latitude. The distribution is binned in latitude with bin widths of 1, 2 and 4 degrees, and a respective average of 47, 95 and 189 sources per bin. There is an apparent increase in complexity for sources closer to the Galactic plane at $|b| < 10°$. For larger latitude bins, this effect is more pronounced at positive Galactic latitudes. Sources that are Faraday complex, with multiple polarised components within the beam volume (i.e. along the line of sight, or within the beam resolution) that are intrinsic to the source, should be uniformly distributed across the sky without a dependency on Galactic coordinates. We propose that the increased complexity towards $b = 0°$ must therefore be Galactic in origin.

The short baselines and the large beam size in the S19 observations can be sensitive to the large-scale, diffuse polarised synchrotron emission in the Milky Way. This could be a likely scenario for added complexities in Stokes Q and U spectra close to the Galactic plane, particularly with the visibility spectra extraction method used in S19. Another possible scenario for an increase in Faraday complexity could be a turbulent foreground Faraday screen caused by small-scale structures and fluctuations in electron density and magnetic fields in the Milky Way (e.g. Haverkorn et al. 2008; Livingston et al. 2021). With higher-angular-resolution broadband observations, we aim to discern between the various scenarios to constrain the origin and scale of the complexity at low Galactic latitudes.

2.2. ATCA observations

We selected a sample of 105 extragalactic sources with high polarised intensities from the S19 catalogue for follow-up observations with the ATCA. We selected sources in close proximity to the Galactic plane, with $1.5° < |b| < 10°$ and $310° < l < 360°$, a polarised intensity lower limit of $P > 6$ mJy and polarised fractions $p_f > 0.01$. Of the selected sources, we classify ten as extended, and 95 as unresolved by inspecting the Stokes I images from the Rapid ASKAP Continuum survey (RACS; McConnell et al. 2020; Hale et al. 2021)-low DR1, at an angular resolution of 25″.

A total of 24 h of observations were obtained over two 12-h observing runs. The observations were done in the ATCA 16 cm band (1.1–3.1 GHz) with the 6 km configuration. 48 sources ($l > 333°$) were observed on 28 January 2022. Each source was observed for a total of 9.5 min over six (95-s) scans every ∼2 h, to optimise uv-coverage and parallactic angle coverage. The primary flux and bandpass calibrator PKS B1934−638 was observed for 20 min at the end of the observing run. We selected the closest secondary phase calibrators from the ATCA calibrator database. The secondary calibrators are summarised in Table 1. The six phase calibrators were observed intermittently throughout the observations, bracketing the scans of the target sources. The remaining 54 sources ($l < 333°$) were observed on 5 February 2022. Each source was observed for a total of 8.2 min over seven (70-s) scans. We observed PKS B1934−638 for 10 min and the four phase calibrators multiple times (∼60 s each) throughout the observation, as in the first observations. Three of the phase calibrators were also science targets (marked in Table 1). With our chosen array configuration, we have baselines from 192 m–6 km, resulting in angular scales of about $5.5'' < \theta < 2.8'$. With a lower maximum angular-scale sensitivity than S19, and a higher angular resolution, we aim to filter out any large-scale diffuse polarised emission from the Galactic plane and minimise beam depolarisation effects. These observations have a factor ∼14 longer integration time than S19, and we expect a factor ∼4 lower thermal noise. These condi-

Table 1. Source names and positions of secondary phase calibrators.

Observation date	Source name	RA (J2000)	Dec (J2000)
28 Jan 2022	PKS B1421−490	14:24:32	−49:13:49
	PKS B1511−47*	15:14:40	−47:48:30
	PKS B1600−44	16:04:31	−44:41:31
	PKS B1613−586*	16:17:17	−58:48:07
	PKS B1511−55	15:15:12	−55:59:33
	PKS B1352−63	13:55:46	−63:26:42
5 Feb 2022	PKS B1600−44	16:04:31	−44:41:32
	PKS B1622−310	16:25:55	−31:08:08
	PKS B1759−39*	18:02:43	−39:40:08
	PKS B1740−517	17:44:25	−51:44:44

Notes. The calibrators also used as science targets are marked with an asterisk.

tions allow us to distinguish whether the S19 observations have been contaminated by diffuse polarised synchrotron Galactic emission and to identify localised small-scale regions of magnetic field structure, for example, turbulence, patchy polarised emission.

2.3. Calibration and imaging

Data calibration was carried out following the standard procedure for Compact Array Broadband Backend (CABB) data with the MIRIAD software (Sault et al. 1995). PKS B1934−638 was used for bandpass, polarisation leakage and flux calibration. The calibrators listed in Table 1 were used for complex gain calibration. We did systematic manual and automatic flagging on all calibrators before and after calibration, using MIRIAD tasks `blflag` and `pgflag`. We flagged 100 MHz at the band edges due to poor sensitivity.

We created shallow Stokes I Multi-Frequency Synthesis (MFS) images for all target sources using MIRIAD's `invert`, `clean` and `restore`. Masks were generated at a 10σ threshold, and phase and amplitude self-calibration was performed with MIRIAD's `selfcal`. We used masked deconvolution to produce full-Stokes MFS images. The image sizes were 2000×2000 pixels with a pixel size of $0.7''$ and we used a Briggs (Briggs 1995) robust weighting of 0.5. We applied primary beam correction and smoothed to a common beam of $15'' \times 15''$, to account for beam variation across the 2 GHz bandwidth. This resolution corresponds to the major axis of the beam at the low-frequency end of the band, and at this angular resolution, 46 sources are spatially unresolved, and 49 have another spatial component within the 2' range of the S19 beam. An example image of source SPASS J160700−452802 is shown in Fig. 3. The Stokes V MFS images have a mean rms of ~97 μJy beam^{-1}, in comparison to the theoretical rms of ~80 μJy beam^{-1}.

We imaged spectral cubes in Stokes I, Q, and U with MIRIAD, aiming to maximise the per-channel signal-to-noise ratio (S/N) with broader channel width but also considering the corresponding increase in bandwidth depolarisation effects. In selecting an optimal channel width, we assumed a reasonable depolarisation limit of 95% (Gaensler et al. 2001). Considering our lowest unflagged frequency channel at 1.3 GHz and the highest |RM| from the S19 selected sample, the maximum channel width with negligible bandwidth depolarisation is $\Delta\nu = 17$ MHz. Therefore, we correspondingly formed spectral cubes with frequency steps of 17 MHz. The per-channel image sizes were 2000×2000 pixels with a pixel size of $0.7''$ and we used a Briggs

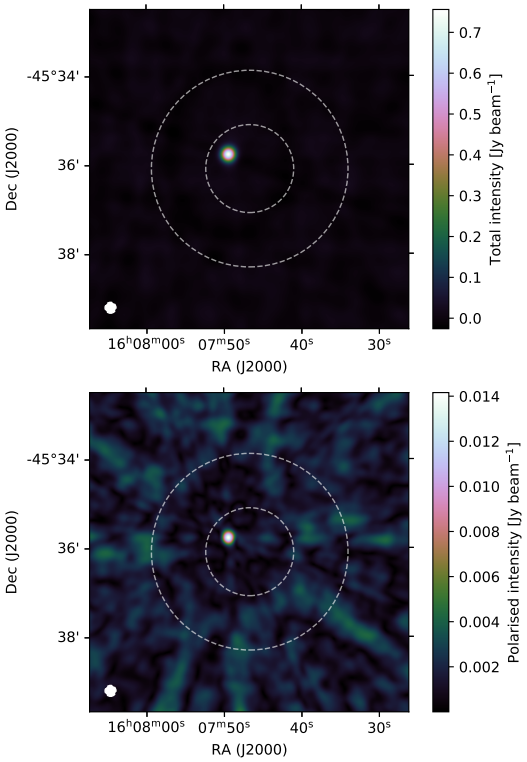

Fig. 3. Example of Stokes I (top) and polarised intensity (bottom) MFS images from our observations for source SPASS J160700−452802. The dashed circles show the major and minor axes of the synthesised beam for the Schnitzeler et al. (2019) data. The restoring beam for the example images is shown in the bottom left corner ($15'' \times 15''$).

robust weighting of 0.5. As with the MFS images, we applied primary beam correction and smoothed to a common beam of $15'' \times 15''$.

In addition to the 95 target sources, we observed ten known extended sources, as identified from RACS cutouts, to test the scale to which the selected array configuration can filter out diffuse, extended emission. The RACS images have an angular resolution of $25'' \times 25''$. We find that these sources show no smoothly varying diffuse emission at scales >3′ in total intensity or polarisation, and that this emission has successfully been filtered out in our observations. In some cases, there is small-scale patchy emission visible in the Stokes I MFS images. This emission all originates from the lobes of resolved radio galaxies and is not Galactic. We measure the peak flux density within the area of the S19 synthesised beam, and find on average that only 5% of the S19 total intensity flux density is detected.

3. Spectro-polarimetric analysis

3.1. Total intensity and polarised data extraction

We used two different methods of extracting the total intensity flux density values. Firstly, we determined the broadband total intensity $I_{\rm MFS}$ by fitting 2D Gaussians to the Stokes I MFS images using CASA (McMullin et al. 2007) `imfit`. Similarly, we fitted 2D Gaussians to the 2100 MHz frequency slice of the Stokes I image cubes to determine the total intensity at 2100 MHz I_{2100}, for a more direct comparison to S19. Secondly, we extracted spectra directly from the Stokes I, Q, and U spectral cubes from the position of the peak pixel in the Stokes I MFS images. We determined the RMS of the spectra from a

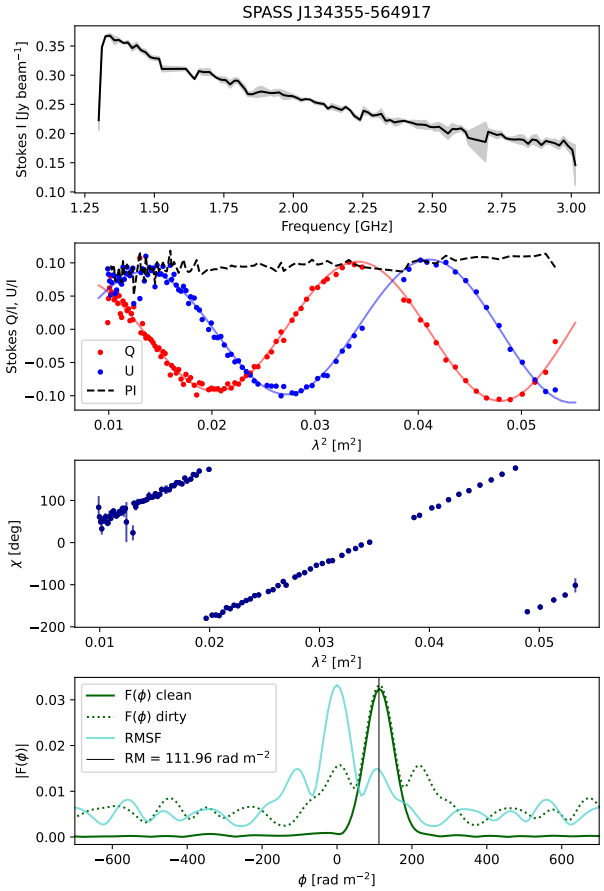

Fig. 4. Example of the spectra for source SPASS J134355−564917. From top to bottom: panel 1 shows the total intensity spectrum as a function of frequency. Panel 2 shows the Stokes Q/I and U/I spectra as a function of λ^2, with the fractional polarisation spectrum indicated by the dashed line. The fitted models for Stokes Q/I and U/I are also shown. In panels 1 and 2, the shaded regions indicate the uncertainties. Panel 3 shows the polarisation angle as a function of λ^2. Panel 4 shows the dirty (green dotted) and cleaned (green solid) Faraday spectrum with the Rotation Measure Spread Function (RMSF) in cyan. The black vertical line shows the peak Faraday depth.

$30'' \times 30''$ box at an angular distance of $\sim 8'$ from the pointing centre. Polarised intensity PI spectra were computed as

$$PI(\lambda^2) = \sqrt{Q(\lambda^2)^2 + U(\lambda^2)^2}. \quad (2)$$

We disregard the correction for noise bias due to the high signal-to-noise ratios of polarised intensity in our observations ($S/N > 10\sigma$, across the band). It should be noted that the PI spectra are only used for visual inspection during QU fitting, and we report our polarised intensity measurements and methods in Sect. 4.1.1. An example of the Stokes I, Q, U and polarised intensity spectra for source SPASS J134355−564917 are shown in Fig. 4.

3.2. QU fitting

We use QU fitting (Farnsworth et al. 2011; O'Sullivan et al. 2012) to characterise the magneto-ionic environment of the emitting source as well as any polarised components within the beam volume. This is done by fitting physical models describing the local and intervening magneto-ionic environments to the polarised emission from a source (i.e. Stokes Q, U as a function of λ^2). Broadband observations offer a unique advantage for this. In particular, we want to characterise the complexity of sources in the sample based on the model with the best fit. Here, we assume all targets to be synchrotron-emitting point sources, with the possibility of the presence of additional synchrotron-emitting Faraday-thin components within the beam volume. This may include cases where the magnetised plasma is intrinsic to the point source, or the Faraday-rotating foreground screen(s) is Faraday thick (see Sect. 3.3) or turbulent. Before fitting, the Stokes Q and U spectra are divided by the Stokes I spectrum to remove all first-order spectral index effects. Following Schnitzeler & Lee (2017) and S19, we fitted models describing the sum of up to five Faraday thin components:

$$q(\lambda^2) = \sum_{j=1}^{n} q_j \left(\frac{\lambda^2}{\lambda_{\rm ref}{}^2}\right)^{-\delta\alpha_j/2} \cos[2(PA_j + \phi_j\lambda^2)] \quad (3)$$

$$u(\lambda^2) = \sum_{j=1}^{n} u_j \left(\frac{\lambda^2}{\lambda_{\rm ref}{}^2}\right)^{-\delta\alpha_j/2} \sin[2(PA_j + \phi_j\lambda^2)], \quad (4)$$

where $u = U/I$ and $q = Q/I$, PA is the intrinsic polarisation angle, ϕ is the rotation measure, $\delta\alpha$ is the remaining spectral index of a given polarised component, and $\lambda_{\rm ref}$ is the wavelength at which the spectral index is determined. We fitted all sources with $n = [1, 2, 3, 4, 5]$. The derivation of this model and any assumptions made are detailed in Appendix A. With this simplified model, any intrinsic complexity within the source or turbulence in intervening Faraday screens will be modelled as separate polarised components. We use this schema in lieu of more complex models for a direct comparison of complexity classification with S19. Here, a linearly polarised synchrotron-emitting source is considered Faraday simple when there is a single polarised component within the beam volume ($n = 1$), and Faraday complex when there are multiple or composite polarised media ($n > 1$). We compute the Bayesian Information Criterion (BIC) to select the best-fit model. For two respective models, a difference in BIC greater than 10 represents "very strong" evidence in favour of the model with the smaller n. Given this definition, we select the model with the lowest BIC as the preferred model, except if the difference between the two lowest BIC values is less than 10. In this case, the model with the smallest n is selected. An example of the fitted QU-model for source SPASS J134355−564917 is shown in Fig. 4.

3.3. RM synthesis

The complex polarised intensity can be expressed as a function of Faraday depth ϕ, defined in Eq. (1),

$$PI(\lambda^2) = Q(\lambda^2) + iU(\lambda^2) = \int_{-\infty}^{\infty} F(\phi) \exp(2i\phi\lambda^2) {\rm d}\phi. \quad (5)$$

We note that $F(\phi)$ is the Faraday spectrum (historically referred to as the Faraday dispersion function), the complex polarised intensity at a given Faraday depth (Burn 1966; Brentjens & de Bruyn 2005). Sources are considered Faraday simple when all polarised emission is at a single value of ϕ (i.e. the Faraday spectrum is a delta function). Physically, this could interpreted as a single polarised component, limited by the given λ^2 sampling. Sources are considered Faraday complex when they emit at multiple ϕ values. In this case, there are multiple peaks at different ϕ in their Faraday spectrum (i.e. multiple polarised components). From the S19 catalogue, we expect a large fraction of our sample to be Faraday complex.

The observed Faraday spectrum $\tilde{F}(\phi)$ is the convolution of $F(\phi)$ with the Fourier transform of a weighted sampling function in the λ^2 domain, called the RM spread function (RMSF). We require a deconvolution algorithm to approximate the true $F(\phi)$. The resolution of a Faraday spectrum and the precision of ϕ measurements determined through RM synthesis are characterised by three quantities, $|\phi_{\rm max}|$ the maximum observable Faraday depth, $\delta\phi$ the resolution in Faraday space, and the maximum scale in Faraday space to which one is sensitive. These quantities are linked to the scale and resolution of the QU-spectra (Brentjens & de Bruyn 2005; Dickey et al. 2019). We determine the theoretical measurements of these quantities to be $|\phi_{\rm max}| = 1732\,{\rm rad\,m^{-2}}$, $\delta\phi = 92\,{\rm rad\,m^{-2}}$ and max-scale = $317\,{\rm rad\,m^{-2}}$ for our observation setup. After flagging, calibration and RMsynthesis, we find the median observed FWHM of the RMSF to be $\delta\phi_{\rm obs} = 80\,{\rm rad\,m^{-2}}$.

We used RM synthesis (Brentjens & de Bruyn 2005) with RM clean (Heald 2009) to determine the $|F(\phi)|$, RMSF and the peak Faraday depth(s) of the sources. RM synthesis was performed using `RM-Tools` (Version 1.1.1, Purcell et al. 2020) from the Canadian Initiative for Radio Astronomy Data Analysis (CIRADA) tools. We used a clean threshold of 3σ for RM clean, and elect to divide the Stokes Q and U spectra by a polynomial fit to the Stokes I spectrum. Throughout this work, peak Faraday depth ϕ and RM are used interchangeably.

4. Results

Of the 105 sources, we excluded extended sources, due to the expected non-detection of large-scale emission. Our final sample consisted of 95 sources. The brightest source in the sample is SPASS J160017−464922, with $I_{\rm MFS} = 5.1 \pm 0.1$ Jy and the mean Stokes I flux density is $I_{\rm MFS} = 0.62 \pm 0.08$ Jy. We present a catalogue of all measured polarisation parameters as well as the results of QU fitting. The catalogue is per the RMTable2023 standards presented in Van Eck et al. (2023), and is available as part of the consolidated RMTable catalogue (v1.2.0)[1]. This includes the following quantities and their associated errors, total intensity $I_{\rm MFS}$, polarised intensity, $\phi_{\rm peak}$. The catalogue also includes ϕ_j as specified in Eqs. (3) and (4). An abridged version of the catalogue is shown in Appendix B.

4.1. Verification of SPASS/ATCA catalogue

To verify the methods used in S19 and to assess our measurements, we compare our results to those from S19. In this section, we compare flux density measurements and RMs.

4.1.1. Flux density measurements

We consider the fractional difference between the Stokes I flux density measurements in our work and various catalogues in the literature. Figure 5 shows a fractional comparison ΔI_{2100} between the total intensity flux density from the S19 catalogues $I_{\rm S19}$ and the measured flux density at 2100 MHz, where

$$\Delta I_{2100} = \frac{I_{2100} - I_{\rm S19}}{I_{2100}}. \quad (6)$$

We find these flux density measurements broadly consistent, with a mean $\Delta I_{2100} = 0.050 \pm 0.018$ (i.e. 5% of I_{2100}). We do expect a non-zero residual due to the difference in uv-coverage between observations. We also compare the measured MFS total intensity flux densities with the RACS catalogue (Hale et al. 2021), assuming a spectral index of $\alpha = -0.7$ to interpolate the RACS flux densities from 887 MHz to 2100 MHz, $I_{\rm RACS,2100}$. Similar to Eq. (6), we define the fractional comparison as

$$\Delta I_{\rm MFS} = \frac{I_{\rm MFS} - I_{\rm RACS,2100}}{I_{\rm MFS}}. \quad (7)$$

A histogram of $\Delta I_{\rm MFS}$ is shown in Fig. 6. We find the flux density measurements to be consistent, with a mean $\Delta I_{\rm MFS} = 0.024 \pm 0.018$ (i.e. 2% of $I_{\rm MFS}$). In doing a fractional comparison of the measured flux densities of $I_{\rm MFS}$ and I_{2100}, we find an inconsistency, with an 11% mean fractional residual. Further investigation into the effect of broadband imaging on flux density measurements and how this compares to visibility spectra is beyond the scope of this work, given our objectives.

For the purpose of the catalogue, we determined the PI of a source as the sum of the peak amplitudes in the Faraday spectrum. We find a broad agreement between the measured PI and the reported values in S19, with a mean fractional residual of 0.06 ± 0.03. The spread of the fractional residuals is significantly larger than for the Stokes I flux densities (Fig. 5), with $\sigma = 0.30$. Furthermore, 18 sources have fractional residuals beyond 3σ. The majority of the outliers have low polarised intensity at $PI < 20$ mJy. Here, we see a deviation from the consistency with S19, with larger PI measurements in S19. On account

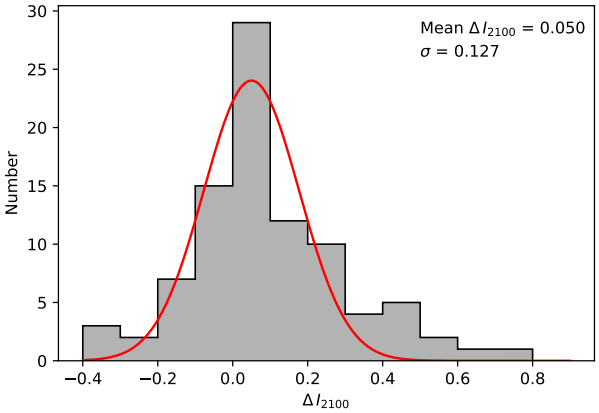

Fig. 5. Histogram of ΔI_{2100}, defined in Eq. (6). A Gaussian fit is plotted in red, with the resultant mean and standard deviation shown on the plot. The bin width is 0.1.

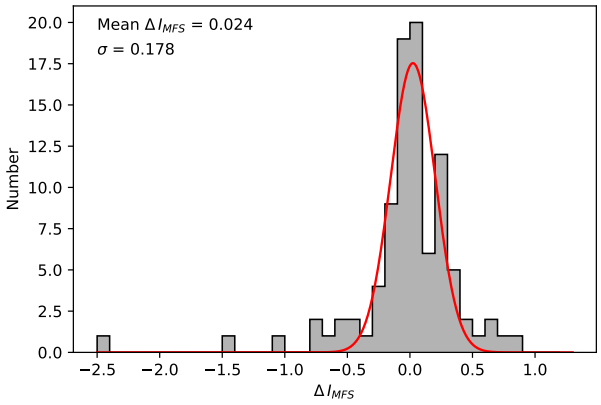

Fig. 6. Histogram of $\Delta I_{\rm MFS}$, defined in Eq. (7). A Gaussian fit is plotted in red, with the resultant mean and standard deviation shown on the plot. The bin width is 0.1.

[1] Source catalogue also available at: https://doi.org/10.17617/3.NRFFQB

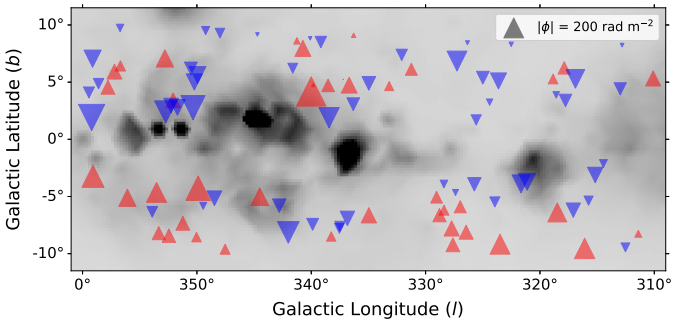

Fig. 7. Spatial distribution of observed sources plotted on the Wisconsin H-Alpha Mapper (WHAM) Sky Survey (Haffner et al. 2003) Hα map of the Galactic plane (greyscale). The marker size is proportional to the amplitude of the measured peak Faraday depth of the source, as indicated in the legend. Red upward triangles are positive ϕ and blue downward triangles are negative ϕ.

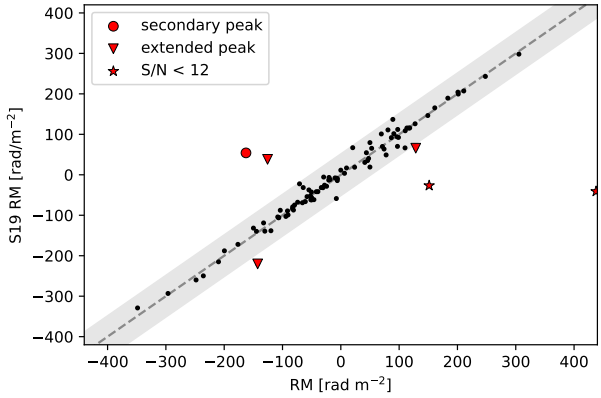

Fig. 8. Comparison between the measured ϕ from this work and those from S19. The uncertainties on our ϕ measurements are typically of order ~1 rad m^{-2} and are not visible on the scale of this plot. The shaded region indicates 5σ of the residuals. The outliers beyond this are plotted in accordance with the explanation in the main text. Cases (i), (ii) and (iii) are plotted as red stars, circles and triangles, respectively.

of different observational setups, we expect these inconsistencies in polarised intensity due to the filtering of and sensitivity to different physical scales of linearly polarised emission.

4.1.2. Rotation measures

The mean ϕ of the sample is -4.50 ± 13 rad m^{-2}, the mean $|\phi|$ is 99 ± 13 rad m^{-2} and the maximum $|\phi|$ is 437.73 rad m^{-2}. The spatial distribution of our sources and their peak Faraday depths are plotted in Fig. 7. Figure 8 shows a comparison between our measurements and those from the S19 catalogue. We find the majority of ϕ measurements consistent with the S19 measurements, with six outliers beyond 5σ. We examine the Faraday spectra of the 5σ outliers on a case-by-case basis and identify three causes of this inconsistency. These causes are listed below and are indicated in Fig. 8.

(i) Sources with low S/N peak Faraday depth (i.e. depolarised in our observations). Here, sources have $S/N < 12$, that is, 10% of the mean S/N of the sample.

(ii) Sources where our peak Faraday depth measurement corresponds to a secondary peak in the S19 Faraday spectra.

(iii) Sources which are Faraday thick in the S19 Faraday spectra, or are composed of multiple unresolved peaks. In this case, our determined ϕ from RM synthesis lies within the Faraday depth range of the S19 extended structure but has an offset from the maxima.

4.2. Galactic latitude dependence of Faraday complexity

In this section, we present the Faraday complexity classification of sources using the QU fitting method outlined in Sect. 3.2. We find that 40 (42%) sources are complex, which is less than half of the 90% complex sources found for the same sample in S19. The number of sources for a given number of Faraday components in comparison to S19 is shown in Fig. 9.

In Fig. 10, we plot the average number of Faraday components as a function of Galactic latitude. It should be noted that our sample is unevenly split on either side of the Galactic plane, with 52 sources above the plane and 43 sources below the plane. We find an overall decrease in the number of components per latitude bin in this work compared to S19, with a mean difference in number of components as $|\Delta n| = 1.1 \pm 0.1$. We find the slope of the increase of the average number of components towards the Galactic plane to be lower below the plane in both samples,

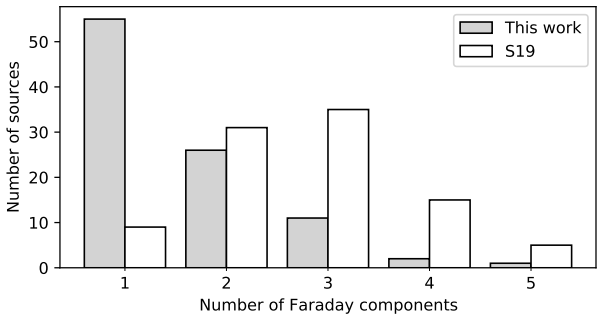

Fig. 9. Histogram comparing the number of sources best fit by a given QU fitting model, as described in Eqs. (3) and (4), for this work (grey) and S19 (white).

which is also observed for the full S-PASS/ATCA catalogue, as shown in Fig. 2. In our measurements, we also find that the average number of components is higher at positive latitudes than at $b < 0°$. We note in Sect. 2.3 that 49 sources have a secondary spatial component within the S19 beam. For these sources, the mean $|\Delta n| = 1.32 \pm 0.1$, and for the unresolved sources, we find $|\Delta n| = 0.96 \pm 0.1$. The increased $|\Delta n|$ for sources with multiple components suggest that the exclusion of these spatial components from our spectra does contribute to our observed reduction of complexity with respect to S19. However, the $|\Delta n| \sim 1$ for unresolved sources indicates that this is not the dominant effect for the reduced number of fitted components in Fig. 10.

We return to the scenarios introduced in Sect. 2.1 for the cause of increased Faraday complexity towards the Galactic plane, first considering the case for small-scale turbulence. It is unlikely that small-scale turbulence has a strong latitude-dependent effect on complexity at the angular resolution of the S19 survey. Because we have an overall consistency of ϕ with the S19 catalogue, we do not spatially resolve turbulence within the Galactic plane foreground. In the cases of multiple spatial components in the S19 beam, we also find consistent ϕ with both the S19 catalogue and the brightest component, with a median difference in ϕ of 7 rad m^{-2}, well within 5σ in Fig. 8. Basu et al. (2019) show through MHD simulations that Faraday depth varies smoothly along the line of sight due to spatially correlated structures in the magnetic field, and that the scale of magnetic field variation is consistent with the driving

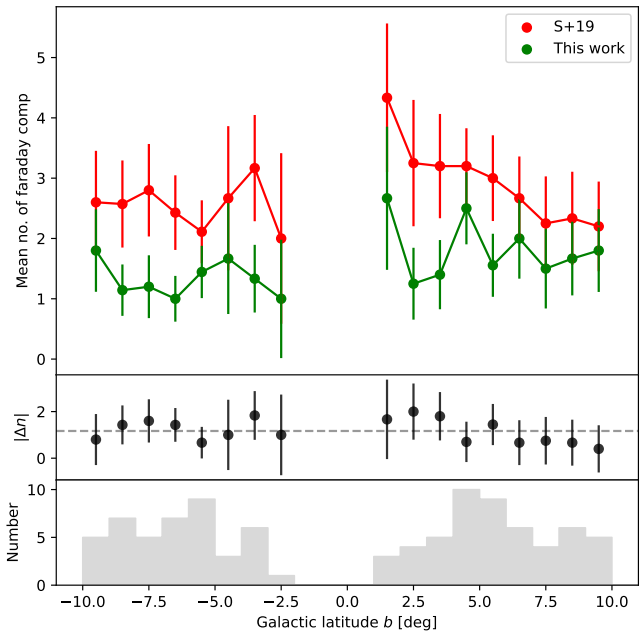

Fig. 10. Average number of fitted Faraday components of the observed sources (green) and the same sources from S19 (red) as a function of Galactic latitude. The errorbars are Poisson uncertainties. The central panel shows the difference in the average number of components per bin between this work and S19. The mean difference ($|\Delta n| = 1.1 \pm 0.1$) is plotted as the dashed line. The bottom panel shows the number of sources in each 1-degree bin.

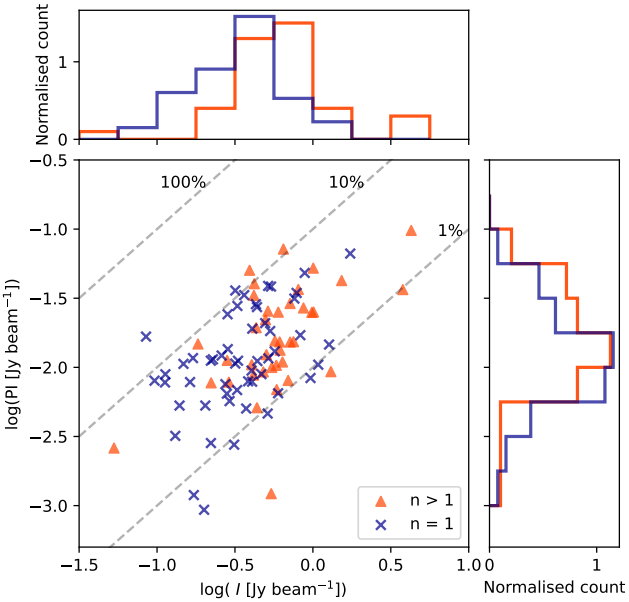

Fig. 11. Scatter plot of the polarised intensity and the MFS total intensity flux densities. Faraday simple sources are plotted as blue crosses and Faraday complex sources are plotted as orange triangles. The grey dashed lines represent constant fractional polarisation, labelled as a percentage. The histograms above (to the right of) the plot shows the distribution of the total intensity (polarised intensity flux densities) for the Faraday simple and complex sources, in blue and orange, respectively.

scale of turbulence. If the increase of complexity in S19 is purely due to Galactic plane turbulence, we would observe the same number of Faraday components between this work and S19.

In the case for mixed-in Galactic diffuse emission, with the low angular resolution S19 observations (∼2′), approximately 64 times more diffuse flux density would be detected than in our observational setup. This would result in S19 detecting one additional Faraday component from diffuse emission, as observed (Fig. 10). Because the average number of Faraday components decreases by one in our observations, it is likely that the filtered-out components correspond to large-scale regions of polarised emission from the Galactic plane at scales >2.8′, corresponding to 2.4 pc at a 3 kpc distance. This follows the assumption that the polarisation angle of the extended Galactic foreground does not vary on large scales, and that polarised intensity remains approximately constant. We can therefore conclude that mixed-in polarised Galactic synchrotron emission is the dominant cause for the increase of the number of Faraday components towards the Galactic plane observed in S19, a trend that we no longer observe in observations with a smaller maximum angular scale. Despite the overall decrease in complexity, there remains complexity in 42% of the sources. We suggest that these complexities are due to turbulence in the Galactic plane or polarised emission at scales <2.8′, and examine these sources on a case-by-case basis in Sect. 5.

It should be noted that Fig. 10 shows an increase in complexity at $b \sim 5°$. This is caused by a bias in observed sources, where we have an overdensity of sources that are within 5 deg of longitude of the Galactic centre at $b \sim 5°$ (see Fig. 16). If we consider Fig. 10 excluding sources with $l > 355°$, we no longer observe this trend.

5. Discussion

In the following section, we outline the various physical mechanisms that introduce Faraday complexity within a beam volume, and discuss how this can be interpreted or perceived differently depending on the observational setup and telescope limitations. In Sect. 5.2 we examine the origin of complexity in our observed sample in detail.

5.1. The perception of complexity

In Fig. 11 we plot the total intensity vs. polarised intensity, along with histograms for the distributions for Faraday simple and complex sources. The majority of sources have a fractional polarisation between 1% and 10%. We find that Faraday complex sources have preferentially higher flux density values in both polarised and total intensity. This shows that it is more likely for a source to be classified as complex if it has a higher S/N polarised intensity (based on the chosen method of classification). For fainter sources in polarised intensity, possible secondary components may not be detected with sufficient S/N, and these sources would preferentially be classified as simple. This bimodality is more evident in total intensity and is consistent with Anderson et al. (2015), who found through simulations that there is a limit to the detection of complex sources with S/N. Although there are significantly lower S/N levels in the S19 catalogue, we observe an overall decrease in the number of complex sources due to the lower resolution and the sensitivity to larger maximum angular scales in S19.

In Sect. 4.2, we find a significant difference in complexity fractions between our observations and S19. The top row in Fig. 12 (panels A and B) shows a depiction of the effect of multi-resolution observations on our perception of Faraday complexity. Both depict a linearly polarised EGS with a smooth polarised

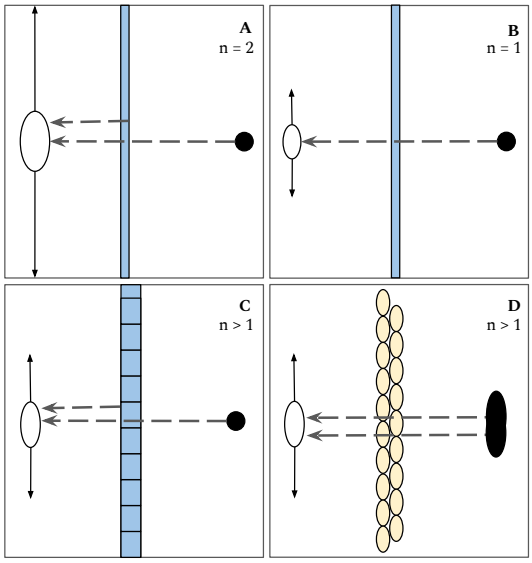

Fig. 12. Diagram illustrating the effect of multi-resolution observations on the interpretation of Faraday complexity. The black circle indicates a linearly polarised, synchrotron-emitting source, spatially unresolved in A, B and C. The white ellipse indicates the angular resolution of the observations, and the vertical arrows indicate the maximum angular scale of the observations. The blue-shaded regions are the polarised emitting foreground, with emission at smaller scales in panel C, and the yellow-shaded region is a turbulent foreground screen. The dashed arrows show the paths of emission from the various sources, and the number of observed Faraday components is indicated in the top right corner.

emitting foreground. Panel A describes a scenario where the observational setup has a lower angular resolution and a larger maximum angular scale (e.g. S19). In this case, the telescope is sensitive to the linearly polarised emission from the observed background EGS, as well as the foreground. The polarised emission of the background source undergoes Faraday rotation when passing through the extended foreground. From the observer's point of view, there are two polarised components within the beam volume, $n = 2$ (Faraday complex), following the classification scheme in Sect. 3.2. Panel B shows an identical system with a different observational setup. Here, we have higher angular resolution, and the maximum angular scale of the observation is smaller than the extended foreground polarised emission, therefore, the majority of the foreground emission is filtered out (e.g. this work). The emission from the EGS will undergo Faraday rotation from the foreground, but only a single polarised component is detected within the beam volume, $n = 1$ (Faraday simple) within this observation setup.

For completeness, we illustrate two cases of foreground-induced complexity detectable with our observational setup. Panel C is a similar case to panel B, with a smooth, extended foreground component that has been filtered out. However, here we consider small-scale (i.e. smaller than the beam), patchy polarised emission in the foreground. The presence of such emission within the beam volume will increase the number of Faraday components, that is, $n > 1$. Panel D illustrates an example of a turbulent foreground screen. Depending on the scale of the turbulent cells (e.g. Livingston et al. 2021), various regions of polarised emission from the background source may experience different amounts of Faraday rotation, while passing through different turbulent cells. This would result in multiple polarised components being detected within the beam volume ($n > 1$,

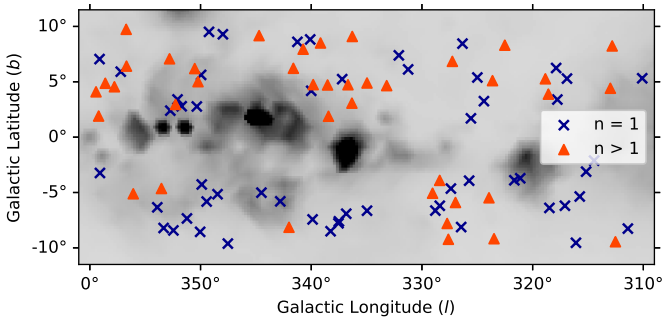

Fig. 13. Spatial distribution of sources, as shown in Fig. 7. The Faraday simple sources are indicated by blue crosses and the Faraday complex sources are plotted as orange triangles.

Faraday complex). To ascertain this and constrain the scale of turbulence, the extent of the background source would have to be larger than the scale of turbulence. Observations of well-modelled extended sources or a dense RM grid are required to investigate this further.

Our results emphasise the importance of observing Faraday complexity at different angular scales to disentangle various polarised components within the beam volume. The removal of the smooth large-scale emission from the foreground is crucial for an accurate interpretation of the linear polarisation signal from background sources for Galactic magnetism studies. The disregard of this can mislead our understanding of small-scale magnetic structures through observation of background EGSs. In general, the effective removal or filtering of Galactic contamination at all scales is important for determining accurate polarisation information from EGSs. The effect of maximum angular scale on Faraday complexity should be carefully considered depending on the science goals. This effect can be further investigated with broadband observations of the Galactic plane regions with more complex interferometer arrays, such as the MPIfR-MeerKAT Galactic Plane Survey, (MMGPS; Padmanabh et al. 2023). Within the footprint of this survey, it is expected that $\sim 2.5 \times 10^4$ linearly polarised sources will be detected. Furthermore, a larger sample will enable a more robust understanding of the effect of Faraday complexity with angular scale. In comparison to cm-wavelengths, m-wavelength observations of extragalactic sources are largely affected by depolarisation, and are therefore not sensitive to Faraday complex sources. However, modern m-wavelength surveys (LoTSS; O'Sullivan et al. 2023) can contribute to the analysis of Faraday complexity by providing a confirmed Faraday simple sample for a holistic investigation of this classification scheme.

5.2. The origin of complexity

In Sect. 4.2 we identified that the Faraday complexities in the observed sample must originate from polarised emission at scales $< 2.8'$ (i.e. the maximum angular scale of our observations), but it is difficult to distinguish whether the additional polarised components are intrinsic to the extragalactic source, or small-scale, patchy Galactic polarised emission (e.g. Schnitzeler et al. 2009) or turbulence. Figure 13 shows the spatial distribution of Faraday simple and complex sources. From this figure, we show that the complex sources are not uniformly distributed on the sky and it is, therefore, unlikely that the observed complexity is solely intrinsic to the sources. We subsequently evaluate this quantitatively in Sect. 5.2.3.

5.2.1. Faraday spectrum classification

With the limitations of our selected *QU* fitting models, we further investigate the Faraday complex sources and the approximations made when fitting these models. To better understand the origin of complexity for our observed sources, we manually inspect and classify the Faraday spectra of the complex sources, also considering the limitations in the Faraday depth domain and Faraday resolution due to the observational parameters. We use four different labels to classify the complex sources:

(i) 'Broad': We fitted Gaussian functions to the dominant peak in the Faraday spectrum and the RMSF. A source is considered broad if the FWHM of the Faraday spectrum peak is 10% greater than that of the RMSF (see e.g. Ma et al. 2019a). Additionally, more than one of the ϕ identified in *QU* fitting should be within the Faraday spectrum peak. This scenario would describe an external Faraday thick source, for instance, a Faraday rotating 'slab' of thermal electrons and magnetic fields overlapping with the synchrotron-emitting volume, leading to a differential Faraday rotation along the line of sight. This scenario could also describe a secondary, low amplitude peak at a $\phi < 3\sigma$ of the dominant peak ϕ, that cannot be fully resolved as a separate peak within our Faraday depth resolution.

(ii) 'Unresolved': The FWHM of the dominant peak is equal to, or up to 10% greater than the FWHM of the RMSF, and there are multiple QU fitting identified ϕ values within the FWHM of the peak. This classification has the same physical scenario as the broad classification, with the exception that the difference in Faraday depth between multiple peaks or the Faraday thickness of the intervening medium is unresolved in Faraday depth space with our frequency sampling.

(iii) 'Big sec': The secondary resolved peak, or any of the non-dominant Faraday spectrum peaks, has an amplitude ≥50% of the amplitude of the dominant peak. This scenario could describe a secondary Faraday rotating and emitting source. From its high amplitude, we could assume this is likely not due to Galactic polarised emission.

(iv) 'Small sec': Any of the non-dominant peaks have an amplitude <50% of the dominant peak.

In this scheme, spectra can be classified with any number of these labels (e.g. broad and small sec) corresponding to properties of multiple peaks, and an example of spectra for the various classifications is shown in Fig. 14. For the broadened and unresolved sources, we cannot reliably derive the amplitude of the multiple polarised components. In these cases, we consider an upper limit as the amplitude of the Faraday spectrum at the Faraday depth of the fitted RM. For sources classified as unresolved, we determine the difference in Faraday depth between the two unresolved components $|\mathrm{RM}_1 - \mathrm{RM}_2|$, for RMs obtained from *QU* fitting. We find 15 unresolved sources, with a mean $|\mathrm{RM}_1 - \mathrm{RM}_2|$ of 34.35 rad m^{-2}. We provide a further discussion on this classification in Sect. 5.2.3.

5.2.2. Multiple spatial components

In Sect. 2.3, we smoothed the MFS images and image cubes to a common resolution of 15″ × 15″ to account for beam variation across the band. To distinguish which sources have multiple spatial components within the beam, we visually inspect the high-frequency end of the unsmoothed image cubes at 3014 MHz. These images have a typical resolution of 3.5″ × 5.2″. We manually identify sources with multiple components in total intensity within the smoothed beam and find 23 (i.e. 24%) sources that have multiple spatial components. We only consider the Stokes

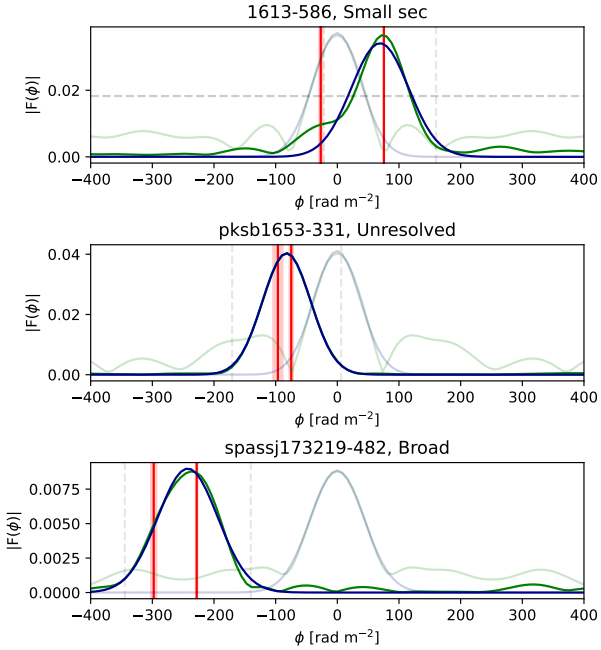

Fig. 14. Examples of the Faraday spectrum classes 'small sec' (top), 'unresolved' (centre), and 'broad' (bottom) as described in Sect. 5.2.1. The plots show the Faraday spectrum (green) and the fitted Gaussian (blue). The same is shown for the RMSF and its Gaussian fit, in lower opacity. The red vertical lines show the fitted ϕ from *QU* fitting and their uncertainties. The 3σ extent and the half-maximum amplitude of the fitted Gaussians are indicated with dashed grey lines.

I images here, as we are unable to reliably manually identify peaks in polarisation due to low S/N in the channel maps. A breakdown of the complexity classification of these sources is given in Table 2.

We do not detect multiple bright Faraday peaks (Big sec class) in any of these sources and find that 8 (34%) of the multi-component sources have a faint secondary Faraday peak (Small sec class). However, we cannot ascertain that the multiple Faraday components correspond to the observed multiple spatial components. Of the 23, 10 sources are Faraday simple. This is consistent with O'Sullivan et al. (2017) and Ma et al. (2019a), who find that spatially extended sources can be Faraday simple, at angular resolutions of 1″ and 45″, respectively. An explanation for this trend could be the Laing-Garrington effect (Laing 1988; Garrington et al. 1988), where we expect a large asymmetry in polarised intensity between the two Faraday components due to depolarisation. This may be an extreme case of the Laing-Garrington effect where one spatial component is completely depolarised. A more likely explanation is the effect of AGN lobe orientation, where both components encounter similar Faraday screens along the line of sight (e.g. O'Sullivan et al. 2017), and therefore have similar ϕ. Given we have only 23 sources with multiple spatial components, we do not have a large enough sample for a deeper investigation into this trend. We would require higher resolution observations across a broad frequency range to analyse these components separately to better understand the individual systems.

We briefly discuss the case of Faraday complexity in sources with a single spatial component (i.e. spatially unresolved). The complexity classification for these sources is detailed in Table 2. We find that 38% of spatially unresolved sources are Faraday complex. Although it has been shown in the literature that Faraday complexities can be linked to source morphology at

Table 2. Number (percentage) of sources with each complexity classification and Faraday spectrum classification (Sect. 5.2.1) for the sources with multiple spatial components, as well as the number of sources with each complexity classification for sources with a single spatial component.

Source classification	Number
Multiple spatial components:	*23*
Faraday simple	10 (44%)
Faraday complex	13 (56%)
Broad	2
Unresolved	6
Big sec	0
Small sec	8
Single spatial component:	*72*
Faraday simple	45 (62%)
Faraday complex	27 (38%)

Notes. It should be noted that Faraday complex sources may be classified into multiple categories.

a $\sim 10^{-2}$ arcsec scale (e.g. Ma et al. 2019a), we would require higher resolution observations to explore this further and a statistically significant sample size to investigate the prevalence of this. Because we find a larger percentage of complex sources in spatially resolved sources (56%) compared to spatially unresolved sources (38%), it is certainly possible that the complexity is purely intrinsic to the EGSs. However, due to the Galactic dependency of complexity in S19 (Sect. 2.1), it is important to investigate whether the remaining complexity in the observed sample is Galactic in origin. We do so in the following section.

5.2.3. Galactic ISM and complexity in the spiral arms

We consider various interstellar media as possible tracers for turbulence or small-scale fluctuations in the Galactic plane. In the presence of a turbulent screen, we expect to observe depolarisation effects and detect multiple fitted polarised components, given the *QU* fitting models we have used. Additionally, Anderson et al. (2015) suggest that HI and Hα regions act as a proxy for identifying regions where complex Faraday screens are present. To investigate this, we measure the HI column densities from the HI4PI survey maps (McClure-Griffiths et al. 2009; HI4PI Collaboration 2016), as well as the Hα flux densities from the WHAM Hα map (Haffner et al. 2003). We do not find a direct relationship between complexity and these various gas density measurements. The typical angular resolution is 14.5′ for the HI4PI maps in the southern sky and 1° for WHAM Hα, all significantly larger than the scale at which we measure the complexity. It is therefore difficult to reliably investigate this relation without higher resolution observations.

We have investigated the Galactic latitude dependence of Faraday complexity and now consider an increase in complexity at particular Galactic longitudes between $310° < l < 360°$. Our observations include the Crux-Centaurus ($l \sim 310°$), Norma ($l \sim 328°$), Inner Perseus ($l \sim 338°$) and Inner Sagittarius ($l \sim 343°$) spiral arm tangents (e.g. Vallée 2022) as well as the Galactic centre, where the spiral arm tangents are estimated from the broad ^{12}CO(1-0) tracer. In Fig. 15 we plot the fraction of complex sources per longitude bin. It should be noted that the longitude range for spiral arms on this figure is indicative, and we cannot constrain the full extent of the individual spiral arms.

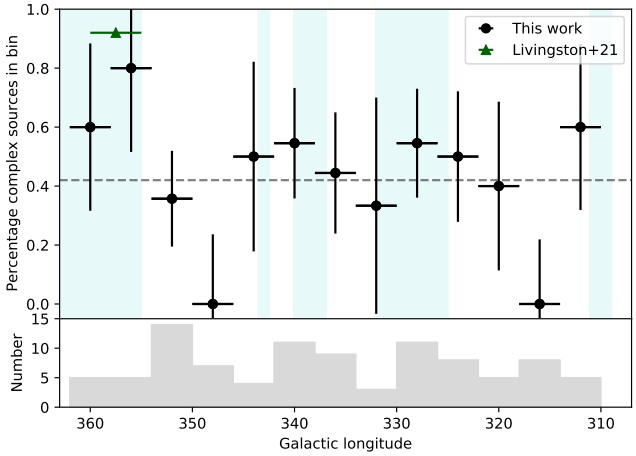

Fig. 15. Percentage of complex sources for each longitude bin of 4 deg (black circles). The x error bars indicate the extent of the bin, and the y errors are determined through bootstrapping. The dashed line shows the percentage of complex sources for the full sample at 42%. The cyan-shaded regions indicate longitudes which correspond to the Galactic spiral arms listed in the text and the longitude range within 5 degrees of the Galactic centre. The bottom panel is a histogram showing the number of sources in each longitude bin. The green triangle shows the percentage of complex sources at $355° < l < 360°$ in Livingston et al. (2021).

We find that in longitude bins including the spiral arms, we have a greater mean complexity than over the whole sample. Considering a comparison of complexity fractions with the literature, we also find this increased complexity within 5 degrees of the Galactic centre, as consistent with Livingston et al. (2021) (95% complexity). This increase could be due to the greater number of Faraday components emitting at small scales in the spiral arms at Galactic latitudes $1.5° < |b| < 10°$. The observed sources in Livingston et al. (2021) and O'Sullivan et al. (2017) are suitable for a direct comparison, as they also use the 16 cm band in the ATCA with the 6 km baseline configuration, ensuring similar spatial and frequency resolution. O'Sullivan et al. (2017) select an extragalactic sample of sources away from the Galactic plane, but with sources up to $|b| > 20°$. They find a 55% complexity fraction. This is congruent with what we find, on average. Anderson et al. (2015) find a complexity fraction of 12% for sources at $b \sim 55°$, considering that they have a lower resolution of ∼1′. This complexity fraction for a non-Galactic region is consistent with the average complexity fraction we find in the interarm regions (Fig. 15).

We determined the correlation between our binned sample and the positions of the spiral arms using the Pearson Correlation Coefficient ρ. Here, each spiral arm is simply modelled as a Gaussian, with the centroid and standard deviation as the centre and width of the cyan bands in Fig. 15. We included an additional component at the Galactic centre, with $x_0 = 0°$ and $\sigma = 5°$, and assume a complexity fraction of 100% at the centroid of all spiral arms and the Galactic centre. We tested this by randomly assigning a boolean complexity classification to 10 000 samples with the same longitude distribution as our observed sources and a total complexity fraction of 42%. We calculate ρ for the random samples and the p-value, determined as the probability of determining a correlation at least as strong as our observed sample across the 10 000 random samples. We repeat this experiment for longitude bin widths of $\Delta l = [3, 4, 5]$ degrees. The smallest possible bin size with at least 1 source per bin is $\Delta l = 3$ deg. The results are displayed in Table 3. We find

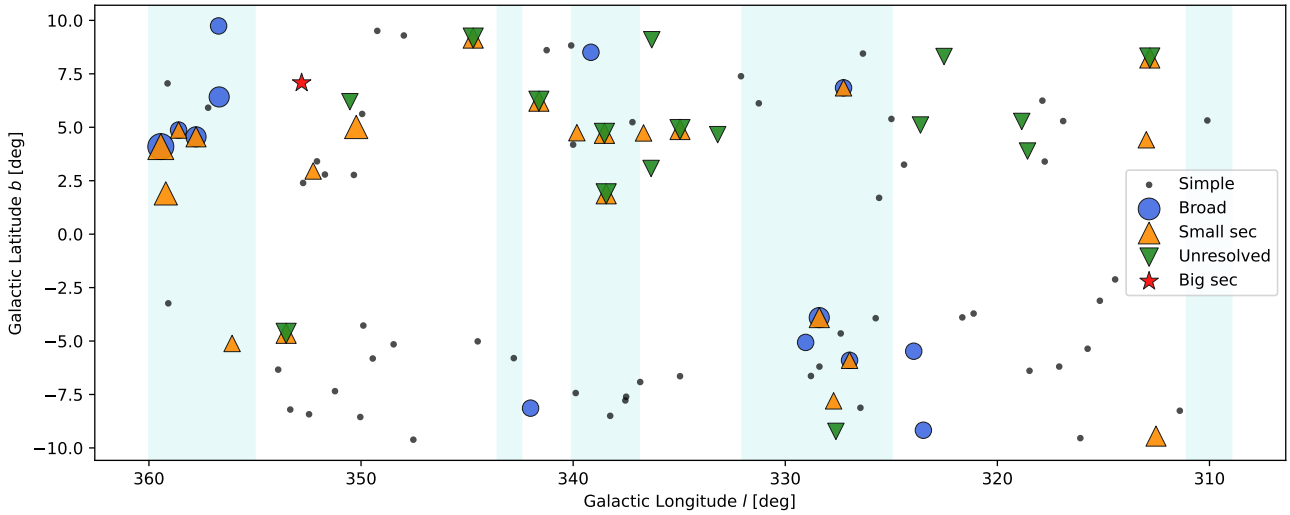

Fig. 16. Spatial distribution of sources, colourised by their Faraday complexity classification, as described in Sect. 5.2.1. The cyan-shaded regions show longitudes that correspond to the Galactic spiral arms listed in the text and the longitude range within 5 degrees of the Galactic centre. The Faraday simple sources are plotted as black dots. The size of the markers for Faraday complex sources is scaled according to the number of QU-fitted components.

Table 3. Pearson Correlation coefficient ρ for the correlation between the increased complexity classification and the positions of the Galactic spiral arms for different longitude bins.

Δl bin	ρ	p
3°	0.57	0.010
4°	0.63	0.011
5°	0.65	0.021

Notes. The associated p-value for 10 000 randomly assigned samples is also shown.

the strongest correlation at $\Delta l = 5$ deg with $\rho = 0.65$, and that the correlation coefficients for all bins are statistically significant with at least 97.9% confidence. This suggests a fair correlation between increased complexity percentage and the longitudes of the Galactic spiral arms. This result is consistent with the RM structure functions in Haverkorn et al. (2008), who find a smaller driving scale of turbulence (~1 pc) in the spiral arm regions than in the interarm regions (~100 pc), and suggests that the increase of complexity is attributed to turbulence at smaller scales in the spiral arms. However, a larger observed sample and a more detailed Galactic plane model are required to draw a more robust conclusion.

To further investigate the origin of this complexity, we plot the distribution of sources, colourised by their complexity classification in relation to the spiral arms and Galactic centre (Fig. 16). Through visual inspection, we find that sources classified as small sec and/or broad are concentrated around the Galactic centre or the spiral arm regions, as expected in the presence of a low flux density polarised emission. Here, it is possible that the broadening is due to smaller amplitude secondary peaks caused by small-scale emission within the Galactic plane that is unresolved at this Faraday depth resolution, or a broadening effect from small-scale Faraday depth fluctuations caused by turbulent cells. Both of these observed effects support the argument for a smaller turbulent cell size in the spiral arm regions that in the interarm regions. We discuss the cases for Faraday rotation and polarised emission separately:

Pure rotation. In the interarm regions, we may be resolving out turbulence, that is, a low number of turbulent cells per beam volume probed. This would simply induce Faraday rotation, without increasing complexity. In the spiral arm regions, with a smaller turbulent cell size, we have an increased number of turbulent cells within the ISM volume probed by the beam. This would result in Faraday dispersion, and cause a broadening in the Faraday spectrum (Sect. 5.2.1) and a complex classification.

Pure emission. We would expect smoother polarised emission in the interarm regions, due to large-scale turbulence. This larger-scale emission is not detected at the scales of our observations. In the spiral arm regions, we are sensitive to the smaller scale, patchy emission, caused by the small-scale turbulence.

As discussed above, both cases or a combination of the two could contribute to the observed complexity in the spiral arm regions. However, we would require higher resolution observations in both angular resolution and Faraday depth to asses this fully.

In Fig. 16 we find that the majority of sources that are classified as unresolved in Faraday depth are distributed on the northern half of the plane. This is also what predominantly contributes to the increase of complexity at northern latitudes, as shown in Fig. 10. This north-south Galactic asymmetry is expected in polarised synchrotron emission (e.g. Vidal et al. 2015; Robitaille et al. 2017). Although we find no relation between HI column density and Faraday complexity at the positions of the individual sources, we find that there is an increased average HI column density above the plane (5.3×10^{21} cm^{-2}) than below the plane (3.1×10^{21} cm^{-2}). Small-scale magneto-ionic structures (e.g. filaments at scales of ~10 pc) with low amplitude $n_e\mathbf{B}$ within this extended HI region could be a possible explanation for this increased complexity (e.g. Clark & Hensley 2019; Ma et al. 2023). With higher Faraday depth resolution observations and QU fitting with more advanced models, we will be able to discern whether this is an effect of unresolved Faraday dispersion by turbulence in the northern Galactic plane Faraday screen or the effect of polarised structures in Galactic HI.

6. Conclusion

In this paper, we investigate the increase of Faraday complexity towards $b = 0°$ in the S-PASS/ATCA RM catalogue (S19; Schnitzeler et al. 2019). We obtain follow-up observations of 95 sources at higher angular resolution, using the 6 km-baseline configuration of ATCA. We determine the peak Faraday depth ϕ of the sources using RM synthesis and find these measurements to be consistent with the S19 catalogue. By fitting Stokes Q and U spectra with models describing the sum of multiple Faraday simple components, we classify sources as Faraday simple or Faraday complex. With the higher resolution observations, we find that 42% of the sources are complex ($n > 1$), in comparison to the 90% complexity in the same sample from S19. Furthermore, we found that there is no longer a strong trend of increased Faraday complexity towards the Galactic plane, limiting the scale of complexity to $\theta < 2.8'$ (2.4 pc at a 3 kpc distance), the maximum angular scale of our observations. From this, we constrain that the increase in complexity in the S19 catalogue can be attributed to, on average, an additional polarised components from mixed-in diffuse Galactic emission at scales $\theta > 2.8'$.

To investigate the remaining complexity at smaller scales, we further classify Faraday complex sources based on the characteristics in their Faraday spectra. We find tentative evidence that there is an above-average complex source percentage at longitudes corresponding to the Galactic spiral arms, suggesting turbulence or small-scale patchy emission within these regions. In addition, we observe a trend in an overdensity of sources with $|\mathrm{RM}_1 - \mathrm{RM}_2|$ smaller than the Faraday spectrum resolution in the northern Galactic plane. This could be attributed to low amplitude $n_\mathrm{e}\mathbf{B}$ fluctuations in the HI disk of the Milky Way.

Overall, we find the total intensity and ϕ measurements in the S19 catalogue reliable and consistent with our observations, with the caveat that particular care should be taken regarding the angular resolution and the maximum angular scale when comparing polarised intensity measurements, QU fitting results, and Faraday complexity between various observations at $|b| < 10°$.

Acknowledgements. We thank Rainer Beck for helpful discussions surrounding this work and feedback on the manuscript, as well as Aritra Basu for QU fitting scripts. SR acknowledges the support from the International Max Planck Research School (IMPRS) for Astronomy and Astrophysics at the Universities of Bonn and Cologne. RPD acknowledges funding from the South African Research Chairs Initiative of the Department of Science and Innovation and National Research Foundation (Grant ID 77948). The Australia Telescope Compact Array is part of the Australia Telescope National Facility (https://ror.org/05qajvd42) which is funded by the Australian Government for operation as a National Facility managed by CSIRO. We acknowledge the Gomeroi people as the Traditional Owners of the Observatory site. The data used in this work will be shared upon reasonable request to the authors.

References

Alger, M. J., Livingston, J. D., McClure-Griffiths, N. M., et al. 2021, PASA, 38, e022
Anderson, C. S., Gaensler, B. M., Feain, I. J., & Franzen, T. M. O. 2015, ApJ, 815, 49
Anderson, C. S., Gaensler, B. M., & Feain, I. J. 2016, ApJ, 825, 59
Anderson, C. S., Heald, G. H., Eilek, J. A., et al. 2021, PASA, 38, e020
Basu, A., Fletcher, A., Mao, S. A., et al. 2019, Galaxies, 7, 89
Beck, R. 2015, A&A Rev., 24, 4
Brentjens, M. A., & de Bruyn, A. G. 2005, A&A, 441, 1217
Briggs, D. S. 1995, PhD Thesis, New Mexico Institute of Mining and Technology, USA
Brown, J. C., Haverkorn, M., Gaensler, B. M., et al. 2007, ApJ, 663, 258
Burn, B. J. 1966, MNRAS, 133, 67
Clark, S. E., & Hensley, B. S. 2019, ApJ, 887, 136
Dickey, J. M., Landecker, T. L., Thomson, A. J. M., et al. 2019, ApJ, 871, 106
Eyles, R. A. J., Birkinshaw, M., Smolčić, V., et al. 2020, A&A, 633, A6
Farnsworth, D., Rudnick, L., & Brown, S. 2011, AJ, 141, 191
Gaensler, B. M., Dickey, J. M., McClure-Griffiths, N. M., et al. 2001, ApJ, 549, 959
Gaensler, B. M., Haverkorn, M., Staveley-Smith, L., et al. 2005, Science, 307, 1610
Garrington, S. T., Leahy, J. P., Conway, R. G., & Laing, R. A. 1988, Nature, 331, 147
Haffner, L. M., Reynolds, R. J., Tufte, S. L., et al. 2003, ApJS, 149, 405
Hale, C. L., McConnell, D., Thomson, A. J. M., et al. 2021, PASA, 38, e058
Haverkorn, M., Brown, J. C., Gaensler, B. M., & McClure-Griffiths, N. M. 2008, ApJ, 680, 362
Heald, G. 2009, in Cosmic Magnetic Fields: From Planets, to Stars and Galaxies, eds. K. G. Strassmeier, A. G. Kosovichev, & J. E. Beckman, 259, 591
HI4PI Collaboration (Ben Bekhti, N., et al.) 2016, A&A, 594, A116
Hutschenreuter, S., Anderson, C. S., Betti, S., et al. 2022, A&A, 657, A43
Laing, R. A. 1988, Nature, 331, 149
Lamee, M., Rudnick, L., Farnes, J. S., et al. 2016, ApJ, 829, 5
Livingston, J. D., McClure-Griffiths, N. M., Gaensler, B. M., Seta, A., & Alger, M. J. 2021, MNRAS, 502, 3814
Livingston, J. D., McClure-Griffiths, N. M., Mao, S. A., et al. 2022, MNRAS, 510, 260
Ma, Y. K., Mao, S. A., Stil, J., et al. 2019a, MNRAS, 487, 3432
Ma, Y. K., Mao, S. A., Stil, J., et al. 2019b, MNRAS, 487, 3454
Ma, Y. K., Mao, S. A., Ordog, A., & Brown, J. C. 2020, MNRAS, 497, 3097
Ma, Y. K., McClure-Griffiths, N. M., Clark, S. E., et al. 2023, MNRAS, 521, 60
Mao, S. A., Gaensler, B. M., Stanimirović, S., et al. 2008, ApJ, 688, 1029
Mao, S. A., Gaensler, B. M., Haverkorn, M., et al. 2010, ApJ, 714, 1170
Mao, S. A., McClure-Griffiths, N. M., Gaensler, B. M., et al. 2012, ApJ, 759, 25
McClure-Griffiths, N. M., Pisano, D. J., Calabretta, M. R., et al. 2009, ApJS, 181, 398
McConnell, D., Hale, C. L., Lenc, E., et al. 2020, PASA, 37, e048
McMullin, J. P., Waters, B., Schiebel, D., Young, W., & Golap, K. 2007, in Astronomical Data Analysis Software and Systems XVI, eds. R. A. Shaw, F. Hill, & D. J. Bell, ASP Conf. Ser., 127
O'Sullivan, S. P., Brown, S., Robishaw, T., et al. 2012, MNRAS, 421, 3300
O'Sullivan, S. P., Purcell, C. R., Anderson, C. S., et al. 2017, MNRAS, 469, 4034
O'Sullivan, S. P., Shimwell, T. W., Hardcastle, M. J., et al. 2023, MNRAS, 519, 5723
Padmanabh, P. V., Barr, E. D., Sridhar, S. S., et al. 2023, MNRAS, 524, 1291
Pasetto, A., Carrasco-González, C., O'Sullivan, S., et al. 2018, A&A, 613, A74
Purcell, C. R., Gaensler, B. M., Sun, X. H., et al. 2015, ApJ, 804, 22
Purcell, C. R., Van Eck, C. L., West, J., Sun, X. H., & Gaensler, B. M. 2020, Astrophysics Source Code Library [record ascl:2005.003]
Robitaille, J. F., Scaife, A. M. M., Carretti, E., et al. 2017, MNRAS, 468, 2957
Sault, R. J., Teuben, P. J., & Wright, M. C. H. 1995, in Astronomical Data Analysis Software and Systems IV, eds. R. A. Shaw, H. E. Payne, & J. J. E. Hayes, ASP Conf. Ser., 77, 433
Schnitzeler, D. H. F. M., & Lee, K. J. 2017, MNRAS, 466, 378
Schnitzeler, D. H. F. M., Katgert, P., & de Bruyn, A. G. 2009, A&A, 494, 611
Schnitzeler, D. H. F. M., Carretti, E., Wieringa, M. H., et al. 2019, MNRAS, 485, 1293
Stil, J. M., Taylor, A. R., & Sunstrum, C. 2011, ApJ, 726, 4
Sun, X. H., Rudnick, L., Akahori, T., et al. 2015, AJ, 149, 60
Taylor, A. R., Stil, J. M., & Sunstrum, C. 2009, ApJ, 702, 1230
Thomson, A. J. M., McConnell, D., Lenc, E., et al. 2023, PASA, 40, e040
Vallée, J. P. 2022, New Astron., 97, 101896
Van Eck, C. L., Gaensler, B. M., Hutschenreuter, S., et al. 2023, ApJS, 267, 28
Vidal, M., Dickinson, C., Davies, R. D., & Leahy, J. P. 2015, MNRAS, 452, 656

Appendix A: QU fitting models

In this appendix, we detail the key assumptions made in the derivation of the QU fitting model. As stated in Sect. 3.2, we consider a model describing the sum of up to five Faraday thin components, where for a given component, the polarised intensity is

$$P(\lambda^2) = P_0 \exp\left(2i(\phi\lambda^2 + PA)\right), \tag{A.1}$$

where P_0 is the polarised intensity, ϕ is the Faraday depth, and PA is the polarisation angle. Because we are fitting the polarisation fraction $p(\lambda^2)$, we divide by by the total intensity spectrum,

$$p(\lambda^2) = \frac{P(\lambda^2)}{I(\lambda^2)}, \tag{A.2}$$

assuming $I(\nu)$ to be a power law as a function of frequency ν:

$$I(\nu) = I_0 \left(\frac{\nu}{\nu_0}\right)^{-\alpha}, \tag{A.3}$$

where I_0 is the total intensity flux density at a reference frequency ν_0 and α is the spectral index. This can be written as,

$$I(\lambda^2) = I_0 \left(\frac{\lambda^2}{\lambda_0^2}\right)^{\alpha/2}, \tag{A.4}$$

resulting in

$$p(\lambda^2) = p_0 \left(\frac{\lambda^2}{\lambda_0^2}\right)^{-\alpha/2} \exp\left(2i(\phi\lambda^2 + PA)\right). \tag{A.5}$$

As specified in the text, dividing the Q and U spectra by the Stokes I spectrum before fitting, will account for the dominant spectral index, (i.e. the spectral index of the background source α_0). This model serves to fit any variation in spectral index as contributed from emitting components within the beam volume, for which Equation A.5 can be rewritten as

$$p(\lambda^2) = p_0 \left(\frac{\lambda^2}{\lambda_0^2}\right)^{-\delta\alpha/2} \exp\left(2i(\phi\lambda^2 + PA)\right), \tag{A.6}$$

where $\alpha = \alpha_0 + \delta\alpha$.

Appendix B: Source catalogue

Table B.1. Catalogue of the 95 analysed sources. Column (1) is the source ID from the S19 catalogue. Columns (2)–(5) have the positional information of each source. Columns (6)–(7) contain the total intensity measurements and columns (8)–(11) contain polarisation properties of each source. Sources identified to have multiple spatial components within the 15"×15" beam (see Sect. 5.2.2) are marked with an asterisk.

	S19 ID (1)	RA (2) (J2000)	Dec (3) (J2000)	l (4) (deg)	b (5) (deg)	$I_{\rm MFS}$ (6) (mJy)	I_{2100} (7) (mJy)	PI (8) (mJy)	$\phi_{\rm peak}$ (9) rad m^{-2}	n (10) (this work)	n (11) (S19)
1	NVSSJ161021-395858	16h10m17s	−39d58m58.0s	339.162	8.507	599±4	613±7	25.08±0.13	−65.82±0.16	2	2
2	NVSSJ161234-390625	16h12m36s	−39d06m59.0s	340.093	8.827	221±6	208±14	11.17±0.10	−5.85±0.35	1	1
3	NVSSJ161737-382827*	16h17m36s	−38d28m32.0s	341.249	8.606	172±6	163±9	1.19±0.10	+20.40±3.17	1	3
4	SPASSJ143426-623949	14h34m26s	−62d39m49.8s	314.448	−2.118	431±5	403±6	28.63±0.12	−30.62±0.15	1	2
5	NVSSJ171148-333841	17h11m48s	−33d38m42.0s	352.078	3.407	200±2	225±9	0.93±0.11	+110.09±4.68	1	4
6	SPASSJ144346-631714*	14h43m46s	−63d17m14.0s	315.168	−3.116	568±15	495±26	13.05±0.22	−119.86±0.38	1	1
7	NVSSJ170918-352521*	17h09m18s	−35d25m24.0s	350.337	2.77	1736±24	1687±30	66.55±0.60	−296.36±0.11	1	3
8	SPASSJ144453-552959*	14h44m53s	−55d29m59.5s	318.578	3.887	503±21	400±32	12.35±0.15	−20.78±0.35	2	3
9	NVSSJ175445-401157	17h54m43s	−40d12m16.0s	351.229	−7.344	326±38	209±43	6.85±0.12	+96.26±0.56	1	2
10	NVSSJ162732-353731*	16h27m31s	−35d37m37.0s	344.712	9.172	544±10	479±9	9.98±0.17	−6.04±0.48	3	3
11	NVSSJ171257-280935*	17h12m55s	−28d09m29.0s	356.689	6.418	4275±94	3766±77	97.83±0.80	+52.87±0.09	3	3
12	SPASSJ153448-604059	15h34m48s	−60d40m60.0s	321.652	−3.894	228±11	170±14	11.43±0.19	−162.65±0.39	1	5
13	NVSSJ163736-330905	16h37m34s	−33d09m9.0s	347.982	9.294	274±3	267±6	7.56±0.09	−46.16±0.50	1	2
14	NVSSJ171309-341830	17h13m09s	−34d18m39.0s	351.703	2.789	598±4	616±9	6.50±0.11	−125.65±0.71	1	3
15	NVSSJ171652-254925	17h16m50s	−25d48m58.0s	359.123	7.052	312±23	290±37	2.76±0.14	−149.86±1.39	1	2
16	NVSSJ171405-334539*	17h14m04s	−33d45m51.0s	352.258	2.955	281±4	252±12	11.23±0.21	−106.89±0.55	2	5
17	SPASSJ155724-603116	15h57m24s	−60d31m16.3s	323.943	−5.476	288±21	251±19	7.82±0.11	−51.38±0.56	2	2
18	NVSSJ171609-280135	17h16m08s	−28d01m37.0s	357.208	5.915	203±23	361±95	5.29±0.15	+110.46±0.84	1	5
19	SPASSJ160009-581104	16h00m09s	−58d11m4.7s	325.737	−3.931	760±21	685±21	31.45±0.24	−90.51±0.16	1	3
20	NVSSJ171736-334208	17h17m35s	−33d42m17.0s	352.731	2.394	786±15	869±17	34.55±0.18	−248.25±0.15	1	2
21	NVSSJ173725-394608*	17h37m24s	−39d46m18.0s	349.892	−4.275	404±7	369±13	9.48±0.11	+305.37±0.45	1	1
22	NVSSJ174840-365150	17h48m38s	−36d51m55.0s	353.531	−4.639	751±39	770±123	15.33±0.15	+201.40±0.31	3	3
23	SPASSJ175715-414936	17h57m15s	−41d49m36.0s	350.035	−8.554	965±31	774±72	8.37±0.15	+45.92±0.69	1	4
24	SPASSJ160017-464922*	16h00m17s	−46d49m22.5s	333.185	4.655	5064±104	4616±98	429.88±1.70	+41.12±0.04	2	3
25	NVSSJ175622-312215	17h56m20s	−31d22m26.0s	359.087	−3.236	437±11	396±13	27.28±0.30	+247.91±0.21	1	3
26	NVSSJ175657-372326	17h56m57s	−37d23m42.0s	353.907	−6.338	162±7	141±13	7.83±0.15	−57.96±0.54	1	2
27	NVSSJ175659-345422*	17h56m58s	−34d54m37.0s	356.079	−5.113	615±17	565±14	13.31±0.21	+149.15±0.38	2	2
28	NVSSJ180347-384729	18h03m51s	−38d47m39.0s	353.336	−8.206	317±9	267±21	35.96±0.13	+86.67±0.14	1	2
29	PKSB1425-692	14h29m46s	−69d29m57.9s	311.399	−8.261	113±12	111±21	8.91±0.10	+23.64±0.54	1	2
30	PKSB1442-699*	14h47m06s	−70d08m4.2s	312.521	−9.447	496±12	433±11	22.10±0.16	−39.34±0.21	3	3
31	PKSB1517-682	15h22m16s	−68d28m11.4s	316.089	−9.542	283±8	224±10	24.21±0.17	+210.84±0.16	1	1
32	SPASSJ160700-452802	16h07m00s	−45d28m3.0s	334.962	4.894	806±14	692±10	36.59±0.33	−94.27±0.14	3	3
33	SPASSJ161717-584807	16h17m17s	−58d48m7.0s	326.969	−5.901	3777±54	4276±108	36.53±0.60	+74.09±0.23	2	2
34	NVSSJ165956-305205	16h59m55s	−30d52m7.0s	352.801	7.078	540±16	434±16	1.22±0.16	+151.50±3.85	2	3
35	SPASSJ134355-564917	13h43m56s	−56d49m17.1s	310.101	5.318	362±12	309±28	33.31±0.16	+113.30±0.15	1	3
36	SPASSJ135734-532128	13h57m34s	−53d21m28.3s	312.813	8.24	392±8	356±9	50.41±0.17	−6.82±0.08	3	3
37	SPASSJ163305-450926*	16h33m05s	−45d09m26.9s	338.442	1.887	514±23	392±30	25.52±0.31	−209.79±0.20	3	4
38	NVSSJ161809-391811	16h18m08s	−39d18m14.0s	340.733	7.946	570±14	517±16	15.56±0.23	+128.50±0.47	2	2
39	PKSB1508-649	15h12m34s	−65d06m47.8s	317.085	−6.195	467±7	440±6	8.93±0.23	−103.82±0.50	1	3
40	SPASSJ144106-561659	14h41m06s	−56d16m59.6s	317.768	3.397	886±31	709±60	48.20±0.17	−79.36±0.12	1	2
41	SPASSJ144233-540746	14h42m33s	−54d07m46.2s	318.85	5.272	432±11	412±12	19.37±0.12	+47.64±0.21	2	2
42	NVSSJ172242-281953	17h22m42s	−28d19m57.0s	357.78	4.554	870±12	794±12	26.90±0.42	+97.56±0.21	3	3
43	SPASSJ163158-593500	16h31m58s	−59d35m0.2s	327.721	−7.796	481±34	...	9.27±0.12	+116.47±0.44	2	3
44	SPASSJ145506-494805*	14h55m07s	−49d48m5.8s	322.515	8.309	612±14	550±20	15.27±0.10	−9.93±0.24	2	4
45	NVSSJ172337-272843	17h23m35s	−27d28m37.0s	358.603	4.869	52±3	42±6	2.61±0.14	−54.74±1.69	2	2
46	SPASSJ151108-520350	15h11m08s	−52d03m50.2s	323.626	5.104	222±3	209±6	7.73±0.15	−130.34±0.41	2	2
47	SPASSJ151739-510634	15h17m39s	−51d06m34.4s	324.994	5.389	139±6	151±17	5.29±0.15	−82.71±0.83	1	1
48	NVSSJ172836-271236	17h28m34s	−27d12m41.0s	359.441	4.097	437±6	373±12	5.11±0.30	−60.90±1.63	5	5
49	SPASSJ152154-531348	15h21m55s	−53d13m49.0s	324.4	3.251	280±12	222±26	6.45±0.11	−20.22±0.70	1	3
50	SPASSJ152426-483956	15h24m26s	−48d39m56.3s	327.252	6.846	404±41	347±63	10.45±0.37	−199.65±1.21	2	3
51	SPASSJ152436-643159*	15h24m36s	−64d31m59.6s	318.485	−6.392	493±13	430±14	20.89±0.21	+183.48±0.21	1	2
52	SPASSJ153023-605032	15h30m23s	−60d50m32.3s	321.12	−3.714	147±4	126±8	10.60±0.14	−144.69±0.36	1	4
53	SPASSJ153419-535113	15h34m19s	−53d51m13.2s	325.575	1.698	518±4	491±8	11.62±0.18	−52.13±0.31	1	4
54	PKSB1653-331	16h56m39s	−33d11m37.0s	350.526	6.196	420±22	396±26	40.28±0.17	−82.56±0.12	2	3

Table B.1. Continued.

	S19 ID (1)	RA (2) (J2000)	Dec (3) (J2000)	l (4) (deg)	b (5) (deg)	$I_{\rm MFS}$ (6) (mJy)	I_{2100} (7) (mJy)	PI (8) (mJy)	$\phi_{\rm peak}$ (9) rad m^{-2}	n (10) (this work)	n (11) (S19)
55	SPASSJ140555-565946*	14h05m55s	−56d59m46.3s	312.978	4.416	713±16	598±24	28.98±0.23	−74.08±0.16	2	2
56	SPASSJ154607-465519	15h46m07s	−46d55m19.9s	331.247	6.12	531±9	482±7	18.31±0.18	+71.33±0.22	1	2
57	SPASSJ155707-412646*	15h57m07s	−41d26m46.0s	336.293	9.095	418±10	361±15	33.13±0.12	+9.76±0.10	2	3
58	SPASSJ143353-533736	14h33m53s	−53d37m36.2s	317.878	6.246	221±8	189±12	2.83±0.15	+77.68±1.24	1	2
59	NVSSJ162743-395303	16h27m43s	−39d53m7.0s	341.615	6.219	1305±24	1128±10	9.31±0.30	−50.04±0.74	3	3
60	SPASSJ145739-650240	14h57m39s	−65d02m40.7s	315.745	−5.362	259±8	215±11	12.18±0.12	−42.07±0.41	1	2
61	SPASSJ161255-573638	16h12m55s	−57d36m38.9s	327.384	−4.645	830±48	360±32	17.10±0.14	−18.32±0.24	1	4
62	SPASSJ161432-562236*	16h14m32s	−56d22m36.6s	328.397	−3.903	1529±28	1401±39	42.43±0.31	−29.45±0.10	3	3
63	SPASSJ154523-452432	15h45m23s	−45d24m32.9s	332.088	7.388	170±14	143±15	11.67±0.13	−64.49±0.35	1	2
64	SPASSJ161451-434125	16h14m50s	−43d41m25.0s	337.204	5.238	512±16	474±35	4.63±0.11	−0.04±0.92	1	4
65	SPASSJ161551-633314	16h15m51s	−63d33m14.4s	323.488	−9.172	693±29	532±72	8.04±0.25	+200.80±0.61	2	4
66	SPASSJ162941-422659	16h29m41s	−42d26m59.0s	340.001	4.187	205±4	181±5	...	+437.73±5.35	1	4
67	SPASSJ161950-455109	16h19m50s	−45d51m9.7s	336.325	3.072	646±19	521±23	71.70±0.28	−81.23±0.08	2	4
68	SPASSJ162202-430822	16h22m02s	−43d08m22.0s	338.525	4.716	984±26	802±54	24.97±0.27	+80.83±0.22	3	3
69	SPASSJ162346-564509	16h23m46s	−56d45m9.8s	329.04	−5.065	582±13	485±6	10.34±0.24	+69.46±0.64	2	2
70	SPASSJ161441-442447*	16h14m41s	−44d24m47.5s	336.682	4.736	1005±15	918±12	52.20±0.25	+127.38±0.08	2	4
71	SPASSJ162628-580020	16h26m28s	−58d00m20.3s	328.389	−6.197	330±16	252±43	11.16±0.15	+49.93±0.36	1	2
72	SPASSJ162650-421129	16h26m50s	−42d11m29.0s	339.824	4.746	714±100	...	15.24±0.28	+6.32±0.52	2	3
73	SPASSJ162701-604320	16h27m01s	−60d43m20.1s	326.456	−8.122	...	78±15	3.89±0.12	+98.83±0.93	1	2
74	NVSSJ173620-283552	17h36m18s	−28d36m2.0s	359.205	1.907	183±4	156±7	14.76±0.21	−348.57±0.35	4	5
75	SPASSJ163056-580102*	16h30m56s	−58d01m2.3s	328.789	−6.635	292±8	246±7	5.70±0.08	+89.20±0.66	1	3
76	SPASSJ163958-603651	16h39m58s	−60d36m51.8s	327.612	−9.227	638±56	207±22	10.94±0.15	+97.14±0.43	2	3
77	SPASSJ165908-532028*	16h59m08s	−53d20m28.0s	334.961	−6.644	538±12	465±11	38.41±0.17	+118.12±0.12	1	2
78	PKSB1637-319*	16h40m38s	−32d04m37.0s	349.235	9.51	327±5	297±6	27.81±0.12	−33.44±0.14	1	1
79	SPASSJ151439-474835	15h14m40s	−47d48m30.0s	326.338	8.448	1082±11	1216±10	10.46±0.16	−7.68±0.30	1	1
80	SPASSJ171405-515258	17h14m05s	−51d52m58.0s	337.501	−7.605	84±34	294±24	16.69±0.16	−50.08±0.27	1	3
81	SPASSJ171510-515708	17h15m09s	−51d57m8.0s	337.541	−7.781	440±18	270±33	11.11±0.19	−50.43±0.42	1	3
82	SPASSJ172135-514628	17h21m34s	−51d46m28.0s	338.253	−8.499	384±18	298±30	7.92±0.15	+43.84±0.54	1	3
83	SPASSJ172139-495033	17h21m38s	−49d50m33.0s	339.879	−7.432	130±30	144±39	3.19±0.15	−70.85±1.47	1	3
84	SPASSJ172315-463135	17h23m14s	−46d31m35.0s	342.798	−5.8	516±40	266±36	38.81±0.16	−91.50±0.13	1	3
85	SPASSJ172456-444054	17h24m56s	−44d40m54.0s	344.5	−5.015	284±6	249±7	13.55±0.14	+161.11±0.32	1	1
86	SPASSJ173219-482740	17h32m19s	−48d27m40.0s	342.008	−8.139	415±15	231±19	8.79±0.14	−235.78±0.52	2	4
87	SPASSJ173720-412636	17h37m19s	−41d26m36.0s	348.465	−5.154	317±31	377±83	10.66±0.13	−108.20±0.52	1	2
88	SPASSJ174304-405729	17h43m03s	−40d57m29.0s	349.448	−5.817	408±6	395±9	19.04±0.13	−24.43±0.23	1	3
89	SPASSJ175548-443006*	17h55m47s	−44d30m6.0s	347.534	−9.615	407±11	363±11	7.88±0.18	+49.90±0.74	1	2
90	SPASSJ143012-545251	14h30m12s	−54d52m51.9s	316.898	5.29	373±21	259±32	5.04±0.13	−176.49±0.96	1	2
91	NVSSJ180242-394005	18h02m42s	−39d40m8.0s	352.451	−8.425	1270±4	1250±5	14.62±0.21	+90.88±0.18	1	1
92	PKSB1654-339*	16h57m07s	−34d00m0.0s	349.947	5.623	112±3	117±8	7.78±0.14	−142.62±0.53	1	4
93	PKSB1657-261	17h00m57s	−26d10m28.0s	356.716	9.74	1009±8	1059±12	25.13±0.21	−27.97±0.22	2	2
94	PKSB1657-340	17h00m15s	−34d09m22.0s	350.227	5.013	585±9	498±9	6.91±0.20	−132.48±0.68	4	4
95	SPASSJ170758-520057	17h07m58s	−52d00m57.0s	336.838	−6.916	96±3	...	8.01±0.14	−106.38±0.53	1	3

APPENDIX E

Paper: A first glimpse at the MeerKAT DEEP2 field at S-band

The paper *"A first glimpse at the MeerKAT DEEP2 field at S-band", Ranchod et al. (2025), MNRAS, 536, 3647*, was published in Monthly Notices of the Royal Astronomical Society under the Creative Commons CC-BY 4.0 license, and is reproduced in its original form below.

Monthly Notices of the ROYAL ASTRONOMICAL SOCIETY

MNRAS **536,** 3647–3662 (2025) https://doi.org/10.1093/mnras/stae2754
Advance Access publication 2024 December 13

A first glimpse at the MeerKAT DEEP2 field at *S*-band

S. Ranchod [1]★ J. D. Wagenveld,[1] H.-R. Klöckner,[1] O. Wucknitz,[1] R. P. Deane [2,3] S. S. Sridhar,[1,4] E. Barr [1] S. Buchner,[5] F. Camilo,[5] A. Damas-Segovia,[1] C. Kasemann,[1] M. Kramer [1] L. S. Legodi [5] S. A. Mao [1] K. Menten,[1] I. Rammala,[1] M. R. Rugel[1,6,7] and G. Wieching[1]

[1]*Max-Planck Institut fur Radioastronomie, Auf dem Hügel 69, D-53121 Bonn, Germany*
[2]*Wits Centre for Astrophysics, School of Physics, University of the Witwatersrand, 1 Jan Smuts Avenue, Johannesburg 2000, South Africa*
[3]*Department of Physics, University of Pretoria, Private Bag X20, Pretoria 0028, South Africa*
[4]*SKA Observatory, Jodrell Bank, Lower Withington, Macclesfield SK11 9FT, UK*
[5]*South African Radio Astronomy Observatory, River Park, Gloucester Road Liesbeek House, Mowbray 7700, South Africa*
[6]*Center for Astrophysics | Harvard & Smithsonian, 60 Garden Street, Cambridge, MA 02138, USA*
[7]*National Radio Astronomy Observatory, PO Box O, 1003 Lopezville Road, Socorro, NM 87801, USA*

Accepted 2024 December 11. Received 2024 December 11; in original form 2024 November 4

ABSTRACT

We present the first wide-field extragalactic continuum catalogue with the MeerKAT *S*-band (2.5 GHz), of the radio-selected DEEP2 field. The combined image over the *S*1 (1.96–2.84 GHz) and *S*4 (2.62–3.50 GHz) sub-bands has an angular resolution of 6.8 arcsec × 3.6 arcsec (4.0 arcsec × 2.4 arcsec) at a robust weighting of $R = 0.3$ ($R = -0.5$) and a sensitivity of 4.7 (7.5) μJy beam^{-1} with an on-source integration time of 70 min and a minimum of 52 of the 64 antennas, for respective observations. We present the differential source counts for this field, as well as a morphological comparison of resolved sources between *S*-band and archival MeerKAT *L*-band images. We find consistent source counts with the literature and provide spectral indices fitted over a combined frequency range of 1.8 GHz. These observations provide an important first demonstration of the capabilities of MeerKAT *S*-band imaging with relatively short integration times, as well as a comparison with existing *S*-band surveys, highlighting the rich scientific potential with future MeerKAT *S*-band surveys.

Key words: catalogues – radio continuum: general.

1 INTRODUCTION

The DEEP2 field, defined by Mauch et al. (2020), is an extragalactic legacy field, selected for its local sparsity of bright radio sources. This field is the only legacy field selected based on radio properties alone and the reduced contribution from bright radio sources maximizes the attainable sensitivity. This, along with its favourable circumpolar position, allows it to serve as an optimal pilot field for the evaluation of new radio observatories and instrumentation in the Southern hemisphere e.g. MeerKAT, Square Kilometre Array (SKA), with the caveat of poor access for ground-based optical and infrared observatories.

Mauch et al. (2020) carried out 128-h observations on this field at 1.28 GHz with MeerKAT, which resulted in a confusion-limited observation with $\sigma = 0.55$ μJy beam^{-1}, and the deepest radio continuum image at *L*-band frequencies. These results have contributed to the computation of source counts in the DEEP2 field over a large range of flux densities (Matthews et al. 2021a) and to the determination of the probability distribution of source confusion $P(D)$ down to 0.25 μJy, allowing for new constraints on the star formation rate of the Universe (Matthews et al. 2021b).

The ∼3 GHz regime provides a window through which to directly study feedback in active galactic nuclei (AGN) and to observe star formation in galaxies without dust obscuration (e.g. Condon 1992; Smolčić et al. 2017; Leslie et al. 2020), both of which are important to constrain galaxy formation and evolution models. At 3 GHz, the spectral energy distributions of nearby normal galaxies are dominated by synchrotron emission, with only ∼ 25 per cent attributed to free–free (thermal) emission (Condon 1992). While for the faint source population, Algera et al. (2020) have shown that at $S_{3\,\mathrm{GHz}} < 50$ μJy, the fraction of sources dominated by thermal emission increases to ∼ 90 per cent. Through the radio–infrared relation, radio luminosity can be used as a direct tracer for star formation rate (e.g. Murphy 2009; Delhaize et al. 2017; Heesen et al. 2019). The high-angular resolution achieved with radio interferometers at *S*-band (1.75—3.50 GHz for MeerKAT) allows for deep observations (<1 μJy), without being limited by confusion, to study the low-flux density source population (e.g. van der Vlugt et al. 2021), and to understand the evolution of the thermal emission fraction with redshift.

We present pilot observations of the DEEP2 field, producing the first *S*-band extragalactic catalogue down to 16 μJy with the new *S*-band system on MeerKAT. This catalogue provides an *S*-band measurement for the deepest *L*-band radio image, allowing for the computation of multiband spectral indices. This is particularly useful for the classification of sources and provides insight into their dom-

★ E-mail: sranchod@mpifr-bonn.mpg.de

Table 1. Summary of DEEP2 observation details for the respective sub-bands.

Parameters	*S*1	*S*4
Observation ID	20230209–0012	20230215–0017
Observation date	2023 March 10	2023 March 12
Frequency range	1968.75 − 2843.75 MHz	2625.00 − 3500.00 MHz
Time on source (h)	1.17	1.17
Number of antennas	52	55

inant emission mechanisms. Furthermore, these pilot observations provide an early science demonstrator of the performance of the MeerKAT *S*-band receiver in the context of extragalactic imaging, to inform future observations at *S*-band frequencies.

In this paper, we present a shallow pilot catalogue of the DEEP2 field in *S*-band, as well as the differential source counts. This paper is organized as follows: in Section 2, we describe the DEEP2 observations and our calibration and imaging strategies. In Section 3, we present the *S*-band DEEP2 image and catalogue, and in Section 4, we present the Euclidean normalized differential source counts for the DEEP2 field at 2.5 GHz. We summarize and conclude in Section 5. Throughout this paper, we define the spectral index α as $S_\nu \propto \nu^\alpha$, where S_ν is the flux density at frequency ν.

2 OBSERVATIONS AND DATA REDUCTION

The DEEP2 field, centred on RA = 04:13:26.4, Dec. = −80.00.00.0 (J2000), is a radio-selected legacy field in the Southern sky. It was defined by (Mauch et al. 2020) as a commissioning deep-field for the MeerKAT telescope, to measure and optimize the performance of the array. The field was selected due to its low demerit score, a parameter which describes the expected gain variation due to pointing and receiver gain error for the known bright sources in the field, to quantify the maximum attainable sensitivity with the MeerKAT *L*-band. The low demerit score of the DEEP2 field of $D = 1.4$ mJy is three orders of magnitude smaller than that for optically selected southern deep-fields e.g. COSMOS, *XMM*–LSS, and Chandra Deep Field South.These properties make this a suitable choice for an early *S*-band catalogue, which will be used for verification ahead of future, deeper observations.

In this section, we detail the observation set-up as well as the calibration and imaging methods used in this work. From these observations, we produce the first multiband extragalactic catalogue using the MeerKAT *S*-band system. A detailed introduction to the new *S*-band receivers, including the system equivalent flux density and the sub-band division can be found in Appendix A.

2.1 Observations

The DEEP2 field was observed with the MeerKAT interferometer (Jonas & MeerKAT Team 2016) as part of the *S*-band science verification (Project ID SSV-20230209-HK-01). We observed a single pointing of the DEEP2 field in the *S*1 (1968.75 − 2843.75 MHz) and *S*4 (2625.00 − 3500.00 MHz) sub-bands with ∼70 min on source integration time each. The flux and bandpass calibrator J0408−6545 (PKS 0408−65) was observed for 8 min at the end of the observation, and the phase calibrator J0252−7104 (PKS 0252−71) was observed every 10 min. In addition, 3C138 was observed as a polarization calibrator for 5 min at the start of the observation and 8 min at the end. The integration time per visibility was 2 s. Further details of the observations are summarized in Table 1. With this choice of sub-bands, we have a maximum total bandwidth of 1531.25 MHz, with an overlapping bandwidth of 218.75 MHz.

2.2 Calibration and imaging

The processing of these observations followed the standard radio interferometric calibration procedure, in which we corrected delay, bandpass, and gain variations and flagged bad visibilities in an iterative process. For calibration and imaging, we used various tasks from CASA

(McMullin et al. 2007) and WSCLEAN (Offringa et al. 2014) respectively, as detailed below. We followed the same procedure for both observations to allow us to validate the calibration strategy and combine both sub-bands for imaging.

Bad visibilities were flagged using `flagdata` and by using an averaged waterfall spectrum of all baselines to remove frequency-dependent radio frequency interference (RFI)[1], after which each data set was divided into 16 uniform spectral windows (SPWs), with an equal number of channels, for further processing. This allowed for sufficient bandwidth per SPW to solve for the per-SPW selfcal solutions. Additionally, as PKS 0408−65 has a non-flat spectral index, it is necessary to divide the band into multiple uniform SPWs to bootstrap the flux scale calibration along the frequency axis. The primary calibrator PKS 0408−65 was used for delay, bandpass, and gain calibration, assuming a point source model with a flux density of 6.986 Jy at a reference frequency of 2.7 GHz.[2] The spectral index terms were set as `spix` = [−1.2897, −0.2353, 0.0861] in `setjy`. Baselines with a projected length of < 100 m were excluded from the calibration process, with reference antenna m000. For completeness, we calibrated the cross-hand polarization measurements, using a model for 3C138 with a `polindex` of 0.078 and a polarization angle of −9.60° to determine the leakage term (`polcal`), cross-hand delay (`gaincal`), and phase/position angle (`polcal`). The polarization data products will be presented in a future work. In a final step, all the corrections were applied to the phase calibrator source (J0252−7104) and the target source, after which the visibilities were further flagged using `flagdata`. The final flagged percentages of the phase calibrator and target source data sets are approximately 30 per cent (*S*1) and 9 per cent (*S*4). As also seen in Fig. A1, this indicates that the *S*1 sub-band is more affected by RFI relative to *S*4.

Initial imaging was carried out using WSCLEAN with a Briggs (Briggs 1995) robust weighting of $R = -0.5$, following the CASA convention. Fig. 1 shows the flux density of the phase-calibrator source J0252−7104 for all SPWs of both sub-band observations. Overall, the SPWs show a smooth decrease in flux density. To investigate the differences between the sub-band observations and how the SPWs are related, a spectral model for J0252−7104 was

[1] https://github.com/hrkloeck/DASKMSWERKZEUGKASTEN

[2] The model was set as specified in the MeerKAT Knowledge Base, using measurements from the NASA/IPAC Extragalactic Database (NED).

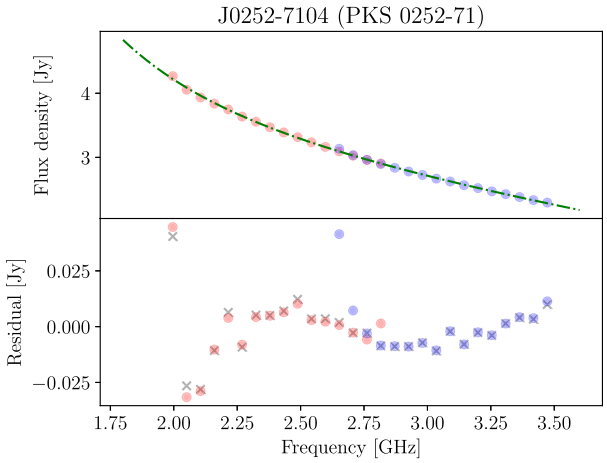

Figure 1. *Top:* flux density of J0252−7104 (PKS 0252−71), the phase calibrator used for the observations, as a function of frequency. *Bottom:* the residual flux density, after applying the flux density model (green), as a function of frequency. Each marker shows the averaged measurement per SPW of both sub-bands (*S*1 in red and *S*4 in blue). The crosses indicates the resulting flux densities of the SPW images of the full concatenated data set. The mean and standard deviation of the residuals are −0.0013 and 0.0123 Jy, respectively.

determined using the same recipe as for the primary calibrator and extracted from the flux densities. The residual measurements show a standard deviation at a percentage level, while some SPWs from *S*1 and *S*4 show some slight offsets at the overlapping frequencies. These SPWs were not used and the final data set for imaging the target source was generated by combining SPWs 0 to 13 (1.97–2.73 GHz) of sub-band *S*1 and SPWs 2 to 15 (2.73–3.50 GHz) of sub-band *S*4.

After primary calibration and concatenating the two sub-bands, we performed phase and amplitude self-calibration using CASA and WSCLEAN.[3] We generated a cleaning mask[4] using the Python Blob Detector and Source Finder (PYBDSF; Mohan & Rafferty 2015, for more information see Section 3.1). The resulting images ($R = -0.5$) over all 27 SPWs each have an rms (i.e. image sensitivity) of $\sigma \approx 15$ μJy beam^{-1}. Through inspection of individual SPW images, we found certain SPWs had increased rms due to a higher system equivalent flux density (SEFD) (Fig. A1) or flagged percentage. We therefore selected a sub-set of SPWs (1–19) for the final multifrequency synthesis (MFS) images. With this, we achieved an rms of $\sigma = 7.5$ μJy beam^{-1} for the same weighting. The final images have a frequency range of 2.02 to 3.06 GHz, covering ~ 1 GHz bandwidth.

For further analysis we created images of two different robust weightings. We selected a weighting of $R = -0.5$ for a higher angular resolution image, a typical weighting selected for MeerKAT *L*-band observations. We also selected a weighting that results in higher sensitivity ($R = 0.3$) and comparable angular resolution to the Mauch et al. (2020) *L*-band image of the DEEP2 field, i.e. $\theta =$ 7.6 arcsec × 7.6 arcsec. The image properties for both images are summarized in Table 2, where the angular resolution is described by the full width at half-maximum (FWHM) of the point spread function (PSF). We present a full analysis of optimal robust parameters at *S*-band frequencies in Appendix B.

[3]https://github.com/hrkloeck/2GC
[4]https://github.com/JonahDW/Image-processing

Table 2. Summary of the resulting image properties for the respective robust weightings.

Parameters	$R = -0.5$	$R = 0.3$
Sensitivity (μJy beam^{-1})	7.5	4.7
Dynamic range	2160:1	3615:1
PSF (maj. × min.)	4.0 arcsec × 2.4 arcsec	6.8 arcsec × 3.6 arcsec
PSF PA (deg)	−1.6	−11.0
N sources	670	1199

2.3 Primary beam correction

Because of the primary beam response of the MeerKAT antennas, flux densities become more attenuated further from the pointing centre. To correct for the primary beam attenuation, an accurate model or measurement of the primary beam response is needed. Analytical models of the MeerKAT primary beam at *S*-band are available,[5] however the most accurate representation of the primary beam is obtained through holographic measurements, which are also available for MeerKAT at *S*-band (Villiers 2023). We therefore elected to use holographic measurements for our primary beam models. These should not differ much from the available analytical models, given that the analytical models are informed by the holographic measurements (de Villiers & Cotton 2022). Because of the large bandwidths of the sub-bands (875 MHz for both *S*1 and *S*4), the frequency evolution of the primary beam must be taken into account when modelling the primary beam. The FWHM of the primary beam evolves with inverse frequency, becoming smaller at higher frequencies. As seen in fig. 1 of Villiers (2023), this relation holds throughout the *S*-band, except for some observed peaks in the FWHM at the higher end of the band. These peaks are an expected feature of the beam elongation at the high-frequency end of the MeerKAT bands. This is more pronounced at *S*-band, with respect to *L*- and *UHF*-band, due to its independent orthomode transducer and feed design (Kramer et al. 2016). This primary beam elongation effect appears at the same frequencies as the peaks in the SEFD seen in Fig. A1.

To produce an accurate primary beam model, we also have to take into account the way in which the MFS image is produced. During imaging, the data was split into 16 SPWs per sub-band, and an MFS image was produced from the weighted average of these SPWs. As specified in Section 2.2, some of these SPWs were excluded from the final imaging, leaving 19 SPWs with which the MFS images were created. Among the excluded SPWs are those at frequencies corresponding to the peaks in FWHM seen in fig. 1 of Villiers (2023). As such, we do not expect to be affected by these in the primary beam correction. To accurately represent the primary beam of the MFS images, we created a set of primary beam models for the individual SPWs and combined them into an MFS primary beam using the same weights used to create the MFS images. While applying the primary beam model, we cut-off the image at the 2 per cent level of the primary beam, producing a nearly circular image with a diameter of 1.54°. The central 54 arcmin × 54 arcmin of the primary beam corrected $R = 0.3$ image (where, a diameter of 54 arcmin corresponds to the 30 per cent level of the primary beam), along with the FHWM of the primary beam, is shown in Fig. 2. Because of the frequency evolution of the primary beam, the *S*1 + *S*4 combined image has a smaller primary beam than if we were to just use *S*1. The primary beam-corrected images at $R = 0.3$

[5]https://github.com/ska-sa/katbeam

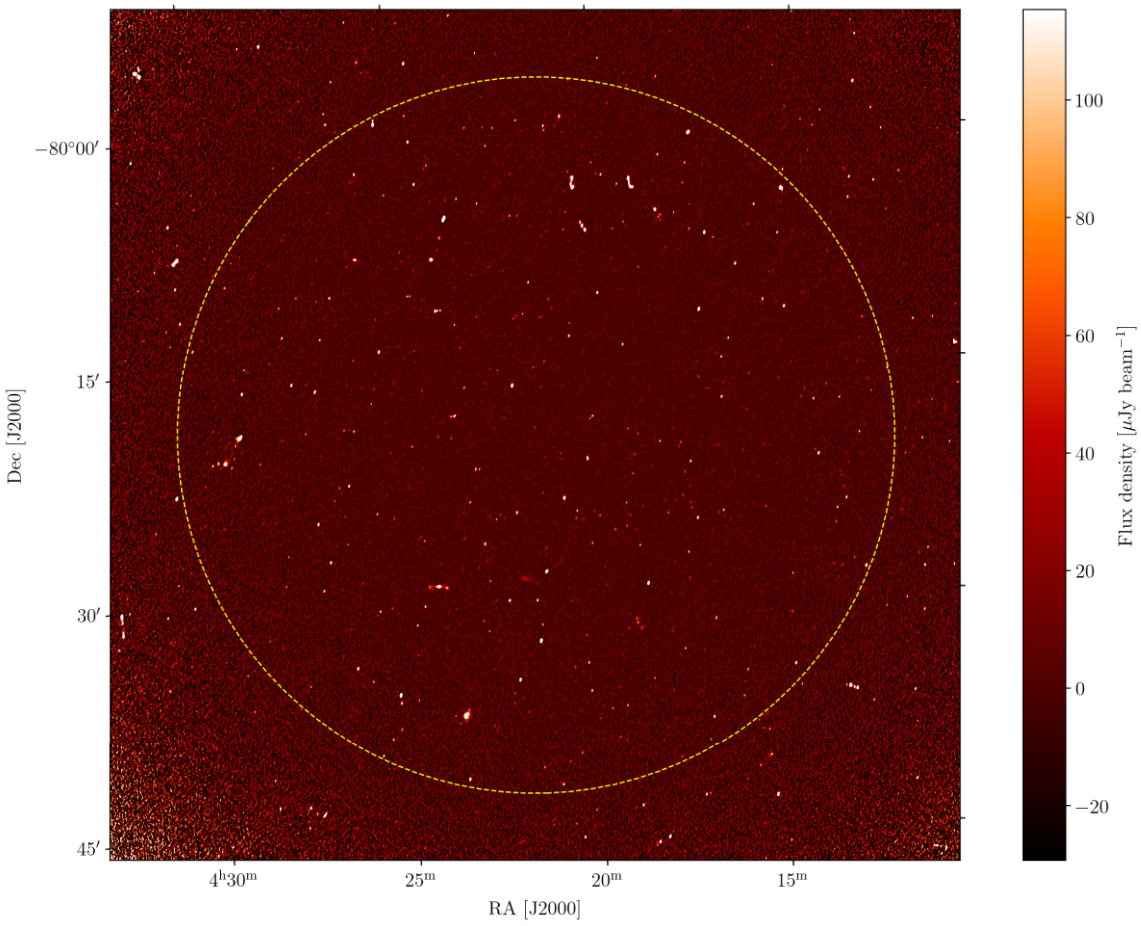

Figure 2. The central 54 arcmin ×54 arcmin of the combined primary beam-corrected *S*1- and *S*4-sub-band image of the DEEP2 field, with a Briggs robust weighting of $R = 0.3$. The FWHM of the primary beam is indicated by the yellow dashed circle, as specified in Section 2.3.

and $R = -0.5$ are available in Flexible Image Transport System (FITS) format on the South African Radio Astronomy Observatory (SARAO) archive[6] at https://doi.org/10.48479/zdyz-8342.

For an accurate comparison with the *L*-band image in Section 3.3.2, we must correct the *L*-band image retrieved from the archive for primary beam attenuation as well. To create an accurate primary beam model, we apply the same method of primary beam correction as described above, using the sub-band frequencies and weights specified in table 5 of Mauch et al. (2020).

3 DEEP2 IMAGE AND CATALOGUING

3.1 Source detection

To generate continuum source catalogues, we use PYBDSFfor source-finding and – extraction. In our PYBDSF run, we select an island threshold of 3σ and a pixel threshold of 5σ. Individual Gaussian components are considered to belong to a single source if they occupy the same island. This assumption is valid for the relatively shallow integration and high resolution of this *S*-band image. We enabled the `adaptive_rms_box` to minimize the false detection of artefacts around bright sources and make use of à trous wavelet decomposition (Holschneider et al. 1989) to improve the fitting of extended sources. We detect 670 sources in the $R = -0.5$ (4.0 arcsec × 2.4 arcsec) image and 1199 sources in the $R = 0.3$ (6.8 arcsec × 3.6 arcsec) image (Table 2). Further assessment of the effectiveness of the source-finding method is discussed in Section 4.1.

3.2 Cross-matching with *L*-band

To compare our results with *L*-band, we retrieve the *L*-band DEEP2 catalogue from Matthews et al. (2021a) and associated *L*-band image (Mauch et al. 2020) from the SARAO archives (Project ID SCI-20180426-TM-01). For a comparison with Matthews et al. (2021a), we cross-match the *L*-band and *S*-band $R = 0.3$ catalogues. We select the $R = 0.3$ (6.8 arcsec × 3.6 arcsec) catalogue for this comparison due to the larger number of sources. We match sources by checking whether source components in the *L*-band catalogue are contained within the *S*-band sources, where we define the area of each *S*-band source as an ellipse with major and minor axes equal to twice the FWHM of the source axes. In total, we find 1289 matches with the Matthews et al. (2021a) *L*-band catalogue, where some *S*-band sources match to multiple components in the *L*-band catalogue. This results matches to 1097 of the *S*-band sources. With a less conservative cut in the distance from the pointing centre, the *S*-band catalogue has 92 sources that do not fall within the area of the *L*-band catalogue.

To verify the astrometric accuracy of the *S*-band observations, we measure the positional offsets of the *S*-band $R = 0.3$ catalogue

[6]https://archive.sarao.ac.za/

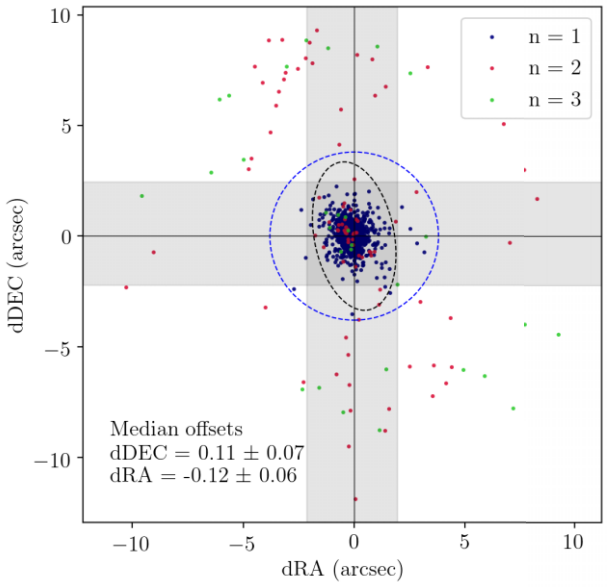

Figure 3. Astrometric offsets of detected sources in the $R = 0.3$ image with respect to the cross-matched components in the *L*-band observations. The points are colourized according to the number of matches n in the *L*-band component catalogue for a given *S*-band source. The synthesized beams of the *S*- and *L*-band observations are shown by the black and blue dashed ellipses, respectively. The standard deviations of the offsets are indicated by the shaded grey regions, and the median offsets are listed on the plot. The inset shows the central 10 arcsec of the plot.

with respect to the *L*-band catalogue. The astrometric offsets are plotted in Fig. 3, and colourized by the number of matches in the *L*-band component catalogue for a given *S*-band source in the $R = 0.3$ image. The positions of the *L*-band and *S*-band detections show good agreement with small overall offsets of $\Delta\mathrm{RA} = -0.12 \pm 0.06$ arcsec and $\Delta\mathrm{Dec.} = 0.11 \pm 0.07$ arcsec. This is well within the pixel size of our images of 0.7 arcsec. The majority of outliers are sources with multiple matches in the *L*-band, i.e. multicomponent sources. We do not correct for these negligible positional offsets in the catalogue.

Given the expected spectral shapes of these sources and the relative noise levels of the respective images, we do not expect sources that are detected in the *S*-band images to be undetected in the *L*-band image. We find 10 of our sources in the $R = 0.3$ catalogue do not have counterparts in the *L*-band Matthews et al. (2021a) catalogue. After visual inspection, we find that the majority of these sources do have associated emission in the Mauch et al. (2020) image with signal-to-noise ratio S/N > 5 and are secondary components to extended sources in *L*-band. Four sources do not correspond to flux density with S/N > 5 in the *L*-band image. Two of these sources have associated emission in the *L*-band image that is below the detection threshold. Using the peak flux density at the position of these sources in the *L*-band image, we calculated the two-point spectral indices α, and find for these sources $\alpha > 2.5$. These extreme values are unphysical (Rees 1967), and we therefore consider the possibility that these are variable sources. However, because these sources have low S/N, i.e. around the detection threshold, we cannot say with any certainty whether these are variable sources, false detections, or boosted by peaks in the additive Gaussian noise. The remaining two sources do not match any emission in the *L*-band image. One has a S/N ~ 5 at *S*-band, and is likely a false detection. For the remaining source J041224−802217 (S/N $= 9.5$), a count of one potential variable source out of the total 1199 sources is consistent with the expected variable source ratio for moderately variable extragalactic sources at *L*-band (< 30 per cent variability on ∼weekly time-scales; Sarbadhicary et al. 2021). However, we would require broader bandwidth coverage and observations at multiple epochs to confirm the variability of this source. Considering the possibility of this source being a variable radio star, we check for any matches in the Gaia Data Release 3 catalogue (Gaia Collaboration 2023). The closest match is a star at RA = 04:12:27.9, Dec. = –80:22:18.42, with a 7.4 arcmin separation from our variable candidate. However, the separation is larger than our angular resolution, particularly for the minor axis of the beam, which is aligned with the direction of the source. It is therefore unlikely that this is the same object.

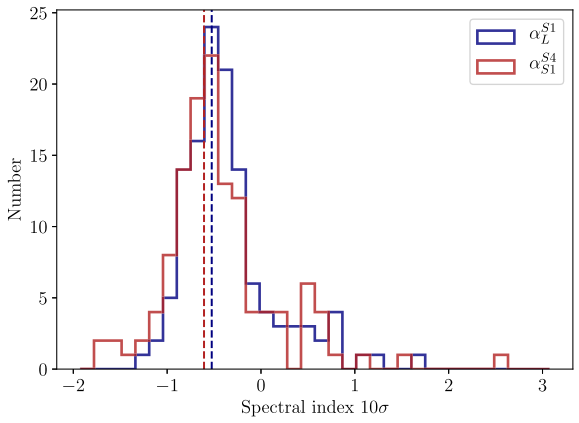

Figure 4. Distribution of spectral indices for $\alpha_{\mathrm{L}}^{\mathrm{S1}}$ (blue) and $\alpha_{\mathrm{S1}}^{\mathrm{S4}}$ (red) for sources above 10σ. The medians of the respective distributions are indicated by the dashed lines.

3.3 Source properties

3.3.1 Multiband spectral indices

The spectral energy distributions of radio sources are particularly useful for the classification of sources and the dominant emission mechanism (e.g. Prandoni et al. 2010; Sinha, Mangla & Datta 2023). Including the *L*-band observations from Mauch et al. (2020), increases our effective bandwidth to $\Delta\nu \sim 1.8$ GHz, allowing for the determination of multiband spectral indices of the detected sources. As discussed in Section 2.2, we make use of 13 SPWs from the *S*1 band and 6 SPWs from the *S*4 band. Although the *L*-band data from Mauch et al. (2020) was also divided into 14 spectral windows, only the full-band images and catalogues are publicly available, giving us a single flux density value at a frequency of 1.28 GHz for each source (Matthews et al. 2021a). For each source in the $R = 0.3$ (6.8 arcsec × 3.6 arcsec) catalogue, we extract the flux densities (in Jy) within an ellipse with major and minor axes at 1.5 times the source extent. This was done using the `imfit` task from CASA. We determine spectral indices for sources above 10σ, where σ is the local rms. This is determined from the `Isl_rms` output in PYBDSF, scaled to the bandwidth of the individual spectral windows, i.e. by $\sqrt{N_{\mathrm{SPW}}}$, where N_{SPW} is the number of SPWs. For this sample of 125 sources, we calculate two spectral indices. First, by fitting a power law to the *L*-band flux density measurement and the 13 SPWs from the *S*1 band α_{L}^{S1}. Secondly, we fit a power law to the combined 19 SPWs across *S*1 and *S*4 $\alpha_{\mathrm{S1}}^{S4}$. The distributions of α_{L}^{S1} and $\alpha_{\mathrm{S1}}^{S4}$ for the 10σ sample are plotted in Fig. 4. The spectral index distributions are as expected for the observed frequency range (Condon 1984). We find a median α_{L}^{S1}

of -0.52 ± 0.16. For α_{S1}^{S4}, we determine a median of -0.61 ± 0.33. The associated errors are determined from the uncertainties on the power-law fits. The distribution of spectral indices including the *L*-band and that including the *S*4 sub-band show good agreement with each other. However, a broader bandwidth is required to identify spectral turnovers with significant reliability. While we expect an increase in the number of flat-spectrum sources due to the selection bias at this frequency range, where sources become increasingly core-dominated (Whittam et al. 2013), both spectral index distributions have a mode of $\alpha = -0.6$.

3.3.2 *Identifying resolved sources*

Due to uncertainties in source fitting, resolved sources cannot be simply identified as sources that are larger than the beam. To confidently identify resolved sources, we consider that due to the aforementioned fitting uncertainties, unresolved sources have Gaussian uncertainties on their measured size parameters. A proxy for the size of a source is the ratio of total flux density to peak flux density, $S_{\rm tot}/S_{\rm peak}$. The distribution of $S_{\rm tot}/S_{\rm peak}$ is expected to be log-normal (e.g. Franzen et al. 2015; Wagenveld et al. 2023), with standard deviation $\boldsymbol{\sigma_\rho}$ described by the sum in quadrature of the relative uncertainties on $S_{\rm tot}$ and $S_{\rm peak}$,

$$\sigma_\rho = \sqrt{\left(\frac{\sigma_{S_{\rm tot}}}{S_{\rm tot}}\right)^2 + \left(\frac{\sigma_{S_{\rm peak}}}{S_{\rm peak}}\right)^2}. \quad (1)$$

The PYBDSF fit uncertainty for $S_{\rm tot}$ includes the uncertainty on $S_{\rm peak}$ as well as the uncertainty on the determined major and minor axes of the source (equation 36 of Condon et al. 1998). To make sure $\sigma_{S_{\rm tot}}$ and $\sigma_{S_{\rm peak}}$ are independent, we subtract the fitted uncertainty on $S_{\rm peak}$, and define $\sigma_{S_{\rm peak}}$ as the local rms noise at the source position. We then identify resolved sources as sources for which

$$\ln\left(\frac{S_{\rm tot}}{S_{\rm peak}}\right) > 2\sigma_\rho, \quad (2)$$

which should reliably select 97 per cent of unresolved sources.

Sources are classified as multicomponent sources, if they are fitted with multiple Gaussian components with PYBDSF. By this definition, all multicomponent sources should also be classified as resolved. With the higher resolution of the *S*-band $R = -0.5$ (4.0 arcsec $\times$ 2.4 arcsec) image, we find an increased percentage of both resolved and multicomponent sources. We find 18 per cent resolved sources with $R = 0.3$ and 22 per cent resolved sources for $R = -0.5$. Similarly, we find 7 per cent of sources in $R = 0.3$ are multicomponent sources, and 10 per cent multicomponent sources for $R = -0.5$. In the Matthews et al. (2021a) catalogue, there is no classification for resolved sources but they identify 35 multicomponent sources (0.2 per cent of the total number of sources). At low flux densities (< 15 μJy), we expect the detected samples in *L*- and *S*-band to be dominated by star-forming galaxies, which should be mostly unresolved at MeerKAT *S*-band angular resolution (Cotton et al. 2018).

Fig. 5 illustrates some examples of the structural detail revealed by *S*-band observations in resolved sources. We plot cut-outs of extended sources at *L*-band (Mauch et al. 2020), and *S*-band $R = 0.3$ (6.8 arcsec $\times$ 3.6 arcsec) and $R = -0.5$ (4.0 arcsec $\times$ 2.4 arcsec). The top row is a radio galaxy J041339–794637, for which we resolve the jets in *S*-band, whereas in the *L*-band image, only the core and lobes are visible. The $R = -0.5$ image also resolves multiple bright components in the southern lobe, unseen at *L*-band. The middle row shows an example of a source J041654–795445 that is detected as two components at *L*-band, but as three components and two discrete sources at *S*-band. Assuming this is a radio galaxy with a central core and two lobes, the core is associated to the same source as the western lobe (Section 3.1). The third row shows star-forming galaxy (SFG) J041622–802052 (Gaia Collaboration 2020) at a redshift of $z = 0.016$ (Fairall & Woudt 2006), which is resolved in all images, with extended emission recovered in the $R = 0.3$ image (centre). However, we do not fully recover the extended emission at $R = -0.5$ due to the higher angular resolution. This illustrates how with the brightness temperature sensitivity of MeerKAT, it is possible to detect extended SFGs at *S*-band frequencies, even with relatively short integration times (e.g. Condon 2015), and shows the great potential for larger area snapshot surveys with the MeerKAT *S*-band for both AGN and star-forming populations.

3.4 Catalogue overview

The final source catalogues of the DEEP2 field with MeerKAT *S*-band includes the 1199 sources detected in the $R = 0.3$ (6.8 arcsec $\times$ 3.6 arcsec) image and the 670 sources detected in the $R = -0.5$ (4.0 arcsec $\times$ 2.4 arcsec) image. We provide a separate catalogue for each image. The $R = 0.3$ catalogue spans a flux density range from 16.9 μJy to 26.0 mJy and for $R = -0.5$, the flux densities range from 31.1 μJy to 25.3 mJy, due to the lower sensitivity of the latter weighting. The flux density distribution of each catalogue is shown in Fig. 6. The catalogues are available in FITS format on the SARAO archive at https://doi.org/10.48479/zdyz-8342. An example of the catalogue structure can be found in Appendix D. Here, we provide the source positions, flux densities, source sizes, and their associated errors as determined from PYBDSF. The catalogue also includes the classification of resolved sources (Section 3.3.2) and the spectral index (Section 3.3.1), where available. The cross-matched source ID and flux density at 1.28 GHz from Matthews et al. (2021a) has been included for convenience. In brief, we summarize the catalogue columns below, with a detailed description in Appendix D.

1–27 PYBDSF output, as described in the PYBDSF documentation.[7]

28 Boolean classification for resolved sources.

29–30 Corresponding source index and flux density from the Matthews et al. (2021a) 1.28 GHz catalogue (only available for $R = 0.3$).

31–32 Spectral index α_L^{S1} over the *L* and *S*1 bands for sources detected above 10σ, and associated uncertainties (only available for $R = 0.3$).

33–34 Spectral index α_{S1}^{S4} over the *S*1 and *S*4 bands for sources detected above 10σ, and associated uncertainties (only available for $R = 0.3$).

While the $R = -0.5$ image and associated catalogue is particularly useful for a higher resolution perspective of resolved galaxies, we recommend the $R = 0.3$ catalogue for general use. The lower rms yields almost a factor of 2 more detected sources and the lower angular resolution of the images allow for a more consistent comparison with the *L*-band catalogue, and better recovery of faint, extended emission (Fig. 5). We therefore only provide the *L*-band catalogue match and spectral indices for the $R = 0.3$ catalogue. Furthermore, we recommend $R = 0.3$ as an optimal robust weighting for such broad-band extragalactic fields with MeerKAT *S*-band. For a detailed analysis on the selection of optimal robust weighting, see Appendix B.

[7] https://pybdsf.readthedocs.io/en/latest/

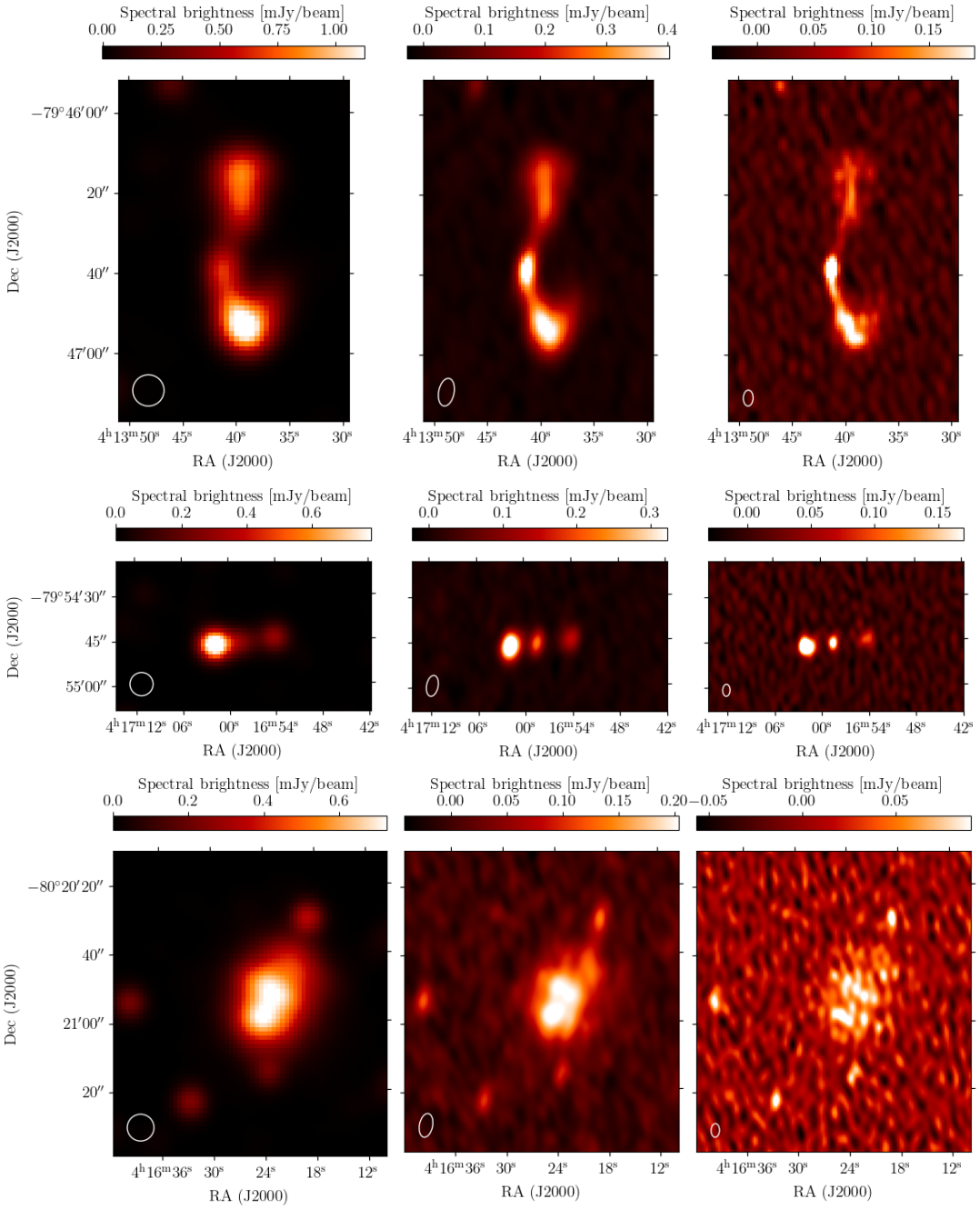

Figure 5. Cut-outs of selected extended sources in *L*-band (Mauch et al. 2020, left), *S*-band $R = 0.3$ (centre) and $R = -0.5$ (right). The restoring beam for each image is shown in the bottom left corner. From top to bottom, the sources shown are J041339–794637, J041654–795445, and J041622–802052.

4 DIFFERENTIAL SOURCE COUNTS

To compare the catalogues with respect to each other and to other surveys, we calculate source count corrections and differential source counts for both the $R = 0.3$ and $R = -0.5$ catalogues. Further results following deeper observations will be presented in future publications.

4.1 Completeness

To assess the completeness of our catalogues and the effectiveness of our source-finding strategy, we test our source-finding methods on simulated images. To do this, we make use of the SKA Design Survey (SKADS) Simulated Skies catalogue (Wilman et al. 2008), for realistic samples of extragalactic sources. We create catalogues of 4500 simulated sources, with sources uniformly distributed in logarithmically spaced bins over a flux density range of $\sigma < S < S_{\rm max}$, where S is the flux density, i.e. $n(S) \propto S^0$. The lower limit is equal to the rms σ of an image and the upper limit is consistent with the brightest detected source. While this is not a physically realistic flux density distribution, it is the best distribution for determining the completeness with the same level of accuracy across the probed flux density range. We convolve the simulated sources to the angular

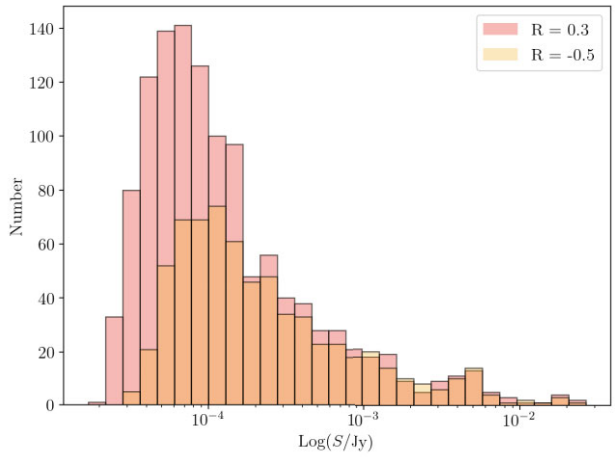

Figure 6. Distribution of source flux densities from the $R = 0.3$ (6.8 arcsec $\times$ 3.6 arcsec, red) and $R = -0.5$ (4.0 arcsec $\times$ 2.4 arcsec, yellow) catalogues described in Section 3.4.

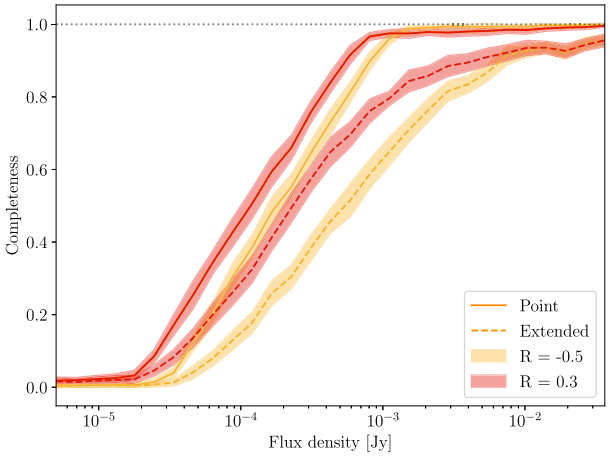

Figure 7. The catalogue completeness for point (solid line) and extended sources (dashed) as a function of flux density. The completeness curves are shown in red and yellow for $R = 0.3$ and $R = -0.5$, respectively. The shaded regions show the standard deviation and the black dotted line indicates 100 per cent completeness.

resolution of our observations and inject them at randomly selected positions in the residual image from PYBDSF. This residual image contains no detectable sources with our chosen source-finding parameters and has consistent noise characteristics with our original image. We then perform the same source-finding routine on the simulated image (i.e. the residual image with injected synthetic sources), with the rms and mean maps determined by PYBDSF from the original image. We consider a source successfully recovered if it is detected within the FWHM of the restoring beam of the injected position. This process is repeated 50 times each for resolved and unresolved sources to achieve a statistically robust result. In the case of resolved sources, we randomly select sources from the SKADS catalogue with major and minor axes larger than zero, and for unresolved sources we randomly select SKADS sources with a major axis of zero, as they are defined as delta functions in the catalogue. Resolved and unresolved sources are respectively modelled as delta functions and Gaussians. These sources are then convolved with the clean beam and injected into the mock images. We calculate the completeness as the ratio between the number of recovered sources to the total number of sources within each flux density bin. The completeness curves for both the $R = -0.5$ and $R = 0.3$ images are plotted in Fig. 7. The respective completeness curves for resolved and unresolved sources do not follow the same distribution, as expected due to the reduced surface brightness of resolved sources. We find that 98.5 per cent of point sources are recovered at flux densities above 5×10^{-5} Jy for $R = 0.3$ and 1×10^{-4} Jy for $R = -0.5$. For extended sources, we reach 93 per cent completeness at $\sim 10^{-2}$ Jy for both images.

4.2 Purity

We assess the false detection rate, or purity of our source finding parameters, to be taken into account when measuring number counts. We do not expect potential false detections to be caused by calibration artefacts around bright sources, as this field was selected in particular not to have any problematic bright sources, with the brightest source in the field at 26 mJy. Any false detections are likely attributed to statistical outliers in the noise, such that the number of negative detections is representative of the number of positive false detections. To determine the purity, we invert the pixel values of the images and execute PYBDSF using the rms and inverted mean maps from the original images, to ensure that the source finding is performed in the same way. In both images, we find zero false detections above 5σ which are attributed to outliers in the noise, i.e. a catalogue purity of 100 per cent. As a further assessment for the false detection rate, we assess the Gaussianity of the noise, by plotting the flux density distributions of the four corners (300 pix $\times$ 300 pix) of the primary beam-uncorrected image ($R = 0.3$). We perform Komolgorov–Smirnov tests on these distributions, resulting in an average p-value of 0.71. As such, we do not reject the null hypothesis that the image noise is Gaussian, and we do expect extreme outliers in the noise that could result in a false detection. However, as per the analysis done in Section 3.2, it is likely that 1–3 of the sources not detected in L-band are false detections.

4.3 Stacking

To obtain a flux density estimate for the sources below our detection threshold, we make use of image-plane stacking. Stacking can be used to statistically determine the average flux density properties of undetected source samples by co-adding their emission, based on their known positions from other catalogues (e.g. Dunne et al. 2009; Karim et al. 2011; Perger, Frey & Gabányi 2024). To do this, we select all sources from the L-band catalogue that were not detected in the $R = 0.3$ (6.8 arcsec $\times$ 3.6 arcsec) S-band image ($< 5\sigma$) and lie within 0.4° of the S-band phase centre (i.e. close to the primary beam FWHM). This resulted in a stacking sample of 7573 sources. We generated 100 pix $\times$ 100 pix cut-outs of all sources in the stacking sample, such that the source position in our L-band catalogue was centred in the cut-out and smoothed the images to the angular resolution of the L-band image (7.6 arcmin $\times$7.6 arcmin). We calculate the stacked mean flux density over these cut-outs. Although the median stacking is particularly useful as it is not sensitive to outliers, its interpretation is limited for faint sources (White et al. 2007), for which the mean flux density is more appropriate. We can account for the local noise for each source, by taking a weighted mean for the stacked flux density,

$$S_{\text{mean}} = \frac{\sum_{i=1}^{N} w_i \times S_i}{\sum_{i=1}^{N} w_i}, \tag{3}$$

Table 3. Stacked flux density and number of stacked sources for logarithmically spaced bins.

Bin width (μJy)	N	$S_{\rm mean}$ (μJy) (S/N)
$10 < S_{1.28\rm GHz} < 16$	2666	5.54 ± 0.17 (33)
$16 < S_{1.28\rm GHz} < 25$	2211	8.47 ± 0.18 (45)
$25 < S_{1.28\rm GHz} < 40$	1454	14.00 ± 0.23 (60)

and constructing a mean map. Here, S is the pixel flux density, w is the weight, as function of the local noise $\sigma_{\rm local}$, determined as $w = \sigma_{\rm local}^{-2}$, and N is the number of stacked sources (e.g. Zwart et al. 2014). We determine the stacked flux density by fitting a 2D Gaussian to the stacked image. The associated uncertainties are calculated as the rms over all stacked sub-images divided by $\sqrt{N}$.

We stacked the full sample and make a 62σ weighted stacked detection, with a flux density of 10.40 ± 0.17 μJy. We aim to use the stacked flux density estimates to probe the source counts below the detection threshold. For this, we divide the sample into three logarithmically spaced flux density bins, using the flux density measurement from the Matthews et al. (2021a) catalogue. The number of sources per bin and the resulting stacked flux density is summarized in Table 3. With a large number of sources in each bin, we can successfully make high S/N stacked detections of the faint source population in the DEEP2 S-band $R = 0.3$ image. However, when measuring the mean flux density of the stacked sources at L-band and scaling to 2.5 GHz (assuming an average spectral index of $\alpha = -0.7$), we find that $S_{\rm mean}$ is, on average, 26 per cent lower than expected. As this would imply that the faint source population have steeper spectral indices of $\alpha = -1.2$, we consider that this missing flux density is likely a systematic effect.

One such systematic, as reported in Matthews et al. (2021a), is the offset between the true flux density and the measured flux density in the DEEP2 L-band for sources with $S_{1.28\,\rm GHz} \lesssim 40$ μJy. This offset is attributed to source confusion at low flux densities. For the flux densities in the stacked source sample, the distribution of these offsets has a positive tail that ranges up to ~ 10 μJy. While this contributes to the inconsistent spectral index measured here, it likely does not account for the full discrepancy. There are likely additional errors introduced by the limitations of stacking which may lead to an underestimation of the S-band flux density. For example sources below the noise are not deconvolved (Karim et al. 2011), which will result in a loss of signal in the main lobe of the PSF. Future deep observations will allow for a more accurate determination of the spectral indices for the μJy 3 GHz source population of the DEEP2 field.

4.4 Euclidean number counts

The differential source counts of these catalogues are shown in Fig. 8, and are also tabulated in Appendix C. The source counts are corrected for completeness, assuming that point sources constitute a third of the population, with the rest being extended.[8] This follows the relative abundances of intrinsic source sizes in the SKADS catalogue, and thus should represent the real size distribution of sources to the extent that SKADS sources accurately represent the observed source population. The uncertainty in the completeness (shown in Fig. 7) is also accounted for in the source count uncertainties. Aside from uncertainties in source counts that arise from Poisson statistics and completeness, cosmic variance in source counts in a limited sky area is also expected to be affected by source clustering. Following Heywood, Jarvis & Condon (2013), we quantify these effects on differential source counts using the SKADS catalogue (Wilman et al. 2008). From the SKADS catalogue, we randomly extract sky areas with an area equal to that of the images, at a frequency of 2.5 GHz (matching the mean frequency of the combined $S1$ and $S4$ images), and compute the differential number counts. We do this 500 times to statistically determine the expected variance in source counts, both due to clustering and Poisson contributions. This variance is also shown in Fig. 8, illustrating that down to the completeness limit, the variation in differential source counts of the two S-band images can be explained by the expected variance.

As a comparison for the source counts obtained here, Fig. 8 includes the combined 1.4 GHz DEEP2 and NRAO VLA Sky Survey (NVSS) source counts from Matthews et al. (2021a), as well as the 3 GHz VLA-COSMOS source counts from Smolčić et al. (2017).Both have been converted to 2.5 GHz assuming a spectral index of $\alpha = -0.7$. At higher flux densities, all measurements agree well within the variance introduced by the small sky coverage of DEEP2. However, at lower flux densities ($S \lesssim 100$ μJy), we enter a regime where different measurements as well as the theoretical expectation start to significantly disagree. Taking into account their respective sky coverages, both the Matthews et al. (2021a) and Smolčić et al. (2017) counts are larger than the expected source counts from SKADS. This is commonly attributed to an underestimation of SFGs in the SKADS catalogue (e.g. Smolčić et al. 2017; der Vlugt et al. 2021; Hale et al. 2023). Though our S-band source counts are roughly in agreement with the Matthews et al. (2021a) source counts, our catalogue is highly incomplete at these flux densities (see Fig. 7), resulting in large uncertainties. At roughly 50 μJy the source counts fall off, for which the completeness corrections are no longer adequate.

As demonstrated in Section 4.3, we can use image plane stacking to detect sources below the noise using the source positions from the L-band catalogue. We can also use this to probe the source counts below the detection threshold. We do this by stacking at the positions of L-band sources for each flux density bin of the Matthews et al. (2021a) source counts (Table 3). Since we can not know how many sources are actually detected in the stacked measurement at S-band, these results can not directly be translated to source counts. However, in measuring the mean flux density of the stacked sample, we can compare it to the expected mean flux density of the sample, assuming, as before, a spectral index of $\alpha = -0.7$. We see that the mean flux densities of the stacked samples are generally low, which could be caused by a number of effects, including systematic effects (as discussed in Section 4.3), or a portion of sources not being detected. If we assume that all missing flux density is caused by missing sources, we can convert this to an estimate of source counts. This is shown in Fig. 8 and compared to the Matthews et al. (2021a) source counts, as these represent the source counts expected if all L-band sources are detected in S-band. As it is unlikely that all missing flux density is due to missing sources, these stacked source counts can be viewed as a lower limit on source counts at S-band. It is worth noting that the amount of missing flux density is essentially the same in all bins, and thus not dependent on flux density.

While deeper observations are needed for more robust source counts, the observing time required to reach the necessary depth at S-

[8]Note, that extended here simply means a major axis larger than zero in the SKADS catalogue with which the completeness simulations were performed. With this definition, star-forming galaxies are always extended even though most are likely unresolved with the current image resolution (Cotton et al. 2018).

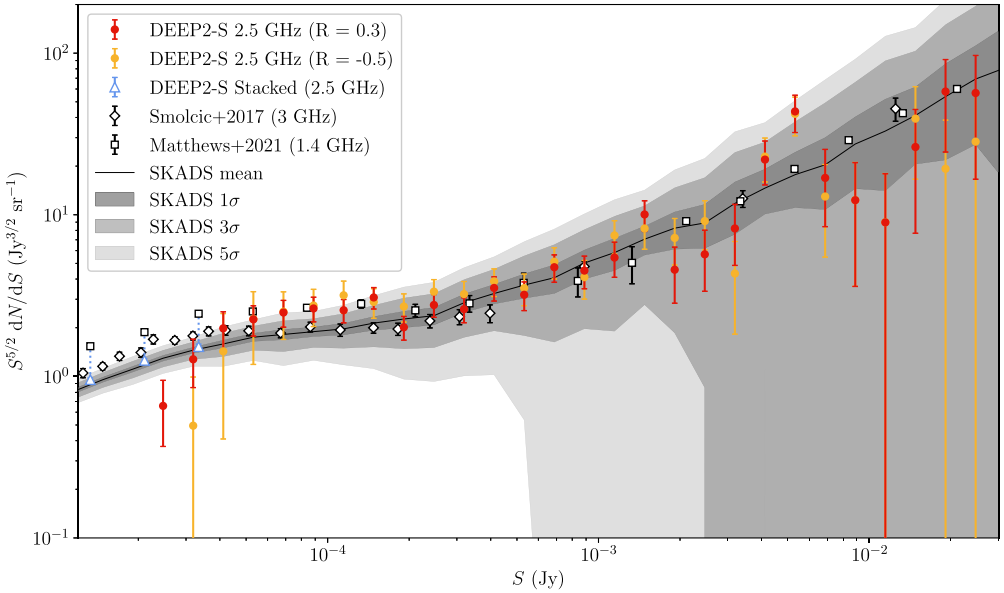

Figure 8. Completeness-corrected differential source counts for the DEEP2 *S*-band catalogues with $R = 0.3$ (red) and $R = -0.5$ (yellow). The expected differential source counts from the SKADS catalogue is shown by the black solid line, with the grey shaded regions indicating the simulated 1σ, 3σ, and 5σ variance stemming from our limited sky coverage and Poisson variance. The 1.4 GHz source counts of DEEP2 and NVSS (Matthews et al. 2021a) and 3 GHz VLA COSMOS source counts (Smolčić et al. 2017) are shown as white squares and diamonds, respectively, converted to 2.5 GHz, assuming a spectral index of $\alpha = -0.7$. For the majority of the probed flux density range, source counts agree between each other. In the range where both simulations and different observations begin to disagree ($S \lesssim 100$ μJy) our counts are still broadly consistent with Matthews et al. (2021a) before they fall off due to increasing incompleteness at around 50 μJy. The stacked source counts (blue triangles) are computed assuming that all missing flux density in the stacking is due to missing sources, presenting a lower limit on *S*-band source counts below our current detection limit, which is consistent with the expected source counts.

band is only a fraction of the best available deep *S*-band surveys. For example ∼5 per cent of the total integration time of VLA-COSMOS 3 GHz (Smolčić et al. 2016) survey is required to achieve the same point source sensitivity, as well as improving brightness temperature sensitivity (for *S*1 sub-band), highlighting the potential for deep *S*-band surveys with MeerKAT (e.g. Jarvis et al. 2016). To achieve the sensitivity levels of the deepest published *S*-band survey, COSMOS-XS (der Vlugt et al. 2021), with a sensitivity of 0.53 μJy beam^{-1}, we would require a comparable integration time to COSMOS-XS. However, the MeerKAT *S*-band returns a 16 times larger sky coverage in a single pointing. In particular, and as discussed above, a larger area has a clear advantage in managing the cosmic variance in differential source counts. In comparison to COSMOS-XS, a survey of similar depth with MeerKAT *S*-band will reduce the scatter due to source clustering by a factor of 1.7 (Heywood et al. 2013) and Poisson statistics by a factor of 4. The observations could be further optimized by observing in sub-band *S*2 (Table A1), which is relatively free of RFI and beam squint effects (Villiers 2023), resulting in a larger usable bandwidth.

5 DISCUSSION AND CONCLUSION

We have presented pilot *S*-band catalogues of the DEEP2 field, a unique radio selected legacy field. With images combining the *S*1 and *S*4 sub-bands, we achieved a sensitivity of 4.7 and 7.5 μJy beam^{-1}, for robust values of $R = 0.3$ (6.8 arcsec × 3.6 arcsec) and $R = -0.5$ (4.0 arcsec × 2.4 arcsec), respectively. We detected 1199 and 670 sources at the respective robust weightings.

While we have found that imaging the combination of two frequency sub-bands (∼1750 MHz) is possible with the MeerKAT *S*-band system, the higher end of the *S*4 sub-band $\nu > 3.06$ GHz has a significantly higher rms and was excluded from MFS images for the best wide-field imaging result. We conducted a spectral index analysis through spectral fitting of the 19 SPWs across the *S*1 and *S*4 sub-bands and the measurement at 1.28 GHz from the Mauch et al. (2020) images, and found a spectral index distribution as expected in the literature. We computed the completeness-corrected differential sources counts for the DEEP2 field at 2.5 GHz down to 20 μJy, and found our source counts to be consistent with simulations and other deep-field source counts. Although these observations do not obtain the sensitivities of the deepest *S*-band surveys in the literature, only a fraction of the observing time was needed to reach similar depth and achieve comparable results. To probe the faint source population $S < 40$ μJy, we performed image-plane stacking on the $R = 0.3$ image and estimated lower limits for source counts down to 10 μJy, which we found to be consistent with simulations but lower than other source counts in the literature. We attributed the lower stacked flux density with respect to Matthews et al. (2021a) to missing sources or systematic effects, which may be caused by assumptions made in the stacking procedure.

Future *S*-band observations of the DEEP2 field, will overcome the confusion limit at 1.28 GHz, allowing for the direct imaging of SFGs below 0.55 μJy beam^{-1}. Furthermore, the availability of a confusion-limited *L*-band image provides a comparison to a near-complete sky model with the same instrument. Through the computation of differential source counts, we aim to address the completeness for shallow observations with the MeerKAT *S*- band. This serves to inform future moderate to large-scale surveys with short per-target integration times. The addition of the *S*-band to the MeerKAT system will allow for more detailed studies of extragalactic

fields across a broader bandwidths and into the sub-μJy regime with longer integration times, among other continuum science goals (e.g. Galactic plane, nearby galaxies), providing great scientific potential for future *S*-band surveys in the pre-SKA era, with MeerKAT and its upcoming 14-antenna extension, MeerKAT + .

ACKNOWLEDGEMENTS

We thank the referee, Allison Matthews, for helpful comments and suggestions that significantly improved this work. We thank Bill Cotton and Rainer Beck for helpful comments on the manuscript. SR and JDW acknowledge the support from the International Max Planck Research School (IMPRS) for Astronomy and Astrophysics at the Universities of Bonn and Cologne. RPD acknowledges funding from the South African Research Chairs Initiative of the Department of Science and Innovation and National Research Foundation (Grant ID 77948). MRR is a Jansky Fellow of the National Radio Astronomy Observatory. The MeerKAT telescope is operated by the South African Radio Astronomy Observatory, which is a facility of the National Research Foundation, an agency of the Department of Science and Innovation.

This work has made use of the 'MPIfR *S*-band receiver system' designed, constructed and maintained by funding of the MPI für Radioastronomie and the Max-Planck-Society. In particular, we acknowledge the contribution and efforts of the experts of the 'Electronics' and 'Digital Signal Processing' departments of the MPIfR in this project.

This research has made use of the NASA/IPAC Extragalactic Database, which is funded by the National Aeronautics and Space Administration and operated by the California Institute of Technology.

DATA AVAILABILITY

All data products specified in this paper are publicly available in FITS format. The MFS images and catalogues for both $R = 0.3$ and $R = -0.5$ can be found on the SARAO archive at https://doi.org/10.48479/zdyz-8342. Please see Section 3.4 and Appendix D for more details. Raw data or other data products can be made available upon reasonable request to the authors.

REFERENCES

Algera H. S. B. et al., 2020, ApJ, 903, 139
Briggs D. S., 1995, PhD thesis, New Mexico Institute of Mining and Technology
Condon J. J., 1984, ApJ, 287, 461
Condon J. J., 1992, ARA&A, 30, 575
Condon J., 2015, Proc. Sci., Radio Continuum Surveys: Lessons Learned. SISSA, Trieste, PoS(EXTRA–RADSUR2015)004
Condon J. J., Cotton W. D., Greisen E. W., Yin Q. F., Perley R. A., Taylor G. B., Broderick J. J., 1998, AJ, 115, 1693
Cotton W. D. et al., 2018, ApJ, 856, 67
de Villiers M. S., 2023, AJ, 165, 78
de Villiers M. S., Cotton W. D., 2022, AJ, 163, 135
Delhaize J. et al., 2017, A&A, 602, A4
Dunne L. et al., 2009, MNRAS, 394, 3
Fairall A. P., Woudt P. A., 2006, MNRAS, 366, 267
Franzen T. M. O. et al., 2015, MNRAS, 453, 4020
Gaia Collaboration, 2020, VizieR On-line Data Catalog: I/350. Gaia EDR3. Centre de Donnees Astronomique de Strasbourg (CDS). Available at: https://doi.org/10.26093/cds/vizier.1350
Gaia Collaboration, 2023, A&A, 674, A1
Hale C. L. et al., 2023, MNRAS, 520, 2668
Heesen V. et al., 2019, A&A, 622, A8
Heywood I., Jarvis M. J., Condon J. J., 2013, MNRAS, 432, 2625
Holschneider M., Kronland-Martinet R., Morlet J., Tchamitchian P., 1989, in Combes J.-M., Grossmann A., Tchamitchian P., eds, Wavelets. Time-Frequency Methods and Phase Space. Springer-Verlag, Berlin, p. 286
Jarvis M. et al., 2016, Proc. Sci., The MeerKAT International GHz Tiered Extragalactic Exploration (MIGHTEE) Survey. SISSA, Trieste, PoS(MeerKAT2016)006
Jonas J., MeerKAT Team, 2016, Proc. Sci., PoS(MeerKAT2016)001The MeerKAT Radio Telescope. SISSA, Trieste, PoS(MeerKAT2016)001
Karim A. et al., 2011, ApJ, 730, 61
Kramer M. et al., 2016, Proc. Sci., PoS(MeerKAT2016)003The MeerKAT Max-Planck S-band System. SISSA, Trieste, PoS(MeerKAT2016)003 , Proceedings of Science
Leslie S. K. et al., 2020, ApJ, 899, 58
Matthews A. M., Condon J. J., Cotton W. D., Mauch T., 2021a, ApJ, 909, 193
Matthews A. M., Condon J. J., Cotton W. D., Mauch T., 2021b, ApJ, 914, 126
Mauch T. et al., 2020, ApJ, 888, 61
McMullin J. P., Waters B., Schiebel D., Young W., Golap K., 2007, in Shaw R. A., Hill F., Bell D. J., eds, ASP Conf. Ser.Vol. 376, Astronomical Data Analysis Software and Systems XVI. Astron. Soc. Pac., San Francisco, p.127
Mohan N., Rafferty D., 2015, Astrophysics Source Code Library, record ascl:1502.007
Murphy E. J., 2009, ApJ, 706, 482
Offringa A. R. et al., 2014, MNRAS, 444, 606
Perger K., Frey S., Gabányi K. É., 2024, MNRAS, 527, 3436
Prandoni I., de Ruiter H. R., Ricci R., Parma P., Gregorini L., Ekers R. D., 2010, A&A, 510, A42
Radcliffe J. F., Beswick R. J., Thomson A. P., Njeri A., Muxlow T. W. B., 2024, MNRAS, 527, 942
Rees M. J., 1967, MNRAS, 136, 279
Sarbadhicary S. K. et al., 2021, ApJ, 923, 31
Sinha A., Mangla S., Datta A., 2023, JA&A, 44, 88
Smolčić V. et al., 2016, A&A, 592, A10
Smolčić V. et al., 2017, A&A, 602, A1
van der Vlugt D. et al., 2021, ApJ, 907, 5
Wagenveld J. D. et al., 2023, A&A, 673, A113
White R. L., Helfand D. J., Becker R. H., Glikman E., de Vries W., 2007, ApJ, 654, 99
Whittam I. H. et al., 2013, MNRAS, 429, 2080
Wilman R. J. et al., 2008, MNRAS, 388, 1335
Zwart J. T. L., Jarvis M. J., Deane R. P., Bonfield D. G., Knowles K., Madhanpall N., Rahmani H., Smith D. J. B., 2014, MNRAS, 439, 1459

APPENDIX A: MEERKAT *S*-BAND SYSTEM

The *S*-band receivers (Kramer et al. 2016) were designed and built by the Max Planck Institute for Radio Astronomy (MPIfR), and through a collaboration with SARAO, are now fully integrated into the MeerKAT system, with a receiver on each of the 64 antennas. Their analogue front end and digitizers deliver a full band from 1750 to 3500 MHz. Half of this bandwidth (875 MHz) can be selected with a digital filter at any given time, positioned at five available sub-bands *S*0–*S*4 with uniform spacing and large overlap, as summarized in Table A1. For the observations described in Section 2.1, sub-bands *S*1 and *S*4 were used (Table 1). When combined, they provide contiguous coverage of the frequency range 1968–3500 MHz. Within this frequency range, we expect negligible (< -50 dB) frequency aliasing due to the decimation filters. At the very high end, additional sampling-induced aliasing is expected from other Nyquist zones. This is minimized with analogue filters.

In order to measure the absolute flux sensitivity, the noise level per frequency and baseline were determined from the final scans of

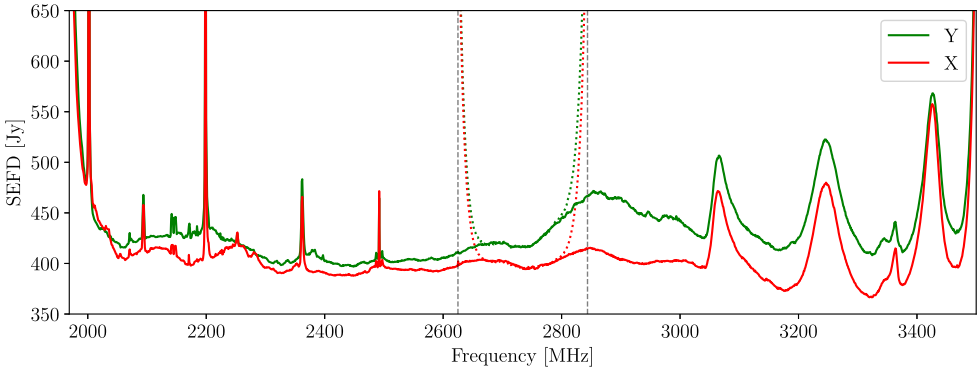

Figure A1. SEFD for a representative antenna over the combined range of our observations (*S*1 and *S*4) for both linear polarizations Y (green) and X (red). The band edges are denoted by vertical dashed lines. In the overlapping regions, the nearer sub-band is plotted in solid lines, the other is shown as dotted lines and shows the expected increase towards the edge. The variations in the upper half of the band are caused by frequency dependent gain and noise levels of the receiver system, which cannot be avoided at such a wide band (e.g. de Villiers 2023). The variations in the gain are stable over time and are removed by the bandpass calibration. Sharp peaks at and below 2500 MHz are caused by various RFI sources, not all of which have been identified yet.

Table A1. Frequency range of the MeerKAT *S* sub-bands.

Sub-band	Frequency range (MHz)
*S*0	1750.00–2625.00
*S*1	1968.75–2843.75
*S*2	2187.50–3062.50
*S*3	2406.25–3281.25
*S*4	2625.00–3500.00

the flux calibrator J0408–6545 in each of our DEEP2 observations (Section 2.1) at elevations of 55° and 48° in *S*1 and *S*4, respectively. These scans were calibrated for the bandpass response, fringe-fitted for dispersive and non-dispersive delays plus residual phases, and the resulting solutions applied. The source spectrum in instrument units was determined from the amplitudes of the calibration solutions. The noise levels in the same units were derived from the data weights, which are based on the autocorrelation powers. To test consistency and confirm the correct scaling, we compared with alternative measures using the rms variations of the visibilities. This was done on the absolute values, but also on differences between adjacent times or frequency channels, so that residual gain variations do not affect the results. All these estimates were consistent with each other.

The baseline-based noise levels were reduced to station-based values and converted to a physical scale using the following flux density model for the calibrator:[9]

$$\log_{10} S = -0.9790 + 3.3662 \log_{10} f - 1.1216 \log_{10}^2 f + 0.0861 \log_{10}^3 f, \quad \text{(A1)}$$

where S is the flux density in Jy and f the frequency in MHz. These total noise levels are the sum of the source flux density and system equivalent flux density (SEFD). The resulting SEFD for a representative antenna is shown as a function of frequency in Fig. A1.

[9]The model was obtained from the MeerKAT Knowledge Base.

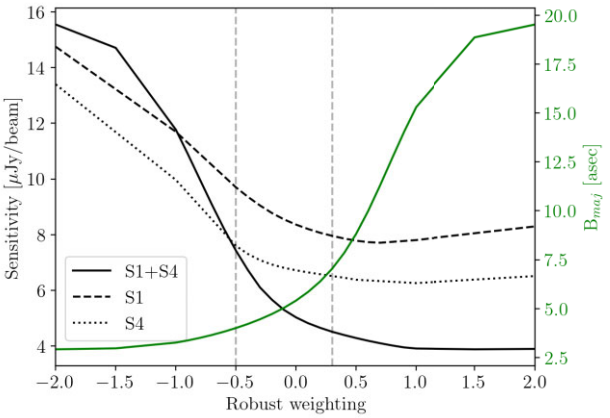

Figure B1. Image sensitivity (black) and the major axis of the restoring beam (green) as a function of robust weighting. The concatenated data are indicated by the solid lines, and the *S*1 and *S*4 sub-bands are shown as dashed and dotted lines, respectively. The grey dashed vertical lines indicated the chosen weighting values for the final images.

APPENDIX B: ROBUST PARAMETERS

We investigate the optimal Briggs robust parameter to maximize the sensitivity of the observations, the number of sources detected and the angular resolution of our images. To test this, we imaged the concatenated data sets at Briggs robust values from $R = [-2, 2]$, with an interval of 0.5, and a decreased interval of 0.1 between $R = -0.5$ and $R = 0.5$. Fig. B1 shows the resultant image sensitivity and angular resolution of the MFS images as a function of robust weighting. Here, the sensitivity is estimated from the residual images provided by `WSClean`. We note that the rms increases slightly at $R > 0.5$ for the *S*1 and *S*4 sub-bands. This trend is not present in the concatenated data set.

For completeness, we execute source-finding for all images with robust weighting $[-2, 2]$, as above. In Fig. B2, we show the number of detected sources, as a function of robust weighting. As expected, the number of sources increases with higher sensitivity, with the maximum number of sources detected at $R = 0.8$. At $R = 0.8$

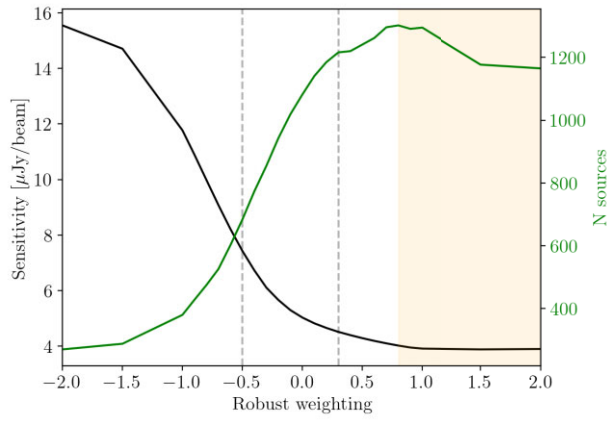

Figure B2. Image sensitivity (black) and the number of detected sources (green) as a function of robust weighting for the concatenated sub-bands. The grey dashed lines indicated the chosen weighting values for the final images. The shaded region indicates the robust values at which the number counts are affected by source confusion.

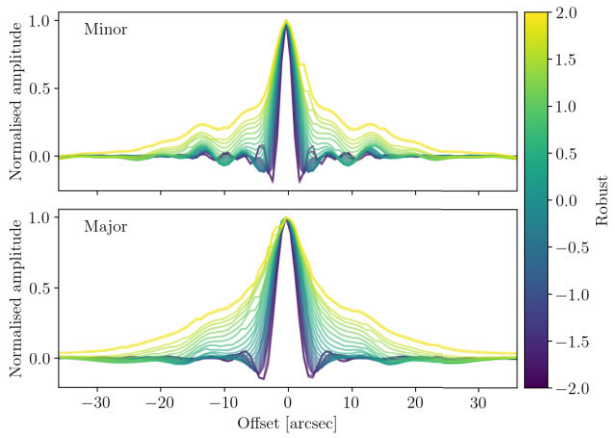

Figure B3. Cross section of the minor (top) and major (bottom) axes of the point spread function, colourized by Briggs robust value.

we have an angular resolution of $\theta = 13$ arcsec at a sensitivity of $\sigma = 4.01$ μJy beam^{-1}, which approaches the theoretical limit for the thermal noise of $\sigma = 3.38$ μJy beam^{-1}. The thermal noise is estimated for an observation using 55 antennas, and for the bandwidth and flagging percentage in the images presented here, and the image sensitivity is calculated as specified in Section 2.2 for Fig. B1. At higher robust values, the number of detected sources decreases, as source confusion and PSF sidelobes start to add to the noise. To quantify this, we consider the residuals between the normalized PSF and restoring beams. We compute this for the cross-section across the major and minor axes of the respective beams, and take the standard deviation $\sigma_{\rm PSF,res}$ to quantify the residuals. The cross-sections of the PSF across the major and minor axes for each robust value are shown in Fig. B3. Between $-2.0 < R < 0.5$, we have typical $\sigma_{\rm PSF,res}$ between 0.02 and 0.04, whereas we find increased residuals beyond $R = 0.6$, rising to $\sigma_{\rm PSF,res} = 0.09$ for $R = 2.0$. The sidelobe amplitudes amount to ∼20 per cent for $R = 0.8$, and increase to ∼40 per cent for $R = 2.0$. Images with such weightings for short observations with MeerKAT *S*-band will be limited in their scientific interpretation. These weightings should be avoided due to resulting systematic errors (e.g. Radcliffe et al. 2024).

APPENDIX C: DIFFERENTIAL SOURCE COUNTS

In Section 4, we present the differential source counts for both robust weightings $R = 0.3$ and $R = -0.5$. Table C1 shows the number of sources for each flux density bin, as well as the Euclidean normalized counts and corrected counts for $R = 0.3$ and $R = -0.5$.

Table C1. Table of source counts for DEEP2 at *S*-band, for both the $R = 0.3$ and $R = -0.5$ images.

S (mJy)	$S_{\rm mean}$ (mJy)	N $R = 0.3$	Counts $R = 0.3$ (Jy$^{3/2}$ sr^{-1})	Corrected counts $R = 0.3$ (Jy$^{3/2}$ sr^{-1})	N $R = -0.5$	Counts $R = -0.5$ (Jy$^{3/2}$ sr^{-1})	Corrected counts $R = -0.5$ (Jy$^{3/2}$ sr^{-1})
0.022–0.028	0.025	31 ± 5	0.0264 ± 0.0047	0.656 ± 0.288	0	–	–
0.028–0.036	0.032	74 ± 8	0.0925 ± 0.0108	1.28 ± 0.42	5 ± 2	0.00625 ± 0.00280	0.495 ± 0.495
0.036–0.046	0.041	127 ± 11	0.233 ± 0.021	1.98 ± 0.53	20 ± 4	0.0367 ± 0.0082	1.43 ± 1.02
0.046–0.06	0.053	141 ± 11	0.38 ± 0.03	2.25 ± 0.48	53 ± 7	0.143 ± 0.020	2.26 ± 1.08
0.06–0.077	0.069	141 ± 11	0.557 ± 0.047	2.48 ± 0.47	66 ± 8	0.261 ± 0.032	2.51 ± 0.82
0.077–0.1	0.089	127 ± 11	0.737 ± 0.065	2.63 ± 0.46	72 ± 8	0.418 ± 0.049	2.74 ± 0.71
0.1–0.13	0.11	101 ± 10	0.86 ± 0.09	2.57 ± 0.42	76 ± 8	0.647 ± 0.074	3.17 ± 0.71
0.13–0.17	0.15	97 ± 9	1.21 ± 0.123	3.08 ± 0.47	59 ± 7	0.738 ± 0.096	2.89 ± 0.60
0.17–0.22	0.19	51 ± 7	0.936 ± 0.131	2.01 ± 0.34	48 ± 6	0.881 ± 0.127	2.70 ± 0.54
0.22–0.28	0.25	54 ± 7	1.45 ± 0.20	2.76 ± 0.44	46 ± 6	1.24 ± 0.18	3.34 ± 0.63
0.28–0.36	0.32	39 ± 6	1.54 ± 0.25	2.61 ± 0.46	35 ± 5	1.38 ± 0.23	3.23 ± 0.63
0.36–0.46	0.41	40 ± 6	2.32 ± 0.37	3.52 ± 0.60	33 ± 5	1.92 ± 0.33	3.87 ± 0.75
0.46–0.6	0.53	27 ± 5	2.30 ± 0.44	3.20 ± 0.65	23 ± 4	1.96 ± 0.41	3.52 ± 0.78
0.6–0.77	0.69	29 ± 5	3.63 ± 0.67	4.73 ± 0.91	25 ± 5	3.13 ± 0.63	5.12 ± 1.12
0.77–1	0.89	20 ± 4	3.67 ± 0.82	4.51 ± 1.03	15 ± 3	2.75 ± 0.71	4.11 ± 1.10
1–1.3	1.1	17 ± 4	4.58 ± 1.11	5.43 ± 1.33	20 ± 4	5.39 ± 1.20	7.45 ± 1.73
1.3–1.7	1.5	22 ± 4	8.70 ± 1.85	10.0 ± 2.2	16 ± 4	6.33 ± 1.58	8.22 ± 2.11
1.7–2.2	1.9	7 ± 2	4.06 ± 1.54	4.57 ± 1.73	10 ± 3	5.8 ± 1.84	7.19 ± 2.30
2.2–2.8	2.5	6 ± 2	5.11 ± 2.09	5.69 ± 2.33	9 ± 3	7.67 ± 2.56	9.14 ± 3.07
2.8–3.6	3.2	6 ± 2	7.50 ± 3.06	8.23 ± 3.37	3 ± 1	3.75 ± 2.17	4.33 ± 2.50
3.6–4.6	4.1	11 ± 3	20.2 ± 6.1	21.9 ± 6.7	11 ± 3	20.2 ± 6.1	22.9 ± 6.9
4.6–6	5.3	15 ± 3	40.4 ± 10.4	43.6 ± 11.3	14 ± 3	37.7 ± 10.1	42.1 ± 11.3
6–7.7	6.9	4 ± 2	15.8 ± 7.9	16.9 ± 8.5	3 ± 1	11.9 ± 6.9	13.0 ± 7.5
7.7–10	8.9	2 ± 1	11.6 ± 8.2	12.3 ± 8.7	2 ± 1	11.6 ± 8.2	12.3 ± 8.7
10–13	11	1 ± 1	8.52 ± 8.52	8.97 ± 8.97	1 ± 1	8.52 ± 8.52	8.99 ± 8.99
13–17	15	2 ± 1	25.0 ± 17.7	26.3 ± 18.6	3 ± 1	37.5 ± 21.7	39.3 ± 22.7
17–22	19	3 ± 1	55.1 ± 31.8	57.9 ± 33.4	1 ± 1	18.4 ± 18.4	19.3 ± 19.3
22–28	25	2 ± 1	53.9 ± 38.1	56.7 ± 40.1	1 ± 1	26.9 ± 26.9	28.3 ± 28.3

APPENDIX D: CATALOGUE

In Section 3.4, we present the MeerKAT DEEP2 catalogue at *S*-band frequencies. In Table D1, we describe each column of the catalogue in detail, and in Table D2, we provide an example of 10 random entries in the catalogue. The full catalogue can be found online on the SARAO archive at https://doi.org/10.48479/zdyz-8342.

Table D1. Description of catalogue columns.

Index	Name	Description
1	Source_name	Name of the source following IAU convention (JHHMMSS.ss±HHMMSS.s).
2	RA	Right ascension (J2000) of the source.
3	E_RA	Error (1σ) on right ascension of the source.
4	DEC	Declination (J2000) of the source.
5	E_DEC	Error (1σ) on declination of the source.
6	Sep_PC	Distance of source from the pointing centre.
7	Total_flux	Integrated flux density of the source based on Gaussian component fits.
8	E_Total_flux	Error (1σ) on Total_flux.
9	Peak_flux	Peak flux density of the source.
10	E_Peak_flux	Error (1σ) on peak flux density of the source.
11	Maj	FWHM of the major axis of the source.
12	E_Maj	Error (1σ) on FWHM of the major axis of the source.
13	Min	FWHM of the minor axis of the source.
14	E_Min	Error (1σ) on FWHM of the minor axis of the source.
15	PA	Position angle of the major axis of the source.
16	E_PA	Error (1σ) on position angle of the major axis of the source.
17	DC_Maj	FWHM of the deconvolved major axis of the source.
18	E_DC_Maj	Error (1σ) on FWHM of the deconvolved major axis of the source.
19	DC_Min	FWHM of the deconvolved minor axis of the source.
20	E_DC_Min	Error (1σ) on FWHM of the deconvolved minor axis of the source.
21	DC_PA	Position angle of the deconvolved major axis of the source.
22	E_DC_PA	Error (1σ) on position angle of the deconvolved major axis of the source.
23	Isl_Total_flux	Integrated flux density of the island on which the source is located.
24	E_Isl_Total_flux	Error (1σ) on Isl_Total_flux.
25	Isl_rms	Average background rms of the island on which the source is located.
26	Isl_mean	Average background mean of the island on which the source is located.
27	S_Code	Code defining the source structure. 'S' = fit by a single Gaussian component. 'M' = fit by multiple Gaussian components. 'C' = fit by a single Gaussian component on an island that contains other sources.
28	Resolved	Boolean indicating whether the source is resolved, as determined in Section 3.3.2.
29	Matthews_idx[a]	Indices of sources from the Matthews et al. (2021a) catalogue to which this source has been matched.
30	Matthews_flux[a]	Sum of integrated flux densities of all sources from the Matthews et al. (2021a) catalogue to which this source has been matched.
31	Alpha_LS[b]	Spectral index between *L*- and *S*-band of the source.
32	E_Alpha_LS[b]	Error (1σ) on spectral index between *L*- and *S*-band of the source.
33	Alpha_S[b]	In-band spectral index of the source.
34	E_Alpha_S[b]	Error (1σ) on in-band spectral index of the source.

Notes.[a]Cross-matching with *L*-band sources has only been performed for sources in the R = 0.3 catalogue.
[b]Spectral indices have only been determined for sources in the R = 0.3 catalogue detected above 10σ.

Table D2. Catalogue entries for 10 random sources out of the DEEP2 R = 0.3 *S*-band catalogue. The full catalogues can be obtained at https://doi.org/10.48479/zdyz-8342.

Source_name	RA	E_RA	DEC	E_DEC	Sep_PC	Total_flux	E_Total_flux	Peak_flux	E_Peak_flux
	(deg)	(deg)	(deg)	(deg)	(deg)	(mJy)	(mJy)	(mJy beam^{-1})	(mJy beam^{-1})
(1)	(2)	(3)	(4)	(5)	(6)	(7)	(8)	(9)	(10)
J040802.06–794945.6	62.008568	0.000157	−79.829332	0.000439	0.292	0.049	0.023	0.027	0.008
J041121.40–794623.8	62.839161	0.000059	−79.773264	0.000187	0.244	0.037	0.012	0.041	0.007
J041211.94–800800.2	63.049736	0.000201	−80.133381	0.000157	0.144	0.143	0.015	0.066	0.006
J041245.23–795936.8	63.188479	0.000033	−79.993568	0.000101	0.030	0.056	0.009	0.054	0.005
J041255.95–802105.5	63.233125	0.000048	−80.351540	0.000099	0.352	0.091	0.017	0.093	0.009
J041323.88–801419.4	63.349503	0.000045	−80.238712	0.000137	0.239	0.057	0.013	0.054	0.007
J041427.55–795357.0	63.614784	0.000087	−79.899159	0.000130	0.110	0.027	0.009	0.029	0.005
J041639.40–802053.5	64.164161	0.000035	−80.348191	0.000104	0.374	0.139	0.022	0.124	0.011
J041813.39–795449.4	64.555785	0.000102	−79.913723	0.000145	0.226	0.111	0.019	0.057	0.007
J042228.16–800416.9	65.617353	0.000010	−80.071365	0.000026	0.397	0.534	0.023	0.528	0.013

Maj	E_Maj	Min	E_Min	PA	E_PA	DC_Maj	E_DC_Maj	DC_Min	E_DC_Min	DC_PA	E_DC_PA
(arcsec)	(arcsec)	(arcsec)	(arcsec)	(deg)	(deg)	(arcsec)	(arcsec)	(arcsec)	(arcsec)	(deg)	(deg)
(11)	(12)	(13)	(14)	(15)	(16)	(17)	(18)	(19)	(20)	(21)	(22)
9.620	3.724	5.242	1.319	178.9	30.3	6.674	3.724	3.317	1.319	7.7	30.3
6.949	1.616	3.532	0.404	169.7	13.0	0.000	1.616	0.000	0.404	0.0	13.0
9.939	2.083	4.738	0.573	37.1	12.7	8.471	2.083	0.000	0.573	48.8	12.7
7.326	0.867	3.840	0.241	170.6	7.2	0.000	0.867	0.000	0.241	0.0	7.2
6.746	0.881	3.955	0.301	161.2	9.5	0.000	0.881	0.000	0.301	0.0	9.5
7.166	1.161	4.066	0.381	178.1	11.2	2.673	1.161	0.000	0.381	38.1	11.2
5.629	1.138	4.381	0.681	162.3	31.7	0.000	1.138	0.000	0.681	0.0	31.7
7.532	0.892	4.051	0.267	170.1	6.7	2.727	0.892	1.114	0.267	0.7	6.7
9.716	1.406	5.460	0.532	147.0	10.4	7.238	1.406	2.711	0.532	131.7	10.4
7.061	0.228	3.898	0.070	165.4	179.9	0.000	0.228	0.000	0.070	0.0	179.9

Isl_Total_flux	E_Isl_Total_flux	Isl_rms	Isl_mean	S_Code	Resolved	Matthews_idx	Matthews_flux	Alpha_LS
(mJy)	(mJy)	(mJy beam^{-1})	(mJy beam^{-1})				(mJy)	
(23)	(24)	(25)	(26)	(27)	(28)	(29)	(30)	(31)
0.037	0.008	0.008	1.216e-4	S	False	4062	0.101	–
0.026	0.006	0.008	−5.406e-4	S	False	6637	0.058	–
0.121	0.012	0.006	−3.955e-4	M	True	7323,7359	0.204	–
0.050	0.006	0.005	−6.689e-5	S	False	7768	0.086	–
0.075	0.011	0.010	4.017e-4	S	False	7915	0.219	–
0.046	0.007	0.007	4.868e-5	S	False	8283	0.087	–
0.019	0.004	0.005	1.738e-4	S	False	9213	0.027	–
0.117	0.013	0.011	9.564e-5	S	False	11113	0.225	–
0.086	0.009	0.007	−2.584e-4	S	True	12408	0.141	–
0.526	0.018	0.013	1.608e-3	S	False	15507	0.948	−0.355

E_Alpha_LS	Alpha_S	E_Alpha_S
(32)	(33)	(34)
–	–	–
–	–	–
–	–	–
–	–	–
–	–	–
–	–	–
–	–	–
–	–	–
–	–	–
0.156	0.169	0.462

This paper has been typeset from a TEX/LATEX file prepared by the author.

Bibliography

Adebahr, B. et al. (2022), *The Apertif science verification campaign. Characteristics of polarised radio sources*, A&A **663**, A103 A103, arXiv: 2203.16925 [astro-ph.GA].

Alger, M. J. et al. (2021), *Interpretable Faraday complexity classification*, PASA **38**, e022 e022, arXiv: 2102.10903 [astro-ph.IM].

Algera, H. S. B. et al. (2020), *A Multiwavelength Analysis of the Faint Radio Sky (COSMOS-XS): the Nature of the Ultra-faint Radio Population*, ApJ **903**, 139 139, arXiv: 2009.13531 [astro-ph.GA].

Anderson, C. S., B. M. Gaensler and I. J. Feain (2016), *A Study of Broadband Faraday Rotation and Polarization Behavior over 1.3–10 GHz in 36 Discrete Radio Sources*, ApJ **825**, 59 59, arXiv: 1604.01403 [astro-ph.HE].

Anderson, C. S., B. M. Gaensler, I. J. Feain and T. M. O. Franzen (2015), *Broadband Radio Polarimetry and Faraday Rotation of 563 Extragalactic Radio Sources*, ApJ **815**, 49 49, arXiv: 1511.04080 [astro-ph.GA].

Anderson, C. S. et al. (2018), *Broadband Radio Polarimetry of Fornax A. I. Depolarized Patches Generated by Advected Thermal Material from NGC 1316*, ApJ **855**, 41 41, arXiv: 1802.04812 [astro-ph.HE].

Anderson, C. S. et al. (2021), *Early Science from POSSUM: Shocks, turbulence, and a massive new reservoir of ionised gas in the Fornax cluster*, PASA **38**, e020 e020, arXiv: 2102.01702 [astro-ph.GA].

Arshakian, T. G. and R. Beck (2011), *Optimum frequency band for radio polarization observations*, MNRAS **418** 2336, arXiv: 1101.2631 [astro-ph.CO].

Ashton, G. et al. (2019), *BILBY: A user-friendly Bayesian inference library for gravitational-wave astronomy*, Astrophys. J. Suppl. **241** 27, arXiv: 1811.02042 [astro-ph.IM].

Baidoo, L. et al. (2023), *A Wideband Polarization Observation of Hydra A with the Jansky Very Large Array*, ApJ **955**, 16 16, arXiv: 2308.05805 [astro-ph.GA].

Baldwin, J. E. et al. (1970), *Maps of the distribution of polarization in five radiosources at 21.1-cm wavelength*, MNRAS **150** 253.

Banfield, J. K. et al. (2014), *Radio galaxies and their magnetic fields out to $z \leq 3$*, MNRAS **444** 700, arXiv: 1404.1638 [astro-ph.GA].

Basu, A. et al. (2017), *Detection of an ~20 kpc coherent magnetic field in the outskirt of merging spirals: the Antennae galaxies*, MNRAS **464** 1003, arXiv: 1609.04266 [astro-ph.GA].

Basu, A. et al. (2019), *An In-depth Investigation of Faraday Depth Spectrum Using Synthetic Observations of Turbulent MHD Simulations*, Galaxies **7** 89, arXiv: 1911.09029 [astro-ph.GA].

Beck, R. (2001), *Galactic and Extragalactic Magnetic Fields*, Space Sci. Rev. **99** 243, arXiv: astro-ph/0012402 [astro-ph].

Beck, R. (2015), *Magnetic fields in spiral galaxies*, A&ARv **24**, 4 4, arXiv: 1509.04522 [astro-ph.GA].

Beck, R., A. Brandenburg, D. Moss, A. Shukurov and D. Sokoloff (1996), *Galactic Magnetism: Recent Developments and Perspectives*, ARA&A **34** 155.

Begelman, M. C., R. D. Blandford and M. J. Rees (1984), *Theory of extragalactic radio sources*, Reviews of Modern Physics **56** 255.

Bell, E. F. (2003), *Estimating Star Formation Rates from Infrared and Radio Luminosities: The Origin of the Radio-Infrared Correlation*, ApJ **586** 794, arXiv: astro-ph/0212121 [astro-ph].

Berger, A. et al. (2021), *Faint polarised sources in the Lockman Hole field at 1.4 GHz*, A&A **653**, A155 A155, arXiv: 2107.02492 [astro-ph.CO].

Berger, A. et al. (2025), *Polarisation results from the GOODS-N field with Apertif and polarised source counts*, A&A **693**, A202 A202.

Best, P. N. and T. M. Heckman (2012), *On the fundamental dichotomy in the local radio-AGN population: accretion, evolution and host galaxy properties*, MNRAS **421** 1569, arXiv: 1201.2397 [astro-ph.CO].

Bhatnagar, S., T. J. Cornwell, K. Golap and J. M. Uson (2008), *Correcting direction-dependent gains in the deconvolution of radio interferometric images*, A&A **487** 419, arXiv: 0805.0834 [astro-ph].

Bhatnagar, S., U. Rau and K. Golap (2013), *Wide-field wide-band Interferometric Imaging: The WB A-Projection and Hybrid Algorithms*, ApJ **770**, 91 91, arXiv: 1304.4987 [astro-ph.IM].

Blandford, R. D. and R. L. Znajek (1977), *Electromagnetic extraction of energy from Kerr black holes.*, MNRAS **179** 433.

Bonaldi, A. et al. (2019), *The Tiered Radio Extragalactic Continuum Simulation (T-RECS)*, MNRAS **482** 2, arXiv: 1805.05222 [astro-ph.GA].

Brentjens, M. A. and A. G. de Bruyn (2005), *Faraday rotation measure synthesis*, A&A **441** 1217, arXiv: astro-ph/0507349 [astro-ph].

Bridle, A. H. and R. A. Perley (1984), *Extragalactic Radio Jets*, ARA&A **22** 319.

Briggs, D. S. (1995), *High fidelity deconvolution of moderately resolved sources*, PhD thesis: New Mexico Institute of Mining and Technology.

Brown, J. C., A. R. Taylor and B. J. Jackel (2003), *Rotation Measures of Compact Sources in the Canadian Galactic Plane Survey*, ApJS **145** 213.

Brown, J. C. et al. (2007), *Rotation Measures of Extragalactic Sources behind the Southern Galactic Plane: New Insights into the Large-Scale Magnetic Field of the Inner Milky Way*, ApJ **663** 258, arXiv: 0704.0458 [astro-ph].

Bruni, G. et al. (2020), *Hard X-ray selected giant radio galaxies - II. Morphological evidence of restarted radio activity*, MNRAS **494** 902, arXiv: 2003.09183 [astro-ph.GA].

Burn, B. J. (1966), *On the depolarization of discrete radio sources by Faraday dispersion*, MNRAS **133** 67.

Carilli, C. L. and G. B. Taylor (2002), *Cluster Magnetic Fields*, ARA&A **40** 319, arXiv: astro-ph/0110655 [astro-ph].

Carretti, E. et al. (2019), *S-band Polarization All-Sky Survey (S-PASS): survey description and maps*, MNRAS **489** 2330, arXiv: 1903.09420 [astro-ph.GA].

Carretti, E. et al. (2022), *Magnetic field strength in cosmic web filaments*, MNRAS **512** 945, arXiv: 2202.04607 [astro-ph.CO].

Chandrasekhar, S. (1946), *On the Radiative Equilibrium of a Stellar Atmosphere. XI.*, ApJ **104** 110.

Clark, S. E. and B. S. Hensley (2019), *Mapping the Magnetic Interstellar Medium in Three Dimensions over the Full Sky with Neutral Hydrogen*, ApJ **887**, 136 136, arXiv: 1909.11673 [astro-ph.GA].

Clarke, D. A., J. O. Burns and M. L. Norman (1992), *VLA Observations of the Inner Lobes of Centaurus A*, ApJ **395** 444.

Collier, J. D. et al. (2018), *High-resolution observations of low-luminosity gigahertz-peaked spectrum and compact steep-spectrum sources*, MNRAS **477** 578, arXiv: 1802.09666 [astro-ph.GA].

Condon, J. J. (1984), *Cosmological evolution of radio sources found at 1.4 GHz*, ApJ **284** 44.

Condon, J. J. (1992), *Radio emission from normal galaxies.*, ARA&A **30** 575.

Condon, J. J. et al. (1998), *The NRAO VLA Sky Survey*, AJ **115** 1693.

Condon, J. J. and S. M. Ransom (2016), *Essential Radio Astronomy*.

Condon, J. (2015), *An Analysis of the VLASS Proposal*, arXiv e-prints, arXiv:1502.05616 arXiv:1502.05616, arXiv: 1502.05616 [astro-ph.IM].

Cooper, B. F. C. and R. M. Price (1962), *Faraday Rotation Effects associated with the Radio Source Centaurus A*, Nature **196** 761.

Cotton, W. D. (1994), *Widefield Polarization Correction of VLA Snapshot Images at 1.4 GHz*, AIPS Memo 86.

Cotton, W. D. et al. (2018), *The Angular Size Distribution of μJy Radio Sources*, ApJ **856**, 67 67, arXiv: 1802.04209 [astro-ph.GA].

Cotton, W. D. et al. (2020), *Hydrodynamical backflow in X-shaped radio galaxy PKS 2014-55*, MNRAS **495** 1271, arXiv: 2005.02723 [astro-ph.GA].

Crutcher, R. M. (2012), *Magnetic Fields in Molecular Clouds*, ARA&A **50** 29.

Darvish, B. et al. (2017), *Cosmic Web of Galaxies in the COSMOS Field: Public Catalog and Different Quenching for Centrals and Satellites*, ApJ **837**, 16 16, arXiv: 1611.05451 [astro-ph.GA].

de Villiers, M. S. (2023), *MeerKAT Holography Measurements in the UHF, L, and S Bands*, AJ **165**, 78 78, arXiv: 2301.06752 [astro-ph.IM].

Delhaize, J. et al. (2017), *The VLA-COSMOS 3 GHz Large Project: The infrared-radio correlation of star-forming galaxies and AGN to $z \lesssim 6$*, A&A **602**, A4 A4, arXiv: 1703.09723 [astro-ph.GA].

Delhaize, J. et al. (2021), *MIGHTEE: are giant radio galaxies more common than we thought?*, MNRAS **501** 3833, arXiv: 2012.05759 [astro-ph.GA].

Delvecchio, I. et al. (2017), *The VLA-COSMOS 3 GHz Large Project: AGN and host-galaxy properties out to $z \lesssim 6$*, A&A **602**, A3 A3, arXiv: 1703.09720 [astro-ph.GA].

Dickey, J. M. et al. (2019), *The Galactic Magneto-ionic Medium Survey: Moments of the Faraday Spectra*, ApJ **871**, 106 106, arXiv: 1812.05399 [astro-ph.GA].

Dunne, L. et al. (2009), *The star formation history of K-selected galaxies*, MNRAS **394** 3, arXiv: 0808.3139 [astro-ph].

Elmouttie, E. et al. (1995), *The polarized radio lobes of the Circinus galaxy*, MNRAS **275** L53.

Eyles, R. A. J. et al. (2020), *The XXL Survey. XXXIX. Polarised radio sources in the XXL-South field*, A&A **633**, A6 A6, arXiv: 1911.03502 [astro-ph.GA].

Fairall, A. P. and P. A. Woudt (2006), *A sample of galaxies near the South Celestial Pole*, MNRAS **366** 267.

Fanaroff, B. L. and J. M. Riley (1974), *The morphology of extragalactic radio sources of high and low luminosity*, MNRAS **167** 31P.

Faraday, M. (1846), *On the Magnetization of Light and the Illumination of Magnetic Lines of Force*. Experimental Researches in Electricity, The Royal Society.

Farnes, J. S., S. P. O'Sullivan, M. E. Corrigan and B. M. Gaensler (2014), *Faraday Rotation from Magnesium II Absorbers toward Polarized Background Radio Sources*, ApJ **795**, 63 63, arXiv: 1406.2526 [astro-ph.GA].

Farnsworth, D., L. Rudnick and S. Brown (2011), *Integrated Polarization of Sources at $\lambda \sim 1$ m and New Rotation Measure Ambiguities*, AJ **141**, 191 191, arXiv: 1103.4149 [astro-ph.CO].

Ferrière, K., J. L. West and T. R. Jaffe (2021), *The correct sense of Faraday rotation*, MNRAS **507** 4968, arXiv: 2106.03074 [astro-ph.GA].

Fletcher, A., R. Beck, A. Shukurov, E. M. Berkhuijsen and C. Horellou (2011), *Magnetic fields and spiral arms in the galaxy M51*, MNRAS **412** 2396, arXiv: 1001.5230 [astro-ph.CO].

Frail, D. A. et al. (2024), *An Image-based Search for Pulsar Candidates in the MeerKAT Bulge Survey*, ApJ **975**, 34 34, arXiv: 2407.01773 [astro-ph.HE].

Franzen, T. M. O. et al. (2015), *ATLAS - I. Third release of 1.4 GHz mosaics and component catalogues*, MNRAS **453** 4020, arXiv: 1508.03150 [astro-ph.GA].

Gaensler, B. M. et al. (2001), *Radio Polarization from the Inner Galaxy at Arcminute Resolution*, ApJ **549** 959, arXiv: astro-ph/0010518 [astro-ph].

Gaensler, B. M. et al. (2005), *The Magnetic Field of the Large Magellanic Cloud Revealed Through Faraday Rotation*, Science **307** 1610, arXiv: astro-ph/0503226 [astro-ph].

Gaensler, B. M. et al. (2025), *The Polarisation Sky Survey of the Universe's Magnetism (POSSUM): Science goals and survey description*, PASA **42**, e091 e091, arXiv: 2505.08272 [astro-ph.GA].

Gaensler, B. M., T. L. Landecker, A. R. Taylor and POSSUM Collaboration (2010), "Survey Science with ASKAP: Polarization Sky Survey of the Universe's Magnetism (POSSUM)", *American Astronomical Society Meeting Abstracts #215*, vol. 215, American Astronomical Society Meeting Abstracts 470.13 470.13.

Gaia Collaboration (2020), *VizieR Online Data Catalog: Gaia EDR3 (Gaia Collaboration, 2020)*.

Gaia Collaboration et al. (2023), *Gaia Data Release 3. Summary of the content and survey properties*, A&A **674**, A1 A1, arXiv: 2208.00211 [astro-ph.GA].

Galluzzi, V. et al. (2018), *Characterization of polarimetric and total intensity behaviour of a complete sample of PACO radio sources in the radio bands*, MNRAS **475** 1306, arXiv: 1711.05373 [astro-ph.GA].

Gardner, F. F. and J. B. Whiteoak (1966), *The Polarization of Cosmic Radio Waves*, ARA&A **4** 245.

Garrington, S. T., J. P. Leahy, R. G. Conway and R. A. Laing (1988), *A systematic asymmetry in the polarization properties of double radio sources with one jet*, Nature **331** 147.

Gaustad, J. E., P. R. McCullough, W. Rosing and D. Van Buren (2001), *A Robotic Wide-Angle Hα Survey of the Southern Sky*, PASP **113** 1326, arXiv: astro-ph/0108518 [astro-ph].

George, S. J., J. M. Stil and B. W. Keller (2012), *Detection Thresholds and Bias Correction in Polarized Intensity*, PASA **29** 214, arXiv: 1106.5362 [astro-ph.IM].

Gozaliasl, G. et al. (2019), *Chandra centres for COSMOS X-ray galaxy groups: differences in stellar properties between central dominant and offset brightest group galaxies*, MNRAS **483** 3545, arXiv: 1812.01604 [astro-ph.GA].

Grant, J. K. et al. (2010), *The DRAO Planck Deep Fields: The Polarization Properties of Radio Galaxies at 1.4 GHz*, ApJ **714** 1689, arXiv: 1003.4460 [astro-ph.CO].

Gressel, O., D. Elstner, U. Ziegler and G. Rüdiger (2008), *Direct simulations of a supernova-driven galactic dynamo*, A&A **486** L35, arXiv: 0805.2616 [astro-ph].

Guidetti, D., R. A. Laing, A. H. Bridle, P. Parma and L. Gregorini (2011), *Ordered magnetic fields around radio galaxies: evidence for interaction with the environment*, MNRAS **413** 2525, arXiv: 1101.1807 [astro-ph.CO].

Haffner, L. M. et al. (2003), *The Wisconsin Hα Mapper Northern Sky Survey*, ApJS **149** 405, arXiv: astro-ph/0309117 [astro-ph].

Hale, C. L. et al. (2023), *MIGHTEE: deep 1.4 GHz source counts and the sky temperature contribution of star-forming galaxies and active galactic nuclei*, MNRAS **520** 2668, arXiv: 2211.05741 [astro-ph.GA].

Hale, C. L. et al. (2021), *The Rapid ASKAP Continuum Survey Paper II: First Stokes I Source Catalogue Data Release*, PASA **38**, e058 e058, arXiv: 2109.00956 [astro-ph.GA].

Hales, C. A., R. P. Norris, B. M. Gaensler and E. Middelberg (2014), *ATLAS 1.4 GHz data release 2 - II. Properties of the faint polarized sky*, MNRAS **440** 3113, arXiv: 1403.5308 [astro-ph.GA].

Hales, C. A. et al. (2012), *BLOBCAT: software to catalogue flood-filled blobs in radio images of total intensity and linear polarization*, MNRAS **425** 979, arXiv: 1205.5313 [astro-ph.IM].

Hamaker, J. P., J. D. Bregman and R. J. Sault (1996), *Understanding radio polarimetry. I. Mathematical foundations.*, A&AS **117** 137.

Harvey-Smith, L., G. J. Madsen and B. M. Gaensler (2011), *Magnetic Fields in Large-diameter H II Regions Revealed by the Faraday Rotation of Compact Extragalactic Radio Sources*, ApJ **736**, 83 83, arXiv: 1106.0931 [astro-ph.GA].

Haslam, C. G. T., C. J. Salter, H. Stoffel and W. E. Wilson (1982), *A 408-MHZ All-Sky Continuum Survey. II. The Atlas of Contour Maps*, A&AS **47** 1.

Haverkorn, M., J. C. Brown, B. M. Gaensler and N. M. McClure-Griffiths (2008), *The Outer Scale of Turbulence in the Magnetoionized Galactic Interstellar Medium*, ApJ **680** 362, arXiv: 0802.2740 [astro-ph].

Haverkorn, M. (2015), "Magnetic Fields in the Milky Way", *Magnetic Fields in Diffuse Media*, ed. by A. Lazarian, E. M. de Gouveia Dal Pino and C. Melioli, vol. 407, Astrophysics and Space Science Library 483, arXiv: 1406.0283 [astro-ph.GA].

Haverkorn, M. and S. R. Spangler (2013), *Plasma Diagnostics of the Interstellar Medium with Radio Astronomy*, Space Sci. Rev. **178** 483, arXiv: 1304.1735 [astro-ph.GA].

Heald, G. (2009), "The Faraday rotation measure synthesis technique", *Cosmic Magnetic Fields: From Planets, to Stars and Galaxies*, ed. by K. G. Strassmeier, A. G. Kosovichev and J. E. Beckman, vol. 259, IAU Symposium 591.

Heald, G. et al. (2020), *Magnetism Science with the Square Kilometre Array*, Galaxies **8**, 53 53, arXiv: 2006.03172 [astro-ph.GA].

Heckman, T. M. and P. N. Best (2014), *The Coevolution of Galaxies and Supermassive Black Holes: Insights from Surveys of the Contemporary Universe*, ARA&A **52** 589, arXiv: 1403.4620 [astro-ph.GA].

Heesen, V. et al. (2019), *Calibrating the relation of low-frequency radio continuum to star formation rate at 1 kpc scale with LOFAR*, A&A **622**, A8 A8, arXiv: 1811.07968 [astro-ph.GA].

Heiles, C. and M. Haverkorn (2012), *Magnetic Fields in the Multiphase Interstellar Medium*, Space Sci. Rev. **166** 293.

Heywood, I. et al. (2022), *MIGHTEE: total intensity radio continuum imaging and the COSMOS/XMM-LSS Early Science fields*, MNRAS **509** 2150, arXiv: 2110.00347 [astro-ph.GA].

Heywood, I., M. J. Jarvis and J. J. Condon (2013), *Sample variance, source clustering and their influence on the counts of faint radio sources*, MNRAS **432** 2625, arXiv: 1302.2010 [astro-ph.CO].

HI4PI Collaboration et al. (2016), *HI4PI: A full-sky H I survey based on EBHIS and GASS*, A&A **594**, A116 A116, arXiv: 1610.06175 [astro-ph.GA].

Högbom, J. A. (1974), *Aperture Synthesis with a Non-Regular Distribution of Interferometer Baselines*, A&AS **15** 417.

Holschneider, M., R. Kronland-Martinet, J. Morlet and P. Tchamitchian (1989), "A Real-Time Algorithm for Signal Analysis with the Help of the Wavelet Transform", *Wavelets. Time-Frequency Methods and Phase Space*, ed. by J.-M. Combes, A. Grossmann and P. Tchamitchian 286.

Hugo, B. and R. Perley (2023), *Absolute linear polarization angle calibration using planetary bodies for MeerKAT and JVLA at cm wavelengths*, Public memo.

Hutschenreuter, S. et al. (2022), *The Galactic Faraday rotation sky 2020*, A&A **657**, A43 A43, arXiv: 2102.01709 [astro-ph.GA].

Hutschenreuter, S., M. Haverkorn, P. Frank, N. C. Raycheva and T. A. Enßlin (2023), *Disentangling the Faraday rotation sky*, arXiv e-prints, arXiv:2304.12350 arXiv:2304.12350, arXiv: 2304.12350 [astro-ph.GA].

Jagannathan, P., S. Bhatnagar, U. Rau and A. R. Taylor (2017), *Direction-dependent Corrections in Polarimetric Radio Imaging. I. Characterizing the Effects of the Primary Beam on Full-Stokes Imaging*, AJ **154**, 56 56, arXiv: 1706.01501 [astro-ph.IM].

Jarvis, M. et al. (2016), "The MeerKAT International GHz Tiered Extragalactic Exploration (MIGHTEE) Survey", *MeerKAT Science: On the Pathway to the SKA* 6 6, arXiv: 1709.01901 [astro-ph.GA].

Johnston-Hollitt, M. and G. Grimwood (2011), *Searching for Excess Rotation Measures in Galaxy Clusters with the NVSS*, Journal of Astrophysics and Astronomy **32** 539.

Jonas, J. and MeerKAT Team (2016), "The MeerKAT Radio Telescope", *MeerKAT Science: On the Pathway to the SKA* 1 1.

Karim, A. et al. (2011), *The Star Formation History of Mass-selected Galaxies in the COSMOS Field*, ApJ **730**, 61 61, arXiv: 1011.6370 [astro-ph.CO].

Kauffmann, G. et al. (2003), *The host galaxies of active galactic nuclei*, MNRAS **346** 1055, arXiv: astro-ph/0304239 [astro-ph].

Kierdorf, M. et al. (2020), *The magnetized disk-halo transition region of M 51*, A&A **642**, A118 A118, arXiv: 2007.00702 [astro-ph.GA].

Klein, U., U. Lisenfeld and S. Verley (2018), *Radio synchrotron spectra of star-forming galaxies*, A&A **611**, A55 A55, arXiv: 1710.03149 [astro-ph.GA].

Kothes, R., K. Fedotov, T. J. Foster and B. Uyanıker (2006), *A catalogue of Galactic supernova remnants from the Canadian Galactic plane survey. I. Flux densities, spectra, and polarization characteristics*, A&A **457** 1081.

Kothes, R., X. Sun, B. Gaensler and W. Reich (2018), *A Radio Continuum and Polarization Study of SNR G57.2+0.8 Associated with Magnetar SGR 1935+2154*, ApJ **852**, 54 54, arXiv: 1711.11146 [astro-ph.HE].

Kramer, M. et al. (2016), "The MeerKAT Max-Planck S-band System", *MeerKAT Science: On the Pathway to the SKA* 3 3.

Lacy, M. et al. (2020), *The Karl G. Jansky Very Large Array Sky Survey (VLASS). Science Case and Survey Design*, PASP **132**, 035001 035001, arXiv: 1907.01981 [astro-ph.IM].

Laing, R. A. (1988), *The sidedness of jets and depolarization in powerful extragalactic radio sources*, Nature **331** 149.

Laing, R. A., D. Guidetti, A. H. Bridle, P. Parma and M. Bondi (2011), *Deep imaging of Fanaroff-Riley Class I radio galaxies with lobes*, MNRAS **417** 2789, arXiv: 1107.2511 [astro-ph.CO].

Laing, R. A. et al. (2008), *Multifrequency VLA observations of the FR I radio galaxy 3C 31: morphology, spectrum and magnetic field*, MNRAS **386** 657, arXiv: 0803.2597 [astro-ph].

Lamee, M. et al. (2016), *Magnetic Field Disorder and Faraday Effects on the Polarization of Extragalactic Radio Sources*, ApJ **829**, 5 5, arXiv: 1607.04914 [astro-ph.GA].

Legodi, L. S., A. R. Taylor and J. M. Stil (2021), *Broad-band radio polarimetry of disc galaxies and AGN with KAT-7*, MNRAS **500** 576, arXiv: 2011.12592 [astro-ph.GA].

Leslie, S. K. et al. (2020), *The VLA-COSMOS 3 GHz Large Project: Evolution of Specific Star Formation Rates out to $z \sim 5$*, ApJ **899**, 58 58, arXiv: 2006.13937 [astro-ph.GA].

Livingston, J. D., N. M. McClure-Griffiths, B. M. Gaensler, A. Seta and M. J. Alger (2021), *Heightened Faraday complexity in the inner 1 kpc of the galactic centre*, MNRAS **502** 3814, arXiv: 2102.01139 [astro-ph.GA].

Livingston, J. D. et al. (2022), *A radio polarization study of magnetic fields in the Small Magellanic Cloud*, MNRAS **510** 260, arXiv: 2112.04044 [astro-ph.GA].

Loi, F. et al. (2025), *The MeerKAT Fornax Survey: IV. A close look at the cluster physics through the densest rotation measure grid*, A&A **694**, A125 A125, arXiv: 2501.05519 [astro-ph.CO].

Lorimer, D. R. and M. Kramer (2012), *Handbook of Pulsar Astronomy*.

Ma, Y. K., S. A. Mao, A. Ordog and J. C. Brown (2020), *The complex large-scale magnetic fields in the first Galactic quadrant as revealed by the Faraday depth profile disparity*, MNRAS **497** 3097, arXiv: 2007.07893 [astro-ph.GA].

Ma, Y. K. et al. (2023), *H I filaments as potential compass needles? Comparing the magnetic field structure of the Small Magellanic Cloud to the orientation of GASKAP-H I filaments*, MNRAS **521** 60, arXiv: 2302.04880 [astro-ph.GA].

Ma, Y. K. et al. (2019a), *A broad-band spectro-polarimetric view of the NVSS rotation measure catalogue - I. Breaking the $n\pi$-ambiguity*, MNRAS **487** 3432, arXiv: 1905.04313 [astro-ph.GA].

Ma, Y. K. et al. (2019b), *A broad-band spectro-polarimetric view of the NVSS rotation measure catalogue - II. Effects of off-axis instrumental polarization*, MNRAS **487** 3454, arXiv: 1905.04318 [astro-ph.GA].

Ma, Y. K. et al. (2025), *A new window into the sub-parsec scale magnetic field in the Milky Way? Unveiling small-scale magneto-ionic structures with Faraday complexity*, MNRAS **541** 306, arXiv: 2506.18968 [astro-ph.GA].

Mahatma, V. H. et al. (2021), *A low-frequency study of linear polarization in radio galaxies*, MNRAS **502** 273, arXiv: 2012.11990 [astro-ph.GA].

Manchester, R. N. (1972), *Pulsar Rotation and Dispersion Measures and the Galactic Magnetic Field.*, ApJ **172** 43.

Mao, S. A., E. Zweibel, A. Fletcher, J. Ott and F. Tabatabaei (2015), *Properties of the Magneto-ionic Medium in the Halo of M51 Revealed by Wide-band Polarimetry*, ApJ **800**, 92 92, arXiv: 1412.8320 [astro-ph.GA].

Mao, S. A. et al. (2008), *A Radio and Optical Polarization Study of the Magnetic Field in the Small Magellanic Cloud*, ApJ **688** 1029, arXiv: 0807.1532 [astro-ph].

Mao, S. A. et al. (2010), *A Survey of Extragalactic Faraday Rotation at High Galactic Latitude: The Vertical Magnetic Field of the Milky Way Toward the Galactic Poles*, ApJ **714** 1170, arXiv: 1003.4519 [astro-ph.GA].

Mao, S. A. et al. (2012), *New Constraints on the Galactic Halo Magnetic Field Using Rotation Measures of Extragalactic Sources toward the Outer Galaxy*, ApJ **755**, 21 21, arXiv: 1206.3314 [astro-ph.GA].

Matthews, A. M., J. J. Condon, W. D. Cotton and T. Mauch (2021a), *Cosmic Star Formation History Measured at 1.4 GHz*, ApJ **914**, 126 126, arXiv: 2104.11756 [astro-ph.GA].

Matthews, A. M., J. J. Condon, W. D. Cotton and T. Mauch (2021b), *Source Counts Spanning Eight Decades of Flux Density at 1.4 GHz*, ApJ **909**, 193 193, arXiv: 2101.07827 [astro-ph.GA].

Matthews, T. A. and A. R. Sandage (1963), *Optical Identification of 3C 48, 3C 196, and 3C 286 with Stellar Objects.*, ApJ **138** 30.

Mauch, T. et al. (2020), *The 1.28 GHz MeerKAT DEEP2 Image*, ApJ **888**, 61 61, arXiv: 1912.06212 [astro-ph.GA].

McClure-Griffiths, N. M., G. J. Madsen, B. M. Gaensler, D. McConnell and D. H. F. M. Schnitzeler (2010), *Measurement of a Magnetic Field in a Leading Arm High-velocity Cloud*, ApJ **725** 275, arXiv: 1009.5849 [astro-ph.GA].

McClure-Griffiths, N. M. et al. (2009), *Gass: The Parkes Galactic All-Sky Survey. I. Survey Description, Goals, and Initial Data Release*, ApJS **181** 398, arXiv: 0901.1159 [astro-ph.GA].

McConnell, D. et al. (2020), *The Rapid ASKAP Continuum Survey I: Design and first results*, PASA **37**, e048 e048, arXiv: 2012.00747 [astro-ph.IM].

McCracken, H. J. et al. (2012), *UltraVISTA: a new ultra-deep near-infrared survey in COSMOS*, A&A **544**, A156 A156, arXiv: 1204.6586 [astro-ph.CO].

McMullin, J. P., B. Waters, D. Schiebel, W. Young and K. Golap (2007), "CASA Architecture and Applications", *Astronomical Data Analysis Software and Systems XVI*, ed. by R. A. Shaw, F. Hill and D. J. Bell, vol. 376, Astronomical Society of the Pacific Conference Series 127.

Mesa, D. et al. (2002), *Polarization properties of extragalactic radio sources and their contribution to microwave polarization fluctuations*, A&A **396** 463, arXiv: astro-ph/0209502 [astro-ph].

Mohan, N. and D. Rafferty (2015), *PyBDSF: Python Blob Detection and Source Finder*, Astrophysics Source Code Library, record ascl:1502.007.

Murphy, E. J. (2009), *The Far-Infrared-Radio Correlation at High Redshifts: Physical Considerations and Prospects for the Square Kilometer Array*, ApJ **706** 482, arXiv: 0910.0011 [astro-ph.CO].

Norris, R. P. et al. (2013), *Radio Continuum Surveys with Square Kilometre Array Pathfinders*, PASA **30**, e020 e020, arXiv: 1210.7521 [astro-ph.CO].

Novak, M. et al. (2017), *The VLA-COSMOS 3 GHz Large Project: Cosmic star formation history since z 5*, A&A **602**, A5 A5, arXiv: 1703.09724 [astro-ph.GA].

O'Sullivan, S. et al. (2008), "Simulation of the Polarized Sky at 1.4 GHz", *The role of VLBI in the Golden Age for Radio Astronomy*, vol. 9 107 107, arXiv: 0902.1995 [astro-ph.CO].

O'Sullivan, S. P. et al. (2012), *Complex Faraday depth structure of active galactic nuclei as revealed by broad-band radio polarimetry*, MNRAS **421** 3300, arXiv: 1201.3161 [astro-ph.CO].

O'Sullivan, S. P. et al. (2015), *The Magnetic Field and Polarization Properties of Radio Galaxies in Different Accretion States*, ApJ **806**, 83 83, arXiv: 1504.06679 [astro-ph.GA].

O'Sullivan, S. P. et al. (2017), *Broad-band, radio spectro-polarimetric study of 100 radiative-mode and jet-mode AGN*, MNRAS **469** 4034, arXiv: 1705.00102 [astro-ph.GA].

O'Sullivan, S. P. et al. (2023), *The Faraday Rotation Measure Grid of the LOFAR Two-metre Sky Survey: Data Release 2*, MNRAS **519** 5723, arXiv: 2301.07697 [astro-ph.CO].

Ocker, S. K., L. D. Anderson, T. J. W. Lazio, J. M. Cordes and V. Ravi (2024), *Implications for Galactic Electron Density Structure from Pulsar Sightlines Intersecting H II Regions*, ApJ **974**, 10 10, arXiv: 2406.07664 [astro-ph.GA].

Offringa, A. R. et al. (2014), *WSCLEAN: an implementation of a fast, generic wide-field imager for radio astronomy*, MNRAS **444** 606, arXiv: 1407.1943 [astro-ph.IM].

Oppermann, N. et al. (2012), *An improved map of the Galactic Faraday sky*, A&A **542**, A93 A93, arXiv: 1111.6186 [astro-ph.GA].

Osinga, E. et al. (2025), *Probing cluster magnetism with embedded and background radio sources in Planck clusters*, A&A **694**, A44 A44, arXiv: 2408.07178 [astro-ph.CO].

Padmanabh, P. V. et al. (2023), *The MPIfR-MeerKAT Galactic Plane Survey - I. System set-up and early results*, MNRAS **524** 1291, arXiv: 2303.09231 [astro-ph.HE].

Pandhi, A. et al. (2025), *Improved Constraints on the Faraday Rotation toward Eight Fast Radio Bursts Using Dense Grids of Polarized Radio Galaxies*, ApJ **982**, 146 146, arXiv: 2502.12263 [astro-ph.GA].

Pasetto, A. et al. (2018), *Broadband radio spectro-polarimetric observations of high-Faraday-rotation-measure AGN*, A&A **613**, A74 A74, arXiv: 1801.09731 [astro-ph.GA].

Perger, K., S. Frey and K. É. Gabányi (2024), *Sub-mJy radio emission from high-redshift active galactic nuclei in the footprint of the VLA Sky Survey*, MNRAS **527** 3436, arXiv: 2311.01128 [astro-ph.GA].

Perley, R. A. (2010), *EVLA Antenna Polarization at L, S, and C Bands*, EVLA Memo 141.

Perley, R. A. and B. J. Butler (2013), *Integrated Polarization Properties of 3C48, 3C138, 3C147, and 3C286*, ApJS **206**, 16 16, arXiv: 1302.6662 [astro-ph.IM].

Perley, R. A. and B. J. Butler (2017), *An Accurate Flux Density Scale from 50 MHz to 50 GHz*, ApJS **230**, 7 7, arXiv: 1609.05940 [astro-ph.IM].

Perley, R. A., C. J. Chandler, B. J. Butler and J. M. Wrobel (2011), *The Expanded Very Large Array: A New Telescope for New Science*, ApJ **739**, L1 L1, arXiv: 1106.0532 [astro-ph.IM].

Perley, R. A., J. W. Dreher and J. J. Cowan (1984), *The jet and filaments in Cygnus A.*, ApJ **285** L35.

Piras, S. et al. (2024), *LOFAR Deep Fields: Probing the sub-mJy regime of polarized extragalactic sources in ELAIS-N1. I. The catalog*, A&A **687**, A267 A267, arXiv: 2406.08346 [astro-ph.CO].

Piras, S. et al. (2025), *LOFAR Deep Fields: Probing the sub-mJy regime of polarized extragalactic sources in ELAIS-N1: II. Analysis*, A&A **693**, A100 A100, arXiv: 2412.00988 [astro-ph.GA].

Planck Collaboration et al. (2016), *Planck 2015 results. XXV. Diffuse low-frequency Galactic foregrounds*, A&A **594**, A25 A25, arXiv: 1506.06660 [astro-ph.GA].

Prandoni, I. et al. (2010), *The ATESP 5 GHz radio survey. III. 4.8, 8.6 and 19 GHz follow-up observations of radio galaxies*, A&A **510**, A42 A42, arXiv: 0911.2697 [astro-ph.CO].

Pshirkov, M. S., P. G. Tinyakov and F. R. Urban (2016), *New Limits on Extragalactic Magnetic Fields from Rotation Measures*, Phys. Rev. Lett. **116**, 191302 191302, arXiv: 1504.06546 [astro-ph.CO].

Purcell, C. R., C. L. Van Eck, J. West, X. H. Sun and B. M. Gaensler (2020), *RM-Tools: Rotation measure (RM) synthesis and Stokes QU-fitting*, Astrophysics Source Code Library, record ascl:2005.003, ascl: 2005.003.

Purcell, C. R. et al. (2015), *A Radio-Polarisation and Rotation Measure Study of the Gum Nebula and Its Environment*, ApJ **804**, 22 22, arXiv: 1502.06296 [astro-ph.GA].

Radcliffe, J. F., R. J. Beswick, A. P. Thomson, A. Njeri and T. W. B. Muxlow (2024), *Revisiting a flux recovery systematic error arising from common deconvolution methods used in aperture-synthesis imaging*, MNRAS **527** 942, arXiv: 2309.00533 [astro-ph.IM].

Ramatsoku, M. et al. (2020), *Collimated synchrotron threads linking the radio lobes of ESO 137-006*, A&A **636**, L1 L1, arXiv: 2004.03203 [astro-ph.GA].

Ranchod, S. et al. (2024), *The Galactic latitude dependency of Faraday complexity in the S-PASS/ATCA RM catalogue*, A&A **686**, A104 A104, arXiv: 2403.13500 [astro-ph.GA].

Ranchod, S. et al. (2025), *A first glimpse at the MeerKAT DEEP2 field at S-band*, MNRAS **536** 3647, arXiv: 2412.09314 [astro-ph.GA].

Raycheva, N. C. et al. (2022), *Turbulent magnetic field in the H II region Sh 2-27*, A&A **663**, A170 A170, arXiv: 2206.01787 [astro-ph.GA].

Rees, M. J. (1967), *Studies in radio structure-II. The relaxation of relativistic electron spectra in self-absorbed radio sources*, MNRAS **136** 279.

Reynolds, S. P., B. M. Gaensler and F. Bocchino (2012), *Magnetic Fields in Supernova Remnants and Pulsar-Wind Nebulae*, Space Sci. Rev. **166** 231, arXiv: 1104.4047 [astro-ph.GA].

Riseley, C. J. et al. (2025), *Relighting the fire in Hickson Compact Group (HCG) 15: Magnetised fossil plasma revealed by the SKA Pathfinders and Precursors*, A&A **697**, A45 A45, arXiv: 2503.08840 [astro-ph.GA].

Robitaille, J. F. et al. (2017), *A new perspective on turbulent Galactic magnetic fields through comparison of linear polarization decomposition techniques*, MNRAS **468** 2957, arXiv: 1703.04469 [astro-ph.GA].

Rudnick, L. and F. N. Owen (2014), *The Distribution of Polarized Radio Sources >15 μJy in GOODS-N*, ApJ **785**, 45 45, arXiv: 1402.3637 [astro-ph.GA].

Ruzmaikin, A. A., D. D. Sokolov and A. M. Shukurov (1988), *Magnetic Fields of Galaxies*, vol. 133.

Rybicki, G. B. and A. P. Lightman (1979), *Radiative processes in astrophysics*.

Ryle, M. and P. A. G. Scheuer (1955), *The Spatial Distribution and the Nature of Radio Stars*, Proceedings of the Royal Society of London Series A **230** 448.

Sabater, J. et al. (2019), *The LoTSS view of radio AGN in the local Universe. The most massive galaxies are always switched on*, A&A **622**, A17 A17, arXiv: 1811.05528 [astro-ph.GA].

Saikia, D. J. and C. J. Salter (1988), *Polarization properties of extragalactic radio sources.*, ARA&A **26** 93.

Sarbadhicary, S. K. et al. (2021), *CHILES VERDES: Radio Variability at an Unprecedented Depth and Cadence in the COSMOS Field*, ApJ **923**, 31 31, arXiv: 2009.05056 [astro-ph.HE].

Sault, R. J., P. J. Teuben and M. C. H. Wright (1995), "A Retrospective View of MIRIAD", *Astronomical Data Analysis Software and Systems IV*, ed. by R. A. Shaw, H. E. Payne and J. J. E. Hayes, vol. 77, Astronomical Society of the Pacific Conference Series 433, arXiv: astro-ph/0612759 [astro-ph].

Schnitzeler, D. H. F. M. (2010), *The latitude dependence of the rotation measures of NVSS sources*, MNRAS **409** L99, arXiv: 1011.0737 [astro-ph.GA].

Schnitzeler, D. H. F. M., J. K. Banfield and K. J. Lee (2015), *Polarization signatures of unresolved radio sources*, MNRAS **450** 3579, arXiv: 1504.00017 [astro-ph.GA].

Schnitzeler, D. H. F. M., P. Katgert and A. G. de Bruyn (2009), *WSRT Faraday tomography of the Galactic ISM at $\lambda \sim 0.86$ m. I. The GEMINI data set at (l, b) = (181°, 20°)*, A&A **494** 611, arXiv: 0810.4211 [astro-ph].

Schnitzeler, D. H. F. M. and K. J. Lee (2017), *Finding a faint polarized signal in wide-band radio data*, MNRAS **466** 378, arXiv: 1611.09865 [astro-ph.IM].

Schnitzeler, D. H. F. M. et al. (2019), *S-PASS/ATCA: a window on the magnetic universe in the Southern hemisphere*, MNRAS **485** 1293, arXiv: 1902.09556 [astro-ph.GA].

Sebokolodi, M. L. L. et al. (2020), *A Wideband Polarization Study of Cygnus A with the Jansky Very Large Array. I. The Observations and Data*, ApJ **903**, 36 36, arXiv: 2009.06554 [astro-ph.GA].

Sekhar, S., P. Jagannathan, B. Kirk, S. Bhatnagar and R. Taylor (2022), *Direction-dependent Corrections in Polarimetric Radio Imaging. III. A-to-Z Solver-Modeling the Full Jones Antenna Aperture Illumination Pattern*, AJ **163**, 87 87, arXiv: 2107.10009 [astro-ph.IM].

Shanahan, R. et al. (2019), *Strong Excess Faraday Rotation on the Inside of the Sagittarius Spiral Arm*, ApJ **887**, L7 L7, arXiv: 1911.08536 [astro-ph.GA].

Shimwell, T. W. et al. (2017), *The LOFAR Two-metre Sky Survey. I. Survey description and preliminary data release*, A&A **598**, A104 A104, arXiv: 1611.02700 [astro-ph.IM].

Shimwell, T. W. et al. (2022), *The LOFAR Two-metre Sky Survey. V. Second data release*, A&A **659**, A1 A1, arXiv: 2202.11733 [astro-ph.GA].

Simard-Normandin, M. and P. P. Kronberg (1980), *Rotation measures and the galactic magnetic field.*, ApJ **242** 74.

Sinha, A., S. Mangla and A. Datta (2023), *The spectral study of the faint radio sources in the ELAIS N1 field*, arXiv e-prints, arXiv:2308.05192 arXiv:2308.05192, arXiv: 2308.05192 [astro-ph.GA].

Smirnov, O. M. (2011), *Revisiting the radio interferometer measurement equation. I. A full-sky Jones formalism*, A&A **527**, A106 A106, arXiv: 1101.1764 [astro-ph.IM].

Smolčić, V. et al. (2017a), *The VLA-COSMOS 3 GHz Large Project: Continuum data and source catalog release*, A&A **602**, A1 A1, arXiv: 1703.09713 [astro-ph.GA].

Smolčić, V. et al. (2017b), *The VLA-COSMOS 3 GHz Large Project: Multiwavelength counterparts and the composition of the faint radio population*, A&A **602**, A2 A2, arXiv: 1703.09719 [astro-ph.GA].

Smolčić, V. et al. (2016), *The XXL Survey. XI. ATCA 2.1 GHz continuum observations*, A&A **592**, A10 A10, arXiv: 1512.04322 [astro-ph.GA].

Šnidarić, I. et al. (2023), *LOFAR Deep Fields: Probing faint Galactic polarised emission in ELAIS-N1*, A&A **674**, A119 A119, arXiv: 2303.13152 [astro-ph.GA].

Sokoloff, D. D. et al. (1998), *Depolarization and Faraday effects in galaxies*, MNRAS **299** 189.

Speagle, J. S. (2020), *DYNESTY: a dynamic nested sampling package for estimating Bayesian posteriors and evidences*, MNRAS **493** 3132, arXiv: 1904.02180 [astro-ph.IM].

Sridhar, S. S., S. Breen, S. Whittley and L. Ball (2025), *SKAO Staged Delivery, Array Assemblies And Layouts*, SKAO-TEL-0002299 Revision 04.

Stil, J. and B. Keller (2015), "Stacking for Cosmic Magnetism with SKA Surveys", *Advancing Astrophysics with the Square Kilometre Array (AASKA14)* 112 112, arXiv: 1501.00390 [astro-ph.IM].

Stil, J. M., B. W. Keller, S. J. George and A. R. Taylor (2014), *Degree of Polarization and Source Counts of Faint Radio Sources from Stacking Polarized Intensity*, ApJ **787**, 99 99, arXiv: 1404.1859 [astro-ph.GA].

Stil, J. M., M. Krause, R. Beck and A. R. Taylor (2009), *The Integrated Polarization of Spiral Galaxy Disks*, ApJ **693** 1392, arXiv: 0810.2303 [astro-ph].

Stil, J. M., A. R. Taylor and C. Sunstrum (2011), *Structure in the Rotation Measure Sky*, ApJ **726**, 4 4, arXiv: 1010.5299 [astro-ph.GA].

Stimpson, M., M. J. Hardcastle and M. G. H. Krause (2025), *Numerical modelling of the lobes of radio galaxies – VI. Polarimetric simulations of universal pressure profile cluster atmospheres*, MNRAS **539** 1668.

Stokes, G. G. (1851), *On the Composition and Resolution of Streams of Polarized Light from different Sources*, Transactions of the Cambridge Philosophical Society **9** 399.

Subrahmanyan, R., R. D. Ekers, L. Saripalli and E. M. Sadler (2010), *ATLBS: the Australia Telescope Low-Brightness Survey*, MNRAS **402** 2792, arXiv: 0911.4571 [astro-ph.CO].

Sun, X. H. and W. Reich (2012), *Polarisation properties of Milky-Way-like galaxies*, A&A **543**, A127 A127, arXiv: 1206.3343 [astro-ph.GA].

Sun, X. H. et al. (2015), *Comparison of Algorithms for Determination of Rotation Measure and Faraday Structure. I. 1100-1400 MHz*, AJ **149**, 60 60, arXiv: 1409.4151 [astro-ph.IM].

Tasse, C. et al. (2018), *Faceting for direction-dependent spectral deconvolution*, A&A **611**, A87 A87, arXiv: 1712.02078 [astro-ph.IM].

Tasse, C. (2023), *killMS: Direction-dependent radio interferometric calibration package*, Astrophysics Source Code Library, record ascl:2305.005.

Taylor, A. R., J. M. Stil and C. Sunstrum (2009), *A Rotation Measure Image of the Sky*, ApJ **702** 1230.
Taylor, A. R. et al. (2003), *The Canadian Galactic Plane Survey*, AJ **125** 3145.
Taylor, A. R. et al. (2007), *Radio Polarimetry of the ELAIS N1 Field: Polarized Compact Sources*, ApJ **666** 201, arXiv: 0705.2736 [astro-ph].
Taylor, A. R. et al. (2024), *MIGHTEE polarization early science fields: the deep polarized sky*, MNRAS **528** 2511, arXiv: 2312.13230 [astro-ph.GA].
Taylor, G. B., C. L. Carilli and R. A. Perley, eds. (1999), *Synthesis Imaging in Radio Astronomy II*, vol. 180, Astronomical Society of the Pacific Conference Series.
Taziaux, S. et al. (2025), *Deep polarimetry study reveals double ring ORC-like structures*, arXiv e-prints, arXiv:2509.04981 arXiv:2509.04981, arXiv: 2509.04981 [astro-ph.GA].
Thomson, A. J. M. et al. (2023), *The Rapid ASKAP Continuum Survey III: Spectra and Polarisation In Cutouts of Extragalactic Sources (SPICE-RACS) first data release*, PASA **40**, e040 e040, arXiv: 2307.07207 [astro-ph.GA].
Thomson, R. C. and A. H. Nelson (1980), *The interpretation of pulsar rotation measures and the magnetic field of the galaxy*, MNRAS **191** 863.
Tucci, M., E. Martínez-González, L. Toffolatti, J. González-Nuevo and G. De Zotti (2004), *Predictions on the high-frequency polarization properties of extragalactic radio sources and implications for polarization measurements of the cosmic microwave background*, MNRAS **349** 1267, arXiv: astro-ph/0307073 [astro-ph].
Tucci, M. and L. Toffolatti (2012), *The Impact of Polarized Extragalactic Radio Sources on the Detection of CMB Anisotropies in Polarization*, Advances in Astronomy **2012**, 624987 624987, arXiv: 1204.0427 [astro-ph.CO].
Urry, C. M. and P. Padovani (1995), *Unified Schemes for Radio-Loud Active Galactic Nuclei*, PASP **107** 803, arXiv: astro-ph/9506063 [astro-ph].
Vallée, J. P. (2014), *Catalog of Observed Tangents to the Spiral Arms in the Milky Way Galaxy*, ApJS **215**, 1 1, arXiv: 1409.4801 [astro-ph.GA].
Vallée, J. P. (2022), *Catalog of spiral arm tangents (Galactic longitudes) in the Milky Way, and the age gradient based on various arm tracers*, New Astron. **97**, 101896 101896, arXiv: 2207.14220 [astro-ph.GA].
van Cittert, P. H. (1934), *Die Wahrscheinliche Schwingungsverteilung in Einer von Einer Lichtquelle Direkt Oder Mittels Einer Linse Beleuchteten Ebene*, Physica **1** 201.
van der Vlugt, D. et al. (2021), *An Ultradeep Multiband VLA Survey of the Faint Radio Sky (COSMOS-XS): Source Catalog and Number Counts*, ApJ **907**, 5 5, arXiv: 2009.13528 [astro-ph.GA].
Van Eck, C. L. et al. (2011), *Modeling the Magnetic Field in the Galactic Disk Using New Rotation Measure Observations from the Very Large Array*, ApJ **728**, 97 97, arXiv: 1012.2938 [astro-ph.GA].
Van Eck, C. L. et al. (2023), *RMTable2023 and PolSpectra2023: Standards for Reporting Polarization and Faraday Rotation Measurements of Radio Sources*, ApJS **267**, 28 28, arXiv: 2305.16607 [astro-ph.IM].
Vanderwoude, S. et al. (2024), *Prototype Faraday Rotation Measure Catalogs from the Polarisation Sky Survey of the Universe's Magnetism (POSSUM) Pilot Observations*, AJ **167**, 226 226, arXiv: 2403.15668 [astro-ph.GA].
Vardoulaki, E. et al. (2021), *FR-type radio sources at 3 GHz VLA-COSMOS: Relation to physical properties and large-scale environment*, A&A **648**, A102 A102, arXiv: 2009.10721 [astro-ph.GA].
Velović, V. et al. (2023), *MeerKAT view of the dancing ghosts - peculiar galaxy pair PKS 2130-538 in Abell 3785*, MNRAS **523** 1933, arXiv: 2304.14692 [astro-ph.GA].

Vernstrom, T. et al. (2021), *Discovery of magnetic fields along stacked cosmic filaments as revealed by radio and X-ray emission*, MNRAS **505** 4178, arXiv: 2101.09331 [astro-ph.CO].

Vidal, M., C. Dickinson, R. D. Davies and J. P. Leahy (2015), *Polarized radio filaments outside the Galactic plane*, MNRAS **452** 656, arXiv: 1410.4438 [astro-ph.GA].

Villiers, M. S. de and W. D. Cotton (2022), *MeerKAT Primary-beam Measurements in the L Band*, AJ **163** 135.

Wagenveld, J. D. et al. (2023), *The MeerKAT Absorption Line Survey: Homogeneous continuum catalogues towards a measurement of the cosmic radio dipole*, A&A **673**, A113 A113, arXiv: 2302.10696 [astro-ph.CO].

West, J. L. et al. (2016), *The connection between supernova remnants and the Galactic magnetic field: A global radio study of the axisymmetric sample*, A&A **587**, A148 A148, arXiv: 1510.08536 [astro-ph.GA].

White, R. L., D. J. Helfand, R. H. Becker, E. Glikman and W. de Vries (2007), *Signals from the Noise: Image Stacking for Quasars in the FIRST Survey*, ApJ **654** 99, arXiv: astro-ph/0607335 [astro-ph].

Whittam, I. H. et al. (2022), *MIGHTEE: the nature of the radio-loud AGN population*, MNRAS **516** 245, arXiv: 2207.12379 [astro-ph.GA].

Wilman, R. J. et al. (2008), *A semi-empirical simulation of the extragalactic radio continuum sky for next generation radio telescopes*, MNRAS **388** 1335, arXiv: 0805.3413 [astro-ph].

Wilson, W. E. et al. (2011), *The Australia Telescope Compact Array Broad-band Backend: description and first results*, MNRAS **416** 832, arXiv: 1105.3532 [astro-ph.IM].

Zernike, F. (1938), *The concept of degree of coherence and its application to optical problems*, Physica **5** 785.

Zwart, J. T. L. et al. (2014), *The star formation history of mass-selected galaxies from the VIDEO survey*, **439** 1459, arXiv: 1401.1648 [astro-ph.CO].

List of Figures

List of Tables